

Universite Libre de Bruxelles
Faculte des Sciences



Detection of high energy electrons in the CMS detector at the LHC

Dissertation presented to obtain
the degree of Doctor of Science
Sherif Elgammal
30 October 2009

Acknowledgements

I would like to express my deepest grateful for my supervisors Prof. Pierre Marage and Prof. Barbara Clerbaux for their continuous support and helpful discussions concerning the analyses done in this thesis. Many thanks for many things I have learned from you not only in physics but also about the life at Brussels, and also for many social supports.

I want to thanks as well Dr. Gilles De Lentdecker and Dr. Matthias Mozer for discussing many aspects in programming using C++, which were really helpful.

Many thanks for Prof. Chris Seez, Prof. Chris Tully and Dr. Pascal Vanlaer (conveners of EGAMMA group at CERN), and Prof. Albert De Roeck and Prof. Greg Landsberg (conveners of Exotica group at CERN), the members of the HEEP group and of the grid team at Brussels for help and support in these analyses.

I am grateful for all my colleagues from IIHE, both from ULB and VUB, for the nice time we had together during my PhD period, special thank for my colleagues Othman Charaf and Vincent Dero, who share with me the office, good times and the hard times as well.

I also want to take the opportunity to thank the “Fonds de la Recherche Scientifique” F.R.S.-FNRS for financing my PhD study at the ULB.

Finally, I am forever indebted to my dear wife and my parents for their understanding, endless patience and encouragement when it was most required. I am also highly grateful to my father and mother in law.

Contents

List of Figures	v
List of Tables	2
1 Introduction	3
2 Search for $Z' \rightarrow e^+e^-$, Drell-Yan and background	7
2.1 Heavy resonance search at hadron colliders	7
2.1.1 Models of extra neutral gauge bosons Z'	8
2.1.2 Model of Randall Sundrum gravitons	9
2.1.3 Constraints on Z' and RS Graviton production from different experiments	10
2.1.3.1 Constraints from CDF experiment	10
2.1.3.2 Constraints from D0 experiment	11
2.1.3.3 Expected constraints from the CMS experiment	12
2.2 Drell-Yan process	14
2.2.1 Differential cross section	14
2.2.2 Drell-Yan process at CDF and D0	16
2.3 Background processes	17
2.3.1 QCD background	18
2.3.1.1 QCD dijet production	18
2.3.1.2 QCD multi-jets production	19
2.3.2 W + Jet background	20
2.3.3 $t\bar{t}$ background	21
2.4 HEEP strategy	21
3 CMS detector	23
3.1 Introduction	23
3.2 The CMS tracking system	25
3.2.1 Pixel tracker	25
3.2.2 Strip tracker	26

3.2.3	Tracker control and read-out scheme	26
3.3	The electromagnetic calorimeter ECAL	27
3.3.1	Lead tungstate crystals	28
3.3.2	The mechanical design of the ECAL barrel (EB)	29
3.3.3	The mechanical design of the ECAL endcaps (EE)	30
3.3.4	The mechanical design of the ECAL preshowerers (ES)	34
3.4	ECAL trigger and data acquisition	35
3.4.1	Trigger primitives	35
3.4.2	Level-1 trigger (L1)	36
3.4.3	High-Level trigger (HLT)	36
3.5	The hadron calorimeter HCAL	37
3.5.1	The mechanical design of the HCAL barrel (HB)	37
3.5.2	The mechanical design of the HCAL endcap (HE)	38
3.5.3	The Outer Calorimeter (HO)	38
3.5.4	The Hadron Forward Calorimeter (HF)	39
3.5.5	The HCAL read-out electronics	39
3.6	The superconducting magnet	41
3.7	The muon system	42
4	Electron reconstruction and shower shape	45
4.1	Ecal clustering and superclustering algorithms	45
4.2	ECAL calibration and linearity	47
4.3	ECAL energy resolution measurements in test beams	48
4.4	Electromagnetic shower shape	51
4.4.1	Electromagnetic interactions	51
4.4.2	Parametrisation of electromagnetic showers	52
4.4.3	Material budgets in CMS	54
4.5	Hadronic shower shape	55
5	Identification of high energy electrons in CMS	57
5.1	Electron identification and HEEP electron selection	57
5.1.1	GSF Electrons	57
5.1.2	Electron identification	58
5.2	Event selection and efficiency	62
5.2.1	Triggers	62
5.2.2	Event selection and efficiencies from MC	63
5.2.3	Efficiency measurements from the data	65
5.2.3.1	Efficiency measurement at the Z pole	65

5.2.3.2	Efficiency measurement at high mass	66
5.3	Loose selection criteria	66
5.4	Background estimate and rejection	66
5.4.1	b-tag method	67
5.4.2	$e\mu$ method	68
5.4.3	Fake rate method	70
5.5	Dielectron mass spectrum	71
5.5.1	Z peak normalisation	71
5.5.2	High mass Drell-Yan cross section	72
6	Recovery of high p_t electrons lost in ECAL cracks	75
6.1	Introduction	75
6.1.1	Electron losses in ECAL cracks and the EB-EE gaps	75
6.1.2	Simulated samples	75
6.2	HCAL response to electromagnetic and hadronic showers	76
6.2.1	Clustering algorithm	76
6.2.2	Recalibration of the HCAL to electromagnetic showers	77
6.3	Effects of ECAL gaps and cracks on electron reconstruction and identification	78
6.3.1	Electron identification and losses	80
6.3.2	Drell-Yan event losses	82
6.4	Electron recovery in the EB-EE gap regions	83
6.4.1	Electron energy reconstruction	83
6.4.2	Electron efficiency after energy reconstruction	85
6.5	Recovery of lost Drell Yan events in the EB-EE gap regions	88
6.5.1	Electron identification criteria	88
6.5.2	Recovery conditions	91
6.5.3	Efficiency of Drell-Yan and heavy resonance production recovery	91
6.6	Backgrounds	92
6.6.1	QCD jet background	92
6.6.2	W+jet background	92
6.7	Electron recovery in case of a missing ECAL endcap at start-up	94
7	Calibration of CMS ECAL crystals for high p_t electrons	95
7.1	Distribution of the E_1/E_{25} energy ratio	96
7.1.1	Simulation of energy deposits	96
7.1.2	X and Y variables	96
7.1.3	Barrel	96
7.1.4	Endcaps	99

7.2	Parameterisation of the E_1/E_{25} distributions and E_1 reconstruction	99
7.2.1	$F(X, Y; E, \eta)$ functions	99
7.2.2	Energy and η dependences of the $F(X, Y; E, \eta)$ functions	103
7.2.3	Reconstruction of E_1 using the $F(X, Y; E, \eta)$ functions	103
7.2.4	Effects of Bremsstrahlung emission	107
7.3	Validation of high energy crystal calibration	109
7.4	Shower shape variable for the validation of high energy electron candidates	112
8	Saturation effect for high energy electrons in CMS ECAL crystals and correction	115
8.1	Energy reconstruction in the case of electronics saturation	115
9	Summary and conclusions	119
A	ECAL readout electronics	123
A.1	Front-end read-out electronics	123
A.2	Off-detector electronics	124
B	Electron recovery in case of a missing ECAL endcap at start-up	127
B.1	HCAL energy deposits and recovery criteria	128
B.2	Electron energy reconstruction; energy deposit $E_{2 \times 2}$	128
B.3	Electron identification criteria	129
B.4	Recovery conditions	132
B.5	Efficiency of Drell-Yan and heavy resonance production recovery	132
B.6	Backgrounds	134
B.7	Conclusions	135
C	Reconstruction of E_1 using the $F(X, Y; E, \eta)$ functions	137
	References	139

List of Figures

2.1	CDF upper limit on $\sigma(p\bar{p} \rightarrow X) \cdot Br(X \rightarrow e^+e^-)$ as a function of the mass of the X particle at 95% C.L., where X refers to a Z' (left) and to a RS graviton (right) [21].	10
2.2	Parameter k/\bar{M}_P as a function of RS graviton mass. The shading indicates the region excluded by CDF at the 95% C.L. [21].	11
2.3	Experimental upper limit, from DO experiment, at 95% confidence level for $Z' \rightarrow e^+e^-$ (left) and $G \rightarrow e^+e^-$ production (right) [23].	12
2.4	Expected 95% C. L. exclusion limits on the cross section of resonance production, normalised to the Z^0 cross section, as a function of the resonance mass for the SSM Z' , Z'_ψ and RS gravitons ($c = 0.1$ and $c = 0.05$) signals; for integrated luminosity of 100 pb^{-1} . The grey band, for SSM Z' , shows the variations of the limit when systematic uncertainties are taken into account [10].	13
2.5	The 2 lowest order Feynman diagrams for Drell-Yan process in hadron-hadron collider.	14
2.6	One of the Feynman diagrams for the higher order QCD corrections to the Drell-Yan process.	16
2.7	Invariant mass distribution of e^+e^- events measured by the CDF collaboration [21], compared to the expected backgrounds. Dots with error bars are data. The light shaded region shows dijet and W +jet backgrounds, and the dark shaded region represents other SM background (see the text). The white region corresponds to the Drell-Yan distribution from Monte Carlo.	17
2.8	Invariant mass spectrum of e^+e^- pairs measured by the D0 collaboration [23] for data (given in the text), with the expected contributions from QCD multijet, W +jet and other SM backgrounds.	18
2.9	(left) Leading order Feynman diagrams for $gg \rightarrow gg$ production via the strong interaction; (right) an example of Feynman diagrams for 3 parton final state in hadron collisions.	18
2.10	The expected cross section of inclusive jet as a function of p_T for different rapidity ranges at the LHC [27].	19
2.11	Dijet mass distribution for different bins in jet p_T [27].	20
2.12	(left) Feynman diagram, at leading order, for W + one jet production via the strong interactions $gg \rightarrow Wq$; (right) one example of Feynman diagram, at next-to-leading order, for W + 2 jet production.	20
2.13	Leading order Feynman diagrams for $t\bar{t}$ production via the strong interaction.	21

3.1	Overall layout of CMS [31].	24
3.2	Layout of the pixel detectors in the CMS tracker [31].	25
3.3	Schematic cross section through the CMS tracker. Each line represents a detector module. Double lines indicates back-to-back modules which deliver stereo hits [30].	27
3.4	Longitudinal view of one quarter of the ECAL calorimeter [31].	28
3.5	Longitudinal trigger division [32].	29
3.6	Construction of the crystal ϕ tilt [32].	30
3.7	Simulation of an electromagnetic shower in crystals tilted in η in the ECAL barrel [32].	31
3.8	The ECAL endcap layout [32].	31
3.9	A single ECAL endcap with Dees moved apart [32].	32
3.10	(left plot) Shows the arrangement and mounting of supercrystals on a quadrant of the EE; (right plot) a front view of the conical cut through the EE [32].	33
3.11	Longitudinal view of the CMS detector showing the location of the hadron barrel (HB), endcap (HE), outer (HO) and forward (HF) calorimeters [31].	37
3.12	Sizes of the HCAL read-out towers in η and ϕ and depth segmentation [31].	40
3.13	Longitudinal view of one quarter of the HCAL calorimeter [31].	41
4.1	Domino construction steps of the Hybrid algorithm [38].	46
4.2	Illustration of the Island clustering algorithm [38].	46
4.3	The energy reconstructed as E_{25} before and after the intercalibration in a whole supermodule [41].	48
4.4	Distribution of the E_{25} peaks normalized to the beam energy, for two different crystals (labelled as 268 and 288) and for several positron beam energies [42].	49
4.5	ECAL energy resolution, $\sigma(E)/E$, as a function of the electron energy, as measured in test beams. The energy was measured in arrays of 3×3 crystals, with the electron impacting the central crystal. The points correspond to events taken when restricting the incident beam position to a narrow $4 \times 4 \text{ mm}^2$ region. The stochastic (S), noise (N) and constant (C) terms are given in the plot [43].	50
4.6	Distribution of the energy reconstructed in a 5×5 matrix, before and after correction for the containment, when 120 GeV electrons are incident over a $20 \times 20 \text{ mm}^2$ area [43].	50
4.7	Energy resolution with electron beam [42].	51
4.8	Longitudinal distribution of the energy deposit, $f(t) = 1/EdE/dt$, as a function of the shower depth, t , expressed in units of X_0 , for 100, 500 and 4000 GeV electrons, following the parametrisation of ref. [44].	53
4.9	(left) Total thickness in X_0 of the ECAL as a function of η , averaged over ϕ [32]; (right) material budget in front of the ECAL as a function of $ \eta $ [48].	54
4.10	The ratio of the depth of the hadronic shower maximum (l_{max}) over the depth of the electromagnetic shower maximum (T) as a function of the energy of the incident particle.	56

- 5.1 Global high energy electron reconstruction and identification efficiencies, for the ECAL barrel ($|\eta| < 1.442$) (open points) and endcaps ($1.560 < |\eta| < 2.5$) (full points) electrons as a function of the electron E_T ; corresponding to HEEP selection criteria given by table.5.3 [9]. 64
- 5.2 Estimation of the $t\bar{t}$ background to the Drell-Yan spectrum, computed from the pseudo-data using the b -tag method for electron $E_t > 30$ GeV and $40 < M < 800$ GeV/ c^2 . The triangles are the background estimates obtained from the pseudo-data, the shaded histogram is the genuine distribution of the top background. The Monte Carlo statistics have been scaled to correspond to an integrated luminosity of 100 pb $^{-1}$ [10]. 68
- 5.3 For events selection using HEEP criteria, with $40 < M < 800$ GeV/ c^2 and each electron with $E_T > 25$ GeV, estimation of the sum of the dielectron backgrounds to the e^+e^- Drell-Yan spectrum, computed from the pseudo-data using $e\mu$ method. The points with error bars are the background estimates obtained from the pseudo-data, the histograms are the genuine distribution of the background. The Monte Carlo statistics have been scaled to correspond to an integrated luminosity of 100 pb $^{-1}$ [10]. 69
- 5.4 Dielectron invariant mass spectrum for a 100 pb $^{-1}$ pseudo-experiment, compared to SM background estimates for the Drell-Yan process, $t\bar{t}$, QCD dijets, W +jet, γ +jet and $\gamma\gamma$ [10]. 72
- 5.5 Dielectron invariant mass spectrum for a 100 pb $^{-1}$ pseudo-experiment including a 1 TeV/ c^2 Z' signal, compared to SM background estimates for the Drell-Yan process, $t\bar{t}$, QCD dijets, W +jet, γ +jet and $\gamma\gamma$ [10]. 73
- 5.6 Expected true dielectron mass spectrum, containing the Drell-Yan and various dielectron, W +jet, γ +jet and QCD multi-jet and $\gamma\gamma$ contributions, with two electrons candidates passing the HEEP selection criteria with $E_t > 50$ GeV and $120 < M < 600$ GeV/ c^2 . The samples are scaled to correspond to an integrated luminosity of 100 pb $^{-1}$ [10]. 73
- 5.7 (left) Expected e^+e^- mass spectrum for an integrated luminosity of 100 pb $^{-1}$, obtained from pseudo-experiments containing the Drell-Yan signal (right) shows the measured Drell-Yan spectrum as (left), after background subtraction the dashed histogram is the Drell-Yan mass spectrum produced by Mont Carlo simulation [10]. 74
- 6.1 (left) The hottest 2×2 HCAL cells among the 3×3 array of cells; (right) 4×4 array of cells including the hottest 2×2 cells. 76
- 6.2 (left) Distribution of the reconstructed over generated energy, with superimposed Gaussian fit, for 200 GeV "single gun" electrons uniformly distributed over the HCAL barrel region $|\eta| < 1.0$ when the ECAL calorimeter is taken as absent; (right) recalibration function for electron showers in the HCAL; the superimposed error bars are the width of the Gaussian fits [52]. 77
- 6.3 Fraction R_{ECAL} of the generated energy measured in the ECAL supercluster, plotted as a function of the supercluser pseudorapidity $|\eta|$, for "single gun" electrons with $p_t = 100$ GeV/ c (left plots) and $p_t = 500$ GeV/ c (right plots); the error bars on the bottom plots represent the rms of the distributions [52]. 79

- 6.4 Efficiency for reconstructing electrons with ECAL $p_t > 80$ GeV/ c and $H/E < 0.10$, for “single gun” samples with $p_t = 100$ GeV/ c , as a function of (a) the pseudorapidity $|\eta|$; (b) the azimuthal angle $|\phi|$ (the η cracks and gap regions quoted in Table 6.2 are excluded), for the barrel region with $|\eta| < 1.44$; (c) and (d) the x and y coordinates, for the endcap region ($1.6 < |\eta| < 2.4$) [52]. 81
- 6.5 Same as figure 6.4, for $p_t = 500$ GeV/ c [52]. 82
- 6.6 Ratio $(E_{17} + E_{19})/(E_{17} + E_{18} + E_{19})$ of the energy deposits in the ϕ -adjacent HCAL cells of tower 17 and in the first segmentation of tower 19 over the energy deposits in towers 17, 18 and 19 (including HCAL recalibration), for “single gun” electrons emitted toward the EB-EE gap region and which do not pass the minimum identification conditions (6.2); (left) $p_t = 100$ GeV/ c ; (right) $p_t = 500$ GeV/ c 84
- 6.7 Ratio $R_{\text{reco}} = E_{\text{reco}}/E_{\text{true}}$ of the reconstructed (including HCAL recalibration) over generated energies, for “single gun” electrons emitted toward the EB-EE gap region and which do not pass the minimum identification conditions (6.2); the reconstructed energy E_{reco} is computed before adding the energy of a possible second associated supercluster: (left) $p_t = 100$ GeV/ c ; (right) $p_t = 500$ GeV/ c 85
- 6.8 Ratio $R_{\text{reco}} = E_{\text{reco}}/E_{\text{true}}$ of the reconstructed (including HCAL recalibration) over generated energies, for “single gun” electrons emitted toward the EB-EE gap region and which do not pass the minimum identification conditions (6.2); the reconstructed energy E_{reco} is computed after adding the energy of a possible second associated supercluster: (top) $p_t = 100$ GeV/ c , bottom $p_t = 500$ GeV/ c ; (left) events with a reconstructed ECAL supercluster; (right) events with no supercluster [52]. 86
- 6.9 Distribution of the azimuthal angle ϕ corresponds to no energy deposit in the HCAL. 86
- 6.10 Fraction R_{ECAL} of the generated energy measured in the ECAL supercluster, after energy correction “ E_{reco} ” in the gap region ($1.453 < |\eta| < 1.563$), plotted as a function of the supercluster pseudorapidity $|\eta|$, for “single gun” electrons with $p_t = 100$ GeV/ c (left plots) and $p_t = 500$ GeV/ c (right plots); the error bars on the bottom plots represent the rms of the distributions. 87
- 6.11 After energy reconstruction (E_{reco}) in the gap region ($1.453 < |\eta| < 1.563$), plots for efficiency are introduced as a function of the supercluster pseudorapidity $|\eta|$, for “single gun” electrons with $p_t = 100$ GeV/ c (left plots) and $p_t = 500$ GeV/ c (right plots), for reconstructing electrons with $p_t > 80$ GeV/ c and $H/E < 0.10$ 87

- 6.12 Discriminating variables for electron identification, for particles emitted toward the EB-EE gap, which do not pass the minimum electron identification conditions (6.2) and for which the transverse momentum computed from E_{reco} is larger than $80 \text{ GeV}/c$: (left) ratio $E_{\text{H2}}/E_{\text{reco}}$ of the energies deposited in the second segmentation of tower 18, E_{H2} , and the energies deposited in the first segmentation and (when applicable) the ECAL supercluster(s), E_{reco} ; (centre) total transverse energy, ΣE_t , deposited in the HCAL between two cones with axes along the electron candidate direction with $0.25 < \Delta R < 0.50$, for $80 < p_t(E_{\text{reco}}) < 200 \text{ GeV}/c$; (right) $\Sigma E_t/E_{t,\text{reco}}$, for $p_t(E_{\text{reco}}) > 200 \text{ GeV}/c$. At least one electron in the event has to pass the HEEP conditions (given in Table 5.9). The distributions for electrons candidates from the Drell-Yan signal are shown as shaded histograms, those from the QCD and W+jet backgrounds as white histograms. The signal and background distributions are normalised to unity [52]. 89
- 6.13 Same as in figure 6.12, for (left) tracker isolation: number of tracks with $p_t > 1.5 \text{ GeV}/c$ emitted between two cones ($0.1 < \Delta R < 0.2$) around the electron candidate direction; (right) tracker isolation: vectorial sum of the transverse momenta of these tracks, divided by $p_t(E_{\text{reco}})$ [52]. 90
- 6.14 Track matching for electron candidates emitted toward the EB-EE gap: number of tracks with $p_t > 20 \text{ GeV}/c$ emitted from the vertex and directed within a cone of radius $\Delta R < 0.15$ around the electron candidate direction; (left) electron candidates with $p_t(E_{\text{reco}}) > 80 \text{ GeV}/c$; (right) only electron candidates passing the isolation criteria are selected [52]. 90
- 6.15 Distribution of the ratio of the reconstructed M_{ee} over generated $M_{\gamma/Z}$ mass for e^+e^- events with both electrons emitted in the angular domain $|\eta| < 2.4$, when one of the electrons is emitted in the EB-EE gap direction and does not pass the minimum electron identification conditions (6.2), and which are recovered following the criteria (6.3): (a) Drell-Yan events with generated mass larger than $200 \text{ GeV}/c^2$; (b) Z' bosons with mass of $1 \text{ TeV}/c^2$ [52]. 92
- 6.16 Mass distribution of QCD and W+jet background for an integrated luminosity of 1 fb^{-1} , when one of the fake electrons is emitted toward the gap region, and which are passing the criteria (6.3). 94
- 7.1 Contributions of crystals from a 5×5 (η, ϕ) matrix to the quantities (a) $\Sigma E_{\text{smaller } |\eta|}$ and $\Sigma E_{\text{larger } |\eta|}$, for the X variable; (b) $\Sigma E_{\text{smaller } \phi}$ and $\Sigma E_{\text{larger } \phi}$, for the Y variable. 97
- 7.2 Energy ratio E_1/E_{25} for 1500 GeV incident electrons with $0.5 < |\eta| < 1.0$ (EB), plotted as a function of the variable X for (a) $0 < |Y| < 0.25$ and (b) $1.75 < |Y| < 2.00$, and as a function of the variable Y for (c) $0 < |X| < 0.25$ and (d) $1.75 < |X| < 2.00$ [48]. 98
- 7.3 Energy ratio E_1/E_{25} for 1500 GeV incident electrons in EB, plotted as a function of the variables X and Y for (a, c) $|\eta| < 0.5$ and (b, d) $1.00 < |\eta| < 1.44$ [48]. 98
- 7.4 Energy ratio E_1/E_{25} for 2500 GeV incident electrons with $1.8 < |\eta| < 2.2$ (EE), plotted as a function of the variable X for (a) $0 < |Y| < 0.25$ and (b) $1.75 < |Y| < 2.00$, and as a function of the variable Y for (c) $0 < |X| < 0.25$ and (d) $1.75 < |X| < 2.00$ [48]. 100

7.5	Energy ratio E_1/E_{25} for 2500 GeV incident electrons in EE, plotted as a function of the variables X and Y for (a, c) $1.56 < \eta < 1.8$ and (b, d) $2.2 < \eta < 2.5$ [48].	100
7.6	Different choices of the one dimensional fit function; (a) $a \cdot (1 + cX^2)$	101
7.7	(left) Fitted functions $F(X, Y; E, \eta)$ for 1500 GeV electrons and corresponding distributions of the residuals $1 - [F(X, Y; E, \eta) / \langle E_1/E_{25} \rangle]$ for EB with $0.5 < \eta < 1.0$ (a-b) and for EE with $1.8 < \eta < 2.2$ (c-d) [48].	102
7.8	Ratio of fitted functions $F(X, Y; E, \eta)$ (a) for 2000 GeV electrons to 1000 GeV electrons, in the η range $0.5 < \eta < 1.0$ (EB); (b) for 4500 GeV electrons to 2500 GeV electrons, in the η range $1.8 < \eta < 1.2$ (EE) [48].	103
7.9	Ratio of fitted functions $F(X, Y; E, \eta)$ (a) in EB, for the η range $1.0 < \eta < 1.4$ to the η range $ \eta < 0.5$, for 1500 GeV electrons; (b) in EE, for the η range $2.2 < \eta < 2.5$ to the η range $1.56 < \eta < 1.8$, for 3500 GeV electrons [48].	104
7.10	Ratio of the fitted functions $F(X, Y; E, \eta)$ for 1500 GeV electrons to 1500 GeV positrons, (a) for $0.5 < \eta < 1.0$ (EB); (b) for $1.8 < \eta < 1.2$ (EE) [48].	104
7.11	Distributions of the normalised difference $(E_1^{\text{meas}} - E_1^{\text{rec}})/\langle E_1^{\text{meas}} \rangle$, for 1500 GeV electrons with $0.5 < \eta < 1.0$ (EB) and $1.8 < \eta < 2.2$ (EE) (a-b), and for 2500 GeV electrons (c-d) [48]. The errors on the average difference are less than 0.002.	105
7.12	Distributions of the normalised difference $(E_1^{\text{meas}} - E_1^{\text{rec}})/\langle E_1^{\text{meas}} \rangle$ for (a-b-c-d-e-f-g) 500, 1000, 1500, 2000, 2500, 3500 and 4500 GeV electrons with $ \eta < 1.44$ (EB). The errors on the average difference are less than 0.003.	106
7.13	Distributions of the normalised difference $(E_1^{\text{meas}} - E_1^{\text{rec}})/\langle E_1^{\text{meas}} \rangle$ for (a-b-c-d-e-f-g) 500, 1000, 1500, 2000, 2500, 3500 and 4500 GeV electrons with $1.56 < \eta < 2.50$ (EE). The errors on the average difference are less than 0.004.	106
7.14	Distributions of the normalised difference $(E_1^{\text{meas}} - E_1^{\text{rec}})/\langle E_1^{\text{meas}} \rangle$ for 500 GeV electrons with (a) $ \eta < 0.5$, (b) $0.5 < \eta < 1.0$, (c) $1.0 < \eta < 1.44$ (EB) and (d) $1.56 < \eta < 1.8$, (e) $1.8 < \eta < 2.2$, (f) $2.2 < \eta < 2.5$ (EE) [48]. The errors on the average difference are less than 0.01.	108
7.15	Energy ratio E_1/E_{25} for 500 GeV incident electrons, plotted as a function of the variable Y , for $0 < X < 0.25$ and (a) $ \eta < 0.5$ (EB, $\langle p_t \rangle \simeq 470$ GeV/c); (b) $1.0 < \eta < 1.44$ (EB, $\langle p_t \rangle \simeq 260$ GeV/c); (c) $1.56 < \eta < 1.8$ (EB, $\langle p_t \rangle \simeq 170$ GeV/c); (d) $2.2 < \eta < 2.5$ (EB, $\langle p_t \rangle \simeq 90$ GeV/c); (e-h) idem, for $1.75 < X < 2.00$ [48].	108
7.16	For 500 GeV incident electrons and no magnetic field: (a-b) energy ratio E_1/E_{25} plotted as a function of the variable Y for $1.75 < X < 2.00$, for $1.0 < \eta < 1.44$ and $1.56 < \eta < 1.8$, respectively; (c-d) distribution of the normalised difference $(E_1^{\text{meas}} - E_1^{\text{rec}})/\langle E_1^{\text{meas}} \rangle$ for electrons with $p_t > 80$ GeV/c and all values of X and Y , in the same $ \eta $ bins [48]. The errors on the average difference are less than 0.002.	109

- 7.17 Distributions of the normalized difference $(E_1^{\text{meas}} - E_1^{\text{rec}})/\langle E_1^{\text{meas}} \rangle$, for electrons (and positrons) from Drell-Yan sample generated with invariant mass $M_{ee} > 120 \text{ GeV}/c^2$, electrons are chosen with $p_t > 50 \text{ GeV}/c$, electrons and positrons are selected with very small background using the HEEP criteria (given in Table 5.3); plots (a-c-e) represent electrons chosen in 3 energy bins, $300 \text{ GeV} < E_{5 \times 5} < 400 \text{ GeV}$, $400 \text{ GeV} < E_{5 \times 5} < 650 \text{ GeV}$ and $650 \text{ GeV} < E_{5 \times 5}$, with $0.00 < |\eta| < 1.44$ (EB) and similarly plots (b-d-f) for $1.56 < |\eta| < 2.50$ (EE). The errors on the average difference are less than 0.002. 111
- 7.18 Ratio of the energy of final state radiation and that of the generated final state electrons after FSR, for the Drell-Yan sample generated with invariant mass $M_{ee} > 120 \text{ GeV}/c^2$ and electrons with $p_t > 50 \text{ GeV}/c$ and $E_{5 \times 5} > 300 \text{ GeV}$ 113
- 8.1 Distributions of the normalised difference $(E_1^{\text{meas},*} - E_1^{\text{rec}})/\langle E_1^{\text{meas},*} \rangle$ for (a-b-c) 2500, 3500 and 4500 GeV electrons with $0.5 < |\eta| < 1.0$ (EB) and (d) for 4500 GeV electrons with $1.8 < |\eta| < 2.2$ (EE). Only “single gun” events with electronics saturation are included. The superimposed curves show the results of Gaussian fits distributions of the peak region over $\pm 1.5\sigma$ [48]. 116
- 8.2 Distributions of the normalised difference $(E_1^{\text{meas},*} - E_1^{\text{rec}})/\langle E_1^{\text{meas},*} \rangle$ for (a-b-c) 2500, 3500 and 4500 GeV electrons with $|\eta| < 1.44$ (EB) and (d-e) for 3500 and 4500 GeV electrons with $1.56 < |\eta| < 2.50$ (EE). Only “single gun” events with electronics saturation are included. The superimposed curves show the results of Gaussian fits distributions of the peak region over $\pm 1.5\sigma$ 117
- A.1 Schematic view of the ECAL off-detector electronics [31]. 125
- B.1 Fraction $R_{2 \times 2} = E_{2 \times 2}/E_{\text{true}}$ of the generated electron energy E_{true} which is reconstructed (after HCAL energy recalibration) in the highest energy 2×2 H1 unit containing the highest energy cell, for “single gun” electrons uniformly distributed with $1.56 < |\eta| < 2.4$ and with $p_t = 100$ (left) and $500 \text{ GeV}/c$ (right) [52]. 129
- B.2 Isolation criteria for electron candidates emitted toward the missing ECAL endcap with $1.56 < |\eta| < 2.4$ and $p_t(E_{2 \times 2}) > 80 \text{ GeV}/c$: (left): ratio $R_{\text{H2}/\text{H1}}$ of the energy deposit $E_{2 \times 2}$ in the 2×2 unit of H2 corresponding to the highest energy 2×2 unit in H1 containing the highest energy cell, divided by the corresponding unit in H2; (right): ratio $R_{12} = E_{t,12}/E_{t,2 \times 2}$, where $E_{t,12}$ is the transverse energy collected in the set of 12 HCAL cells surrounding the highest energy 2×2 unit of H1 containing the highest energy cell. The distributions for electron candidates from the Drell-Yan signal are shown as shaded histograms, those from the QCD and W+jet backgrounds as white histograms. The signal and background distributions are normalised to unity [52]. 130

- B.3 Same as in figure 6.12, for (left) tracker isolation: number of tracks with $p_t > 1.5 \text{ GeV}/c$ emitted between two cones ($0.1 < \Delta R < 0.2$) around the electron candidate direction; (right) tracker isolation: vectorial sum of the transverse momenta of these tracks, divided by $p_t(E_{2 \times 2})$ [52]. 131
- B.4 For electron candidates emitted toward the missing ECAL endcap with $1.56 < |\eta| < 2.4$ the track matching: number of tracks with $p_t > 20 \text{ GeV}/c$ emitted from the vertex and directed within the $|\eta|$ and ϕ limits of the highest energy cell of the highest energy 2×2 HCAL unit, (left) electron candidates with $p_t(E_{2 \times 2}) > 80 \text{ GeV}/c$; (right) only electron candidates passing the isolation criteria are selected [52]. 131
- B.5 Distribution of the ratio of the reconstructed over generated M_{ee} mass for e^+e^- events with both electrons emitted in the angular domain $|\eta| < 2.4$, when one of the electrons is emitted toward the missing ECAL endcap, and which are recovered following the criteria (B.1): (left) Drell-Yan events with $M_{\gamma/Z} > 200 \text{ GeV}/c^2$; (right) Z' production events with $M = 1 \text{ TeV}/c^2$ [52]. 133
- B.6 Mass distribution of QCD and W+jet background for an integrated luminosity of 1 fb^{-1} , when one of the fake electrons is emitted toward the missing ECAL endcap, and which are passing following the criteria (B.1). 135

List of Tables

2.1	Expected and observed 95% C.L. lower limits on Z' 's masses [21].	11
2.2	Expected and observed 95% C.L. lower limits on SSM Z' 's mass form different experiments.	13
2.3	Expected and observed 95% C.L. lower limits on Z'_{ψ} 's mass form different experiments.	13
2.4	Expected and observed 95% C.L. lower limits on RS gravitons masses, with different coupling values c , form different experiments.	13
2.5	Axial and axial-vector couplings of electron and quarks.	16
3.1	Physical properties of the ECAL crystals.	28
3.2	Cracks [in mm] between modules [32].	29
3.3	Physical properties of the HCAL Barrel brass absorber.	38
4.1	Average fraction of the shower energy contained within given calorimeter depths, expressed in terms of the number of radiation lengths X_0 , for several incident electron energies, following the parametrisation of ref. [44].	54
5.1	GSF pre-selection cuts [9].	58
5.2	HEEP electron selection v1.2 [7].	61
5.3	HEEP electron selection v2.0 [9].	61
5.4	Relaxed Single Electron trigger [7].	62
5.5	High E_t trigger [7].	62
5.6	Very High E_t trigger [7].	63
5.7	Global acceptance, reconstruction and selection efficiency, and number of generated events, of events with electrons generated in the acceptance, and of events with electrons reconstructed in the acceptance and selected with the HEEP criteria, for an integrated luminosity of 100 pb^{-1} for Drell-Yan events with $M_{ee} > 40, 120, 200$ and $500 \text{ GeV}/c^2$ and for SSM Z' resonance production with mass of $1 \text{ TeV}/c^2$ [9].	64

5.8	Number of tag-and-probe pairs, N_{TP} , where the tag passes the full HEEP selection and the probe is selected as a GSF electron candidate, and of pairs where the probe passes the HEEP selection, N_{TT} , for Drell-Yan events, and jet events (W +jet and multi-jet) and for an integrated luminosity of 100 pb^{-1} ; corresponding efficiencies of the HEEP selection criteria applied to GSF electron candidates, for Drell-Yan events, and corresponding rejection powers for background jet events [9].	66
5.9	Loose HEEP electron selection v1.1 in addition to a track reconstructed as a "PixelMatchGsf-Electron" [52].	67
5.10	Criteria used to identify jets originating from b quarks.	67
5.11	Numbers of events with one electron passing the HEEP criteria and one muon passing the muon selection and isolation criteria, with $M_{e\mu} > 40 \text{ GeV}/c^2$, both leptons having $E_t > 25 \text{ GeV}$ and the HEEP electron being detected outside a cone of radius $\Delta R = 0.1$ around the direction of any muon, for an integrated luminosity of 100 pb^{-1}	70
5.12	The very loose electron cuts used for constructing the jet faking electron sample [7].	71
6.1	The mean (μ) and standard deviation (σ) of the Gaussian fits, to the reconstructed over generated energy distributions, for single gun electrons and pions generated with several fixed energies. The energy was reconstructed using 4×4 HCAL cells around the particle direction in HCAL barrel, with no simulated ECAL.	77
6.2	Limits of the ECAL cracks and EB-EE gaps, as obtained from "single gun" electrons with $p_t = 100$ and $500 \text{ GeV}/c$	79
6.3	Fractions of e^+ and e^- "single gun" electrons (uniformly distributed in η with $ \eta < 2.4$), lost because of intermodule cracks and of EB-EE gaps (defined as in Table 6.2), for $p_t = 100$ and $500 \text{ GeV}/c$. The losses in ϕ cracks are computed in the barrel ($ \eta < 1.44$), outside the η crack limits and within $\pm 1.5^\circ$ of the supermodule limits.	81
6.4	Repartition of the "lost" Drell-Yan events, i.e. events generated with $M_{\gamma/Z} > 200 \text{ GeV}/c^2$ and both (real) electrons generated with $ \eta < 2.4$ and $p_t > 80 \text{ GeV}/c$, and for which one of the electrons does not pass the minimum identification conditions (6.2). The cracks are defined as in Table 6.2. The errors are the statistical errors for a luminosity of 1.9 fb^{-1}	83
6.5	Peak values and resolutions of the distributions in Figure 6.8.	85
6.6	Effect of the recovery conditions (6.3) for Drell-Yan events with mass $> 200 \text{ GeV}/c^2$ and for Z' bosons with mass = $1 \text{ TeV}/c^2$, with two (real) electrons generated with $p_t > 80 \text{ GeV}/c$ and $ \eta < 2.4$, when one of the electrons is emitted in the EB-EE gap direction and does not pass the minimum electron identification conditions (6.2). The errors are the statistical errors for a luminosity of 1.9 fb^{-1} for Drell-Yan events and 19.2 fb^{-1} for Z' production.	91

6.7	QCD jet background to the gap recovery procedure: \hat{p}_t scale range, integrated luminosity, number of generated events, number of events containing an electron candidate passing the HEEP identification criteria (5.9), number of events containing in addition an electron candidate passing the recovery cuts (6.3), corresponding number of di-electron events for 1 fb^{-1}	93
6.8	Same as Table 6.7, but for W+jet jet background (the quoted luminosities and numbers of events are for W bosons decaying into an electron and a neutrino).	93
7.1	Fit parameters of the $F(X, Y; E, \eta)$ functions given by eq. (7.5), for 1500 GeV fixed energy "single gun" electrons in the $ \eta $ ranges $0.5 < \eta < 1.0$ (EB) and $1.8 < \eta < 2.2$ (EE).	102
7.2	Mean values and RMS of the distribution of the normalised difference $(E_1^{\text{meas}} - E_1^{\text{rec}})/\langle E_1^{\text{meas}} \rangle$, for several electron energies and for EB and EE, respectively.	107
7.3	For three electron energy ranges, average value and RMS of the normalized difference $(E_1^{\text{meas}} - E_1^{\text{rec}})/\langle E_1^{\text{meas}} \rangle$, for EB and EE separately; expected number of electrons with $p_t > 50 \text{ GeV}/c$ from Drell-Yan events with mass $M_{e^+e^-} > 120 \text{ GeV}/c^2$, selected using the HEEP criteria for electron identification (see Table 5.3), and error on the mean of the normalized difference, for an integrated luminosity of 100 pb^{-1} at 10 TeV. The Drell-Yan sample is fitted using fit parameters obtained from the Drell-Yan sample itself for different energy bins. The errors on the average difference are less than 0.002.	110
7.4	Same as Table 7.3, except that the Drell-Yan sample is fitted using fit parameters obtained from single gun electron samples as explained in the text.	112
7.5	Average and RMS values of the distributions of the normalised difference $(E_1^{\text{meas}} - E_1^{\text{rec}})/\langle E_1^{\text{meas}} \rangle$ for electrons with non-saturating electronics, with energies from 500 to 3500 GeV: average and RMS values of the distributions, for three $ \eta $ bins in EB and three $ \eta $ bins in EE.	113
8.1	Fractions of electron showers of various energies with electronics saturation in EB ($ \eta < 1.44$) and in EE ($1.56 < \eta < 2.5$).	115
8.2	Normalised differences $((E_1^{\text{meas},*} - E_1^{\text{rec}})/\langle E_1^{\text{meas},*} \rangle)$ for electrons with saturated electronics, with energies 2500, 3500 and 4500 GeV: average and RMS values of the distributions (see Figure 8.2), and mean μ and width σ of Gaussian fits in the peak, for EB and EE.	117
B.1	Percentages of the total number of Drell-Yan electron pairs with $M_{\gamma/Z} > 200 \text{ GeV}/c^2$ and of Z' bosons with mass of $1 \text{ TeV}/c^2$ with both (real) electrons generated with $ \eta < 2.4$ and $p_t > 80 \text{ GeV}/c$, for which one or both electrons are emitted in the direction of the missing endcap.	127
B.2	Effect of the recovery conditions (B.1), for Drell-Yan events with $M_{\gamma/Z} > 200 \text{ GeV}/c^2$ and for Z production events with mass = $1 \text{ TeV}/c^2$, with two (real) electrons generated with $p_t > 80 \text{ GeV}/c$ and $ \eta < 2.4$, when one of the electrons is emitted toward the missing ECAL endcap with $1.56 < \eta < 2.4$	133

B.3	QCD jet background to the gap recovery procedure: \hat{p}_t scale range, integrated luminosity, number of generated events, number of events containing one electron candidate passing the HEEP identification criteria (given in Table 5.9) in the ECAL barrel or installed endcap and a candidate emitted toward the missing endcap with $E_T > 60$ GeV collected within a cone of radius 0.2 , number of events containing in addition an electron candidate passing the recovery cuts (B.1), corresponding number of di-electron events for 1 fb^{-1}	134
B.4	Same as Table B.3, but for W+jet jet background (the quoted luminosities and numbers of events are for W bosons decaying into an electron and a neutrino).	134

Chapter 1

Introduction

In 1960 Weinberg, Salam and Glashow built a structural piece of what is known as the Standard Model (SM) in particle physics. Their model describes how the electromagnetic and weak interactions are unified to form the electroweak interaction, with 4 gauge bosons W^\pm , Z and γ . The W^\pm and Z bosons were discovered by the UA1 and UA2 experiments at the CERN SPS proton anti-proton collider in the year 1983. The masses of the three gauge bosons were measured with high accuracy by the LEP experiments (electron - positron collider at CERN), which are $80.398 \pm 0.025 \text{ GeV}/c^2$ and $91.1876 \pm 0.0021 \text{ GeV}/c^2$ respectively. In the Standard Model, the Brout - Englert - Higgs mechanism is a theoretical framework which explains how the masses of the W^\pm and Z bosons arise as a result of the electroweak symmetry breaking. It requires an extra scalar field, the Higgs field (H), which interacts with itself and with the gauge fields and which has a nonzero value in its lowest energy state, a vacuum expectation value. Direct searches for the Standard Model Higgs boson have been performed at the LEP and at the Tevatron proton anti-proton collider by the CDF and D0 experiments. The data gathered at the LEP collider allow an experimental lower bound to be set for the mass of the Standard Model Higgs boson of $114.4 \text{ GeV}/c^2$ at 95% confidence level, while at the Tevatron, combined data from the CDF and D0 experiments exclude the Higgs boson in the range between $160 \text{ GeV}/c^2$ and $170 \text{ GeV}/c^2$ at 95% confidence level.

The SM has been tested during more than 30 years, and its predictions agree very well with all experimental observations. However, the SM is nowadays considered as a low energy manifestation of other theories realized at high energy, generically known as BSM (Beyond the Standard Model) theories. One motivation for BSM physics is to have a unified theory for the electromagnetic, weak and strong interactions, in a unique Grand Unified Theory (GUT). A new symmetry (the Super-Symmetry “SUSY”) is also invoked. Attempts to also include gravitation lead to models with extra spatial dimensions. The BSM models typically predict the existence of new particles at the TeV scale and higher.

The proton proton Large Hadron Collider (LHC) at CERN, which is expected to be operational in 2009-2010, is a discovery machine. Its main goal is to search for the Higgs boson and for new particles predicted by BSM models. The LHC has been designed to collide two proton beams, circulating in opposite directions, with centre-of-mass energy of 14 TeV. In the first year of data taking, it is planned that the LHC will reach a centre-of-mass energy of 7 and 10 TeV. Four experiments, CMS, ATLAS, LHCb and ALICE will take data at the LHC.

The CMS detector, “Compact Muon Solenoid”, at the LHC is a general-purpose detector, capable of study-

ing all major aspects of proton-proton collisions at the LHC. It includes sub-detectors which are designed to measure the energy and/or momentum of photons, electrons, muons, jets and other products of the collisions. The innermost layer is a silicon-based tracker, which is surrounded by the crystal electromagnetic calorimeter ECAL. The latter is surrounded with a sampling calorimeter for hadrons, HCAL. The tracker and the calorimetry are compact enough to fit inside the CMS solenoid, which generates a powerful magnetic field of 4 T. Outside the magnet are the large muon detectors, which are installed inside and outside the return yoke of the magnet.

The analyses, which are presented in this thesis, are contributions to the CMS HEEP group (High Energy Electrons Pairs) effort, which aims at preparing the measurement in CMS of high mass electron and photon pairs, in search of new physics beyond the Standard Model. Heavy resonances are predicted by various BSM models, in particular GUT models and extra spatial dimension models. Promising decay channels for the Z' gauge bosons or gravitons G are the leptonic ones; $Z' \rightarrow l^+l^-$ or $G \rightarrow l^+l^-$, where l is an electron or a muon, and also $G \rightarrow \gamma\gamma$. In this thesis, we are interested in the di-electron final state. Other groups in CMS study the di-muon or di-photon final states, which are complementary to our study.

Our personal work has focused on developing tools to identify and reconstruct electrons with high transverse momenta with respect to the incident beam, P_T , (up to several hundreds GeV/c), using the various sub-detectors (tracker, ECAL and HCAL) of CMS.

In the context of HEEP analyses, heavy resonances from BSM models could be shown up at the tail of very high mass Drell-Yan events, which are an irreducible background to heavy resonances. The measurements of the Drell-Yan process will also be used to check detector understanding.

In the first few months of data taking, only a few high mass Drell-Yan events are expected. Some of these events could be lost when they are emitted toward the gap between the ECAL barrel and endcap. We present a procedure which has been designed to recover these electrons using the CMS hadronic calorimeter ‘‘HCAL’’; this procedure increases the hermeticity of the electromagnetic calorimeter. For this procedure, we have shown that the segmentation of the endcap parts of the hadronic calorimeter can be used to discriminate electromagnetic showers from hadronic showers.

A quarter of the ECAL crystals have been calibrated using electron beam tests at CERN, up to 300 GeV. The ECAL linearity was shown to be better than 1% in the energy range 9 to 100 GeV. Since the ECAL crystals are calibrated only up to 300 GeV, we propose a method to validate the extrapolation to high energy (> 300 GeV) of the ECAL crystals response to electromagnetic showers. It is shown that the energy deposit in the central, highest energy crystal of a 5×5 matrix of crystals, can be parameterized as a function of the energy deposits in the 24 surrounding crystals. Using high energy electrons from Drell-Yan events, the comparison of the measured energy with that estimated from the surrounding crystals offers a mean to validate crystal calibration. Conversely, this comparison provides a new shower shape variable, useful to validate samples of high energy electrons.

At very high energy (of the order of a few TeV) the crystal electronics are saturated, causing wrong measurement of the energy of electromagnetic shower. In order to solve this problem, the same parametrization

technique of the electromagnetic showers has been used to compute the energy deposit in the central crystal of a very high energy shower, using the energy deposits in the 24 surrounding crystals.

The thesis is organized as follows. In chapter 2, the search for heavy resonances decaying into an electron pairs is presented. First, two models predicting high mass resonances are briefly described; the limits on the mass of these new heavy resonances put at the Tevatron by the CDF and D0 experiments, and the discovery potential of the CMS experiment are presented. The irreducible Drell-Yan background and other reducible backgrounds are also explained. The last part of chapter 2 describes the strategy of the HEEP group in the preparation of data taking. The CMS detector is introduced in chapter 3, describing the structure and composition of each sub-detector, with an emphasis on the electromagnetic calorimeter ECAL as it is widely used in this thesis. In chapter 4 we present how electromagnetic objects are reconstructed in the ECAL. The calibration and linearity of the ECAL crystals are also discussed in this chapter. The identification of electromagnetic objects and how they can be discriminated from hadronic objects is discussed in chapter 5. In chapter 6, we present the procedure which has been designed to recover high energy electrons lost because they were emitted toward the ECAL barrel – endcap gaps. In chapters 7 we present a method to calibrate the ECAL crystals at high energy (> 300 GeV) with electrons from Drell-Yan events, using a parametrization of the distribution of electromagnetic shower energy deposits among crystals in a 5×5 matrix. A technique to recover saturated channels is explained in chapter 8, with the same type of parametrization used as for the calibration. Finally, in chapter 9, we conclude the works which we have been done in this thesis, in the framework of HEEP analyses in preparation to the startup of the data taking.

Chapter 2

Search for $Z' \rightarrow e^+e^-$, Drell-Yan and background

In this chapter we introduce, theoretically and experimentally, the search for new physics beyond the Standard Model (SM), like heavy neutral gauge boson [1] $Z' \rightarrow l^+l^-$ and heavy gravitons [2] $G \rightarrow l^+l^-$ ($l = e, \mu$), which are presented in the section 2.1.1 and 2.1.2, respectively. Such searches are performed at the Tevatron [3] by the CDF [4] and D0 [5] experiments, with imposing limits on the new resonance mass and production cross section.

There are two main categories of background for the $Z' \rightarrow e^+e^-$. The first is the Drell-Yan production, which is presented in section 2.2. It is the dominant source of background and is irreducible. It plays an important role for the discovery of heavy neutral gauge boson, since the discover region of massive resonance decaying to e^+e^- is expected to be at the tail of the Drell-Yan (DY) mass spectrum ($M_{e^+e^-} > 800 \text{ GeV}/c^2$). Other reducible backgrounds are presented in 2.3.

At the end of this chapter (see section 2.4) we introduce the search strategy, which has been done by HEEP (High Energy Electron Pairs) group [6] for new resonant structures in the e^+e^- invariant mass spectrum using the CMS detector, for 100 pb^{-1} of integrated luminosity [7–10].

2.1 Heavy resonance search at hadron colliders

The existence of heavy neutral bosons is a feature of many extensions of the Standard Model. They arise in extended gauge theories, including grand unified theories (GUT) [1], and other models like left-right symmetric models (LRM) [11]. A specific case is the sequential standard model (SSM), in which the Z' boson has the same coupling as the SM Z^0 [12]. Model of extra dimensions like Randall and Sundrum model (RS) [2] shows the existence of heavy Kaluza-Klein gravitons.

In this section we focus on these models which predict the existence of extra neutral gauge bosons and Kaluza-Klein gravitons. We introduce the present constraints on Z' and RS graviton production from CDF and D0. The expected constraints from CMS are also given.

2.1.1 Models of extra neutral gauge bosons Z'

Grand Unification Theories (GUT's) suppose that strong and electroweak interactions can be described by a simple gauge group G at very high energies $E > E_{GUT}$. H. Georgi and S.L. Glashow have shown, in 1974, that the minimal simple group which can contain the SM gauge groups is $SU(5)$ (i.e $SU(5) \rightarrow SU(3)_c \times SU(2)_L \times U(1)_Y$, where $SU(3)_c$ is the gauge group of the strong interaction). E_{GUT} is defined as the energy where the three running gauge coupling constants of the SM gauge groups become equal. From the non-observation of proton decay [13–15], the value of E_{GUT} is found to be greater than 10^{15} GeV, which is much larger than the E_{weak} , experimentally, $E_{weak} = O(100)$ GeV. But it is smaller than the Planck mass $M_P \sim 1.2 \times 10^{19}$ GeV.

The precision measurements at LEP and SLC prove that the three running gauge couplings do not meet at one point if they run as predicted in the $SU(5)$ GUT. Therefore, it is needed to search for other theories if one wants to describe all SM interactions by one simple gauge group, with avoiding the problems arise from the $SU(5)$ GUT. All GUT's with gauge groups larger than $SU(5)$ can solve the problem, predicting at least one extra neutral gauge boson (Z'). It was seen by H. Fritzsch and P. Minkowski in 1975 that the next gauge group larger than $SU(5)$ is $SO(10)$. $SO(10)$ GUT predicts the existence of one extra neutral gauge boson, Z'_χ . GUT's with gauge groups larger than $SO(10)$ predict more than one extra neutral gauge bosons and many new (exotic) fermions, which must be heavy to make the theory consistent with present experiments [1].

In the following we introduce briefly two models of these which predict the existence of extra heavy neutral gauge bosons.

The largest set of extended gauge theories are those which are based on GUTS. Known examples are $SO(10)$ and E_6 [16]. $SO(10)$ is GUT group of rank¹ 5:

$$SO(10) \rightarrow SU(5) \times U(1)_\chi. \quad (2.1)$$

E_6 is GUT group of rank 6:

$$\begin{aligned} E_6 &\rightarrow SO(10) \times U(1)_\psi \rightarrow SU(5) \times U(1)_\chi \times U(1)_\psi \\ &\rightarrow SU(3)_C \times SU(2)_L \times U(1)_Y \times U(1)', \end{aligned} \quad (2.2)$$

where $U(1)'$ is a linear compination of $U(1)_\chi$ and $U(1)_\psi$, thus

$$U(1)' = U(1)_\chi \cos(\theta) + U(1)_\psi \sin(\theta), \quad (2.3)$$

where θ , for E_6 , is a free parameter [17]; if $\theta = 0$, one extra gauge boson Z'_χ exists from $SO(10)$, while for $\theta = \pi/2$ only Z'_ψ from E_6 is obtained. Finally, $U(1)_\eta$ is a particular compination of $U(1)_\chi$ and $U(1)_\psi$, i.e., $\theta = 2\pi - \tan^{-1} \sqrt{5/3}$, which produces Z'_η [17]. The additional neutral Z boson is more massive than the SM Z^0 , it is a neutral, colorless, self-adjoint (i.e it is its own antiparticle) and spin-1 gauge boson. The coupling of

¹For $SO(N)$, the number of generators is $N/2(N-1)$ and rank is $N/2$ if N is even or $(N-1)/2$ if N is odd.

these new heavy neutral bosons to quarks and leptons are different from the couplings of the SM Z^0 boson [18].

Another model, which predicts the existence of heavy gauge boson, is the sequential Standard Model (SSM) which consists of a Z' with the same couplings to fermions as the SM Z^0 boson. Although it is not a gauge invariant model, it is often used for phenomenological studies as benchmark model.

2.1.2 Model of Randall Sundrum gravitons

The model of Randall and Sundrum (RS) has been introduced [2] in order to solve the hierarchy problem. The hierarchy problem originates from the large disparity between the electroweak scale ($\sim 10^3$ GeV) and the traditional scale of gravity defined by the Planck scale ($M_P \sim 10^{19}$ GeV). The source of the physics which generates and stabilises this sixteen order of magnitude difference between the two scales is unknown.

The RS model introduces a solution to the hierarchy problem by considering the electroweak scale to be the fundamental scale in the nature instead of the Planck scale. In order to take the electroweak scale as the ultraviolet cut-off of the theory, the RS model proposes the existence of one compact extra dimension of radius r_c . The reduced effective Planck scale (\bar{M}_P) at 4 dimensions is related to the fundamental $(4+n)$ dimensional Planck scale (M_{4+n}), where n is the number of extra dimension (in case of RS model $n = 1$), via the following relation [2]

$$\bar{M}_P^2 = \frac{M_{4+n}^3}{k} [1 - e^{-2\pi k r_c}], \quad (2.4)$$

where the parameter k is the curvature of the bulk. In order to make the RS model consistent with low energy data it is required that the curvature is not too large, i.e. k/\bar{M}_P should not be larger than 0.1 [19]. It was found that $k r_c \sim 11 - 12$ is the condition for the RS model to be a solution to the hierarchy problem; r_c is thus only two or three orders of magnitude larger than the 4-dimensional Planck length.

The RS model introduced a space-time with two $(3+1)$ dimensional branes separated in the fifth dimension. The metric, which describes the space-time, has the following form [2]

$$ds^2 = e^{-2kr_c\phi} \eta_{\mu\nu} dx^\mu dx^\nu - r_c^2 d\phi^2, \quad (2.5)$$

where $\eta_{\mu\nu}$ is the ordinary Minkowski metric, x are the coordinates of the space-time $(3+1)$ dimensions on the branes, and $-\pi < \phi < \pi$ is the coordinate of the extra dimension. The size of the extra dimension is set by the parameter r_c which is known as the compactified radius of the extra dimension. The warp factor ($e^{-2kr_c\phi}$) in eq.2.5 gives an exponential dependence on the extra dimension ϕ .

In the RS model, the only particles that propagate in the extra dimension are the gravitons G . While in our three spatial dimensions, these gravitons appear as excited Kaluza-Klein modes, with each mode being a narrow spin 2 resonance. The masses of these excitations are given by [20]

$$m_n = k x_n e^{-\pi k r_c} \quad (n = 1, \dots, \infty), \quad (2.6)$$

where x_n are the roots of the Bessel function of order 1 ($J_1(x_n) = 0$).

Due to the fact that the extra dimension is strongly curved, the spectrum of Kaluza-Klein excitations is not equidistant, and the separation between the excitation levels are large enough for them to be observed as individual resonances. Typical values of the parameters in this model give a mass of the order of 1 TeV for the first graviton excitation m_1 . In the RS model, it is needed to know not only the position of each peak but also its width $\sim (k/\bar{M}_P)^2 = c^2$. The RS model has two free parameters m_1 and $c = k/\bar{M}_P$.

One of the interesting decay mode of a massive Kaluza-Klein graviton is e^+e^- pair (i.e. $q\bar{q}(or\,gg) \rightarrow G \rightarrow ee$), which is an interesting channel for searching for new physics at the LHC.

2.1.3 Constraints on Z' and RS Graviton production from different experiments

2.1.3.1 Constraints from CDF experiment

At CDF a search for additional neutral heavy bosons (Z') has been performed, in the e^+e^- decay mode, using a data sample collected during CDF run II [21] corresponding to 2.5 fb^{-1} of integrated luminosity. The observed dielectron invariant mass spectra are consistent with the expectations from the Z^0 and Drell-Yan productions and other known backgrounds.

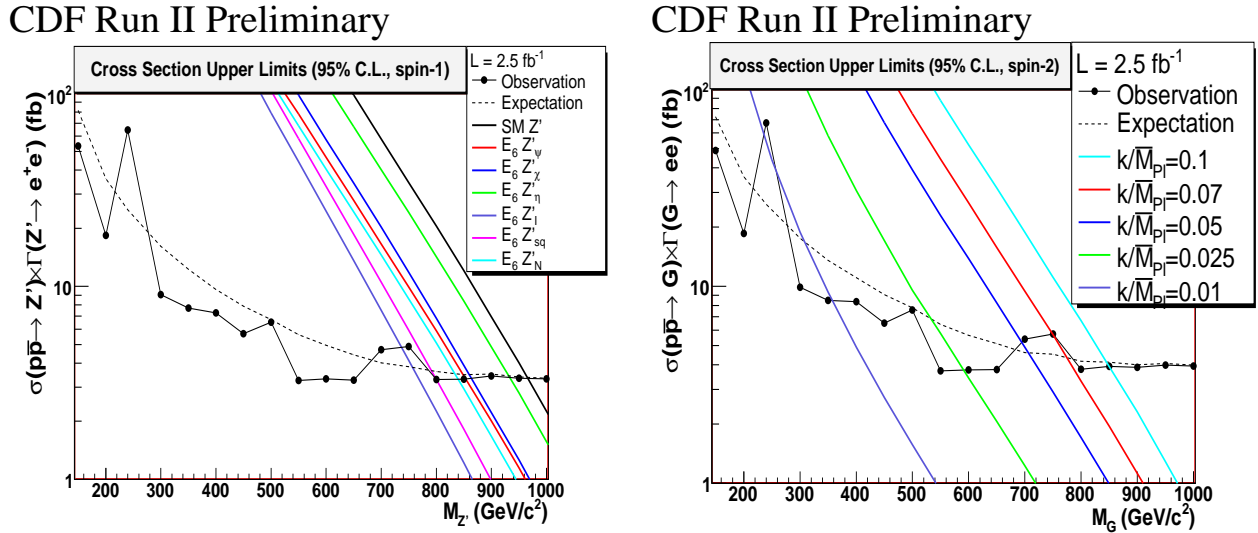


Figure 2.1: CDF upper limit on $\sigma(p\bar{p} \rightarrow X) \cdot Br(X \rightarrow e^+e^-)$ as a function of the mass of the X particle at 95% C.L., where X refers to a Z' (left) and to a RS graviton (right) [21].

Figure 2.1 (left) shows the 95% C.L. upper limits for the signal data which has been obtained. The cross sections for both Z' s and RS gravitons are calculated for leading order with PYTHIA [22] Monte Carlo event generator and then multiplied by a K -factor 1.3 in order to approximate a next-to-leading-order prediction. The observed upper limit from data (at the 95% C.L.) on $\sigma(p\bar{p} \rightarrow X) \cdot Br(X \rightarrow e^+e^-)$ is shown as the solid line with circles, the dashed line in Figure 2.1 is the expected limits from the background-only simulated events for spin 1 particles and solid lines correspond to the possible predictions from theory for the production of Z' in

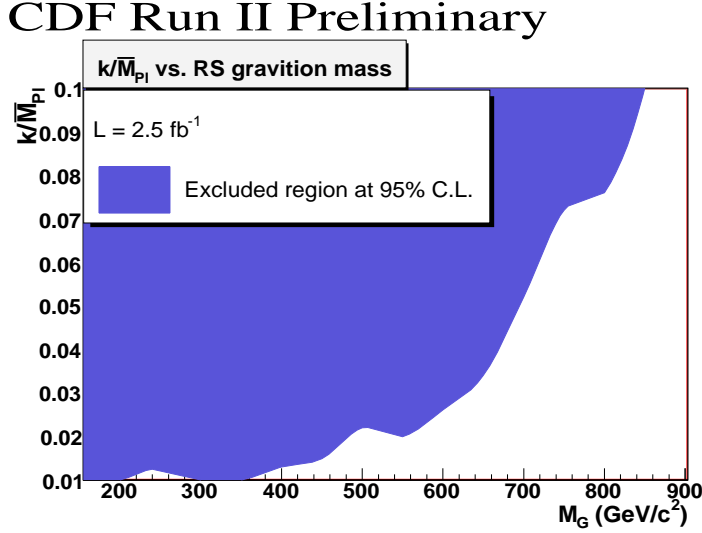


Figure 2.2: Parameter k/\bar{M}_P as a function of RS graviton mass. The shading indicates the region excluded by CDF at the 95% C.L. [21].

different models. At high mass (i.e. $M_{Z'} > 600 \text{ GeV}/c^2$) the $\sigma(p\bar{p} \rightarrow X) \cdot Br(X \rightarrow e^+e^-)$ limit is 4 fb. The intersections of the solid curve with the theoretical predictions determine the 95% C.L. lower limits on the Z' mass for different models, which are quoted in Table 2.1. Figure 2.1 (right) shows the same information for spin 2 particles, together with the expected cross section for RS gravitons. RS gravitons with masses below 848 GeV/c^2 are excluded at 95% C.L. for $k/\bar{M}_P = 0.1$. Figure 2.2 shows the excluded RS graviton mass region with respect to k/\bar{M}_P .

Z' Model	SSM	ψ	χ	η
expected limit (GeV/c^2)	961	846	857	873
observed limit (GeV/c^2)	963	851	862	877

Table 2.1: Expected and observed 95% C.L. lower limits on Z' 's masses [21].

As seen from Table 2.1, one can conclude that, SSM Z' with mass below 963 GeV/c^2 and the E_6 Z' 's with masses below 851 GeV/c^2 are excluded at 95% C.L. [21].

2.1.3.2 Constraints from D0 experiment

With the use of the collected data by D0 detector run II, corresponding to 3.6 fb^{-1} , Figure 2.3 (left) shows the experimental limit together with the theoretical cross section. The existence of a Z' boson with standard model coupling to fermions (i.e SSM Z') was excluded below a mass of 944 GeV/c^2 at 95% confidence level. In Figure 2.3 (right), spin 2 RS gravitons with $k/\bar{M}_P = 0.1$ and $= 0.07$ are excluded, at 95% confidence level, with masses below 767 and 700 GeV/c^2 respectively [23].

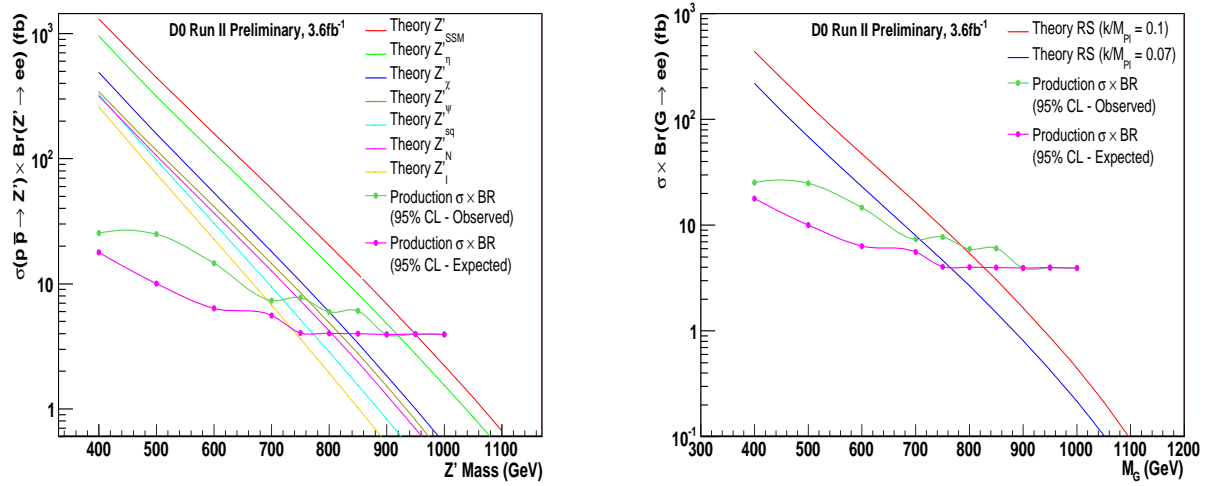


Figure 2.3: Experimental upper limit, from DO experiment, at 95% confidence level for $Z' \rightarrow e^+e^-$ (left) and $G \rightarrow e^+e^-$ production (right) [23].

2.1.3.3 Expected constraints from the CMS experiment

The potential discovery of $Z' \rightarrow e^+e^-$ at CMS experiment (see chapter. 3) has been studied by the HEEP group (see section 2.4). In case of no signal is observed, an upper limit on the production cross section, including the branching ratio to electrons, $\sigma_{Z'}^{\text{limit}}$ is presented in ref. [10] as

$$\sigma_{Z'}^{\text{limit}} = \frac{N_{Z'}^{\text{limit}}}{\epsilon_{Z'}^{\text{tot}} \cdot \mathcal{L}}, \quad (2.7)$$

where $N_{Z'}^{\text{limit}}$ is the limit on the observed decays as described in ref. [10], $\epsilon_{Z'}^{\text{tot}}$ is the total reconstruction efficiency (which is presented in chapter 5), and \mathcal{L} is the integrated luminosity. Due to the dominance of the uncertainty from the measurements of the integrated luminosity in the early data, $\mathcal{L} = 100 \text{ pb}^{-1}$, the cross section limit is normalized to the cross section of Z^0 bosons production, given in the mass range $60 \leq M_{e^+e^-} \leq 120 \text{ GeV}/c^2$. This normalization eliminates the uncertainty from the luminosity measurements.

Figure 2.4 shows the resulting limit on the cross section, after normalisation to the cross section of Z^0 bosons production, as expected for 95% C. L. for three different resonance models. CMS experiment, in case of absence of signal at 10 TeV centre-of-mass energy and an integrated luminosity of 100 pb^{-1} , can put lower limits of $1.59 \text{ TeV}/c^2$ on SSM Z' boson mass, of $1.26 \text{ TeV}/c^2$ on the Z'_{ψ} mass, and $1.49 \text{ TeV}/c^2$ on the mass of RS graviton with coupling $c = 0.1$ and $1.21 \text{ TeV}/c^2$ for $c = 0.05$.

In Tables 2.2 and 2.3, we quote the lower limits on SSM Z' and Z'_{ψ} boson mass, respectively, from different experiments, which have been observed or expected for 95% confidence level. Similar results are presented in Table 2.4 for RS model, with different coupling values c , from different experiments.

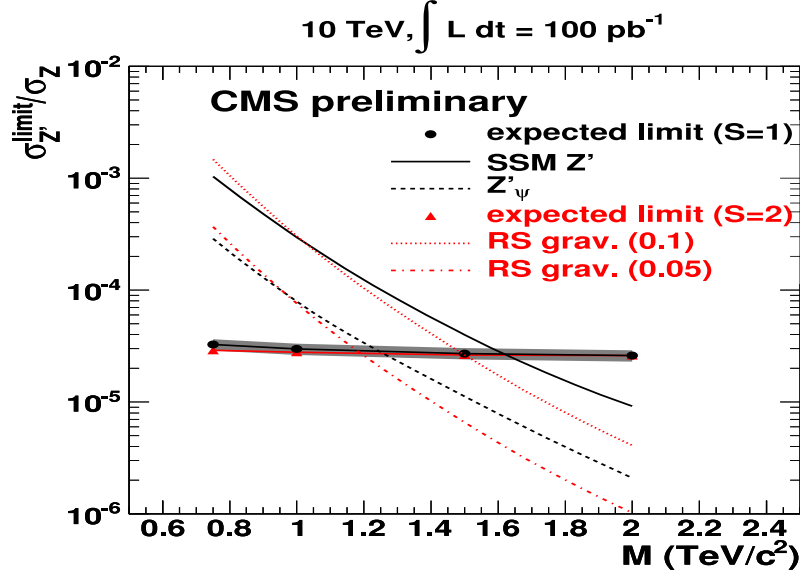


Figure 2.4: Expected 95% C. L. exclusion limits on the cross section of resonance production, normalised to the Z^0 cross section, as a function of the resonance mass for the SSM Z' , Z'_ψ and RS gravitons ($c = 0.1$ and $c = 0.05$) signals; for integrated luminosity of 100 pb^{-1} . The grey band, for SSM Z' , shows the variations of the limit when systematic uncertainties are taken into account [10].

Experiment	\mathcal{L} (fb^{-1})	observed limit (GeV/c^2)	expected limit (GeV/c^2)
D0 (data)	3.6	944	-
CDF (data)	2.5	963	-
CMS (MC)	0.1	-	1590

Table 2.2: Expected and observed 95% C.L. lower limits on SSM Z' 's mass form different experiments.

Experiment	\mathcal{L} (fb^{-1})	observed limit (GeV/c^2)	expected limit (GeV/c^2)
D0 (data)	3.6	751	-
CDF (data)	2.5	851	-
CMS (MC)	0.1	-	1260

Table 2.3: Expected and observed 95% C.L. lower limits on Z'_ψ 's mass form different experiments.

RS model ($c =$)	Experiment	\mathcal{L} (fb^{-1})	observed limit (GeV/c^2)	expected limit (GeV/c^2)
0.1	D0 (data)	3.6	767	-
0.07	D0 (data)	3.6	700	-
0.1	CDF (data)	2.5	848	-
0.1	CMS (MC)	0.1	-	1490
0.05	CMS (MC)	0.1	-	1210

Table 2.4: Expected and observed 95% C.L. lower limits on RS gravitons masses, with different coupling values c , form different experiments.

2.2 Drell-Yan process

The Drell-Yan process describes, at parton level, the annihilation of a quark-antiquark pair and the production of a dilepton pair via interfering intermediate virtual Z-boson and photon (γ^*), as shown in Figure 2.5. The Drell-Yan process offers many interesting and important features for our study, since it is directly comparable to the Standard Model theory.

The lowest order Drell-Yan cross section, $d\hat{\sigma}(q\bar{q} \rightarrow \gamma^*/Z^0 \rightarrow e^+e^-)/d\theta$, where θ is the polar emission angle of the electron in the rest frame of the e^+e^- pair, is presented in this section, based on ref [24].

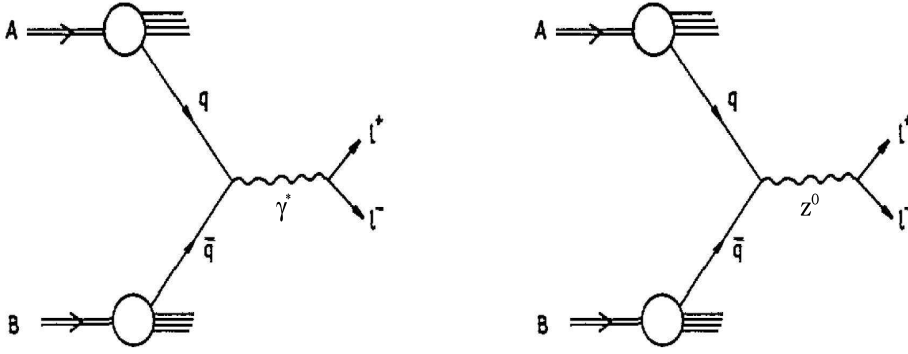


Figure 2.5: The 2 lowest order Feynman diagrams for Drell-Yan process in hadron-hadron collider.

2.2.1 Differential cross section

The differential cross section is given by

$$\frac{d\hat{\sigma}}{d\cos\theta} = \frac{1}{32\pi\hat{s}} |\bar{M}|^2 (q\bar{q} \rightarrow \gamma^*/Z^0 \rightarrow e^+e^-), \quad (2.8)$$

where \hat{s} is the centre-of-mass energy of the $q\bar{q}$ interaction and $|\bar{M}|^2$ is the square of the sum of the Feynman amplitudes. The Feynman diagrams corresponding to the Drell-Yan process are shown in Figure 2.5.

$$|\bar{M}|^2 = \left(\frac{1}{3}\right)_{q \text{ colors}} \cdot \left(\frac{1}{3}\right)_{\bar{q} \text{ colors}} \cdot \left(\frac{1}{2}\right)_{q \text{ spin}} \cdot \left(\frac{1}{2}\right)_{\bar{q} \text{ spin}} \cdot \sum_{\text{spin}} |\widetilde{M}|^2. \quad (2.9)$$

The spins and colors of the incoming quarks are unknown, so we must average over these quantities and then sum over the spins of final state leptons; the quantity $|\widetilde{M}|^2$ is given by eq. (2.9), where

$$|\widetilde{M}|^2 = \left(\widetilde{M}_{\gamma^*} + \widetilde{M}_Z\right)^\dagger \cdot \left(\widetilde{M}_{\gamma^*} + \widetilde{M}_Z\right), \quad (2.10)$$

where \widetilde{M}_{γ^*} is the invariant amplitude for the photon propagator diagram and \widetilde{M}_Z is the invariant amplitude for the Z boson propagator diagram, respectively given by

$$\widetilde{M}_{\gamma^*} = -e_q^2 \left[\bar{u}(p_3) \gamma^\mu v(p_4) \right] \frac{g_{\mu\nu}}{k^2} \left[\bar{v}(p_2) \gamma^\nu u(p_1) \right], \quad (2.11)$$

$$\widetilde{M}_Z = -\frac{g_Z^2}{4} \left[\bar{u}(p_3) \gamma^\mu (c_V^f - c_A^f \gamma^5) v(p_4) \right] \left[\bar{v}(p_2) \gamma^\nu (c_V^e - c_A^e \gamma^5) u(p_1) \right] \cdot \left(\frac{g_{\mu\nu} - q_\mu q_\nu / M_Z^2}{k^2 - M_Z^2 + ik^2 \Gamma_Z / M_Z} \right), \quad (2.12)$$

where p_1, p_2, p_3, p_4 are the 4-momenta of the e^-, e^+, q, \bar{q} ; k is the 4-momentum of the propagator; e is the electron charge, e_q is the quark charge; $g_Z = e / \sin \theta_W \cos \theta_W$; θ_W is the weak mixing angle; $g_{\mu\nu}$ is the metric tensor; M_Z, Γ_Z are the mass and total decay width of the Z boson; and c_V, c_A are the vector and axial-vector couplings of quarks and leptons. The Dirac particle and antiparticle spinors are $u(p)$ and $v(p)$, while $\bar{u}(p)$ and $\bar{v}(p)$ are the conjugate spinors.

Using eqs. (2.8,...,2.12), including the γ^*/Z^0 interference term along with the pure γ^* and Z^0 terms, the following form of the differential cross section for the parton level process $q\bar{q} \rightarrow \gamma^*/Z^0 \rightarrow e^+e^-$ is obtained:

$$\begin{aligned} \frac{d\hat{\sigma}(q\bar{q} \rightarrow \gamma^*/Z^0 \rightarrow e^+e^-)}{d\cos\theta} &= \frac{3C_F}{8} \frac{4\pi\alpha^2}{3\hat{s}} \left[e^2 e_q^2 (1 + \cos^2\theta) + ee_q \text{Re}(\chi(\hat{s})) (2c_V^f c_V^e (1 + \cos^2\theta) + 4c_A^f c_A^e \cos\theta) \right. \\ &\quad \left. + |\chi(\hat{s})|^2 \left((c_V^f)^2 + (c_A^f)^2 \right) \left((c_V^e)^2 + (c_A^e)^2 \right) (1 + \cos^2\theta) \right) \\ &\quad \left. + |\chi(\hat{s})|^2 \left(8c_V^f c_A^f c_V^e c_A^e \cos\theta \right) \right], \end{aligned} \quad (2.13)$$

where C_F is the color factor; $\chi(\hat{s}) = (1/\cos^2\theta_W \sin^2\theta_W) \cdot (\hat{s}/\hat{s} - M_Z^2 + i\Gamma_Z M_Z)$. Integrating equation 2.13 with respect to $\cos\theta$ from -1 to 1 , the following simplified form of the total parton cross section is obtained

$$\hat{\sigma}(q\bar{q} \rightarrow \gamma^*/Z^0 \rightarrow e^+e^-) = C_F \frac{4\pi\alpha^2}{3\hat{s}} R_f, \quad (2.14)$$

where $\hat{s} = k^2 = (2E)^2$, and the quantity R_f is given by,

$$R_f = e^2 e_q^2 + 2ee_q c_V^f c_V^e \text{Re}(\chi(\hat{s})) + |\chi(\hat{s})|^2 \left[\left((c_V^f)^2 + (c_A^f)^2 \right) \left((c_V^e)^2 + (c_A^e)^2 \right) \right], \quad (2.15)$$

which mainly depends on the values of the vector and axial-vector couplings of quarks and electron, which are summarized in Table 2.5.

Basically, the total parton cross section given by eq. (2.14) depends strongly on the centre-of-mass energy of the $q\bar{q}$ interaction: when $\sqrt{\hat{s}}$ becomes much bigger than the M_Z , the cross section drops rapidly, contributing to the tail of the Drell-Yan distribution which is seen in Figure 2.7.

One of the higher order QCD corrections to the Drell-Yan process is presented in Figure 2.6 (next-to-leading-order (NLO) correction). The NLO cross section σ_{NLO}^{DY} is related to the the LO cross section σ_{LO}^{DY} via the following equation

$$\sigma_{NLO}^{DY}(s, Q^2) = K(s, Q^2) \sigma_{LO}^{DY}(s, Q^2), \quad (2.16)$$

Particle	c_V	c_A	charge Q_f
e	$-\frac{1}{2} + 2 \sin^2 \theta_W$	$-\frac{1}{2}$	-1
q (u-type)	$\frac{1}{2} + \frac{4}{3} \sin^2 \theta_W$	$\frac{1}{2}$	2/3
q (d-type)	$-\frac{1}{2} + \frac{2}{3} \sin^2 \theta_W$	$-\frac{1}{2}$	-1/3

Table 2.5: Axial and axial-vector couplings of electron and quarks.

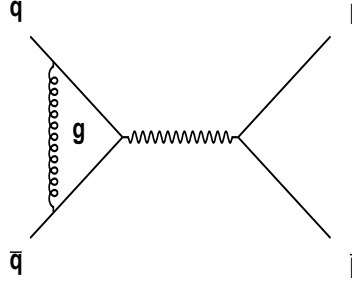


Figure 2.6: One of the Feynman diagrams for the higher order QCD corrections to the Drell-Yan process.

where $K(s, Q^2)$ is known as the K -factor [25]. Its value depends on the total hadron centre-of-mass energy squared s and the invariant mass squared of the lepton pair Q^2 . The K -factor, which is applied for the calculation of the NLO cross section, is 1.35 for the Drell-Yan process [10].

2.2.2 Drell-Yan process at CDF and D0

Analyses in the e^+e^- decay mode have been done at the CDF and D0 experiments for searching for signals from new physics beyond the SM.

For CDF, the analysis is based on data collected in the Tevatron run II, corresponding to 2.5 fb^{-1} integrated luminosity, with centre-of-mass energy of $p\bar{p}$ collision $\sqrt{s} = 1.96 \text{ TeV}/c^2$ [21]. The main sources of background for the Drell-Yan production of e^+e^- pairs are the dijet and $W + jet$ production (see sections 2.3.1.1 and 2.3.2), where one or more jets is misidentified as electron. Other contributions including $t\bar{t}$ (see section 2.3.3) and diboson ($W\gamma, WW, WZ, ZZ, \gamma\gamma$) production, which are designed here as “other SM” backgrounds.

In Figure 2.7, the invariant mass distribution of e^+e^- events, compared to the expected backgrounds, is shown. Dots with error bars are data. The white region corresponds to the Drell-Yan production as estimated from MC and normalised to the data after subtracting backgrounds. The light shaded region shows dijet and W +jet backgrounds, which are estimated from the experimental data using the probability for a jet to be misidentified as an electron. The dark shaded region represents other SM background, estimated with simulated samples. These simulated samples are normalised to the product of the theoretical cross sections and the integrated luminosity.

A similar analysis has been done by the D0 collaboration [23] using data corresponding to an integrated

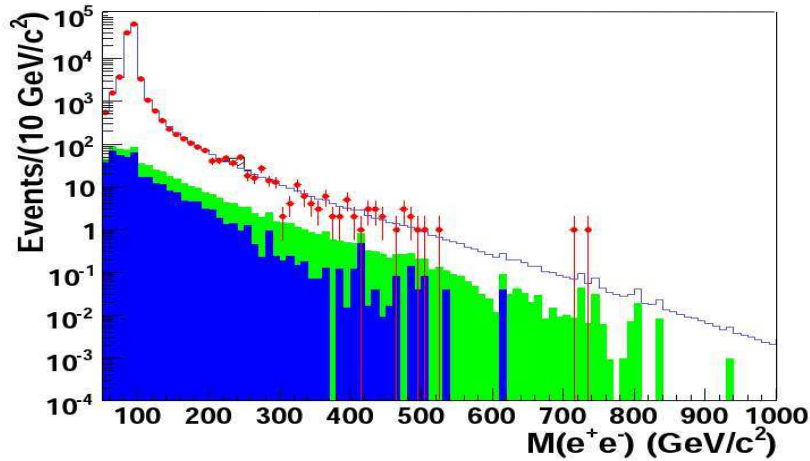


Figure 2.7: Invariant mass distribution of e^+e^- events measured by the CDF collaboration [21], compared to the expected backgrounds. Dots with error bars are data. The light shaded region shows dijet and W +jet backgrounds, and the dark shaded region represents other SM background (see the text). The white region corresponds to the Drell-Yan distribution from Monte Carlo.

luminosity of 3.6 fb^{-1} collected by the D0 detector during run II. In Figure 2.8, e^+e^- mass spectrum is shown, the points correspond to e^+e^- pairs (data); the solid line shows the Drell-Yan production of e^+e^- pairs. For D0 and CDF, The Drell-Yan production is modeled with the PYTHIA Monte Carlo event generator, and the cross section is estimated by multiplying the leading order (LO) calculated from PYTHIA by a mass independent K-factor of 1.3. The light shaded histogram illustrates the instrumental background arising from QCD multijet events (see section 2.3.1) and W +jet, in which both jets have been misidentified as isolated electrons; the data were used to estimate the shape of the di-electron invariant mass spectrum of the events with misidentified electrons. The other SM backgrounds, shown in Figure 2.8 as the black histogram, is obtained from Monte Carlo studies and normalised to the integrated luminosity and subtracted from the measured di-electron invariant mass spectrum.

2.3 Background processes

In this section we introduce the background processes to Z' and graviton signals. Such backgrounds are $t\bar{t}$ production, tW production, WW pair production and Standard Model $Z \rightarrow \tau\tau \rightarrow ee$, with the topology of two real electrons in the final state. The second topology includes processes for which at least one jet is misidentified as an electron. The relevant processes are QCD dijet, W +jet and γ +jet production. Among these backgrounds, we will concentrate here on the QCD dijet, the W +jet and $t\bar{t}$ backgrounds.

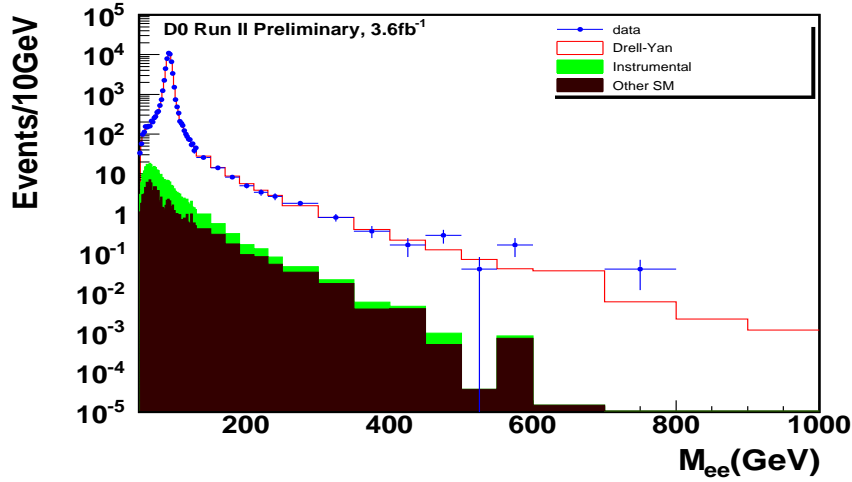


Figure 2.8: Invariant mass spectrum of e^+e^- pairs measured by the D0 collaboration [23] for data (given in the text), with the expected contributions from QCD multijet, W +jet and other SM backgrounds.

2.3.1 QCD background

The theory of Quantum Chromodynamics is the theory of the strong interaction, it is one of the four fundamental forces in nature, and describes the interaction between quarks and gluons, in particular how they bind together to form the class of particles called hadrons. QCD was considered as a mathematically consistent theory in 1970s, and nowadays it is regarded as one of the cornerstones of the Standard Model of elementary particles and their interactions.

2.3.1.1 QCD dijet production

At hadron colliders all studies must take into account QCD effects, resulting from collisions between quarks and gluons in each proton. At LO parton level four subprocesses (gluon-gluon fusion, quark-gluon scattering, quark-quark elastic scattering and quark-antiquark annihilation) can produce dijet in the final state. Figures 2.9 (left) shows an example of a leading order Feynman diagram corresponding to these subprocesses at the LHC.

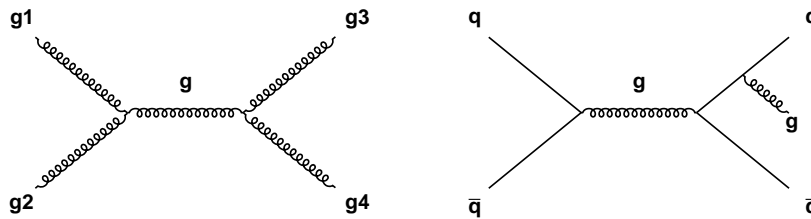


Figure 2.9: (left) Leading order Feynman diagrams for $gg \rightarrow gg$ production via the strong interaction; (right) an example of Feynman diagrams for 3 parton final state in hadron collisions.

One of the most important QCD measurements is the inclusive jet cross section as a function of the jet transverse momentum p_T , which is defined with respect to the beam direction, and computed from the x and y components of the momentum [26]. At the LHC with 10 TeV pp collisions, the jet p_T will reach values far beyond the limits of any other experiments, thus probing the TeV scale of QCD.

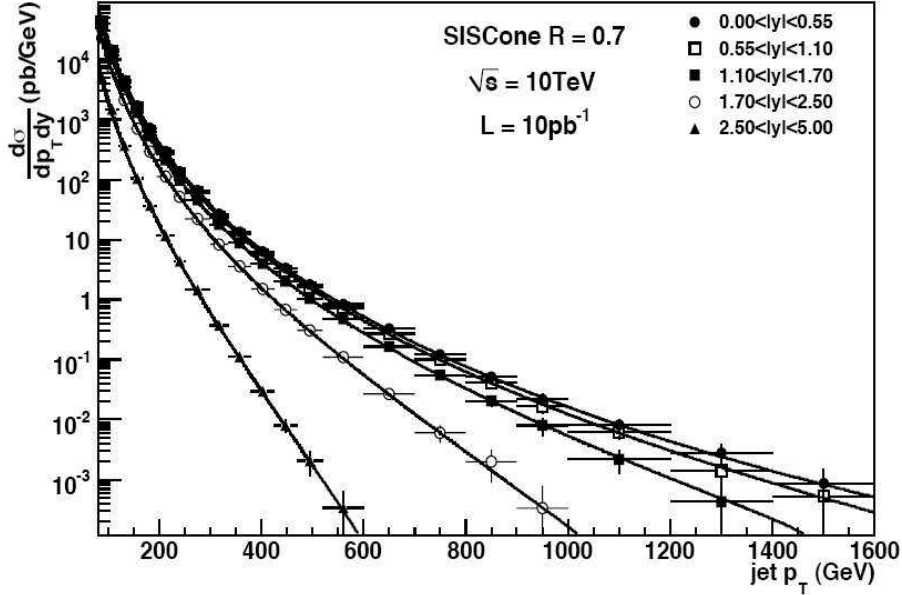


Figure 2.10: The expected cross section of inclusive jet as a function of p_T for different rapidity ranges at the LHC [27].

For centre-of-mass energy $\sqrt{s} = 10$ TeV and integrated luminosity $\mathcal{L} = 10$ pb^{-1} , Figure 2.10 shows the expected cross section of inclusive jet production for different pseudorapidity ranges as a function of jet p_T , where the pseudorapidity (η) is defined as $\left(\eta = -\ln \tan(\theta/2)\right)$, the polar angle (θ) is measured from the z axis. It is seen also that the cross section is decreasing fast with the increase of jet p_T , and strongly dependent on the pseudorapidity.

Figure 2.11 illustrates the dijet mass spectrum expected for different bins in jet p_T . These data samples correspond to an integrated luminosity of $\mathcal{L} = 10$ pb^{-1} and a centre-of-mass energy $\sqrt{s} = 10$ TeV.

The number of expected events with 2 jets decreases rapidly with the increase of the invariant mass.

2.3.1.2 QCD multi-jets production

In addition to LO contributions, other Feynman diagrams correspond to hard gluon emission. Such a next-to-leading order contribution (NLO) diagram is shown in Figure 2.9 (right), giving in the detector events with 3 jets.

QCD dijet or multi-jet production contributes as a background for the search for heavy neutral gauge boson

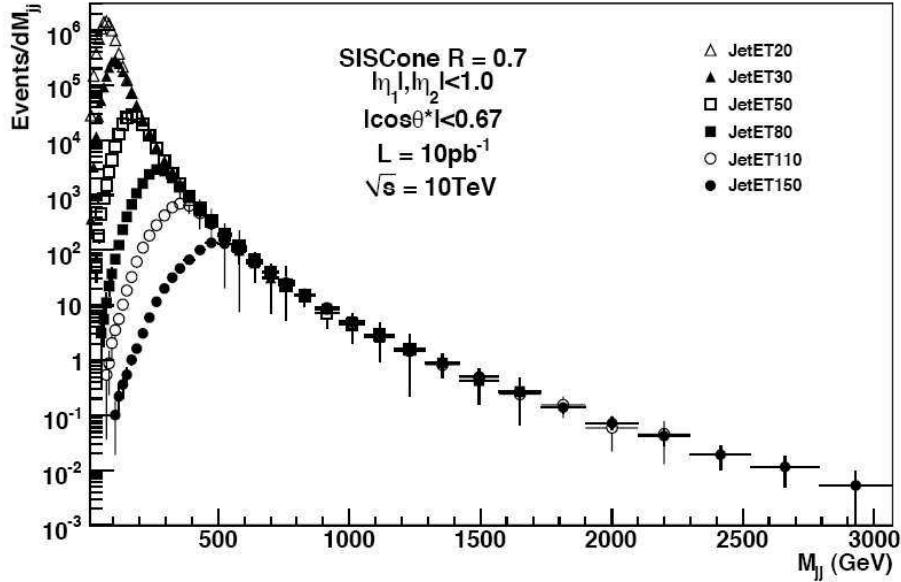


Figure 2.11: Dijet mass distribution for different bins in jet p_T [27].

$Z' \rightarrow e^+e^-$, since two jets from QCD production can fake electrons, as it will be explained in chapter 5.

2.3.2 $W + \text{Jet}$ background

The $W + \text{Jet}$ process is described at parton level in Figure 2.12. If the W boson decays leptonically (e.g. $W \rightarrow l\nu, l = e, \mu$), it is characterised by an event topology of one isolated lepton from the W decay (this lepton could be electron or muon) + one jet + missing transverse energy [28] E_T . This process can mimic a dielectron final state if the jet is faking an electron. The K -factor, which is applied for the calculation of the NLO cross section, is 1.14 for $W + \text{Jet}$.

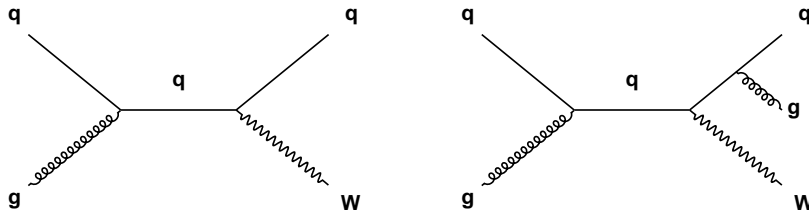


Figure 2.12: (left) Feynman diagram, at leading order, for $W + \text{one jet}$ production via the strong interactions $gg \rightarrow Wq$; (right) one example of Feynman diagram, at next-to-leading order, for $W + 2 \text{ jet}$ production.

2.3.3 $t\bar{t}$ background

The discovery of the top quark [29] at the Tevatron collider in 1995 by the CDF and D0 collaborations opened up the new field of top physics. Due to the high mass of the top quark ($m_{\text{top}} \sim 175 \text{ GeV}/c^2$) in comparison to any other fermion masses (~ 35 times the mass of the next heaviest quark), only Tevatron collider with centre-of-mass energy 1.96 TeV was able to produce top quarks. The pp LHC collider with 10 TeV centre-of-mass energy will be a $t\bar{t}$ factory. The $t\bar{t}$ pair production can be achieved, at parton level, via quark-antiquark ($q\bar{q}$) annihilation or gluon-gluon fusion.

Figure 2.13 shows the (LO) Feynmann diagrams for $t\bar{t}$ pair production. The K -factor, which is applied for the calculation of the NLO cross section, is 1.30 for $t\bar{t}$.

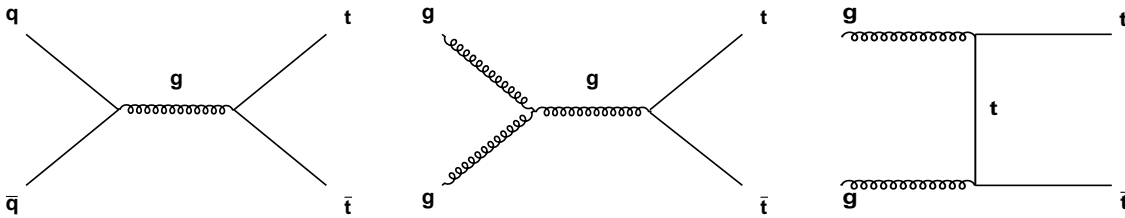


Figure 2.13: Leading order Feynmann diagrams for $t\bar{t}$ production via the strong interaction.

Since the lifetime of the top quark ($\tau_{\text{top}} \sim 10^{-25}$ sec) is smaller than the characteristic hadronisation time of QCD by an order of magnitude, the top quark is the only quark which can be studied as a free quark. Since 99.9% of top quarks, within SM, decay into a Wb pairs, the $t\bar{t}$ pair will decay essentially to two b -quark jets and two W -bosons. Each W -boson will in turn decay either hadronically ($B(W \rightarrow q\bar{q}) = 2/3$) or leptonically ($B(W \rightarrow l\bar{\nu}_l) = 1/3$).

At the LHC, the semi-leptonic decay $t\bar{t} \rightarrow l^-\bar{\nu}_l l^+ \nu_l b\bar{b}$ ($l = e, \mu$) is characterised by final state topology of two hadronic jets originate from two b -quarks, two isolated leptons (e, μ) and missing transverse momenta from the two neutrinos. This channel is one of the possible backgrounds for the Z' signal decaying to e^+e^- pairs, due to the existence of the two isolated leptons in the decay of $t\bar{t}$, which can fake the two electrons from the decay of a Z' signal. A further cut on the missing transverse momenta, due to the non-detection of two neutrinos, is helpful to reduce the $t\bar{t}$ background.

2.4 HEEP strategy

A search strategy for new resonant structures in the e^+e^- invariant mass spectrum using the CMS detector has been designed by the HEEP group, for 100 pb^{-1} of integrated luminosity with 7 TeV proton beams (i.e. 14 TeV proton-proton centre of mass energy) [7, 8], and 5 TeV proton beams (i.e. 10 TeV proton-proton centre of mass energy) [9, 10]. This strategy uses the Drell-Yan (DY) mass spectrum to check the detector response to high energy electrons, and uses the data as far as possible to determine the level of non-DY background

and all triggering and reconstruction efficiencies. In most cases more than one method have been designed to determine these quantities.

Two triggers have been designed by the HEEP group, corresponding to instantaneous luminosities of $8 \times 10^{29} \text{ cm}^{-2}\text{s}^{-1}$ as expected at startup, and $10^{31} \text{ cm}^{-2}\text{s}^{-1}$ as expected after a few months of data taking. Both triggers are considered as single particle triggers with an E_t above a threshold based on the instantaneous luminosity, more details about these triggers and the HEEP selection are given in section 5.2.1.

The full Drell-Yan (DY) mass spectrum, including Z pole ($60 < M_{e^+e^-} < 120 \text{ GeV}/c^2$), will be used to extract the efficiencies of well identified electrons, and the background contributions are estimated directly from data themselves. For such a study, the Drell-Yan (DY) mass spectrum is divided into 2 main control regions in addition to discover region ($M_{e^+e^-} > 800 \text{ GeV}/c^2$) of massive resonance decaying to e^+e^- . The first control region is at Z pole ($60 < M_{e^+e^-} < 120 \text{ GeV}/c^2$), which is characterised by the large statistics of low p_T electrons available in the Z resonance with little background, as seen with the CDF and D0 experiments. This region is used mainly to compare the result from the data with those from the Monte Carlo, and check if the Monte Carlo describes the data well or not. In the second control region of the Drell-Yan spectrum, with $120 < M_{e^+e^-} < 600 \text{ GeV}/c^2$ (it therefore does not depend critically on the triggers with 25 GeV threshold), no evidence of new physics is expected in view of the Tevatron results. This crucial region requires that all procedures (like electron identification, electron selection criteria and background estimate) only make use of information accessible directly at high energy closer to that relevant for heavy resonance search.

The Drell-Yan cross section will be measured and compared with the theoretical SM prediction, in order to check the detector response to high energy electrons.

In order to study e^+e^- pairs due to the decay of heavy resonances or the high mass Drell-Yan process in CMS experiment, HEEP group has designed identification criteria for electron measurement (a detailed description of electron identification and background rejection is presented in chapter 5). These criteria require a track-cluster matching and use shower shape and isolation criteria in order to discriminate e^+e^- pairs from the jet backgrounds. The target of the HEEP electron identification criteria is to select high mass dielectron pairs with a very high efficiency in view of the low expected number of signal events in the discovery region ($M_{e^+e^-} > 800 \text{ GeV}/c^2$).

Chapter 3

CMS detector

The description of the CMS detector is given in detail in [30,31]. In this chapter we present the sub-detectors relevant for the analysis performed in the thesis. After the introduction, the tracking system, the electromagnetic calorimeter and trigger are described. Sections 3.5, 3.6 and 3.7 present the hadronic calorimeter and briefly the magnet and the muon system, respectively.

3.1 Introduction

The Compact Muon Solenoid (CMS experiment) will play an important role in exploiting the physics potential offered by the LHC. Its main functions are to identify and measure precisely the energy and direction of photons, electrons, muons and τ leptons, to measure the energy and direction of jets, and to provide hermetic coverage for measuring missing transverse energy. In addition, good efficiency for photon and lepton identification as well as excellent background rejection against hadrons and jets are required.

The coordinate system adopted by the CMS experiment has the origin at the nominal collision point inside the experiment, the y axis pointing vertically upward, and the x axis pointing radially inward toward the center of the LHC. The z axis points along the beam direction toward the Jura mountains from the LHC, where the CMS experiment is located. The azimuthal angle ϕ is measured from the x axis in the $x - y$ plane and the radial coordinate in this plane is denoted by r . The polar angle θ is measured from the z axis, and the pseudorapidity is defined as

$$\eta = -\ln \tan(\theta/2). \quad (3.1)$$

Thus, the transverse momentum and the transverse energy of particles, which are denoted by p_t and E_t , respectively, and are defined with respect to the beam direction, are computed from the x and y components of the momentum.

The overall layout of CMS is presented in Figure 3.1. Every sub-detector of the CMS detector consists of two main sections. The central cylinder parallel to the beam pipe (barrel) is needed to detect final state particles at low $|\eta|$. The second section consists of 2 disks perpendicular to the beam pipe (endcaps), to close the barrel cylinder; the endcaps are used to detect particles at high $|\eta|$. At the core of CMS sits a 13 m long, 6 m inner diameter, 4 T superconducting solenoid providing a large bending power (12 Tm). This large solenoid radius

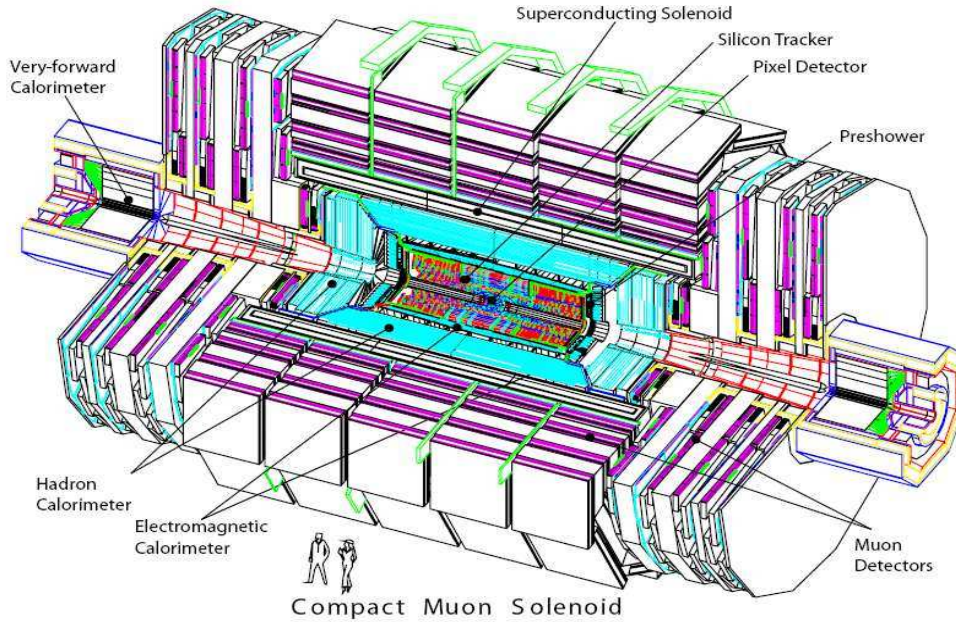


Figure 3.1: Overall layout of CMS [31].

has been chosen to allow the calorimetry and the tracker to be located inside the solenoid. The magnet return field is large enough to saturate 1.5 m of iron, allowing 4 muon stations to be installed to ensure robustness and full geometric coverage. Each muon station consists of several layers of aluminium drift tubes (DT) in the barrel region and cathode strip chambers (CSC) in the endcap region, complemented by resistive plate chambers (RPC). The bore of the magnet coil is large enough to accommodate the inner tracker and the calorimetry. The tracker covers pseudorapidities up to $|\eta| < 2.5$. The tracking volume is given by a cylinder of 5.8 m long and 2.6 m diameter. The tracker consists of 3 layers of silicon pixel detectors, placed close to the interaction region to improve the measurement of the impact parameter of charged particle tracks as well as the position of the secondary vertices. The silicon pixel detectors are followed by 10 layers of silicon microstrip detectors in order to deal with the tracker high multiplicity.

The electromagnetic calorimeter of CMS (ECAL) uses lead tungstate (PbWO_4) crystals. The ECAL covers pseudorapidities up to $|\eta| < 3.0$. It is composed of two parts, the barrel and the endcaps. The scintillation light is detected by silicon avalanche photodiodes (APDs) in the barrel region and vacuum photodiodes (VPTs) in the endcaps. A preshower system is installed in front of the endcaps for π^0 rejection.

The ECAL is surrounded by a brass absorber and scintillator sampling hadronic calorimeter (HCAL), which covers $|\eta| < 3.0$. The scintillation light is converted by wavelength shifting (WLS) fibers embedded in the scintillator tiles and channeled to photodetectors via clear fibers. This light is detected by photodetectors, which are hybrid photodiodes (HPDs) that can provide gain and operate in a high axial magnetic field. The

HCAL is completed, in the barrel region, by another sub-detector called the outer HCAL (HO) to ensure complete containment of the hadronic showers. The hadronic forward sub-detector (HF) covers pseudorapidity up to 5.0. It is made of iron and quartz fibres, the Cerenkov light emitted in the quartz fibres being detected by photomultipliers. The forward calorimeters ensure full geometric coverage for the measurement of the transverse energy in the event.

3.2 The CMS tracking system

The tracking system of CMS is described in detail in [30, 31]. It has been designed to provide a precise and efficient measurement of the trajectory of charged particles emerging from LHC collisions, and to provide a precise reconstruction of secondary vertices. It surrounds the interaction point and has a length of 5.8 m and a diameter of 2.6 m. It is composed of a pixel detector with three barrel layers at radii between 4.4 cm and 10.2 cm and a silicon strip tracker with 10 barrel detection layers extending outwards to a radius of 1.1 m. Each system is completed by endcaps, which consist of 2 disks in the pixel detector and 9 plus 3 disks in the strip tracker on each side of the barrel, extending the acceptance of the tracker up to a pseudorapidity of $|\eta| < 2.5$, with about 200 m² of active silicon area.

3.2.1 Pixel tracker

The pixel detector consists of 3 barrel layers with 2 endcap disks on each side (see Figure 3.2). The 3 barrel

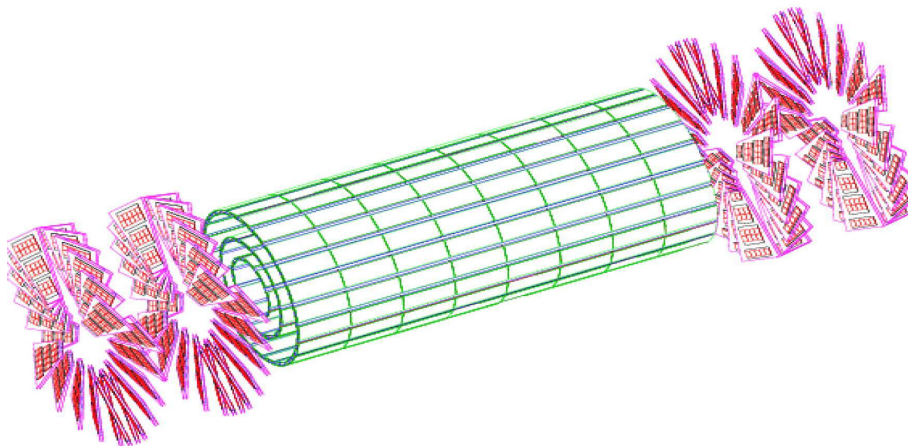


Figure 3.2: Layout of the pixel detectors in the CMS tracker [31].

layers are located at radii of 4.4 cm, 7.3 cm and 10.2 cm, and have a length of 53 cm. The two end disks, extending from 6 to 15 cm in radius, are placed on each side at $|z| = 34.5$ cm and 46.5 cm. In order to achieve the optimal vertex position resolution, a design with an “almost” square pixel shape of $100 \times 150 \mu\text{m}^2$ in both the (r, ϕ) and the z coordinates has been adopted. The barrel comprises 768 pixel modules, which are arranged into half-ladders of 4 identical modules each. The large Lorentz effect (the Lorentz angle is 23°) improves

the (r,ϕ) resolution through charge sharing. The endcap disks are assembled in a turbine-like geometry with blades rotated by 20° to also benefit from the Lorentz effect. They comprise 672 pixel modules with 7 different modules in each blade. The spatial resolution is measured to be $10\ \mu\text{m}$ for the (r,ϕ) measurement and about $20\ \mu\text{m}$ for the z measurement. The pixel detector is read-out using approximately 16000 read-out chips, which are bump-bonded to the detector modules.

3.2.2 Strip tracker

The barrel strip tracker region is divided into 2 parts, see Figure 3.3, TIB (Tracker Inner Barrel) and TOB (Tracker Outer Barrel).

The TIB is made of 4 layers and covers up to $|z| < 65\ \text{cm}$, using silicon sensors with a thickness of $320\ \mu\text{m}$ and a strip pitch which varies from 80 to $120\ \mu\text{m}$. The first 2 layers are made with “stereo” modules in order to provide a measurement in both (r,ϕ) and (r,z) coordinates. A stereo angle of $100\ \text{mrad}$ has been chosen. This leads to a single-point resolution of $23 - 24\ \mu\text{m}$ in the (r,ϕ) direction and $230\ \mu\text{m}$ in z . The TOB comprises 6 layers with half-length $|z| < 110\ \text{cm}$. The strip pitch varies from 120 to $180\ \mu\text{m}$. The first two layers provide a “stereo” measurement in both r,ϕ and r,z coordinates. The stereo angle is again $100\ \text{mrad}$ and the single-point resolution varies from 35 to $52\ \mu\text{m}$ in the r,ϕ direction and $530\ \mu\text{m}$ in z .

The endcaps are divided into the TEC (Tracker EndCap) and TID (Tracker Inner Disk). Each TEC comprises 9 disks that extend into the region $120 < |z| < 180\ \text{cm}$, and each TID comprises 3 small disks that fill the gap between the TIB and the TEC. The TEC and TID modules are arranged in rings, centred on the beam line, and have strips that point towards the beam line, therefore having a variable pitch. The first two rings of the TID and the inner most two rings and the fifth ring of the TEC have “stereo” modules. The thickness of the sensor is $320\ \mu\text{m}$ for the TID and the 3 inner most rings of the TEC and $500\ \mu\text{m}$ for the rest of the TEC.

The entire silicon strip detector consists of almost 15400 modules, which are mounted on a carbon-fibre structure and housed inside a temperature controlled outer support tube, with operating temperature around $-20^\circ\ \text{C}$.

3.2.3 Tracker control and read-out scheme

The silicon strip tracker readout system is based on front-end readout chips, analogue optical links and an off-detector front-end driver (FED) processing board. The “APV 25” chip samples, amplifies, buffers and processes signals from 128 channels of silicon strip sensor. Each microstrip is readout by a charge sensitive amplifier with $\tau = 50\ \text{ns}$. The output voltage is sampled at the beam crossing rate of $40\ \text{MHz}$. Samples are stored in an analogue pipeline for up to the Level-1 latency of $3.2\ \mu\text{s}$. Following a trigger, a weighted sum of 3 samples is formed in an analogue circuit. This confines the signal to a single bunch crossing and gives the pulse height. The buffered pulse height data from pairs of APV25 chips are multiplexed onto a single line and analogue data are converted to optical signals before being transmitted via optical fibers to the off-detector FED boards. The output of the transmitting laser is modulated by pulse height for each strip. The FEDs digitise, process and format the pulse height data from up to 96 pairs of APV25 chips, before forwarding

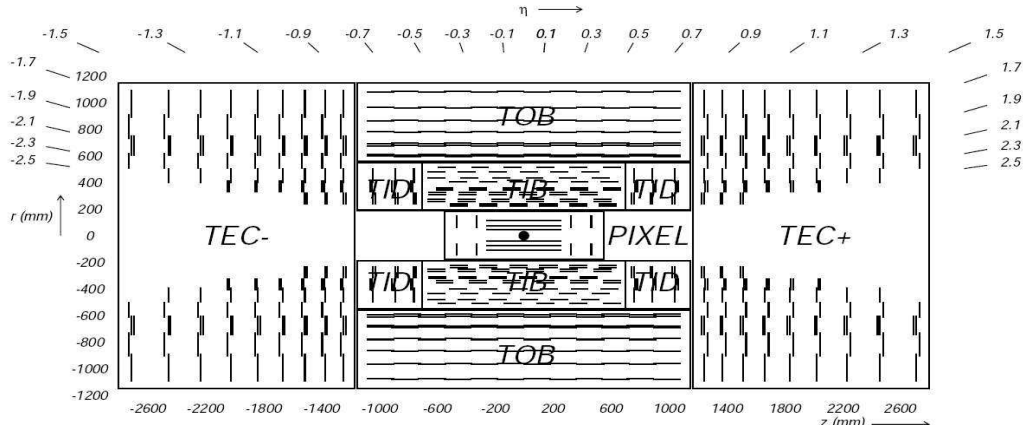


Figure 3.3: Schematic cross section through the CMS tracker. Each line represents a detector module. Double lines indicates back-to-back modules which deliver stereo hits [30].

zero-suppressed data to the data acquisition system (DAQ) online farm. The electronic noise per channel of the tracking system is about 1000 to 1500 electrons before and after irradiation, respectively. The silicon strip tracker control system comprises $\simeq 300$ control rings that start and end at the off-detector Front-End Controller (FEC) boards. Slow control commands, clock and Level-1 triggers are distributed via digital optical links to Digital Opto-Hybrids (DOHs), which perform optical to electrical conversion before the control signals are distributed to the front end electronics. A single pixel barrel module is readout by 16 Read-Out Chips (ROC). In the endcaps, the number of ROCs per module varies from 2 to 10. Each ROC reads an array of 52×80 pixels. Analogue signals and corresponding pixel addresses are stored in a data buffer, waiting for the Level-1 trigger decision. Following a Level-1 trigger accept, data are transmitted on optical links to the FED boards. In the barrel, groups of 8 or 16 ROCs are connected to 1 link, whereas in the endcaps there are 21 to 24 ROCs per link. The 40 FEDs perform digitization and data formatting.

3.3 The electromagnetic calorimeter ECAL

The CMS electromagnetic calorimeter (ECAL) [30–32] is a hermetic homogeneous calorimeter, which is composed of two parts, the barrel and the endcaps, as shown in Figure 3.4. It is made of 61200 lead tungstate (PbWO_4) crystals mounted in the barrel, closed by 7324 crystals in each of the two endcaps. A preshower is placed in front of the endcap crystals. Avalanche photodiodes (APDs) are used as photodetectors in the barrel and vacuum photodiodes (VPTs) in the endcaps. The use of high density crystals has allowed the design of a calorimeter which is fast, has fine granularity and is radiation resistant.

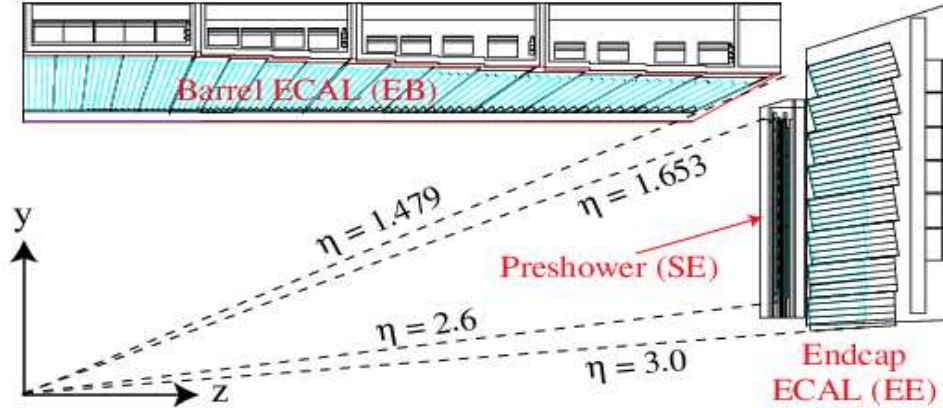


Figure 3.4: Longitudinal view of one quarter of the ECAL calorimeter [31].

3.3.1 Lead tungstate crystals

The characteristics of PbWO_4 crystals make them an appropriate choice for an electromagnetic calorimeter. The high density (8.28 g/cm^3), short radiation length (0.89 cm) and small Moliere radius ($R_M = 2.2 \text{ cm}$), as summarized in Table (3.1), result in a fine granularity and a compact calorimeter. The PbWO_4 crystals are optically clear, fast and radiation-hard.

chemical composition	PbWO_4
density	8.28 g/cm^3
radiation length	0.89 cm
R_M	2.2 cm

Table 3.1: Physical properties of the ECAL crystals.

The scintillation decay time of these crystals is of the same order of magnitude as the LHC bunch crossing time: about 80% of the light is emitted in 25 ns. The light output is relatively low and varies with the temperature: at 18°C about 4.5 photoelectrons per MeV are collected in both APDs and VPTs. The crystals emit blue-green scintillation light with a broad maximum at 420-430 nm.

To exploit the total internal reflection for optimum light collection on the photodetectors, the crystals are polished after machining. In the endcaps, the light collection is naturally more uniform because the crystal faces are nearly parallel.

Ionizing radiation produces absorption bands through the formation of colour centres due to oxygen vacancies and impurities in the lattice. To ensure adequate performance through LHC operation, the crystals are required to exhibit radiation hardness properties quantified as an induced light attenuation length (at high dose rate) greater than approximately 3 times the crystal length, even when the damage is saturated. Hadrons have been measured to induce a specific, cumulative reduction of light transmission, but the extrapolation to LHC conditions indicates that the damage will remain within the limits required for good ECAL performance.

3.3.2 The mechanical design of the ECAL barrel (EB)

The barrel part of the ECAL (EB) covers the pseudorapidity range $|\eta| < 1.479$. The granularity of the barrel is 360-fold in ϕ and (2×85) -fold in η , resulting in a total of 61200 crystals. These crystals are made of lead tungstate (PbWO_4) with a tapered shape, slightly varying with position in η . The crystals cross-section corresponds approximately to 0.0174×0.0174 (1°) in η - ϕ or $22 \times 22 \text{ mm}^2$ at the front face of the crystal, and $26 \times 26 \text{ mm}^2$ at the rear face. The centres of the front faces of the crystals are at radius 1.29 m from the beam pipe axis, as shown in Figure 3.5. The length of each crystal is 320 mm, which corresponds to $25.8X_0$. The barrel crystal volume is 8.14 m^3 and the weight is 67.4 t. The trigger division of $\Delta\eta \times \Delta\phi = 0.087 \times 0.087$ corresponds to groups of 5×5 crystals.

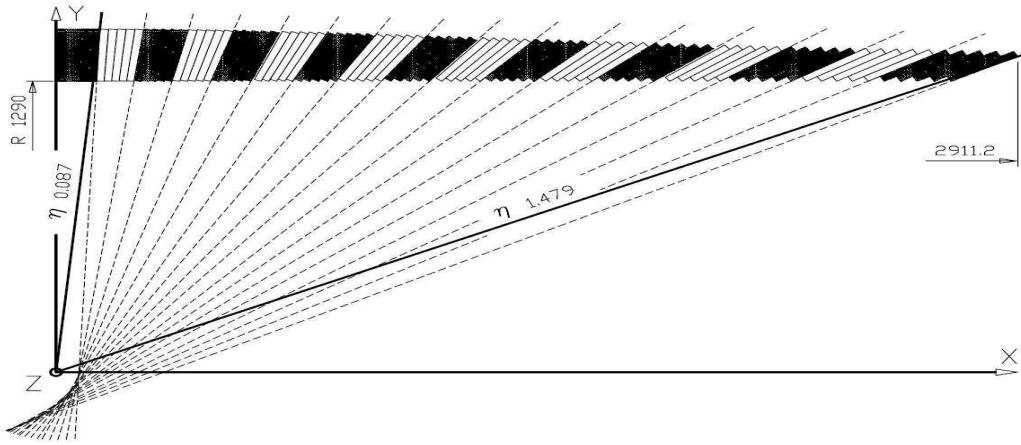


Figure 3.5: Longitudinal trigger division [32].

The crystals are contained in thin-walled glass-fiber alveolar structures called submodules. Each submodule contains 10 crystals, the η extent of a submodule corresponding to a trigger tower. The nominal crystal to crystal distance is 0.35 mm inside a submodule, and 0.5 mm between the submodules. In order to reduce the number of different types of crystals, the crystals in each submodule have the same shape.

The submodules are assembled into modules of different types, each module consists of 50 or 40 submodules containing 500 or 400 crystals according to the position in η . The most inner modules count 25 crystals in η , and 20 for others modules. They correspond to 20° ($= 20$ crystals) in ϕ . Each module in the central region of the ECAL barrel contains 5 submodules, and 4 submodules in the rest of the barrel (see Figure 3.4). Table 3.2 gives the site of cracks in mm between modules in the ECAL barrel.

	$\eta = 0$	No. 1-2	No. 2-3	No. 3-4
Stair-like shape (normal to crystal face)	1.00	1.00	1.53	1.89
Crack value (normal to basket wall)	6.00	6.00	6.00	6.00

Table 3.2: Cracks [in mm] between modules [32].

Four modules form a supermodule. Supermodules, which are separated by aluminium webs of 6 mm (as seen from Table 3.2) thick, contain 1700 crystals (see Figure 3.4). A cylindrical plate in front of the supermodules also provides the fixation of the monitoring system, and the holders for its optical fibers. There are 80 supermodules, each covering 20° in ϕ , forming a half barrel. Between two supermodules (in ϕ) there is a crack of 6 mm.

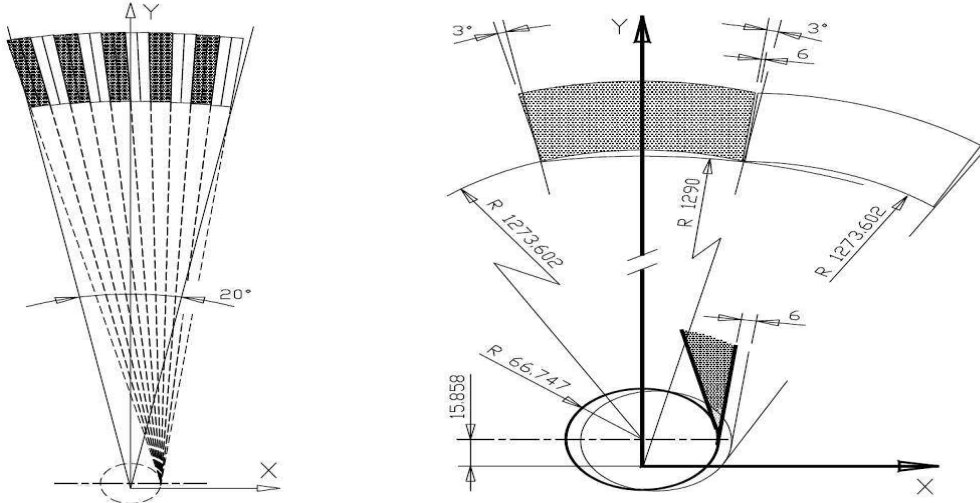


Figure 3.6: Construction of the crystal ϕ tilt [32].

The crystals are mounted in a quasi-projective geometry to avoid cracks aligned with particles trajectories. For that reason their axes make a small angle (3°) with respect to the direction from the nominal vertex, in both the ϕ and η projections. The 3° - ϕ tilt, as seen in Figure 3.6, produces a step between adjacent pairs of crystals in the same η position. The crystals in the next η position fit into this stepped shape, because the submodule walls can follow the individual crystal shape. This effect slightly increases the gap between the modules. The first crystal in η has one side face normal to the beam axis. To produce the η tilt as smoothly as possible, the five crystals of the first submodule have an angular increment of 0.6° in excess of the normal angular increment of a pointing geometry. In this way the 3° η tilt is fully applied from the second to the last submodules as it is shown in Figure 3.5. This tilt in the η direction affects the energy containment of electromagnetic showers in sets of the 5×5 crystals (see Figure 3.7).

3.3.3 The mechanical design of the ECAL endcaps (EE)

To have good resolution in the ECAL endcaps, the amount of energy deposited in the non-instrumented material or lost through gaps or cracks must be minimized. The calorimeter must provide good geometrical acceptance and extend the range of pseudorapidity coverage as far as possible. Excellent calorimeter hermeticity is also required, reinforcing the requirements for minimal gaps or cracks. For these reasons, the endcaps (EE) cover the rapidity range $1.479 < |\eta| < 3.0$, as shown in Figure 3.8.

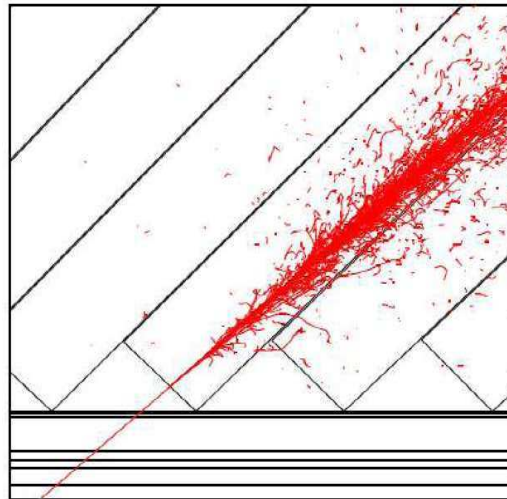


Figure 3.7: Simulation of an electromagnetic shower in crystals tilted in η in the ECAL barrel [32].

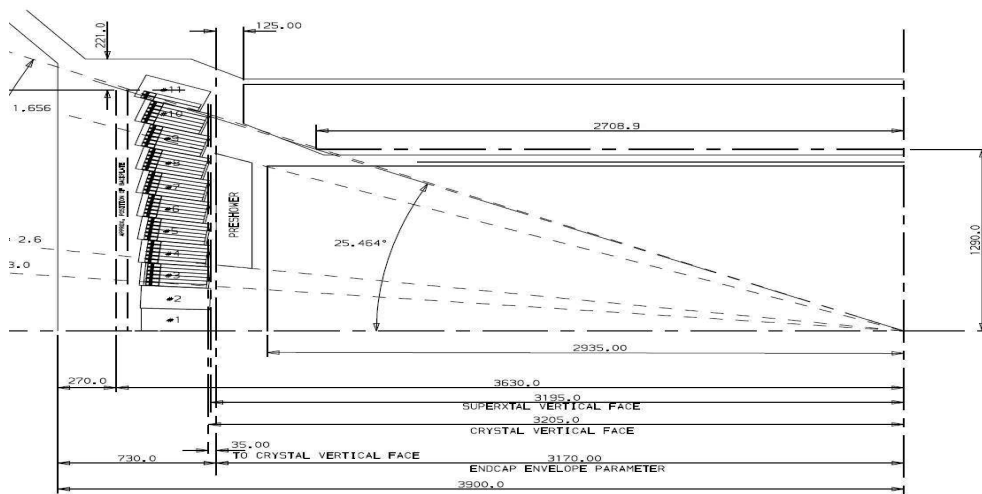


Figure 3.8: The ECAL endcap layout [32].

The longitudinal distance between the nominal interaction point and the endcap envelope is 3.15 m, taking into account the estimated shift toward the interaction point by 1.6 cm when the 4 T magnetic field is switched on. Each endcap consists of identically shaped crystals, grouped in mechanical units of 5×5 crystals forming a supercrystal. The crystals and supercrystals are arranged in a rectangular $x - y$ grid. Each endcap is divided into 2 halves which are known as Dees, as illustrated in Figure 3.9.

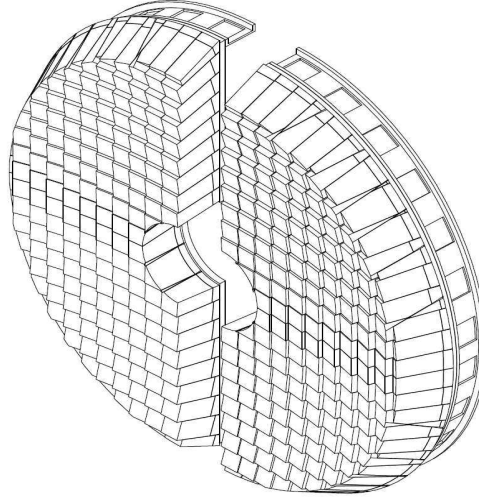


Figure 3.9: A single ECAL endcap with Dees moved apart [32].

Each Dee holds 3662 crystals, which are contained in 138 standard supercrystals and 18 special partial supercrystals on the inner and outer circumferences. The supercrystals are arranged on each Dee in columns, as shown in the elevation ($z - y$) view, see Figure 3.10 (left). The crystals are oriented nearly parallel to the beam axis (see Figure 3.8). This allows identical crystals to be used. The crystals have rear face cross sections $30 \times 30 \text{ mm}^2$ while $28.62 \times 28.62 \text{ mm}^2$ at the front face. To achieve the required resolution the calorimeter must be of sufficient thickness and this has led to the choice of 220 mm long crystals, which corresponds to $24.7X_0$. The endcap crystal volume is 2.90 m^3 and the weight is 24 t. If each endcap had a geometry pointing exactly at the interaction point, it would have inherent gaps between the crystals, through which photons or electrons can escape undetected. For that reason the crystals point at a focus 1300 mm beyond the interaction point, giving off-pointing angles ranging from 2 to 8 degrees with decreasing η . The off-pointing to the far side of the intersection point is required in order to ensure maximum path length through the EE crystals.

The space available for the EE is tightly constrained on the inside by the need to maintain adequate tracking length, and on the outside by the desired thickness for the hadronic calorimeter (HCAL) and the need for the first muon chamber to be inside the coil. The allocation of 730 mm must accommodate 220 mm long crystals, the photodetector and the read-out. All materials used in the EE construction must also be able to withstand the radiation level encountered in the endcap region.

The supercrystals are stacked vertically above one other with reference to one of the long sides. Each supercrystal subdetector unit is supported in position by means of a cantilever support from stiff backplate (see

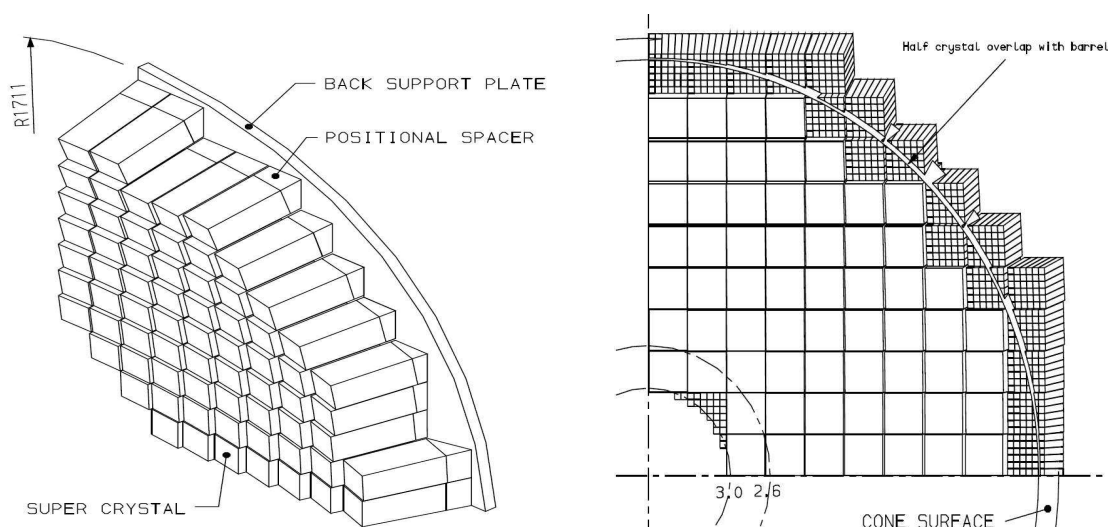


Figure 3.10: (left plot) Shows the arrangement and mounting of supercrystals on a quadrant of the EE; (right plot) a front view of the conical cut through the EE [32].

Figure 3.10 (left)), and has a special seating element interposed between the rear plate of the supercrystal and the back support plate to enable each supercrystal to be precisely positioned and pointed in the correct direction. Due to the wedge shape of the supercrystals the opposite long side overhangs the supercrystal which is seated below it (as shown in Figure 3.10 (left) in the $(z - x)$ plane). It is with respect to this overhang, at the top of a column of supercrystals, that the next column of supercrystals is positioned. This introduces a complex set of cracks between the supercrystals columns. The cracks are between 1 and 3 mm from crystal to crystal, across the supercrystal boundaries, at a depth of 80 mm from the front face of the crystals. The clearance between the supercrystals is 0.5 mm at the front face and 1.0 mm at the back face, giving a net 1.0 to 1.5 mm crystal to crystal crack across the supercrystal boundaries. The first column of supercrystals in each Dee will be aligned vertically with the long straight edge of the Dee. The clearance between the Dees in each endcap will be 2 mm, with a consequent crystal to crystal crack, from one Dee to the other of 2.5 mm. Within a Dee there is quadrant symmetry about the mid-plane $(z - x)$, through reflection. The supercrystals on either side of this plane will have clearance of 0.8 mm, giving a net crystal to crystal crack of 1.3 mm.

The backplates for the Dees are made of aluminium alloy which has been machined to obviate distortion and to avoid a flat front face on which to mount the supercrystals. Dimensionally the backplates have 1711 mm outer radius, 370 mm inner radius with 50 mm thick. Holes of 40 mm diameter are provided in the Dees at each supercrystals position. These allow services to pass through the backplates between the supercrystals at the front and the electronic packages mounted on the rear. The Dees are mounted from the front face of the hadronic endcap (HE) via a mounting ring and an annular spacer.

It is required that the crystal temperature be stabilized at 18° . Since the crystals are cantilevered, good thermal contact with them can only be made at their rear ends through the supercrystal mount to the backplate. The temperature is controlled by passing a coolant through a serpentine pipe fixed to the rear face. The su-

percrystals are totally enclosed by a shield, which has three functions. Firstly, to provide thermal screening between the endcap and its environment, it will incorporate serpentine cooling pipes carrying coolant at the same temperature as that in the backplate. Secondly, it will act as a containment for dry air streamed through the endcap against humidity and He contamination to the Vacuum photoTriode (VPTs). Thirdly, it will provide the supercrystals with protection against accidental damage.

The **barrel-endcap transition** has a crucial importance for the hermeticity of the detector. The outer perimeter of the EE has been designed by considering a conical cut which intercepts the last crystal in the EB to give a half crystal overlap in EE, as shown in the front view of Figure 3.10 (right), where crystals are shown outside the cone. They are for illustration only and are not included in the final detector. This special structure implies poor clustering in the barrel-endcap transition regions. The energy collected for an electron or a photon emitted in the direction of this crucial region will be poor as well. This region is studied in detail in chapter 6.

3.3.4 The mechanical design of the ECAL preshower (ES)

The principle aim of the CMS preshower detector is to identify neutral pions and to separate them from the single photons. This requires very good energy resolution, since π^0 s with a transverse energy of the order of 60 GeV lead to a separation between the 2 decay photons of about 0.8 cm in the ECAL barrel region, while it is only a few mm in the ECAL endcaps. The photon pair will give a broader shower than for a single photon and π^0 rejection can be achieved in the ECAL barrel, but the endcap crystals can not resolve the 2 photons from π^0 decay. A preshower with good granularity has thus been installed, to act as a good photon sensitive detector within the fiducial region $1.653 < |\eta| < 2.6$. It also helps the identification of the electrons against minimum ionizing particles. Finally, it improves the position determination of electrons and photons thanks to the high granularity [33].

The preshower is a sampling calorimeter with two layers: lead radiators initiate electromagnetic showers from the incoming electrons or photons, whilst silicon strip sensors placed after each radiator measure the deposited energy and the transverse shower profiles of the incident particles. The total thickness of the preshower is 20 cm. The material thickness traversed at $\eta = 1.653$ before reaching the first sensor plane is $2 X_0$, followed by $1 X_0$ before reaching the second plane. Thus about 95% of the incident photons start showering before the second sensor plane. The orientation of the strips in the two planes is orthogonal. The lead planes are arranged in two Dees, one on each side of the beam pipe, with the same orientation as the crystal Dees. Each silicon sensor measures $63 \times 63 \text{ mm}^2$, with an active area of $61 \times 61 \text{ mm}^2$ divided into 32 strips (1.9 mm pitch). The nominal thickness of the silicon is $320 \mu\text{m}$, in which a minimum ionizing particle (MIP) will deposit 3.6 fC of charge (at normal incidence). The sensors are precisely glued to ceramic supports, which also support the front-end electronics assembly, and this is in turn glued to an aluminium tile that allows a 2 mm overlap of the active part of the sensors in the direction parallel to the strips. In order to improve noise performance the tile is constructed in two parts, with a glass fibre insulation in between. The combination of sensor, front-end electronics and supports is known as micromodule of area $61 \times 61 \text{ mm}^2$. The micromodules are placed on baseplates in groups of 7, 8 or 10 that, when coupled to an electronics system motherboard (SMB) placed above

the micromodules, form a ladder. The spacing between silicon strips (at the edges) in adjacent micromodules within a ladder is 2.4 mm, whilst the spacing between strips in adjacent ladders is normally 2.5 mm. For the region where the two Dees join, this spacing is increased to 3.0 mm. The ladders are attached to the radiators in a $x - y$ configuration. Around 500 ladders are required, corresponding to a total of around 4300 micromodules and 137000 individual read-out channels.

3.4 ECAL trigger and data acquisition

The LHC bunch crossing rate is 40 MHz, which leads to $\sim 10^9$ interactions/s at designed luminosity. Data from only about 10^2 crossings/s can be written to archival media. Hence, the trigger system has to achieve a rejection factor of nearly 10^6 .

The CMS trigger and data acquisition system consists of 4 parts:

- (1) the detector electronics,
- (2) the read-out network system (Trigger Primitives),
- (3) the Level-1 trigger processors,
- (4) the on-line event filter system (processor farm) that executes the CMS software [34] for the High Level Trigger (HLT).

The HLT of CMS is described in detail in [35, 36].

3.4.1 Trigger primitives

For each bunch crossing, the ECAL data in the form of trigger primitives are sent to Level-1 calorimeter trigger processors. Each trigger primitive refers to one trigger tower. It consists of the summed transverse energy deposited in the tower, and of a compactness bit, which characterizes the lateral extension of the electromagnetic shower. For accepted events, the “accept” signal will be returned from the global trigger in about $3\mu\text{s}$. The selected events are then read out through the data acquisition system and sent to the Filter Farm, where further rate reduction is performed using the full detector data.

The ECAL read-out system is structured into sets of 5×5 crystals. The Front-End (FE) card stores the data in memory banks with depth of 256-clock cycles (25 ns). A Level-1 trigger decision is awaited during at most 128 bunch crossings after the collision occurred. The FE cards implement most of the Trigger Primitives Generation (TPG) pipeline. In the barrel, each FE card is served by 3 optical links which transmit the clock, control and Level-1 trigger signals. These 5×5 crystal sets correspond to the trigger towers, of extension $\Delta\eta \times \Delta\phi = 0.087 \times 0.087$, which match directly with the HCAL towers. Each trigger tower is divided into 5 ϕ oriented strips, whose energy deposits are summed by the FE to give the total transverse energy of the tower, called the main trigger primitive.

In the ECAL endcaps, the read-out modularity maps onto 5×5 mechanical units (supercrystals). However the sizes of the trigger towers vary, in order to approximately follow the η and ϕ geometry of the HCAL and the Level-1 trigger processors. The supercrystals are divided into groups of 5 contiguous crystals; these groups

are of variable shapes and referred to as pseudo-strips. The trigger towers are composed of several pseudo-strips and may extend over more than one supercrystal. Since the read-out structure does not match the trigger structure, only the pseudo-strips summations are performed on the detector. The total transverse energy of the trigger tower is computed by the off-detector electronics. Hence, each endcap FE board is served by 7 optical links, 5 of them being used to transmit the trigger primitives.

3.4.2 Level-1 trigger (L1)

The size of the LHC detectors and of the underground caverns imposes a minimum transmit time for the signals from the front end electronics to reach the service caverns housing the Level-1 trigger logic and return back to the detector front-end electronics. The total time allocated for the transmit and for reaching a decision to keep or discard data from a particular beam crossing is $3.2\mu\text{s}$, which is equivalent to a rate of 312.5 kHz. During this time the detector data is held in buffers, while the trigger data is collected from the front-end electronics, and the decisions of discarding a large fraction of events while retaining the small fraction of the interactions of interest (nearly 1 crossing in 1000) are reached. The time allocated for Level-1 trigger calculations is less than $1\mu\text{s}$.

The Level-1 triggers involve the calorimetry and muon systems, as well as some correlation of information between these systems. The decision taken by the Level-1 is based on the presence of “trigger primitive” objects such as photons, electrons, muons and jets above E_T thresholds. It also employs global sums of E_T and E_T^{miss} . At startup the Level-1 rate will be limited to 50 kHz (the designed value is 100 kHz). Taking the safety margin of a factor of 3 into account for simulation uncertainties as well as beam and detector conditions not included in the simulation programs, this leads to an estimated rate of 16 kHz. The designed value, which is 100 kHz, is set by the average time to transfer full detector information through the read-out system. During the Level-1 decision making period, all the high resolution data is held in pipeline memories.

3.4.3 High-Level trigger (HLT)

Upon receipt of a Level-1 trigger, the data from the pipelines are transmitted to the front-end read-out buffers. After signal processing, zero suppression and/or data compression, the data are stored in dual port memories to be accessed later by the DAQ system. Each event, of average size 1.5 MB (for pp interactions), is kept in several hundreds front-end read-out buffers. Then the data from a given event is sent to a processor, which starts to run the high-level trigger software code, in order to reduce the Level-1 output rate from 100 kHz to only 100 Hz to be stored. A big processor farm is used for all selections behind the Level-1 trigger.

There are different strategies for the development of the HLT code. At HLT level the reconstruction of all possible objects in the event, from different parts of the detector, is performed, while the decision of discarding unwanted events is taken as soon as possible. This leads to the idea of partial reconstruction and to the notation of many virtual trigger levels. In the HLT code the calorimeter and muon informations are used, followed by the use of the tracker pixel data, and finally the use of the full event information including full tracking.

3.5 The hadron calorimeter HCAL

The CMS hadron calorimeter (HCAL) is described in detail in [30,31,37]. HCAL in conjunction with the ECAL forms a complete calorimetry system for the measurement of jets and missing transverse energy. The HCAL is important for the measurement of hadronic jets and neutrinos or exotic particles, resulting in apparent missing transverse energy. The hadron calorimeter barrel and endcaps sit behind the tracker and the electromagnetic calorimeter as seen from the interaction point. As shown in Figure 3.11, the barrel hadron calorimeter is radially mounted between the outer extent of the electromagnetic calorimeter ($R = 1.77$ m) and the inner extent of the magnet coil ($R = 2.95$ m). This constrains the total amount of material which can be put in to absorb the hadronic shower. For that reason an outer hadron calorimeter or tail catcher is placed outside the solenoid, complementing the barrel calorimeter. Beyond $|\eta| = 3$, the forward hadron calorimeters are placed at 11.2 m from the interaction point, extending the pseudorapidity coverage down to $|\eta| = 5.2$. They use a Cherenkov-based, radiation-hard technology.

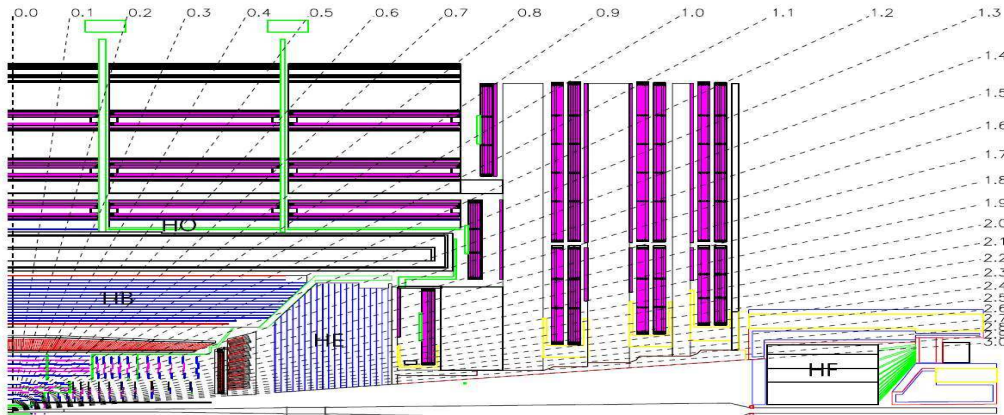


Figure 3.11: Longitudinal view of the CMS detector showing the location of the hadron barrel (HB), endcap (HE), outer (HO) and forward (HF) calorimeters [31].

3.5.1 The mechanical design of the HCAL barrel (HB)

The barrel hadron calorimeter extends out to $|\eta| = 1.4$. It has a polygonal structure with an assembly of 18 wedges to form one half-barrel. The two half-barrels are then joined to make the complete HB. Each wedge subtends 20° in ϕ and extends from the CMS detector mid-plane by 4.33 m. The wedge is composed of copper alloy absorbers (see Table 3.3) which are bolted together. The radiation length for the brass alloy is $X_0 = 1.49$ cm and the hadronic interaction length (λ) 16.42 cm. The amount of material between the ECAL and the HCAL, due to the presence of the ECAL electronics, cooling, cables and support, corresponds to about $3 X_0$ in average.

The inner and outer plates are made out of stainless steel. There are 17 slots at constant radial gaps, the inner and outer slots being 14 mm thick and the remaining ones 9.5 mm. Each slot is composed of scintillator

chemical composition of absorbers	70% Cu, 30% Zn
chemical composition of scintillators	plastic
density	8.53 g/cm ³
radiation length	1.49 cm
interaction length	16.42 cm

Table 3.3: Physical properties of the HCAL Barrel brass absorber.

mega-tiles of thickness 9 mm (for the first and last layers) and 3.7 mm (for the remaining layers), covered with plastic of thickness 2 mm on the inner side and 1 mm on the outer side. Each mega-tile subtends 5° in ϕ (size of $\Delta\eta \times \Delta\phi = 0.087 \times 0.087$). There are 61 mm of stainless steel between layer 0 and layer 1, then 50.5 mm thick brass between layers till layer 9, and 56.5 mm thick brass till layer 15. The back plate is 75 mm thick stainless steel, in front of HB layer 16. The HB effective thickness increases with the polar angle θ as $1/\sin\theta$, resulting in 10.6λ at $\eta = 1.3$, while the electromagnetic crystal calorimeter in front of the HB adds about 1.1λ material.

3.5.2 The mechanical design of the HCAL endcap (HE)

The endcap parts of the hadron calorimeter cover the η range $1.3 < |\eta| < 3.0$. They are also made of copper alloy absorbers with sampling layers of plastic scintillators. Each endcap has a 18 fold symmetry in ϕ and is made of 35 mm thick sector plates each covering 20° in ϕ . The sector layers are separated by 9 mm thick brass spacers covering 10° in ϕ for scintillator inserts. The top edge, of the front part of each endcap module, has a slope of 53° corresponding to the gap angle between HB and HE. The gap between HB and HE is used for the cable path of the tracker, the electromagnetic calorimeter and HB itself. The absorber design has been chosen to minimize the gap between HB and HE. The plates are bolted together in a staggered geometry to have configurations, which contain no dead material. This design provides a self supporting construction without dead zone. The absorber thickness between successive layers amounts to 78 mm of brass corresponding to the thickness of two sector plates and one spacer, with 9 mm gap to accommodate the scintillators. Each scintillator thickness is 3.7 mm. The total length of the HE calorimeter, including the electromagnetic crystals, is about 10 interaction lengths (λ). The outer layers of HE have a cutout region for the installation of the photodetectors and the front-end electronics. The outer layers are fixed to 10 cm thick stainless steel support plates. The optical elements are inserted into the gaps after the absorber is completely assembled.

3.5.3 The Outer Calorimeter (HO)

The HB alone fails to provide a sufficient containment for hadron showers in the central pseudorapidity region. To ensure adequate sampling depth for $\eta < 1.3$, the hadron calorimeter is extended outside the solenoid, where it is called HO. HO utilises the solenoid coil as an additional absorber to $1.4/\sin\theta$ interaction length. It will be used to identify the late starting showers and to measure the shower energy beyond the geometrical reach of the HB. Outside the vacuum tank of the solenoid, the magnetic field is returned through an iron yoke designed

in the form of five 2.53 m wide (along the z -axis) rings. HO is placed as the first sensitive layer in each of these five rings. The nominal central z positions of the five rings are, respectively, -5.342m , -2.686m , 0 , $+2.686\text{m}$ and $+5.342\text{m}$. Near $\eta = 0$, HB provides a minimum interaction length to hadrons produced in pp collisions. Therefore, the central ring (ring 0) has two layers of HO scintillators on either side of a 19.5mm thick piece of iron (the tail catcher iron) at radial distances of 3820 mm and 4070 mm, respectively. All other rings have a single HO layer at radial distance of 4070 mm. The total depth of the calorimeter system is extended to a minimum of 11.8λ , except at the barrel-endcap boundary region. The HO scintillators follow the HCAL barrel tower geometry in η and ϕ .

3.5.4 The Hadron Forward Calorimeter (HF)

The hadron forward calorimeters cover the pseudorapidity regions between 3.0 and 5.2. They are composed of a sandwich of steel and quartz fibres. The front face is located at 11.2 m from the interaction point. The depth of the absorber is 1.65 m. The absorber structure is created by machining 1 mm square grooves into steel plates, which are then diffusion welded. The signal originates from the Cerenkov light emitted in quartz fibres, which is then channeled by the fibres to photomultipliers. The diameter of the quartz fibres is 0.6 mm and they are placed 5 mm apart in a square grid. The quartz fibres, which run parallel to the beam line, have two different lengths (namely 1.43 m and 1.65 m) which are inserted into the grooves, creating 2 effective longitudinal samplings. There are 13 towers in η , all with size given by $\Delta\eta \simeq 0.175$, except for the lowest η tower with $\Delta\eta \simeq 0.1$ and the highest η tower with $\Delta\eta \simeq 0.3$. The η segmentation of all towers is 10° , except for the highest η one which has $\Delta\phi = 20^\circ$. This leads to 900 towers and 1800 channels in the 2 HF modules.

3.5.5 The HCAL read-out electronics

The HCAL read-out consists of an optical to electrical transducer followed by a fast charge integrating ADC. The digital output of the ADC is transmitted for every bunch over gigabit digital optical fibres to the service cavern, housing the off-detector electronics. In the service cavern, the signal is kept and used to construct trigger primitives which are sent to the calorimeter trigger. The data and trigger primitives are also pipelined for transmission to the DAQ upon Level-1 Accepted (L1A) decision. The optical signals from the scintillator-based detectors (HB/HE/HO) are converted to electrical signals using multichannel hybrid photodiodes (HPDs), which provide a gain of $\simeq 2000$. The optical signals from individual sampling layers are brought out on clear fibres. In the forward calorimeter, where the magnetic fields are much smaller than in the central detector, the photomultiplier tubes are used, and quartz fibre bundles are routed directly to the phototube windows. Several PCs in the CMS control room are used to control the high and low voltages. The control systems also downloads pedestal DAC and timing parameters to front-ends, and it controls many of the calibration and monitoring systems, including the source calibration drives, the LED pulsers, the laser system, and systems which record the temperature, humidity and other constants useful for correction studies of the detector and calibration stability.

Tower index	η range		Detector	Size		Depth segments
	Low	High		η	ϕ	
1	0.000	0.087	HB, HO	0.087	5°	HB=1, HO=1
2	0.087	0.174	HB, HO	0.087	5°	HB=1, HO=1
3	0.174	0.261	HB, HO	0.087	5°	HB=1, HO=1
4	0.261	0.348	HB, HO	0.087	5°	HB=1, HO=1
5	0.348	0.435	HB, HO	0.087	5°	HB=1, HO=1
6	0.435	0.522	HB, HO	0.087	5°	HB=1, HO=1
7	0.522	0.609	HB, HO	0.087	5°	HB=1, HO=1
8	0.609	0.696	HB, HO	0.087	5°	HB=1, HO=1
9	0.696	0.783	HB, HO	0.087	5°	HB=1, HO=1
10	0.783	0.870	HB, HO	0.087	5°	HB=1, HO=1
11	0.879	0.957	HB, HO	0.087	5°	HB=1, HO=1
12	0.957	1.044	HB, HO	0.087	5°	HB=1, HO=1
13	1.044	1.131	HB, HO	0.087	5°	HB=1, HO=1
14	1.131	1.218	HB, HO	0.087	5°	HB=1, HO=1
15	1.218	1.305	HB, HO	0.087	5°	HB=2, HO=1
16	1.305	1.392	HB, HE	0.087	5°	HB=2, HE=1
17	1.392	1.479	HE	0.087	5°	HE=1
18	1.479	1.566	HE	0.087	5°	HE=2
19	1.566	1.653	HE	0.087	5°	HE=2
20	1.653	1.740	HE	0.087	5°	HE=2
21	1.740	1.830	HE	0.090	10°	HE=2
22	1.830	1.930	HE	0.100	10°	HE=2
23	1.930	2.043	HE	0.113	10°	HE=2
24	2.043	2.172	HE	0.129	10°	HE=2
25	2.172	2.322	HE	0.150	10°	HE=2
26	2.322	2.500	HE	0.178	10°	HE=2
27	2.500	2.650	HE	0.150	10°	HE=3
*28	2.650	3.000	HE	0.350	10°	HE=3
29	2.853	2.964	HF	0.111	10°	HF=2
30	2.964	3.139	HF	0.175	10°	HF=2
31	3.139	3.314	HF	0.175	10°	HF=2
32	3.314	3.489	HF	0.175	10°	HF=2
33	3.489	3.664	HF	0.175	10°	HF=2
34	3.664	3.839	HF	0.175	10°	HF=2
35	3.839	4.013	HF	0.174	10°	HF=2
36	4.013	4.191	HF	0.178	10°	HF=2
37	4.191	4.363	HF	0.172	10°	HF=2
38	4.363	4.538	HF	0.175	10°	HF=2
39	4.538	4.716	HF	0.178	10°	HF=2
40	4.716	4.889	HF	0.173	20°	HF=2
41	4.889	5.191	HF	0.302	20°	HF=2

Figure 3.12: Sizes of the HCAL read-out towers in η and ϕ and depth segmentation [31].

The hadron calorimeter is read-out in a tower-like structure. The hadron calorimeter has a pointing geometry with towers segmented along ϕ . Figure 3.12 shows the size of the HCAL read-out towers in η and ϕ as well as the segmentation in depth. HB has 16 towers (1 – 16) on either side of the $z = 0$ plane, while HE has 14 towers (16 – 29). As illustrated in Figure 3.13, all layers in HB which belong to a given η and ϕ section are grouped into one tower. For tower 15, layers 13, ..., 16 belong to the second depth index. For tower 16, layer 3 belongs to the depth index 2. For HE, the first two towers (16, 17) have only one depth slice, while the next 9 towers (18 – 26) have two depth slices and the remaining ones have 3 depth slices. The third depth slices, corresponding to the last two towers (28, 29), belong to the same readout tower. The granularity in ϕ changes as a function of the tower number. The tower size along ϕ is 5° for the first 20 towers ($|\eta| < 1.74$) and 10° for towers from 21 to 29. Tower 18 covers η range $1.479 < |\eta| < 1.566$ matching the gap between EB and EE.

The CMS trigger granularity is given by the ECAL trigger size, thus determined by the HCAL granularity and the muon chamber structure. The ECAL barrel trigger towers consist of arrays of 5×5 crystals, which match with the HCAL tower granularity of $\Delta\eta \times \Delta\phi = 0.087 \times 0.087$. In the endcaps, trigger towers have the same $\Delta\eta \times \Delta\phi$ granularity as the barrel for $|\eta| < 2.1$. For larger η values, the trigger towers have a granularity of $\Delta\eta = 2 \times 0.087 = 0.174$.

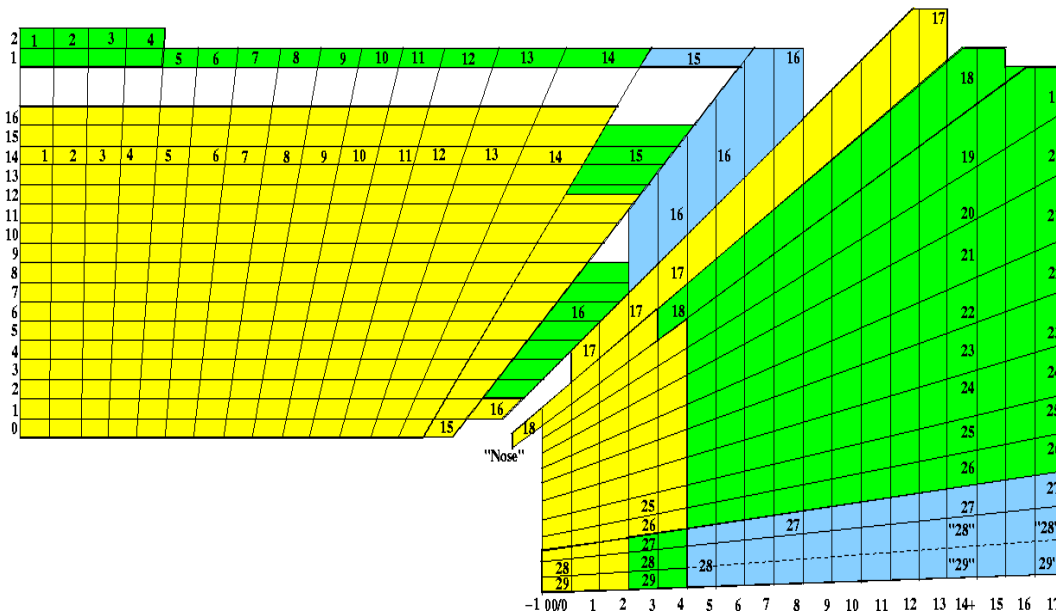


Figure 3.13: Longitudinal view of one quarter of the HCAL calorimeter [31].

3.6 The superconducting magnet

In order to have good momentum resolution within a compact spectrometer without making stringent demands on the muon chamber resolution and alignment, high magnetic field was chosen. The magnet strength is also important for the inner tracker. The superconducting solenoid magnet of CMS has been designed to reach 4

T in a free bore of 6 m diameter and 12.5 m length, with storage energy of 2.6 GJ at full current. The flux is returned through a 10000 t yoke comprising 5 wheels and 2 endcaps. The distinctive feature of the 220 t cold mass is 4 layers winding, which are made of stabilized reinforced NbTi conductor with large cross section. The overall conductor cross section is $64 \times 22 \text{ mm}^2$, that can afford an outward pressure of 64 atmospheres. The conductor carries a current of 20 kA. It has a compound structure. The ratio between the stored energy and cold mass is high (11.6 kJ/kg), causing a large mechanical deformation (0.15%) during energising.

3.7 The muon system

The muon system has special required performance in order to detect a narrow states decaying into muons, also to determine the sign for muons with a momentum of $\sim 1 \text{ TeV}/c$. This requires a momentum resolution of $\Delta p/p \sim 10\%$ at $p = 1 \text{ TeV}/c$. The CMS muon system is designed to have the capability of reconstructing the momentum and charge of muons over the entire kinematic range of the LHC. CMS uses 3 types of gaseous particle detectors for muon reconstruction. Due to the shape of the solenoid magnet, the muon system was naturally driven to have a cylindrical barrel section and two planer endcap regions. Because the muon system consists of about 25000 m^2 of detection planes, the muon chambers had to be inexpensive, reliable, and robust.

In the barrel region, where the muon rate is low and the 4-T magnetic field is uniform and mostly contained in the steel yoke, drift chambers with standard rectangular drift cells are used. The barrel drift tube (DT) chambers cover the pseudorapidity region $|\eta| < 1.2$ and are organized into 4 stations interspersed among the layers of the flux return plates. The first 3 stations each contain 8 chambers, in 2 groups of 4, which measure the muon coordinate in the (r,ϕ) bending plane, and 4 chambers provide measurements in the z direction along the beam line. The forth station does not contain the z -measuring planes. The 2 sets of 4 chambers in each station are separated as much as possible to achieve the best angular resolution. The drift cells of each chamber are offset by a half-cell width with respect to their neighbors to eliminate dead spots in the efficiency. This arrangement also provides a convenient way to measure the muon time with excellent time resolution, using simple mean timer circuit, for efficient, standalone bunch crossing identification. The number of chambers in each station and their orientation were chosen to provide good efficiency for linking together muon hits from different stations into a single muon track and for rejecting background hits.

In the 2 endcap regions of CMS, where the muon rates and background levels are high and the magnetic field is large and non-uniform, the muon system uses cathode strip chambers (CSC). The fast response time, fine segmentation, and radiation resistance of CSC help to identify muons between $|\eta|$ values of 0.9 and 2.4. There are 4 stations of CSCs in each endcap, with chambers positioned perpendicular to the beam line and interspersed between the flux return plates. The cathode strips of each chamber run radially outward providing a precision measurement in the (r,ϕ) bending plane. The anode wires run approximately perpendicular to the strips. They are also read out in order to provide measurements of η and the beam-crossing time of a muon. Each 6-layer CSC provides robust pattern recognition for rejection of non-muon backgrounds and efficient matching of hits to those in other stations, and to the CMS inner tracker.

Because the muon detector elements cover the full pseudorapidity interval $|\eta| < 2.4$ with no acceptance gaps, muon identification is ensured over the range corresponding to $10^\circ < \theta < 170^\circ$. The offline reconstruction efficiency of simulated single muon samples is typically 95–99%, except in the regions around $|\eta| = 0.25$ and 0.8 (the regions between 2 drift tubes “DT” wheels) and $|\eta| = 1.2$ (the transition region between the DT and CSC systems), where the efficiency drops. Negligible punchthrough reaches the system due to the amount of material in front of the muon system, which exceeds 16 interaction lengths.

Due to multiple scattering in the detector material before the first muon station, the offline muon momentum resolution of the standalone muon system is about 9% for small values of η and p , for transverse momenta up to 200 GeV. At 1 TeV the standalone momentum resolution varies between 15% and 40% depending on $|\eta|$. A global momentum fit using also the inner tracker improves the momentum resolution by an order of magnitude at low momenta. At high momenta (1 TeV) both detector parts together yield a momentum resolution of about 5%.

Both DT and CSC systems can each trigger on the p_T of the muons with good efficiency and high background rejection. The level-1 trigger p_T resolution is about 15% in the barrel and 25% in the endcap. A complementary trigger system consisting of Resistive Plate Chambers (RPC) was added in both barrel and endcap regions, to avoid the uncertainty in the eventual background rates and the inability of the muon system to measure the correct beam-crossing time when the LHC reaches full luminosity.

A total of 6 layers of RPCs are embedded in the barrel muon system, 2 in each of the first 2 stations, and 1 in each of the last 2 stations. The redundancy in the first 2 stations allows the trigger algorithm to work even for low p_T muon tracks, that may stop before reaching the outer 2 stations. In the endcap region, there is a plane of RPCs in each of the first 3 stations in order for the trigger to use the coincidences between stations to reduce the background rate, to improve the time resolution for bunch-crossing identification, and to achieve a good p_T resolution.

The alignment system measures the positions of the muon detectors with respect to each other and to the inner tracker, in order to optimize the muon momentum resolution.

Chapter 4

Electron reconstruction and shower shape

4.1 Ecal clustering and superclustering algorithms

For single showers, such as those produced by unconverted photons or electrons, the energy deposited in the ECAL calorimeter is determined on basis of the collected electronic signal, as the energy sums of fixed arrays of crystals. Such energy reconstruction procedures aim at the determination of the true incident particle energy. The procedure to reconstruct and identify electrons and photons in CMS is described in refs [38, 39] and is summarised in this section. Local maxima (“seeds”) in energy deposit, above some threshold (see below), are identified, to which neighboring cells with monotonically decreasing energies are joint as long as they contain an energy deposit significantly higher than the background (60 MeV in EB, 300 MeV in EE). Electromagnetic “clusters” are thus formed, which in turn can be associated into “superclusters”. The supercluster algorithms are designed to collect a fraction as large and as stable as possible of the shower energy, in particular by recovering the energy spread in ϕ due to secondary Bremsstrahlung emission and photon conversions in the material in front of the ECAL. On the other hand, these algorithms must also avoid collecting in the same supercluster energy deposits due to different particles, and to minimize the effects of noise fluctuation. The CMS standard algorithms are the **Hybrid algorithm** in the ECAL barrel region and the **Island algorithm** for the endcap.

For the **Hybrid algorithm**, a list of “seed” crystals with transverse energy above 1 GeV is first constructed. Starting from a seed crystal, a cluster is formed as an ensemble of ϕ contiguous “dominos” which have collected an energy larger than 100 MeV (as shown in Figure 4.1). Each domino consists of 5 crystals with the same ϕ value, which corresponds to a domino width of 0.087 rad in η . If the central crystal energy is smaller than 1 GeV, only 3 crystals are used to form a domino, corresponding to a width of 0.053 rad in η . Whereas less than 100 MeV are collected in a domino, separated different clusters are formed. The dominos are then clustered in ϕ , each distinct cluster of dominos being requested to have a seed domino with energy greater than 0.35 GeV. The ϕ roads are allowed to extend up to ± 10 crystals around the seed, which corresponds to ± 0.175 rad.

For the **Island algorithm**, the “seed” crystals are required to contain a transverse energy larger than 0.18 GeV. Starting from the most energetic seed, the Island algorithm collects energy deposits, first in the ϕ direction, then in η , until a rise in energy or a hole is found. Superclusters are built around the highest transverse energy cluster and then collecting all other nearby clusters in a very narrow η -window, and a much wider ϕ -window. The road for superclustering is allowed to extend up to ± 0.2 rad in ϕ (i.e. ± 11 crystals) and ± 0.14 rad in η (Figure 4.2).

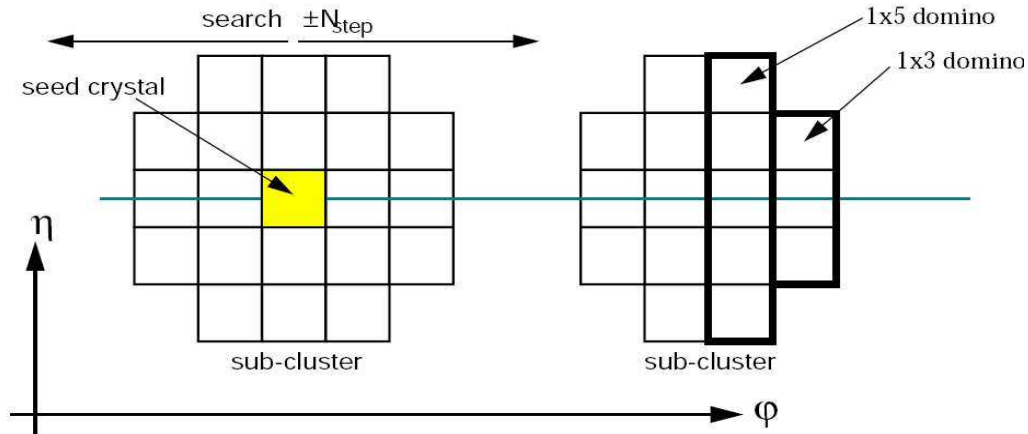


Figure 4.1: Domino construction steps of the Hybrid algorithm [38].

The two algorithms differ slightly in the maximum ϕ extension for Bremsstrahlung recovery (± 10 crystals for the Hybrid algorithm versus ± 0.2 rad for Island algorithm), and more significantly in maximum lateral (η) extension of superclusters.

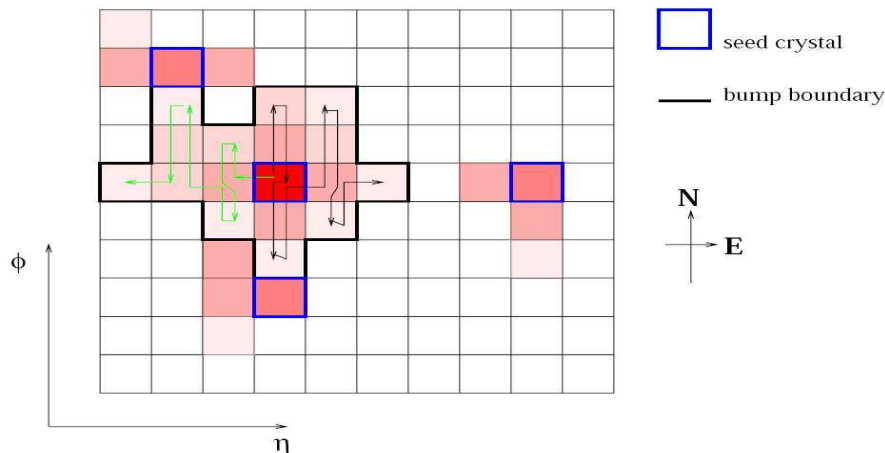


Figure 4.2: Illustration of the Island clustering algorithm [38].

Electron and photon showers deposit their energy in several crystals in the ECAL. Approximately 94% of the incident energy of single electrons or photons is contained in a 3×3 crystal matrix (E_9), and 97% in 5×5 crystals (E_{25}). Summing the energies measured in such fixed arrays gives the best performance for unconverted photons, or for electrons in test beams. The presence, in CMS, of material in front of the calorimeter results in Bremsstrahlung emission and photon conversion. Because of the strong magnetic field the energy reaching the calorimeter is spread in ϕ .

The lack of containment in cluster reconstructed energy can be corrected for as a function of the number of

crystals N_{cry} ($f(N_{cry})$) which make up the seed cluster of the supercluster. This lack is strongly observed for low p_T electromagnetic showers (5 to 100 GeV), where the Bremsstrahlung effect is strong, causing formation of Bremsstrahlung clusters far from the supercluster. For that reason it was needed to use the $f(N_{cry})$ correction function to allow better containment of the Bremsstrahlung energy. This could be achieved by increasing the number of crystals N_{cry} , sufficiently close in the ϕ -direction according to some length of ϕ road, in the formation of the seed cluster of the superclusters. Due to the different clustering algorithms in ECAL barrel and ECAL endcaps, it was found that the $f(N_{cry})$ correction function in the barrel are different from that in the endcaps. After applying the $f(N_{cry})$ correction function to the supercluster energy, it was seen that the distribution of the corrected energy normalized by the generated energy peaks at one in both the barrel and the endcap parts of the ECAL. The distributions are more Gaussian than the uncorrected distributions, plus a gain in the resolution of 5% in the barrel and 10% in the endcaps over the whole 5 to 100 GeV p_T range.

This ϕ road has been optimized for very low p_T electrons and is unnecessarily large for higher p_T electrons, which bend less in the magnetic field. By searching for clusters in an unnecessarily large region the superclustering process risks adding spurious clusters due to pileup or noise. For higher p_T electrons, the appropriate optimization of the ϕ road as a function of the measured E_T in a seed region is investigated in ref. [40]. This new robust clustering algorithm was mainly designed for the ECAL endcaps, where the size of the crystals matrix is fixed around local maxima. The clusters produced by Bremsstrahlung effect will be added using the optimal ϕ road. The energy resolution by the resulting supercluster is equivalent to that of the standard Island algorithm, but with much smaller number of crystals in the seed cluster, at high energies.

4.2 ECAL calibration and linearity

In 2006, ECAL crystals were calibrated in the H2 test beam line at CERN. The combined electromagnetic and hadronic calorimeters (ECAL and HCAL) were exposed to beams of electrons and positrons with different energies between 2 and 120 GeV [41, 42]. 5×5 crystal arrays were used to reconstruct the energies of the electromagnetic showers (E_{25}). The main goal of the calibration is to achieve the most accurate energy measurement for electrons and photons. The reconstructed energy after calibration is given by [31],

$$E_{e,\gamma} = G \times F \times \sum_i c_i \times A_i, \quad (4.1)$$

where G is a global absolute scale, F is a correction function depending on the type of particle, its impact position and also the clustering algorithm, and c_i and A_i are intercalibration coefficients and the signal amplitudes in the ADC counters (which are summed over the clustered crystals), respectively. The function F is also used to correct for the energy loss due to the Bremsstrahlung.

The intercalibration coefficients c_i can be estimated from laboratory measurement of crystal light yield, test beam precalibration of some supermodules and the commissioning of further supermodules with cosmic

rays. It is preferred to intercalibrate the energy in clusters rather than single crystal calibration. For this reason energy intercalibration was measured by summing the energies in the 5×5 crystal array around the crystal with maximum energy (E_{25}). The choice to use (E_{25}) rather than the supercluster algorithms was because of the wish to separate the intercalibration from the algorithmic corrections, which are required for the superclustering algorithms. During the test beam in 2006, the electron beam has been set to energies of 90 and 120 GeV, allowing the study of precalibration of some supermodules. The electron test beam provided very precise measurement of the intercalibration coefficients c_i (better than 0.5%) on a fraction of the detector [41].

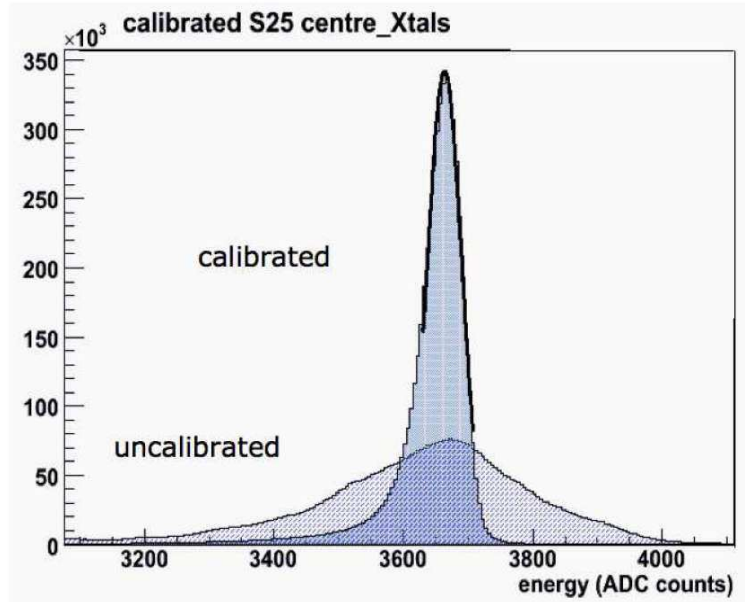


Figure 4.3: The energy reconstructed as E_{25} before and after the intercalibration in a whole supermodule [41].

Figure 4.3 shows the energy reconstructed as E_{25} before and after the intercalibration in a whole supermodule, with no corrections for the global or local variations of the energy deposited in the detector.

After fitting the E_{25} distribution with a Crystal Ball function, which is defined in ref. [42], the ECAL linearity was studied by computing the ratio E_{25}^{peak} / E_{beam} , where E_{25}^{peak} is the Crystal Ball peak. The distribution of the E_{25} peaks, normalized to the beam energies, is illustrated in Figure 4.4, showing a linearity better than 1% in the energy range 9 to 100 GeV.

4.3 ECAL energy resolution measurements in test beams

In 2004 a fully equipped barrel supermodule was tested in the CERN H4 beam of electrons, with momenta between 20 and 250 GeV/c [43].

The electron shower energy contained in a finite crystal matrix depends on the particle impact position with respect to the matrix boundaries. The intrinsic performance of the calorimeter was studied using events where

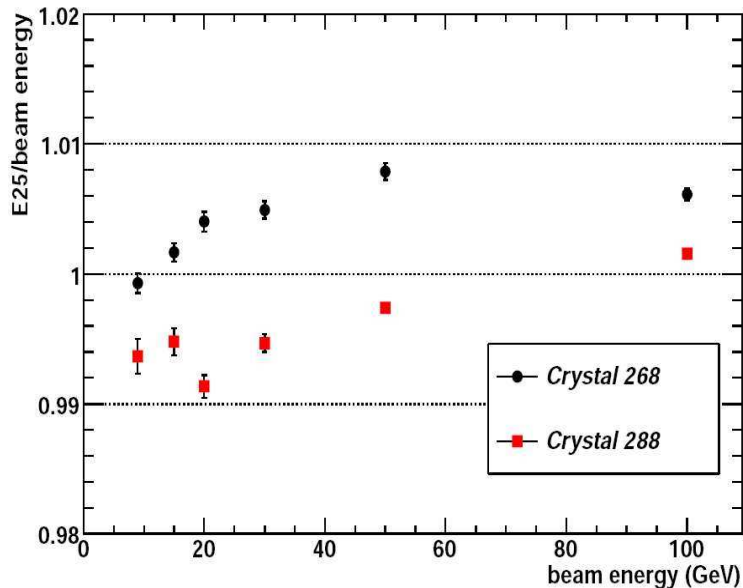


Figure 4.4: Distribution of the E_{25} peaks normalized to the beam energy, for two different crystals (labelled as 268 and 288) and for several positron beam energies [42].

the electron impact point was limited to a $4 \times 4 \text{ mm}^2$ region around the point of maximum containment (central impact).

Figure 4.5 shows the resolution as a function of energy, as reconstructed by summing the energy deposits in 3×3 crystals. The energy resolution was found to be

$$\left(\frac{\sigma}{E}\right)^2 = \left(\frac{2.8\%}{\sqrt{E}}\right)^2 + \left(\frac{0.12}{E}\right)^2 + (0.30\%)^2, \quad (4.2)$$

where E is given in GeV. The energy resolution was also measured with no restriction on the lateral extension of the electromagnetic showers produced by the incident electrons, except that provided by the use of a $20 \times 20 \text{ mm}^2$ trigger for the selection of a given crystal. For the energy reconstruction in either 3×3 or 5×5 crystal arrays, an energy resolution better than 0.45% was found for 120 GeV electrons, after correction for the containment.

Figure 4.6 shows the energy distributions before and after correction for the case of reconstruction in a 5×5 matrix.

The resolution of the ECAL supermodule has been restudied in 2006 H2 test beam of electrons. Electron data below 10 GeV has been collected, to check if the energy resolution in 2 and 9 GeV region is similar for different crystals [42].

The peak width of the E_{25} distributions, normalized to the peak value, is shown in Figure 4.7 as a function of the beam energy for 16 different crystals; the agreement is very satisfactory.

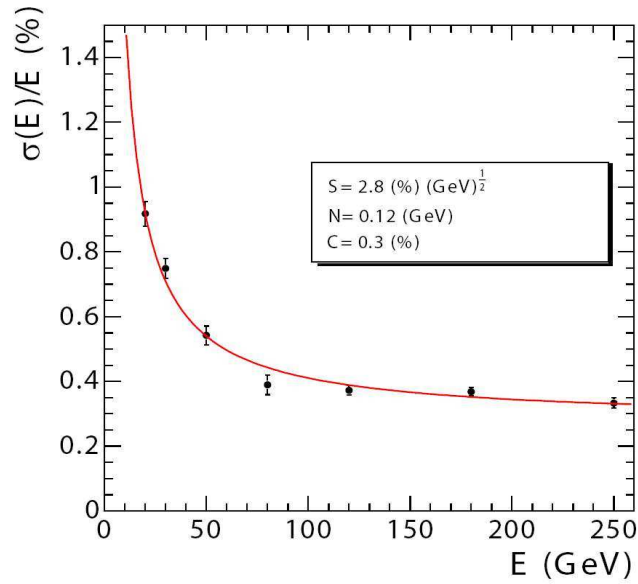


Figure 4.5: ECAL energy resolution, $\sigma(E)/E$, as a function of the electron energy, as measured in test beams. The energy was measured in arrays of 3×3 crystals, with the electron impacting the central crystal. The points correspond to events taken when restricting the incident beam position to a narrow $4 \times 4 \text{ mm}^2$ region. The stochastic (S), noise (N) and constant (C) terms are given in the plot [43].

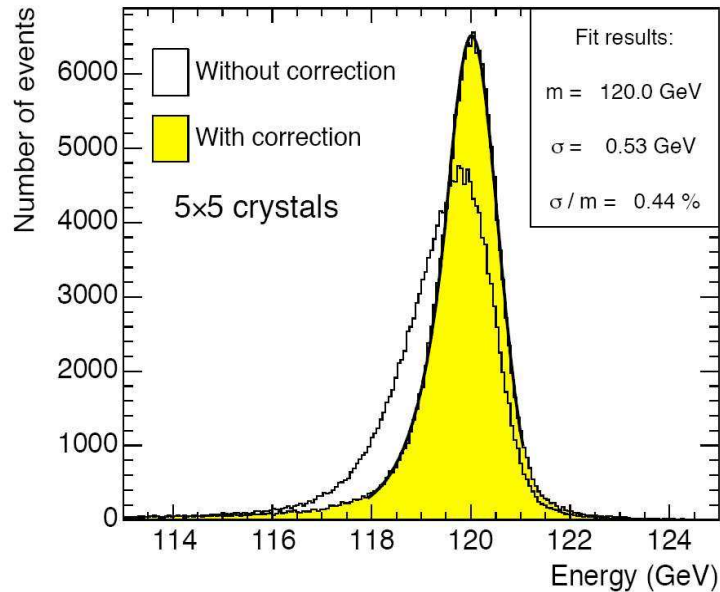


Figure 4.6: Distribution of the energy reconstructed in a 5×5 matrix, before and after correction for the containment, when 120 GeV electrons are incident over a $20 \times 20 \text{ mm}^2$ area [43].

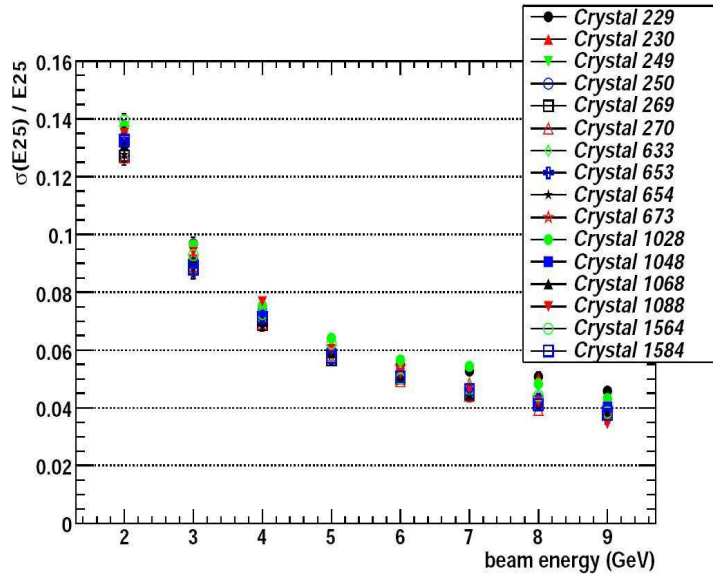


Figure 4.7: Energy resolution with electron beam [42].

4.4 Electromagnetic shower shape

4.4.1 Electromagnetic interactions

Typical electromagnetic interactions in high energy physics are:

- (1) Coulomb scattering (e.g. electron-nucleon scattering),
- (2) Bahbha scattering (electron-positron scattering),
- (3) Moller scattering (electron-electron scattering),
- (4) Compton scattering (photon-electron scattering),
- (5) Bremsstrahlung (photon emission in deacceleration or acceleration),
- (6) Annihilation (e.g. $e^-e^+ \rightarrow \gamma\gamma$),
- (7) Pair creation (e.g. $\gamma \rightarrow e^-e^+$),
- (8) Decay of π^0 mesons.

Bremsstrahlung and electron pair production are the dominant processes for high energy electrons and photons, respectively. The dominance of these electromagnetic processes and their small fluctuations distinguish electromagnetic showers from hadronic showers. Secondaries produced in electromagnetic processes are again mainly e^- , e^+ and γ . Most of the energy is consumed for particle production. A cascade develops in absorber material through repeated similar interactions. By continuing the process, and assuming equal energy sharing among the generated particles, particles will double themselves every radiation length. The number of particles at the depth t is $N(t) \simeq 2^t$, while their energy is $E_p(t) = E_0/2^t$, where E_0 is the energy of the incident particle. When the particle energy reaches the critical energy E_c , the multiplication no longer continues. From this point

the shower decays slowly through ionization losses for electrons (i.e also positron) and Compton scattering for photons. This change is characterized by the critical energy ϵ in the absorber material [44].

The electromagnetic shower shape, to good approximation, scales longitudinally with the radiation length X_0 , and laterally with the Moliere radius R_M , as will be explained in the next subsection.

4.4.2 Parametrisation of electromagnetic showers

The longitudinal electromagnetic shower development in homogeneous media has been calculated analytically by Rossi [44]. This calculation shows that longitudinal shower moments (mean, dispersion, ...) are similar in different materials. One can thus measure lengths in units of the radiation length (X_0) and energies in units of the critical energy (E_c).

Numerically, Moliere radius R_M of the medium and E_c can be calculated, respectively, using ref [45]

$$R_M = 0.0265 \times X_0(Z + 1.2), \quad (4.3)$$

where Z is the atomic number (number of protons in a nucleus) of the medium. Atomic number (Z) of an absorber material plays an important role in the longitudinal containment of electromagnetic showers. Since nuclei with higher numbers of protons create stronger electric field, they induce a higher rate of energy loss by Bremsstrahlung. For this reason electromagnetic absorber materials are chosen with a high atomic number (Z).

A critical energy E_c is defined as:

$$E_c = 21.2\text{MeV} \times \left(\frac{X_0}{R_M} \right). \quad (4.4)$$

The 95% radial containment (R_e) for electromagnetic cascades is given by [46]

$$R_e = 2 \times R_M, \quad (4.5)$$

which is equivalent to 0.035 rad for CMS electromagnetic calorimeter (ECAL), i.e 2 crystals for CMS ECAL barrel and about 1.5 crystals for CMS ECAL endcap.

We now present different variables that parametrise the electromagnetic shower, as given by [44].

The depth of the shower maximum (T): when the average energy per particle becomes low enough to stop further multiplication, the depth of the shower maximum (T) is reached, i.e the depth with the largest number of particles. The value of T is given by,

$$T = \ln \left(\frac{E}{E_c} \right) + t_0, \quad (4.6)$$

where T is measured in radiation length, E is the energy of the electromagnetic shower, and $t_0 = -0.858 (+0.858)$ for electrons (photons). This formula shows the logarithmic dependence of the shower length on the particle energy, and therefore of the detector thickness needed to absorb a shower.

The average longitudinal shower profile, which can be described by the gamma distribution $\Gamma(\alpha)$,

$$\left\langle \frac{1}{E} \frac{dE(t)}{dt} \right\rangle = f(t) = \frac{(\beta t)^{\alpha-1} \beta \exp(-\beta t)}{\Gamma(\alpha)}, \quad (4.7)$$

where t is the longitudinal depth, which is counted in units of X_0 , the shape parameter of the shower (α) and a scaling parameter (β). These two parameters (α and β) are related to the nature of the incident particle (e^- , e^+ or γ).

The shape parameter of the shower (α) is given by,

$$\alpha = 0.21 + (0.492 + 2.38/Z) \ln \left(\frac{E}{E_c} \right). \quad (4.8)$$

A scaling parameter (β), is defined as,

$$\beta = \frac{\alpha - 1}{T}, \quad (4.9)$$

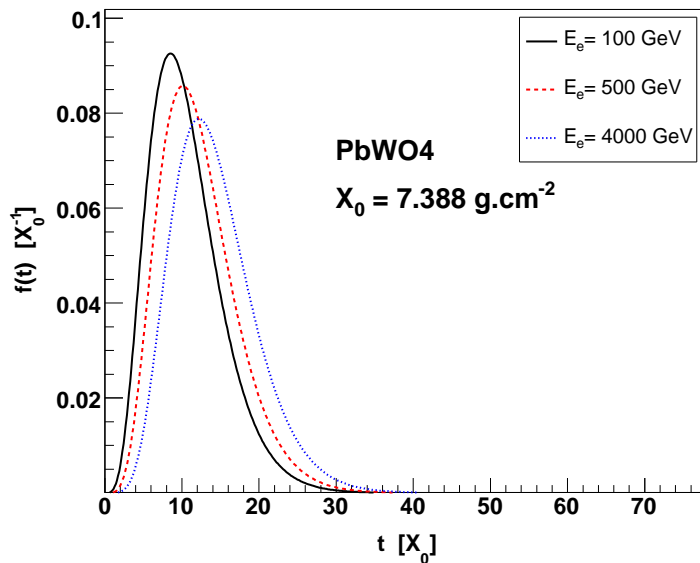


Figure 4.8: Longitudinal distribution of the energy deposit, $f(t) = 1/EdE/dt$, as a function of the shower depth, t , expressed in units of X_0 , for 100, 500 and 4000 GeV electrons, following the parametrisation of ref. [44].

Figure 4.8, using equation 4.7, shows the average longitudinal distribution of the energy deposit as a function of the shower depth, expressed in units of X_0 , for showers which are initiated by electrons of energies 100, 500 and 4000 GeV. The maximum of the energy deposit, for showers which are initiated by 500 GeV electrons, is $1.6X_0$ deeper than for 100 GeV showers, while at 4000 GeV it is $3.7X_0$. The fraction of the shower energy contained within given calorimeter depths, expressed in term of X_0 , is given in Table 4.1 for several incident electrons energies [47]. For example, for a crystal length of $26X_0$ for the ECAL barrel and $28X_0$ in the ECAL endcap ($25X_0$ for crystals + $3X_0$ for the preshowers), average shower containments of 97.7% and 99.1% are

expected for 1000 GeV electrons, according to the parametrisation of ref. [44] (see Table 4.1).

The effective ECAL depth is reduced for electrons entering into a crack and impacting on a crystal side face instead of the front face because of shower leakage in inter-module cracks these effects will be discussed in detail in chapter 6.

X_0	25	26	27	28	29	30
500	98.3	98.7	99.1	99.3	99.5	99.7
1000	97.7	98.3	98.7	99.1	99.3	99.5
2000	97.0	97.7	98.3	98.8	99.1	99.3
4000	96.1	97.0	97.8	98.3	98.8	99.1

Table 4.1: Average fraction of the shower energy contained within given calorimeter depths, expressed in terms of the number of radiation lengths X_0 , for several incident electron energies, following the parametrisation of ref. [44].

4.4.3 Material budgets in CMS

A good longitudinal containment of electromagnetic showers is provided by the ECAL, with crystal lengths corresponding to $25.8 X_0$ in EB and $24.7 + 3.0 X_0$ (preshower) in EE (see section 3.3) plus nearly $1X_0$ from the tracker material. Given the limited calorimeter depth, the longitudinal containment of high energy electron and photon showers depends critically on the initial particle energy, on shower length fluctuations and on the actual shower path in the ECAL.

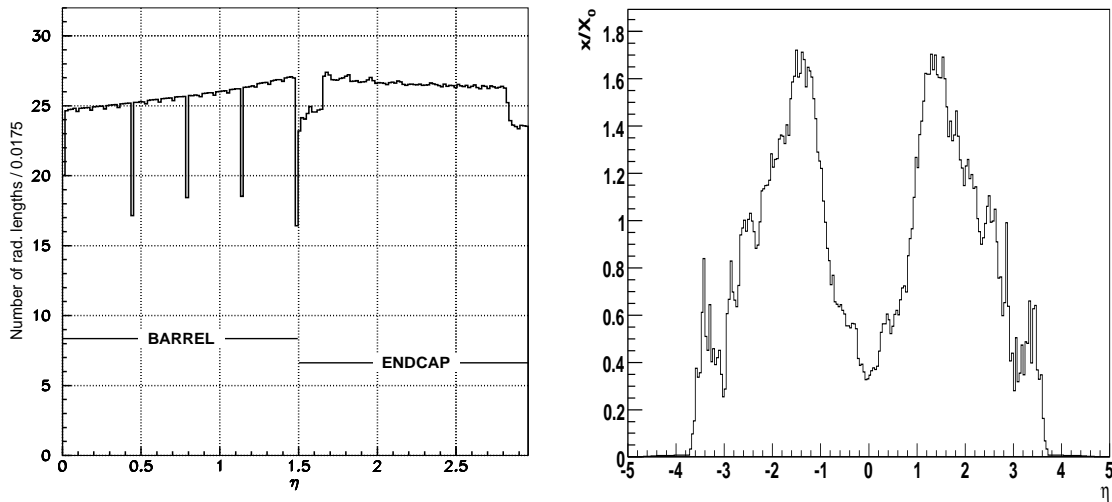


Figure 4.9: (left) Total thickness in X_0 of the ECAL as a function of η , averaged over ϕ [32]; (right) material budget in front of the ECAL as a function of $|\eta|$ [48].

Figure 4.9 (left) presents the total thickness (in radiation lengths) of the ECAL as a function of the pseudorapidity. In the barrel region $|\eta| < 1.479$ one can see an increase in the total thickness as η increases. This is due

to the increase of the crystal off-pointing in the η direction, which increases the ECAL effective depth. Drops in the number of radiation lengths are observed due to the cracks between the ECAL modules, filled with 6 mm air or low density support material. A large drop is also visible in the EB-EE transition region $1.479 < |\eta| < 1.56$. The endcaps also include the preshower detectors, which cover the pseudorapidity $1.653 < |\eta| < 2.6$, adding about 3 more X_0 to the endcap longitudinal depth.

The ECAL calorimeter is surrounding the tracker, and is inserted into the hadronic calorimeter HCAL. Figure 4.9 (right) shows the material budget in front of the ECAL crystals, due to beam pipe, tracker, cables and supports, which varies with η from a minimum of $0.35X_0$ at $\eta = 0$ to a maximum of $1.4X_0$ for $|\eta| = 1.6$, with $0.8X_0$ for $|\eta| = 2.5$.

For CMS experiment, the electromagnetic calorimeter ‘‘ECAL’’ consists of the PbWO_4 crystals. Moliere radius of the PbWO_4 crystal is $R_M = 2.2$ cm, and its radiation length is $X_0 = 0.89$ cm (see Table 3.1). For PbWO_4 crystals, the Atomic number is $Z = 92$, while the critical energy could be calculated using equation 4.4 ($E_c = 8.6$ MeV).

4.5 Hadronic shower shape

The hadronic shower process is dominated by a succession of inelastic hadronic interactions, secondaries being mostly pions and nucleons. Due to the relatively high generation of π^0 's [$\langle n_{\pi^0} \rangle = 1/2(\langle n_{\pi^+} \rangle + \langle n_{\pi^-} \rangle)$] for high energy showers, there is also an electromagnetic component in hadronic showers. The hadronic multiplication process is measured as the nuclear interaction length (λ), which is essentially energy independent.

Intrinsic limitations on the energy resolution of hadronic calorimeters are due to the following:

(i) The presence of a π^0 component among secondaries, fluctuating from event-to-event, which is of purely electromagnetic ($\pi^0 \rightarrow \gamma\gamma$), without any further nuclear interaction. The average fraction of π^0 's is given by $\pi^0/all \simeq 0.11 \times \ln(E)$ [E in GeV] [49], but at very high energies this formula becomes non-physical, and has to be replaced by the Groom parametrization equation $F_G(\pi^0) = 1 - (E/0.96)^{0.816-1}$ [49].

(ii) Most of the available energy is converted into excitation and breakup of nuclei, and only a fraction of the energy appears as a detectable signal, with large event-to-event fluctuations.

(iii) A considerable fraction of the the incident particle energy is spent on reactions which do not result in an observable signal. Such processes may be energy leakage of various forms, like leakage due to μ , ν or slow neutrons, nuclear excitation, nuclear breakup, nuclear evaporation.

The average ratio between signals from electromagnetic and hadronic particles of the same incident energy is calorimeter and energy dependent, for non compensating calorimeter. It is given by $e/h \simeq 1.1 - 1.35$, where e is the response of the calorimeter to the electromagnetic components of the hadron shower, and h is the response to the hadronic component of the hadron shower. Incident hadrons, on the other hand, may start their showering in the electromagnetic calorimeter, but will nearly always be absorbed fully only in later layers, i.e. in the hadronic calorimeter, which is built precisely for their containment. Hadronic showers have a

widely fluctuating shape; their average extension does not scale with the calorimeter's radiation length, but is determined by the interaction length λ .

At high energies some characteristic quantities of hadronic showers can be described by a simple parametrization in terms of the interaction length (λ) (see ref. [50])

shower maximum:

$$l_{max} = [0.6 \log(E) - 0.2]\lambda, \quad (4.10)$$

shower depth for 95% longitudinal containment:

$$l_{95\%} = l_{max} + 4E^a \lambda, \quad (a = 0.15) \quad (4.11)$$

shower radius for 95% radial containment:

$$R_{95\%} \simeq \lambda, \quad (4.12)$$

where the energy of the hadronic shower, E , is given in GeV. For the CMS HCAL, the interaction length is $\lambda = 16.42$ cm, and the shower radius for 95% radial containment of hadronic shower is about 0.14 rad, i.e 4 times broader than this of electromagnetic shower (this result could be obtained using equations 4.5 and 4.12), while hadronic shower is longer than electromagnetic shower as seen from Figure 4.10.

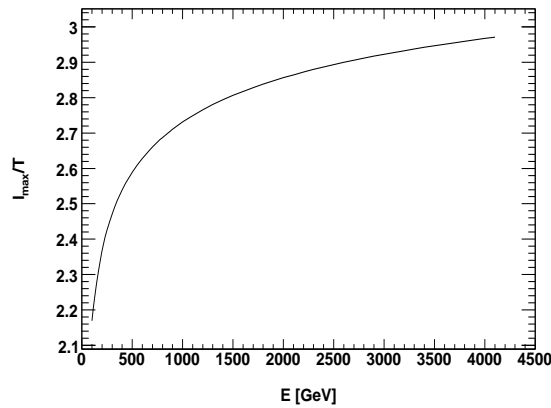


Figure 4.10: The ratio of the depth of the hadronic shower maximum (l_{max}) over the depth of the electromagnetic shower maximum (T) as a function of the energy of the incident particle.

Chapter 5

Identification of high energy electrons in CMS

In CMS, e^+e^- pairs due to the decay of heavy resonances or the high mass Drell-Yan process should be discriminated from the jet backgrounds. Identification criteria for electron measurement have been designed such that they are basically based on shower shape and isolation criteria. The procedure for identifying electrons and photons in CMS is described in refs [7, 8, 39, 51] for 14 TeV proton-proton center of mass energy, [9, 10] for 10 TeV proton-proton center of mass energy, and is summarized in this chapter.

5.1 Electron identification and HEEP electron selection

This section describes the algorithms and definition of GSF (Gaussian Sum Filter) electrons, the electron identification criteria, final event selection criteria, the efficiencies of these algorithms and the determination of these efficiencies from the data. The electron identification criteria described here are used everywhere in this thesis.

5.1.1 GSF Electrons

Electron candidates (known as “PixelMatchGsfElectron”) are defined by a supercluster (e.g. an electromagnetic shower in the ECAL, as defined in section 4.4) and a track which matches with the electromagnetic supercluster. This procedure is described here.

Starting from a supercluster with $E_T^{SC} > 1$ GeV which has been reconstructed in the ECAL calorimeter, we search for exciting track which matches with this supercluster. A track is built outward, thus a seed is created when two hits are found in the pixel detector. In the case of electron tracks, the search for seeds is restricted to regions compatible with a supercluster in the ECAL.

Starting from a seed, a trajectory is created. Compatible hits on the next silicon layers are first searched for, then extrapolation is performed. This procedure is iterated up to the last tracker layer, unless no hit is found in two successive layers. The compatibility among trajectories is defined in term of a χ^2 test, where χ^2 is obtained from the track fit. A track is fitted using a Gaussian Sum Filter (GSF).

If many hits are found on a compatible layer, many candidate trajectories are grown in parallel. Finally, only the best trajectory candidates, giving the smallest χ^2 , are kept. A minimum of 5 hits is required to create

a track.

Since track hits are collected up to the calorimeter, a good estimate of the track parameters at the ECAL entrance is possible. This gives the possibility of both improving the matching between tracker and calorimeter, and of estimating the amount of Bremsstrahlung radiated by the initial particle. Due to Bremsstrahlung emission, the matching between the track and the supercluster is often done using the track parameters at vertex. These track parameters are known with good precision at the initial vertex, and the initial track can be matched with the energy weighted average impact point as calculated from the supercluster. While the track parameters at the outermost layers are known with larger uncertainty than those at vertex, they can however be used for the matching. The knowledge of the track momentum, which is obtained from the weighted mean of the GSF at the outermost layers, gives the possibility of estimating the fraction of energy lost by Bremsstrahlung from the track fit.

The GSF pre-selection (which is loose selection) cuts are summarized in table 5.1, the definitions of these cuts are introduced in the next section.

cut quantity	cut value
H/E	< 0.1
$\Delta\eta_{in}$	< 0.02
$\Delta\phi_{in}$	< 0.1

Table 5.1: GSF pre-selection cuts [9].

5.1.2 Electron identification

Electron identification makes use of a complete set of estimators. These estimators are combined together to establish a fully compatible set of cuts, which are used as criteria for electron identification. The performance (i.e efficiency, rejection power and purity) of this identification set depends of the strength of these cuts. This identification criteria are imposed on the electron candidates, and on the background, an important background is QCD dijet (which was introduced in section 2.3.1.1). These jets appear in the detector as hadronic shower, with multi-cluster in the electromagnetic calorimeter.

To achieve a high efficiency and purity for electron candidates and high exclusion of background, the electron identification criteria have been designed and mainly divided into 4 types of categories:

- (1) **Kinematic conditions,**
- (2) **Track matching conditions,**
- (3) **Shower shape conditions,**
- (4) **Isolation conditions.**

(1) Kinematic conditions:

- η_{sc} : Defined as pseudorapidity of the supercluster based on its position in the calorimeter with respect to 0,0,0. This variable is primarily used to check if the electron is within a fiducial region of the detector and is not used for constructing invariant masses or other similar quantities.

- **E_T cut:** Defined as the transverse energy of the GSF electron candidates, it is computed as the GSF energy of the electron candidate times $\sin(\theta)$, where θ is the polar angle of the GSF electron candidate position in the ECAL calorimeter with respect to the vertex position.

At off-line analysis, strong cut on the transverse energy E_T is needed to identify two electron candidates, coming from the hard interaction, from the possible estimated background, and to eliminate the contribution of the underlying events produced from the soft interactions. These two electron candidates have to be chosen in the tracker acceptance ($|\eta| < 2.4$) to get benefit of the tracker properties.

- **Classification:** An electron is classified as either golden ($= 0$), big brem ($= 10$), narrow ($= 20$), showering ($= 3\chi$, where χ is the number of clusters in the supercluster) or in η cracks ($= 40$). For electrons in the endcap, 100 is added to the classification code. High energy electron ID does not make use of this classification scheme, except to distinguish between barrel and endcap electrons and, for barrel, to reject electrons in the 6 mm wide inter-modules cracks, with a cut of 0.036 in η .

(2) Track matching conditions

- **$\Delta\eta_{in}$ cut:** The difference in η between the track position as measured in the inner layer, extrapolated to the interaction vertex and then extrapolated to the calorimeter and the η of the supercluster.
- **$\Delta\phi_{in}$ cut:** The difference in ϕ between the track position as measured in the inner layer, extrapolated to the interaction vertex and then extrapolated to the calorimeter and the ϕ of the supercluster.

(3) Shower shape conditions:

- **$\sigma_{\eta\eta}$ cut:** Defined as

$$\sigma_{\eta\eta} = \frac{\sum_i^{5 \times 5} w_i (\eta_i - \bar{\eta}_{5 \times 5})^2}{\sum_i^{5 \times 5} w_i}, \quad (5.1)$$

where the index i runs over all the crystals in a 5×5 matrix of crystals centered on the seed crystal, η_i is the position of i^{th} crystal, $\bar{\eta}_{5 \times 5}$ is the energy weighted mean η of the 5×5 block of crystals and w_i is the weight of the i^{th} crystal and is defined as

$$w_i = 4.2 + \ln(E_i/E_{5 \times 5}), \quad (5.2)$$

where E_i and $E_{5 \times 5}$ are the energy of the i^{th} and 5×5 block of crystal respectively.

- **$E^{1 \times 5}/E^{5 \times 5}$ and $E^{2 \times 5}/E^{5 \times 5}$ variables:** They are defined as the fraction of the energy deposit in the 5×5 crystal matrix centred on the seed crystal, which is deposited in the ϕ strip of 5 crystals centred on the seed, or on the two highest energy ϕ strips, respectively. These two variables are used in the barrel.
- **$\sigma_{i\eta i\eta}$ cut:** This cut is used only in the endcaps, measures the spread in η of the energy deposit in the 5×5 crystal matrix centred on the seed crystal, it is measured in unit of the crystal size. Comparing to $\sigma_{\eta\eta}$ variable, the cut based on $\sigma_{i\eta i\eta}$ improves the performance around the cracks and does away with need for rescaling with η in the endcaps.

(4) Isolation conditions:

- **$H/E = E_{HCAL}/E_{ECAL}$:** It is the ratio of the energy deposits (E_{HCAL} and E_{ECAL}) in the HCAL and ECAL calorimeters, respectively, E_{HCAL} being computed from the energy deposits in the HCAL within a cone

of radius $R = \sqrt{\Delta\eta^2 + \Delta\phi^2} < 0.1$ around the ECAL supercluster direction. The ratio of hadronic to electromagnetic energy of an electron is a very good criteria to discriminate electron and jet, since at low energies, electrons will be fully contained in the electromagnetic calorimeter (ECAL) and deposit very little energy in the hadronic calorimeter (HCAL), while at high energies electrons will deposit most of the energy in the ECAL and deposit some energy in the HCAL. On the other side the jet will leak more energy in the HCAL due to longer maximum depth of hadronic showers (see section 4.5).

- **ECAL isolation (EM Isol.):** The ECAL isolation variable $E_t(\text{ECAL iso})$ is the sum of the transverse energies, which are deposited in the ECAL of all rec-hits (rec-hits are the energy and time for each hit per crystal), with energy noise cut, contained in a cone of radius ($R = 0.3$) around the barycentre of the supercluster in the calorimeter, excluding towers inside an inner cone of radius ($R = 0.045$ in the barrel) and ($R = 0.070$ in the endcap) or within an η strip of ± 0.02 .

- **HCAL isolation (Had. Isol.):** It is the sum of the transverse hadronic energies of all the HCAL towers (with energy noise cut) in a cone of 0.3 radius centred on the electron supercluster position, excluding rec-hits in a cone of 0.15 radius. HCAL 1 (**Had. depth 1 Isol.**) refers to the HCAL barrel or the first longitudinal segmentation of the endcap, while HCAL 2 (**Had. depth 2 Isol.**) refers to the second segmentation of the endcaps as explained in section 3.5.5.

- **Track isolation (Tracker Isol.):** Three variables are used, they are defined as the following,

(a) Number of isolated tracks N_{tr} : the number of tracks with $p_T > 1.5$ GeV/c in a cone of 0.2 radius in ΔR , in (η, ϕ) plane, centered on the electron's track position at the primary vertex excluding tracks within an inner cone of 0.02 in ΔR to avoid including tracks of electrons from hard interaction. The use of track measurements at primary vertex for electron isolation avoids the complication due to severe external bremsstrahlung, photon conversion, and early showering in the tracker material. Tracks are required to have a dz to be within 0.1 of the electrons track. The variable dz is defined as vertex position of the track as measured in the inner layer with respect to 0, 0, 0.

$$\Delta R_{cone} = \sqrt{(\Delta\eta_{in})^2 - (\Delta\phi_{in})^2}, \quad (5.3)$$

where $\Delta\eta_{in}$ is the difference in η between the track as measured in the inner layer, extrapolated to the interaction vertex and then extrapolated to the calorimeter and the η_{SC} of the supercluster (i.e $\Delta\eta_{in} = \eta_{SC} - \eta_{track}$). $\Delta\phi_{in}$ is the difference in ϕ between the track as measured in the inner layer, extrapolated to the interaction vertex and then extrapolated to the calorimeter and the ϕ_{SC} of the supercluster (i.e $\Delta\phi_{in} = \phi_{SC} - \phi_{track}$).

(b) Trk Pt : is the sum of the transverse momenta of the isolated tracks reconstructed with $p_T > 1.5$ GeV/c.

(c) Track R_{p_T} : additional useful cut is the ration, R_{p_T} , of summing the transverse momenta of the isolated tracks reconstructed with $p_T > 1.5$ GeV/c to the transverse momentum of the electron candidate E_T .

$$R_{p_T} = |\Sigma \vec{p}_T| / E_T. \quad (5.4)$$

The variables N_{tr} and R_{p_T} are used in section 5.3 (see Table 5.9).

The criteria applied on reconstructed electron candidates are designed to ensure high efficiencies for high energy electrons, whilst efficiently rejecting the QCD background. They are required to be insensitive to the quality of the detector calibration. High Energy electrons are selected within the tracker acceptance ($|\eta| < 2.5$), using the criteria summarised in Table 5.2. The values of the cuts on the shower shape, track matching and isolation variables are chosen to be different for electrons emitted in the barrel ($|\eta| < 1.442$) and in the endcap ($1.560 < |\eta| < 2.5$) regions, because of the different detector geometries and activities in the isolation cones. This criteria of selecting an electron in addition to the procedure of “PixelMatchGsfElectron” is known as HEEP electron selection.

Variable	Barrel	Endcap
E_t	$> 30 \text{ GeV}$	$> 30 \text{ GeV}$
η_{SC}	$ \eta_{SC} < 1.442$	$1.560 < \eta_{SC} < 2.5$
classification	< 40	≥ 100
$\Delta\eta_{in}$	$ \Delta\eta_{in} < 0.005$	$ \Delta\eta_{in} < 0.007$
$\Delta\phi_{in}$	$ \Delta\phi_{in} < 0.09$	$ \Delta\phi_{in} < 0.09$
$\sigma_{\eta\eta}$	< 0.011	< 0.0275
H/E	< 0.05	< 0.1
EM + Had. depth 1 Isol.	$< 5 \text{ GeV}$ for $E_t < 65 \text{ GeV}$ else $< 5 \text{ GeV} + 0.02 * (E_t - 65)$	$< 4 \text{ GeV}$ for $E_t < 65 \text{ GeV}$ else $< 4 \text{ GeV} + 0.04 * (E_t - 65)$
Had. depth 2 Isol.	n/a	$< 1 \text{ GeV} + 0.005 * E_t[\text{GeV}]$
Tracker Isol.: Trk Pt	$< 7.5 \text{ GeV}$	$< 15 \text{ GeV}/c$

Table 5.2: HEEP electron selection v1.2 [7].

The recent version of HEEP selection criteria, which will be used for the startup of the LHC with 10 TeV proton-proton centre of mass energy, is summarised in table 5.3.

Variable	Barrel	Endcap
E_t	$> 25 \text{ GeV}$	$> 25 \text{ GeV}$
η_{SC}	$ \eta_{SC} < 1.442$	$1.560 < \eta_{SC} < 2.5$
classification	< 100	≥ 100
H/E	< 0.05	< 0.05
$ \Delta\eta_{in} $	< 0.005	< 0.007
$ \Delta\phi_{in} $	< 0.09	< 0.09
$E^{2 \times 5} / E^{5 \times 5}$	> 0.94 or $E^{1 \times 5} / E^{5 \times 5} > 0.83$	n/a
$\sigma_{in\eta}$	n/a	< 0.0275
EM + Had. depth 1 Isol.	$< 3 + 0.02 * E_T \text{ GeV}$	$< 5.5 \text{ GeV}$ if $E_T < 50 \text{ GeV}$ $< 5.5 + 0.05 * (E_T - 50) \text{ GeV}$
Had. depth 2 Isol.	n/a	$< 0.5 \text{ GeV}$
Tracker Isol.: Trk Pt	$< 7.5 \text{ GeV}$	$< 15 \text{ GeV}/c$

Table 5.3: HEEP electron selection v2.0 [9].

5.2 Event selection and efficiency

This section describes the triggers used for the event selection, and the event selection criteria, introducing the procedure for the extraction of the electron identification efficiency from the data.

5.2.1 Triggers

The Level 1 trigger (see section 3.4.2) for electrons requires a minimum energy deposit in the electromagnetic ECAL calorimeter, with additional isolation criteria for em objects with $E_t < 64$ GeV. The L1 trigger efficiency for high E_t electrons is found to be close to 100%, using the L1 emulator.

For 14 TeV proton-proton centre of mass energy, the high level trigger (HLT) (see section 3.4.3), three trigger paths have been designed. The Relaxed Single Electron trigger requires an energy deposit where $E_t > 18$ GeV in the ECAL calorimeter, direction and energy matching between the ECAL deposit and a track in the tracking detector, and imposes isolation requirements in the ECAL, the HCAL hadronic calorimeter and the tracker. The High E_t trigger requires an ECAL deposit where $E_t > 80$ GeV and loose isolation requirements in the HCAL and the tracker; no track matching the ECAL energy deposit is required, which makes this trigger very robust against detector alignment and calibration problems. The Very High E_t trigger only requires an ECAL energy deposit where $E_t > 200$ GeV. No other conditions are imposed. More stringent selection criteria are imposed for the trigger with a lower E_t threshold in order to reject the potentially large background from QCD events where a jet fakes an electron. The event rates for the three triggers are estimated to be 9.1, 0.8 and 0.14 Hz, respectively, for a luminosity of $10^{32} \text{ cm}^{-2}\text{s}^{-1}$.

cut quantity	cut value
number of L1 matched superclusters	>0
E_t	> 18 GeV
Pixel Match	> 0
$ 1/E - 1/p $	< 0.03
R_{p_T}	< 0.06

Table 5.4: Relaxed Single Electron trigger [7].

cut quantity	cut value
number of L1 matched superclusters	>0
E_t	> 80 GeV
EM Isol.	< 5 GeV
H/E	< 5%
Had. Isol.	< 8 GeV
N_{tr}	< 4

Table 5.5: High E_t trigger [7].

cut quantity	cut value
number of L1 matched superclusters	>0
E_t	>200 GeV

Table 5.6: Very High E_t trigger [7].

The global efficiency of the L1 trigger and of the combined HLT triggers for events containing a pair of electrons emitted within the tracker acceptance ($|\eta| < 2.5$) is found to be 94% for Drell-Yan production with mass $M > 200 \text{ GeV}/c^2$, 98% for DY with $M > 500 \text{ GeV}/c^2$, and 99% for SSM Z' bosons with $M = 1$ or $M = 4 \text{ TeV}/c^2$ [7].

At the startup of the LHC, for 5 TeV proton beams (i.e. 10 TeV proton-proton centre of mass energy), two triggers have been designed by HEEP group, corresponding to instantaneous luminosities of $8 \times 10^{29} \text{ cm}^{-2}\text{s}^{-1}$, and $10^{31} \text{ cm}^{-2}\text{s}^{-1}$ as expected after a few months of data taking. Both triggers are considered as single particle trigger with an E_t above such threshold based on the instantaneous luminosity, the following triggers are used:

- At low instantaneous luminosity, the electron trigger HLT-Ele10-LW-L1R, which requires in the ECAL a cluster with transverse energy $E_t^{clus} > 10 \text{ GeV}$, that linked to a pair of pixel hits compatible with the cluster E_t (more detail about cluster-pixel match was introduced in chapter 5.1.1), if trigger rate is too high, the backup trigger with $E_t^{clus} > 15 \text{ GeV}$ electron is used. Also photon trigger HLT-Photon15-L1 can be used a backup to the electron trigger, the photon trigger characterised by requiring a single cluster with $E_t^{clus} > 15 \text{ GeV}$, without any other further conditions.
- At high instantaneous luminosity, the electron trigger HLT-Ele20-SW-L1R will be used as the main trigger, which is similar to the main trigger at low instantaneous luminosity but with a threshold of 20 GeV instead of 25 GeV but (loose) tracker isolation conditions, and photon trigger with either a higher E_T threshold or additional isolation condition.

5.2.2 Event selection and efficiencies from MC

The final HEEP event selection requires the identification of two electrons with $E_T > 25 \text{ GeV}$, emitted outside the ECAL barrel-endcap gaps region ($1.442 < |\eta| < 1.560$) and within the tracker acceptance ($|\eta| < 2.5$), and passing the full set of HEEP criteria given in table.5.3.

The efficiencies for individual cuts and the (N-1) efficiencies for the different selection criteria, which are introduced in Table 5.3, are estimated using Drell-Yan Monte Carlo simulation samples at high masses, namely; $M > 40$, $M > 120$, $M > 200$ and $M > 500 \text{ GeV}/c^2$, and heavy $SSMZ'$ resonance production at $M = 1 \text{ TeV}/c^2$. The lowest efficiency comes from the ECAL + HCAL isolation criterion. The total selection efficiency not including the GSF preselection cuts is about 0.93 in both the barrel and the endcaps regions of the ECAL.

The global efficiencies of high energy electron reconstruction and identification are presented in fig. 5.1 as a function of the electron transverse energy E_T , separately for the ECAL barrel and endcaps. In the transverse

energy range ($150 < E_T < 700$ GeV) corresponding to the high mass region of Drell-Yan mass distribution, the global efficiencies are of (89.4 ± 0.1) % in barrel and (88.1 ± 0.1) % in the endcaps.

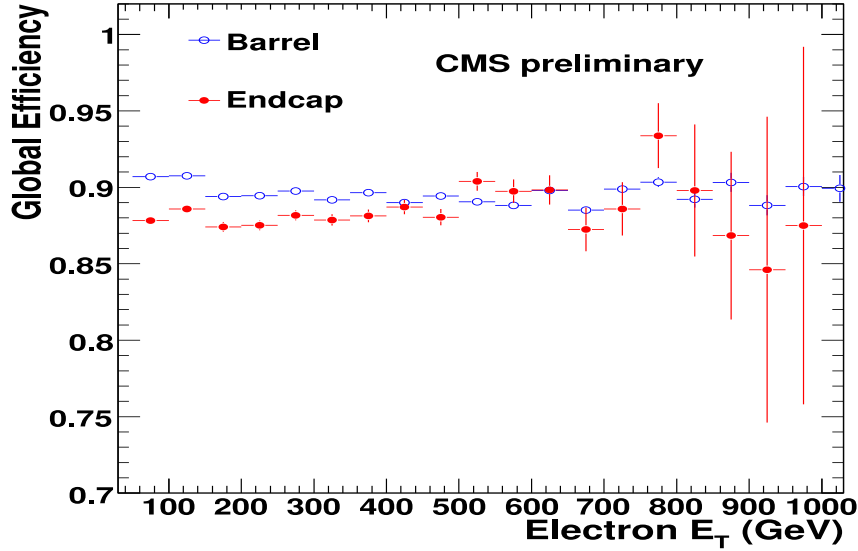


Figure 5.1: Global high energy electron reconstruction and identification efficiencies, for the ECAL barrel ($|\eta| < 1.442$) (open points) and endcaps ($1.560 < |\eta| < 2.5$) (full points) electrons as a function of the electron E_T ; corresponding to HEEP selection criteria given by table.5.3 [9].

Table 5.7 summarise the information on the global acceptance, reconstruction and selection efficiency, and presents the number of produced events for an integrated luminosity of 100 pb^{-1} . Also the number of events emitted within the tracker acceptance and toward the ECAL barrel and ECAL endcaps, and the final number of accepted events are quoted.

masses in GeV/c^2	$M > 40$	$M > 120$	$M > 200$	$M > 500$	$Z' (M = 1000)$
Global acceptance, reconstruction and selection efficiency	0.27	0.40	0.49	0.61	0.67
nb. of ev. for 100 pb^{-1}	123×10^3	1220	157	5.5	23.6
nb. of gen. ev. with 2 el. with $E_t > 25$ GeV and $ \eta < 1.442$ or $1.560 < \eta < 2.5$	42,650	598	92	4.1	19.1
nb. of rec. ev. with HEEP selection	33,700	487	76	3.4	15.7

Table 5.7: Global acceptance, reconstruction and selection efficiency, and number of generated events, of events with electrons generated in the acceptance, and of events with electrons reconstructed in the acceptance and selected with the HEEP criteria, for an integrated luminosity of 100 pb^{-1} for Drell-Yan events with $M_{ee} > 40, 120, 200$ and $500 \text{ GeV}/c^2$ and for SSM Z' resonance production with mass of $1 \text{ TeV}/c^2$ [9].

5.2.3 Efficiency measurements from the data

At the startup of the data taking, it is very important to minimize as much as possible the use of the Monte Carlo to estimate the electron selection efficiencies, since these efficiencies have to be measured mainly and directly from the data itself. For measuring these efficiencies from data, tag-and-probe method is used, such that the events containing two electron candidates are selected, with tight selection criteria (full HEEP selection) applied in one of the two electrons, this electron is known as the “tag” electron, while the second electron is chosen according to loose set of cuts and this electron is known as “probe” electron. Then the efficiency ϵ for an electron to pass a given set of cuts is given by the fraction of the probes which pass these cuts. The main idea of tag-and-probe method is to examine the efficiency of each cut of the HEEP selection criteria directly from the data. The electron reconstruction and identification efficiencies are factorized as the product of the two contributions, implying the two main parts of the selection: $\epsilon = \epsilon_{\text{cand}} \times \epsilon_{\text{id}}$, where ϵ_{cand} is the efficiency for an electron to be reconstructed as a GSF electron candidate, and ϵ_{id} is the efficiency for a GSF electron candidate to pass HEEP selection criteria.

Efficiency measurements will be done in two regions of the Drell-Yan mass spectrum, the first region is at the Z peak which is characterized by a large abundance of data of electrons with low E_T and with little background, the second region is at the highest possible mass range, closer to the conditions relevant to the discovery region of new heavy resonances production, but this region is affected by smaller statistics. The data used in this subsection, for the efficiency measurements using tag-and-probe method, is pseudo-experiment Monte Carlo sample containing simulated events from the Drell-Yan process and from all significant background processes ($t\bar{t}$, tW , WW , $Z \rightarrow \tau\tau$, which contribute to various dielectron background, and QCD multi-jet, W +jet, γ +jet, $\gamma\gamma$).

5.2.3.1 Efficiency measurement at the Z pole

The efficiency ϵ_{id} at the Z peak for an electron candidate to be selected following the HEEP criteria (tag electron) is given by the number of tag-and-probe pairs (see Table 5.8), where the probe passes the HEEP selection (N_{TT}) over the number of tag-and-probe pairs (N_{TP}). The Table also gives the corresponding rejection power on jet events containing a (genuine or fake) electron candidate (W +jet and multi-jet events). In view of the small background under the Z peak, the tight selection of the tag electrons ensures that the probes form an essentially unbiased, high purity electron sample.

The reliability of the Monte Carlo simulation and thus of the evolution procedure is estimated quantitatively by comparing the efficiencies obtained by the tag-and-probe method when applied to the data and to Monte Carlo samples, respectively. The ratio of these two efficiencies is defined as the “efficiency scale factor”. The statistical error on the scale factor is given by the statistical error on the efficiency measurement using the tag-and-probe method applied to the data, as summarised in Table 5.8 for an integrated luminosity of 100 pb^{-1} .

	Barrel		Endcap	
	$Z \rightarrow ee$	jet bg.	$Z \rightarrow ee$	jet bg.
N_{TP}	37263	1250	10880	820
N_{TT}	34988	2.3 ± 1.2	10259	13.3 ± 6.7
efficiencies	$93.9 \pm 0.1\%$	–	$94.3 \pm 0.2\%$	–
rejection power	–	$99.8 \pm 0.1\%$	–	$98.4 \pm 0.4\%$

Table 5.8: Number of tag-and-probe pairs, N_{TP} , where the tag passes the full HEEP selection and the probe is selected as a GSF electron candidate, and of pairs where the probe passes the HEEP selection, N_{TT} , for Drell-Yan events, and jet events (W +jet and multi-jet) and for an integrated luminosity of 100 pb^{-1} ; corresponding efficiencies of the HEEP selection criteria applied to GSF electron candidates, for Drell-Yan events, and corresponding rejection powers for background jet events [9].

5.2.3.2 Efficiency measurement at high mass

Efficiencies are also estimated using events in the Drell-Yan tail with $M > 120 \text{ GeV}/c^2$. To reduce the background contaminations from W +jet and QCD multijet events in the tag-and-probe samples, stronger selection conditions are imposed: both electron candidates are required to have $E_t > 50 \text{ GeV}$, they must be produced roughly back to back in the transverse plane ($|\Delta\phi| > 2.6$) and the ratio of their transverse momenta must be larger than 0.75 and smaller than 1.33. In addition, a stronger cut is imposed on the energy deposit in the HCAL calorimeter by the tag electron. For 100 pb^{-1} , approximately 400 probe electrons are available.

The ε_{id} efficiency for the HEEP selection criteria is measured to be 0.95 ± 0.01 (stat.) The background, dominated by the W +jet channel, is measured from the events where the two electron candidates have the same charge; the small charge mis-measurement in the Drell-Yan signal ($\sim 5\%$) and the charge correlation between the quark and the lepton in W +jet events are taken into account [9].

5.3 Loose selection criteria

For electron identification, the previous electron identification (HEEP identification) conditions, which are summarized in Tables 5.2 and 5.3, differ slightly for the study used in the next chapter, in particular higher E_t cut. And the wording ‘‘HEEP conditions’’ thus refers, in the next chapter, to criteria given in Table 5.9 (see the definition of these variables in section 5.1.2).

5.4 Background estimate and rejection

The aim of the analysis in this section is to estimate the contribution of different backgrounds from the data themselves. All background samples discussed in this section (see section 2.3) have been generated for proton-proton centre of mass energy of 10 TeV. The principle backgrounds in the high mass Drell-Yan region in electron channel are:

- (1) processes with two real electrons: These processes are $t\bar{t}$ production, tW production, boson pair production

Variable	Barrel	Endcap
E_t	$> 80 \text{ GeV}$	$> 80 \text{ GeV}$
η_{SC}	$ \eta_{SC} < 1.453$	$1.563 < \eta_{SC} < 2.4$
H/E	< 0.05	< 0.05
EM Isol.	$< 6 \text{ GeV} + 0.01 * E_t$	$< 6 \text{ GeV} + 0.01 * E_t$
Had. Isol.	$< 4 \text{ GeV} + 0.005 * E_t$	$< 4 \text{ GeV} + 0.005 * E_t$
Track Isol.: N_{tr}	< 4	< 4
Track Isol.: R_{pt}	< 0.2	< 0.2

Table 5.9: Loose HEEP electron selection v1.1 in addition to a track reconstructed as a ‘‘PixelMatchGsfElectron’’ [52].

WW and finally $Z \rightarrow \tau\tau \rightarrow ee$ decay. For an integrated luminosity of 100 pb^{-1} , these processes are expected to contribute in total 284 dielectron background events selected with the HEEP criteria for $M_{ee} > 40 \text{ GeV}/c^2$ and each electron having $E_T > 25 \text{ GeV}$ (191, 15.5, 26.0 and 51.9 events, respectively), while they contribute to 55 events with $M_{ee} > 120 \text{ GeV}/c^2$ and each electron with $E_T > 50 \text{ GeV}$ (44.3, 3.6, 7.2 and 0.1 events, respectively). On the other hand the expected number of Drell-Yan events is 45495 for $M_{ee} > 40 \text{ GeV}/c^2$ with $E_T > 25 \text{ GeV}$, and 443 for $M_{ee} > 120 \text{ GeV}/c^2$, with $E_T > 50 \text{ GeV}$. To estimate the number of these backgrounds to the selected e^+e^- samples two methods are used, which are b-tag and $e\mu$ methods.

(2) processes with at least one jet misidentified as an electron: These processes are QCD multi-jet, W+jet and γ +jet production, which contribute in total to 222 jet background events for an integrated luminosity of 100 pb^{-1} , for $M > 40 \text{ GeV}/c^2$ with each electron having $E_T > 25 \text{ GeV}$, and 4.5 events for $M > 40 \text{ GeV}/c^2$ and each electron having $E_T > 50 \text{ GeV}$. Jet background are estimated using fake rate method.

5.4.1 b-tag method

This method has been used to estimate the $t\bar{t}$ events. In this method the number of events with only one b-tag is measured (n_1), or two observed b-tags (n_2), of a jet originating from a b quark. The jet is reconstructed and tagged by criteria given in Table 5.10. Then the efficiency ε_b , which is the ratio of the number of events with

Parameter	Value
Jet Algorithm	iterativeCone5CaloJets
Jet E_T	$> 20 \text{ GeV}$
Jet $ \eta $	< 2.4
B Tagger	jetBProbabilityBJetTags
B Discriminant	> 4.0

Table 5.10: Criteria used to identify jets originating from b quarks.

two b -tags divided by number of events with one b -tag, is measured. Given the measured value of ε_b the true number of $t\bar{t}$ events can be found from the measured numbers of n_1 and n_2 .

Using the events in the high energy selected sample with $M > 40 \text{ GeV}/c^2$, the ε_b efficiency is thus

estimated to be 0.322 ± 0.012 (the error is from Monte Carlo statistics), which is in excellent agreement with b -tagging efficiency obtained from the Monte Carlo simulation. The events satisfying $70 < M < 110 \text{ GeV}/c^2$ have been excluded to suppress the contamination from $Z + b\bar{b}$ events, which contain real b jets but in different acceptances.

The background distribution obtained from the b -tag method is shown in figure. 5.2, and compared to the genuine distribution of the top background (shaded histogram), the Monte Carlo statistics have been scaled to correspond to an integrated luminosity of 100 pb^{-1} .

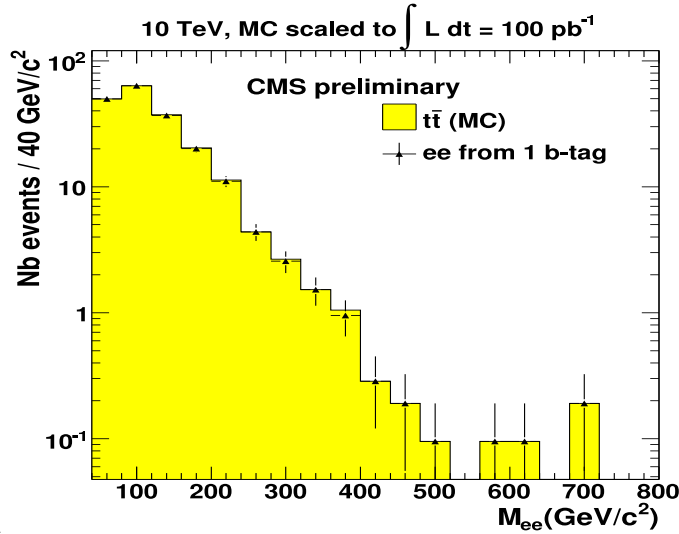


Figure 5.2: Estimation of the $t\bar{t}$ background to the Drell-Yan spectrum, computed from the pseudo-data using the b -tag method for electron $E_t > 30 \text{ GeV}$ and $40 < M < 800 \text{ GeV}/c^2$. The triangles are the background estimates obtained from the pseudo-data, the shaded histogram is the genuine distribution of the top background. The Monte Carlo statistics have been scaled to correspond to an integrated luminosity of 100 pb^{-1} [10].

5.4.2 $e\mu$ method

This method has been used to estimate the contributions from processes with two real electrons in the final state (i.e. $xy \rightarrow ee$), such processes are $t\bar{t}$, tW , WW , $Z \rightarrow \tau\tau \rightarrow ee$. The estimated number of events could be achieved directly from data using di-lepton events with different lepton flavours, i.e. one electron and one muon ($e\mu$ events), coming from the two W boson decays. The event kinematics are identical to those of dielectron decays so that, when correcting for the differences in acceptance and selection efficiencies between muons and electrons, the number of selected $xy \rightarrow e\mu$ events should be twice that of $xy \rightarrow ee$ events.

A contamination from W +jet events has to be taken into account, where either the muon originates from

the W and the electron is a fake, or the electron originates from the W and the muon is a fake, such that:

$$N_{ee}^{est} = \frac{N_{xy \rightarrow ee}}{N_{xy \rightarrow e\mu}} \cdot \left[\frac{1}{1 + \frac{N_{Wj \rightarrow e\mu}}{N_{xy \rightarrow e\mu}}} \right] \cdot N_{e\mu}^{obs} \quad (5.5)$$

$$= \frac{A}{2} \cdot N_{e\mu}^{obs} \cdot \frac{1}{1 + R}, \quad (5.6)$$

where A denotes the ratio of acceptance times selection efficiencies for the ee and $e\mu$ channels (i.e $A = 2 \times N_{xy \rightarrow ee} / N_{xy \rightarrow e\mu}$), that will be determined from the Monte Carlo simulations, and R represents the fractional contamination of the $e\mu$ sample from W +jet events, its contribution is estimated as well from Monte Carlo simulations to be 5%.

In figure 5.3, for an integrated luminosity of 100 pb^{-1} , the spectrum of ee events is computed from the $e\mu$ events, with one electron passing HEEP criteria and one muon passing TeVMu criteria, is compared to the sum of the true dielectron background contributions, determined from MC simulation (shaded histograms). Good agreement is observed between the number of ee events obtained from the MC and those computed from $e\mu$ method, which confirms the validity of the method.

For an integrated luminosity of 100 pb^{-1} , the number of events are summarised in table. 5.11 for different backgrounds, with one electron passing the HEEP criteria and one muon passing the TeVMu criteria, and both leptons having $E_t > 25 \text{ GeV}$ and invariant mass $M_{e\mu} > 40 \text{ GeV}/c^2$.

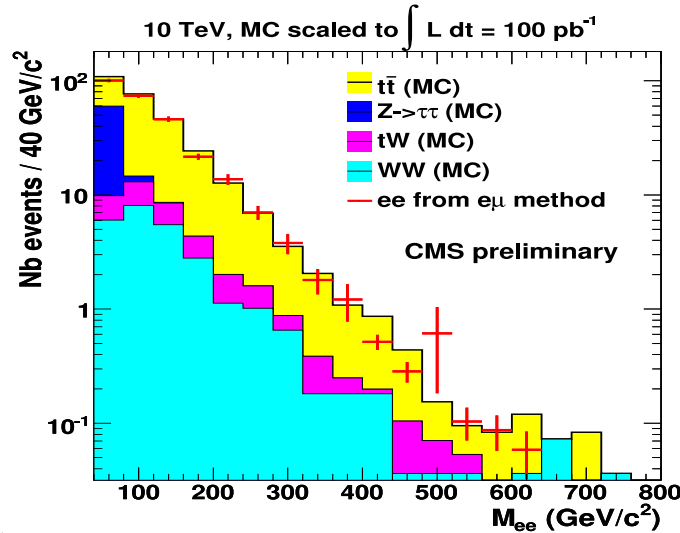


Figure 5.3: For events selection using HEEP criteria, with $40 < M < 800 \text{ GeV}/c^2$ and each electron with $E_T > 25 \text{ GeV}$, estimation of the sum of the dielectron backgrounds to the e^+e^- Drell-Yan spectrum, computed from the pseudo-data using $e\mu$ method. The points with error bars are the background estimates obtained from the pseudo-data, the histograms are the genuine distribution of the background. The Monte Carlo statistics have been scaled to correspond to an integrated luminosity of 100 pb^{-1} [10].

Process	nb. of $e\mu$ events
$t\bar{t}$	486.6
$Z \rightarrow \tau\tau$	113.1
WW	60.3
tW	36.0
total dielectron bg.	696.0 ± 26.4
W +jets	237.1
$Z \rightarrow \mu\mu$	30.6
total contamination	267.7 ± 16.3

Table 5.11: Numbers of events with one electron passing the HEEP criteria and one muon passing the muon selection and isolation criteria, with $M_{e\mu} > 40 \text{ GeV}/c^2$, both leptons having $E_t > 25 \text{ GeV}$ and the HEEP electron being detected outside a cone of radius $\Delta R = 0.1$ around the direction of any muon, for an integrated luminosity of 100 pb^{-1} .

5.4.3 Fake rate method

There are several physical processes for producing one jet or more in the final state which can take place at the LHC (as explained in section 2.3). Such jet background events are due to QCD multijets events, where two jets pass the high energy electron selection requirements (events with two fake electrons), W +jet events (events with a real electron from the W decay and a fake electron) and γ +jet events (events with a γ reconstructed as an electron and a jet faking an electron). From Monte Carlo simulations studies, the contributions of these backgrounds are expected to be small. Nevertheless, the production cross section of these processes have large uncertainties. The estimate of jet background is done in two steps:

- The first step is the use of “jet fake-rate” method to determine the probability for a jet to fake an electron, this probability is defined as the number of jets passing the electron selection criteria (HEEP criteria defined in Table 5.3) over the total number of jets, for measuring this probability the data with jet triggered events are used. The probability is computed in E_T bins, and it is estimated to be $0.04 \pm 0.01(0.3) \pm 0.0110^{-3}$ in the ECAL barrel (endcap) region for a jet with E_T around 200 GeV.
- The second step, a second jet sample is constructed where there is one object that passes the full HEEP electron selection cuts in Table 5.3 (which is a jet faking an electron), and additional jet in the event, and no other electron candidate in the event that passes the very loose cuts in Table 5.12 (in order to minimize the Drell-Yan contributions). The event is then weighted by the fake rate for the second jet, the energy of which is also corrected as described above. The invariant mass of the di-jet event where both jets faked an electron is calculated.

These two steps are then used to estimate the di-electron invariant mass distribution produced when backgrounds containing jets produce two objects that pass the electron selection criteria. The method is used in the following sections to estimate the jet contributions, as shown in figures 5.4, 5.5 and 5.7. As an example, the estimated number of jet background events with $M > 40 \text{ GeV}/c^2$ and both electrons have E_t above 25 GeV is measured to be 222; while for $M > 120 \text{ GeV}/c^2$ and E_t above 50 GeV, it is 4.4 events.

Variable	Barrel	Endcap
E_t	≥ 20 GeV	≥ 20 GeV
η_{sc}	$ \eta_{sc} \leq 1.442$	$1.560 \leq \eta_{sc} \leq 2.5$
H/E	< 0.2	< 0.2
$ \Delta\eta_{in} $	< 0.02	< 0.02
$ \Delta\phi_{in} $	< 0.1	< 0.1

Table 5.12: The very loose electron cuts used for constructing the jet faking electron sample [7].

5.5 Dielectron mass spectrum

To test and understand both the detector performance and particle reconstruction algorithms, the di-electron spectrum is reconstructed including low masses where only Standard Model (SM) contributions dominate and no new physics is expected. In this control region data driven estimates of the non-Drell-Yan backgrounds are made allowing the Drell-Yan distribution to be determined. Demonstrating that this agrees with the SM expectation constitutes the principal control test in this analysis. For this analysis two control regions are used, the first control region considers the reconstructed di-electron spectrum including the Z resonance peak, this region is characterised by high statistics of low energy electrons. The second control region covers the mass spectrum where $120 < M < 600$ GeV/ c^2 .

5.5.1 Z peak normalisation

In the low mass region near the Z peak ($60 < M_{ee} < 120$ GeV/ c^2), which is characterised by high statistics of low transverse energy electrons, a comparison between Monte Carlo (MC) simulation and data is possible, to examine if the Monte Carlo describes well the data or not. The data mentioned in this analysis is a sample of “pseudo-data” containing simulated events from the Drell-Yan process and from all significant background processes $t\bar{t}$, tW , WW , $Z \rightarrow \tau\tau$, which contribute to various dielectron background, and QCD multi-jet, W +jet, γ +jet, $\gamma\gamma$), in addition to 1 TeV/ c^2 Z' , for integrated luminosity 100 pb $^{-1}$. The sample is run through the event selection described in section 5.1.2 as if it were real data. It is then divided into low-mass and high-mass control regions, and the data driven techniques discussed in section 5.4 are used on the control regions to estimate the backgrounds contributions to the signal region. This is performed both with and without the addition of a 1 TeV/ c^2 Z' signal. The distribution of this 100 pb $^{-1}$ of “pseudo-data” is presented in figure 5.4, together with the data derived background estimates for number of $t\bar{t}$, tW , WW , $Z \rightarrow \tau\tau$ (using the $e\mu$ method), and QCD jets, W +jet, γ +jet (using the fake-rate method) and $\gamma\gamma$ ¹ production. The Drell-Yan estimate is obtained by taking the shape from MC, normalised to the Z peak in the low-mass control region. Taken together, these form the total estimated SM background (shown by the dashed histograms in the figure). Good agreement is found between the observed spectrum and the total SM prediction estimate in the high-mass control region. The Z peak cross section obtained from the pseudo-data is 1.517 ± 0.008 (stat.) $\times 10^6$ fb, which

¹Since the diphoton contribution is expected to be quite small, it is estimated from Monte Carlo simulation.

is in agreement with the SM LO Drell-Yan cross section obtained from PYTHIA multiplied by K -factor of 1.35, which is of 1.525×10^6 fb.

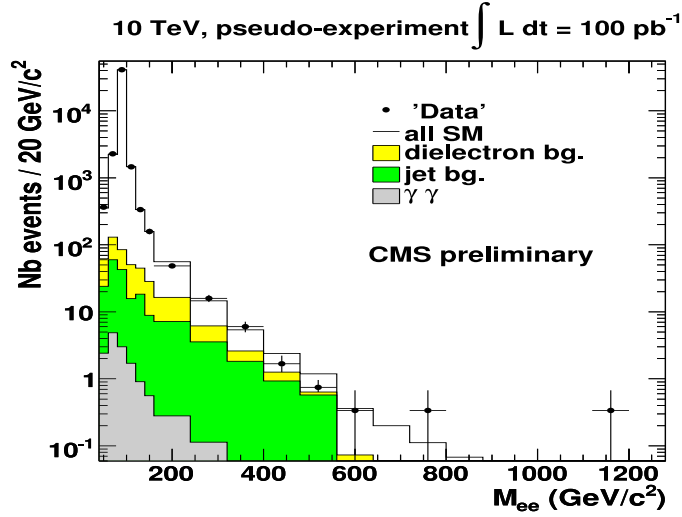


Figure 5.4: Dielectron invariant mass spectrum for a 100 pb^{-1} pseudo-experiment, compared to SM background estimates for the Drell-Yan process, $t\bar{t}$, QCD dijets, W +jet, γ +jet and $\gamma\gamma$ [10].

Figure 5.5 shows the same plot with a $1 \text{ TeV}/c^2$ Z' resonance added to the pseudo-data. A clear signal above background is "observed".

5.5.2 High mass Drell-Yan cross section

For high-mass di-electron events, the expected mass spectrum from SM processes only is seen in figure 5.6 and 5.7 for two electrons candidates passing the HEEP selection criteria with $E_t > 50 \text{ GeV}$ and invariant mass $120 < M < 600 \text{ GeV}/c^2$.

Figure 5.7 (a) shows an example of the result of a pseudo-experiment in this mass region, with contributions of the Drell-Yan process and of the backgrounds. The total number of events shown in this Figure is 501, of which 54.1 ± 4.3 events are from the dielectron background, and 4.5 events from the jet background. After the background subtraction, Drell-Yan distribution is demonstrated in figure. 5.7(b), where the SM for Drell-Yan prediction is represented by the histogram. The number of Drell-Yan events at $M > 120 \text{ GeV}/c^2$ and electron $E_T > 50 \text{ GeV}$ is then measured to be 442.4 ± 22.8 (stat.). The measured cross section obtained from a pseudo-experiment corresponding to an integrated luminosity of 100 pb^{-1} is 15.92 ± 0.89 (stat.) $\times 10^3$ fb. The measurement is in agreement with the SM LO Drell-Yan cross section multiplied by the K -factor of 1.35, which is 16.47×10^3 fb at 10 TeV proton-proton centre of mass energy.

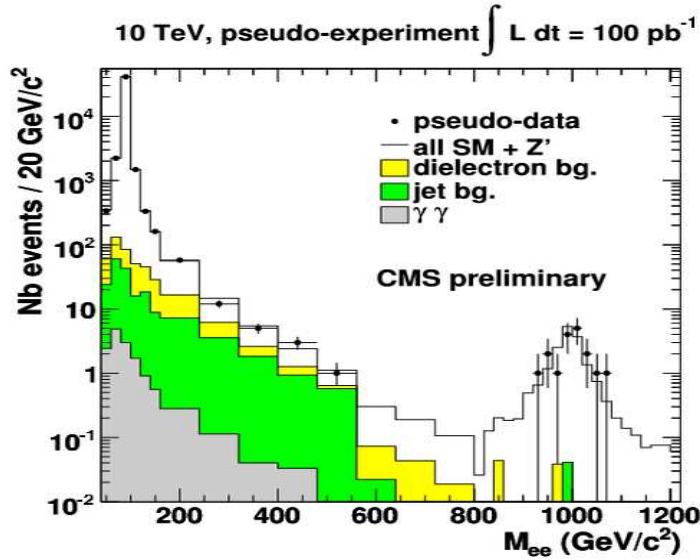


Figure 5.5: Dielectron invariant mass spectrum for a 100 pb^{-1} pseudo-experiment including a $1 \text{ TeV}/c^2$ Z' signal, compared to SM background estimates for the Drell-Yan process, $t\bar{t}$, QCD dijets, W +jet, γ +jet and $\gamma\gamma$ [10].

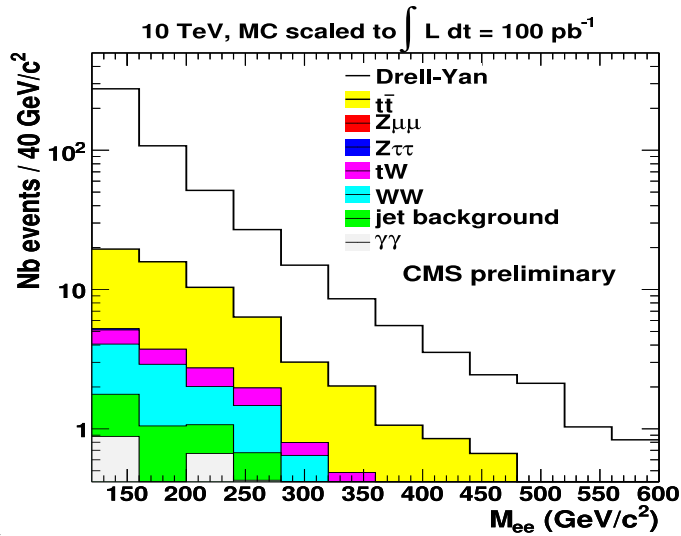


Figure 5.6: Expected true dielectron mass spectrum, containing the Drell-Yan and various dielectron, W +jet, γ +jet and QCD multi-jet and $\gamma\gamma$ contributions, with two electrons candidates passing the HEEP selection criteria with $E_t > 50 \text{ GeV}$ and $120 < M < 600 \text{ GeV}/c^2$. The samples are scaled to correspond to an integrated luminosity of 100 pb^{-1} [10].

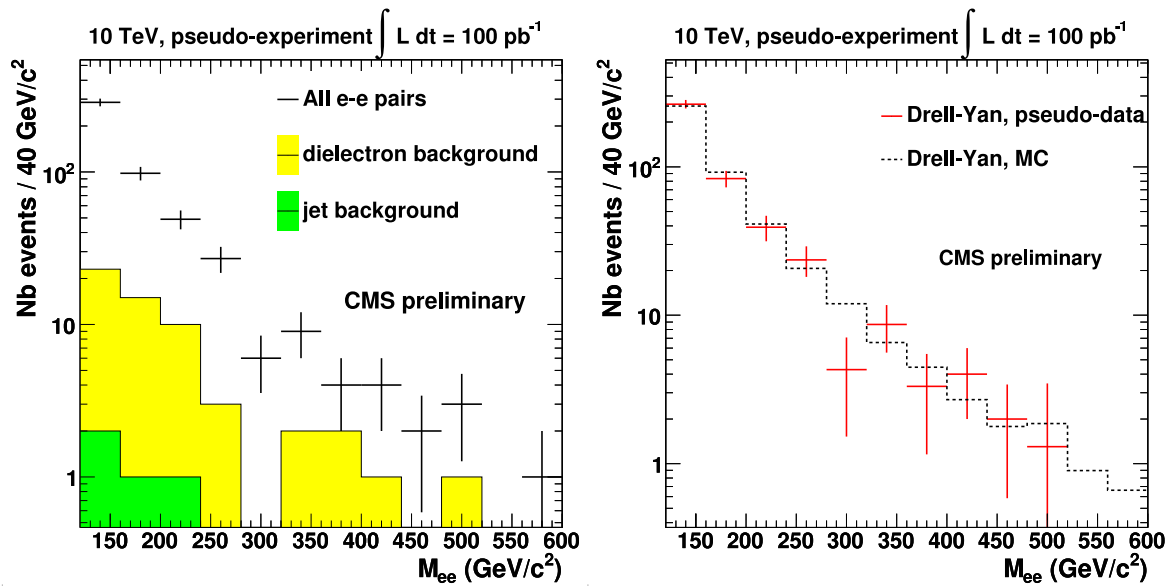


Figure 5.7: (left) Expected e^+e^- mass spectrum for an integrated luminosity of 100 pb^{-1} , obtained from pseudo-experiments containing the Drell-Yan signal (right) shows the measured Drell-Yan spectrum as (left), after background subtraction the dashed histogram is the Drell-Yan mass spectrum produced by Monte Carlo simulation [10].

Chapter 6

Recovery of high p_t electrons lost in ECAL cracks

6.1 Introduction

The possible discovery of heavy particles decaying in electron or photon pairs with TeV energies, using the reconstruction of the electromagnetic shower energies, implies detailed understanding of the ECAL response including possible energy leakage in the hadronic calorimeter (HCAL).

Due to the cracks in ECAL, as it will be explained in section 6.1.1, the efficiency for reconstructing electron pairs with normal criteria, which has been explained in section 4.1, is not optimal. The main aim of this chapter is to define a new tool to recover, with high efficiency, electron pairs, both to save the small expected statistics and to minimize uncertainties on the efficiency estimates. The precision of the efficiency measurements will thus depend on the available statistics, with smaller relative error for high efficiencies.

6.1.1 Electron losses in ECAL cracks and the EB-EE gaps

Electrons emitted in the direction of cracks between ECAL super-modules and gaps between the ECAL barrel and endcaps, as was discussed in chapter 3 (see Figure 3.4 and Table 3.2), could be lost. These cracks and gap can induce poor energy measurement and/or electron identification losses because of the requirements concerning the transverse momentum ($p_t > 80 \text{ GeV}/c$) and/or the energy ratio condition, $R_{H/E} < 0.10$, are not fulfilled.

6.1.2 Simulated samples

The samples of events, which have been used for performing the studies in this chapter, were generated and fully reconstructed using the CMS simulation program (CMSSW, version 1.6.5).

To study the detector response, several samples of “single gun” electrons (e^+ and e^-), with no additional particle pile-up, were generated with fixed energy or fixed p_t values, in particular $p_t = 100$ and $500 \text{ GeV}/c$, which are the peak values for electron pairs with masses $M_{ee} = 200$ and $1000 \text{ GeV}/c^2$, respectively ¹. “Single

¹The p_t variable is relevant for trigger and electron identification, while energy is the physically relevant variable for longitudinal shower containment in the ECAL.

gun" electrons were generated uniformly in η and in ϕ , the position of the emission point being distributed in z according to a Gaussian law centred at the nominal interaction point with a width of 53.0 mm, as implied by the proton bunch lengths.

For signal simulation, Drell-Yan events with $M_{\gamma/Z} > 200 \text{ GeV}/c^2$ and SSM Z' bosons were generated using the PYTHIA program, version 6.409, with the CTEQ5L parton distribution functions and including simulation of final state electromagnetic hard radiation. For background studies, nine samples of QCD multi-jet events generated with CMSSW version 1.5.2 in view of the CSA07 exercise and seven samples of W+jet events generated with version 1.6.7, with \hat{p}_t scales from 80 to 1000 GeV/c and corresponding to variable integrated luminosities, were used.

6.2 HCAL response to electromagnetic and hadronic showers

In order to recover high mass electron pairs ($M_{ee} > 200 \text{ GeV}/c^2$), when one of the electrons is emitted in the direction of the ECAL EB-EE gaps, the HCAL is used and specific criteria are defined to determine the energy of electrons emitted toward the ECAL gaps. It must be taken into account that the CMS HCAL calorimeter is of a non-compensating nature, and thus provides different responses for electromagnetic and hadronic showers.

6.2.1 Clustering algorithm

In order to study the HCAL response to electromagnetic (and hadronic) showers the "single gun" electrons and pions were used, the ECAL calorimeter being taken as absent. The HCAL response was determined in the barrel region (HB) with $|\eta| < 1$, using the simulation of energy deposits in 4×4 HCAL cells around the electron direction. The clustering algorithm is illustrated in figure 6.1. Starting from the position of the hottest

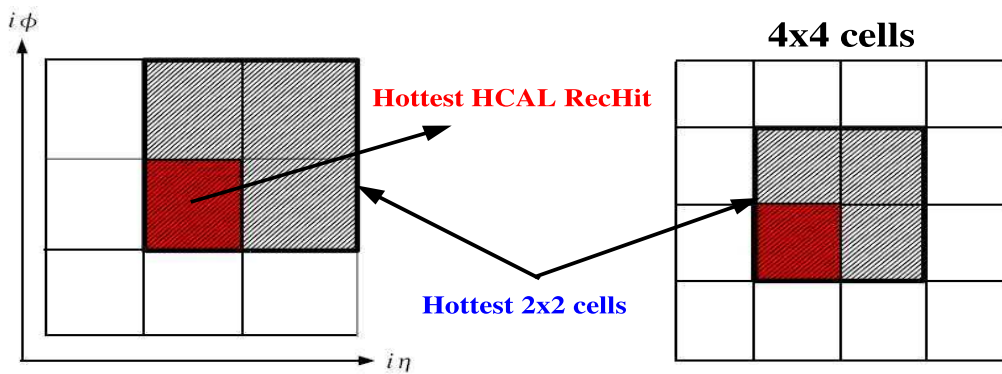


Figure 6.1: (left) The hottest 2×2 HCAL cells among the 3×3 array of cells; (right) 4×4 array of cells including the hottest 2×2 cells.

HCAL RecHit², energy of each HCAL RecHit, above 0.9 GeV in HB to avoid adding noise, is added to form the hottest 2x2 cells. Similarly, we add the RecHit energies of the 12 cells around the hottest 2×2 cells to form the 4×4 array of cells.

6.2.2 Recalibration of the HCAL to electromagnetic showers

The standard HCAL calibration is not suited to adequately provide purely electromagnetic shower measurements. A recalibration for electron showers is thus performed, using a simple empirical parameterisation of the HCAL response as described by the Monte Carlo simulations. The recalibration parameters are determined as a function of electron energy.

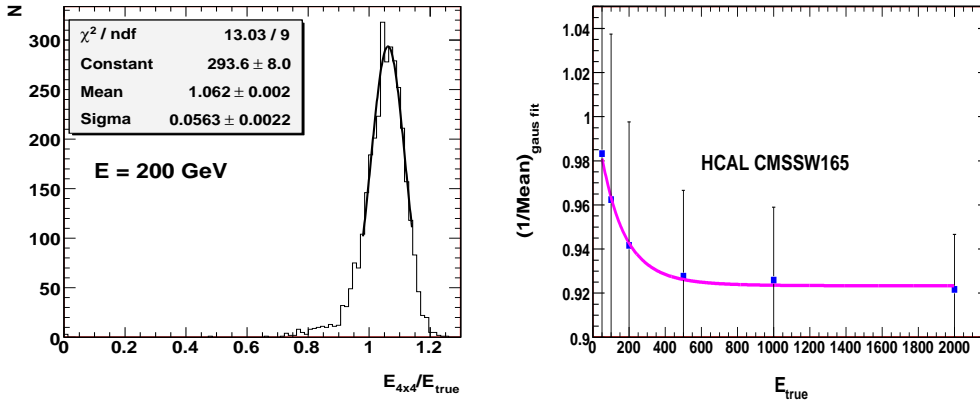


Figure 6.2: (left) Distribution of the reconstructed over generated energy, with superimposed Gaussian fit, for 200 GeV “single gun” electrons uniformly distributed over the HCAL barrel region $|\eta| < 1.0$ when the ECAL calorimeter is taken as absent; (right) recalibration function for electron showers in the HCAL; the superimposed error bars are the width of the Gaussian fits [52].

E (GeV)	e^-		π^-	
	μ	σ	μ	σ
50	1.017	0.091	0.909	0.156
100	1.039	0.075	0.936	0.113
200	1.062	0.056	0.959	0.103
500	1.078	0.039	0.972	0.072
1000	1.080	0.033	0.975	0.069
2000	1.085	0.025	0.978	0.056

Table 6.1: The mean (μ) and standard deviation (σ) of the Gaussian fits, to the reconstructed over generated energy distributions, for single gun electrons and pions generated with several fixed energies. The energy was reconstructed using 4×4 HCAL cells around the particle direction in HCAL barrel, with no simulated ECAL.

²RecHit is the energy and time for each hit (per channel).

Table 6.1 illustrates the mean (μ) and standard deviation (σ) of the Gaussian fits, of the reconstructed over generated energy distribution, for single gun electrons (and pions) generated with several fixed energies and no simulated ECAL. The electrons (and pions) energy was reconstructed using 4×4 HCAL cells around the electron direction in HCAL barrel. The fact that the mean of the Gaussian fits for pions do not peak at 1.0 is attributed to the fact that 4×4 HCAL cells (~ 0.4 radian) is not enough to fully contain the hadronic shower. Since the radius of the iterative cone, which is used to reconstruct the hadronic jets, is about 0.5 or 0.7 radian [31]. While the resolution for pions is greater than that of the electrons by about 4% on average. This is because hadronic showers contain energy dependent contributions of purely electromagnetic (essentially photons from π^0 and η decays) and purely hadronic components, with event to event fluctuations which are responsible for most of the spread of the calorimeter resolution [49], as was discussed in section 4.5.

Figure 6.2 (left) shows the reconstructed over generated energy distribution in the case of 200 GeV "single gun" electrons, with a superimposed Gaussian fit. The inverse of the peak values and the widths are shown for six different energies (see Table 6.1) on figure 6.2 (right), indicating that HCAL recalibration factors for electrons range from about 0.98 at 50 GeV to 0.92 for electron energies ≥ 500 GeV³.

The recalibration function is parameterised in the following empirical form:

$$C(E) = 0.0865 \cdot (10.7 + e^{-7.91E+2.25E^2}), \quad (6.1)$$

with E in TeV.

6.3 Effects of ECAL gaps and cracks on electron reconstruction and identification

This section is dedicated to the study of the electron energy collected in ECAL superclusters which have been defined as in section 4.1, E_{ECAL} , as a function of the supercluster position, defined by its pseudorapidity η and its azimuthal angle ϕ and, for the endcaps, by the x and y coordinates of the crystal front face. In case no ECAL supercluster is reconstructed, the generated η and ϕ values are used. Single gun electron samples are used to study the effect of ECAL gaps and cracks on energy deposits in the ECAL (section 6.3), on energy deposit in the HCAL and ensuing electron identification inefficiencies (section 6.3.1).

Figure 6.3 presents, as a function of the pseudorapidity $|\eta|$, the fraction $R_{\text{ECAL}} = E_{\text{ECAL}} / E_{\text{true}}$ of the generated electron energy, E_{true} , which is collected in ECAL superclusters. On the bottom plots, the error bars represent the rms of the distributions.

Small fluctuations around $R_{\text{ECAL}} \simeq 1$ are due to effects related to lateral shower extension (Bremsstrahlung emission, photon conversion and energy deposit in dead material in front and within the ECAL) and longitudinal shower leakage (losses due to incomplete electromagnetic shower containment at very high energy). A

³The HCAL electronics saturates for 3.1 TeV for HB and 3.35 for HE, which corresponds to a p_t of 570 GeV/ c for $\eta = 2.4$. This effect is not taken into account here.

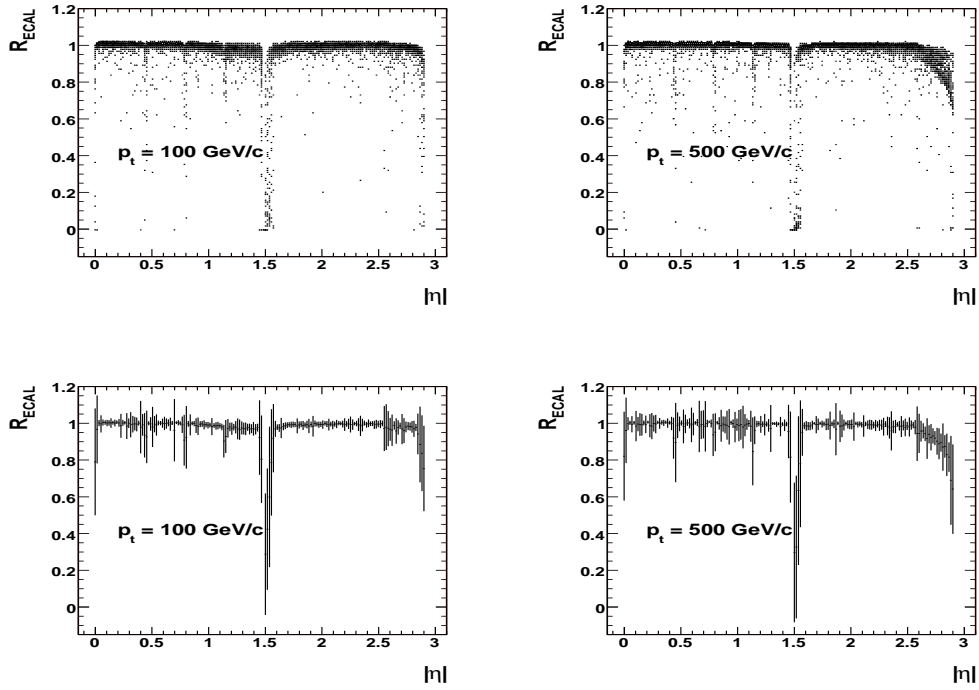


Figure 6.3: Fraction R_{ECAL} of the generated energy measured in the ECAL supercluster, plotted as a function of the supercluster pseudorapidity $|\eta|$, for “single gun” electrons with $p_t = 100 \text{ GeV}/c$ (left plots) and $p_t = 500 \text{ GeV}/c$ (right plots); the error bars on the bottom plots represent the rms of the distributions [52].

$|\eta|$ dependence of these effects is observed, attributed to the varying amount of material in front of the ECAL leading to different effective material depths (see e.g. [47]).

In addition, significant energy losses, observed both as a decrease of the average value of R_{ECAL} and as an increase of the measurement spread, are visible for electrons emitted close to barrel intermodule cracks and in the EB-EE gap region. In this region, cases are also observed where no ECAL supercluster is reconstructed ($R_{\text{ECAL}} = 0$). Note that effects of energy losses due to the barrel cracks in ϕ (see section 6.3.1) are averaged over in the $|\eta|$ distributions. Table 6.2 lists the crack and gap limits, as obtained from the ECAL geometry

position	limits
$z = 0$ EB separation	$0.000 < \eta < 0.007$
intermodule 1-2	$0.437 < \eta < 0.451$
intermodule 2-3	$0.777 < \eta < 0.800$
intermodule 3-4	$1.127 < \eta < 1.147$
EB - EE gap	$1.453 < \eta < 1.563$

Table 6.2: Limits of the ECAL cracks and EB-EE gaps, as obtained from “single gun” electrons with $p_t = 100$ and $500 \text{ GeV}/c$.

simulated in CMSSW 1.6.5 using electrons with $p_t = 100$ and $500 \text{ GeV}/c$. The limits were determined visually. The energy collections are affected over a width corresponding roughly to one crystal size ($\simeq 0.017$)

for intermodule cracks and 6 crystals for the EB-EE gaps. The realistic vertex distribution used in the simulation implies a partial cancellation of the effect of crystal off-pointing, with some electron trajectories being (nearly) aligned with cracks. This leads to larger energy losses than for electrons emitted from the nominal interaction point. The smearing in the vertex position distribution affects the $|\eta|$ distributions but not the ϕ distributions. The decrease of R_{ECAL} for the largest $|\eta|$ values is due to the incomplete shower containment in the ECAL due to the absence of preshowers and to lateral shower leakage. In the following, only the region covered by the tracker ($|\eta| < 2.4$) will be considered. For the endcaps, no crack effects are expected in $|\eta|$ since the gaps between Dees are along the y axis and the supercrystal arrangement follows a rectangular $x - y$ structure.

6.3.1 Electron identification and losses

The fraction of the electron energy which is not collected in the ECAL because of gaps and cracks is lost in dead material between ECAL and HCAL and/or is collected in the HCAL ⁴.

For the study of the effects of cracks and gaps using single gun electron, the ECAL and tracker isolation conditions of the standard HEEP identification criteria (5.9) are relaxed, and the following minimum electron identification conditions are imposed:

$$\begin{aligned} |\eta| &< 2.4, \\ p_t &> 80 \text{ GeV}/c, \\ H/E &< 0.10, \end{aligned} \tag{6.2}$$

where H/E is defined in section 5.1.2, the electron pseudorapidity η and p_t are computed from the ECAL supercluster. Energy leakage into the HCAL directly translates into electron identification losses when $H/E > 0.10$ (only deposits above 0.9 GeV for barrel and 1.4 GeV for endcap HCAL cells are used for computing the HCAL energy, in order to take into account the noise fluctuations). Standard HCAL calibration is used.

Figures 6.4 and 6.5 present the resulting reconstruction efficiencies as a function of the geometrical variables for electrons with $p_t = 100$ and $500 \text{ GeV}/c$, respectively; only electrons in the tracker acceptance ($|\eta| < 2.4$) are considered. Intermodule cracks and EB-EE gaps corresponding to the features of figure 6.3 are visible as a function of η in pannels (a). For the barrel, cracks in ϕ are observed in pannels (b), spaced by 20 degrees, which corresponds to the division in 18 modules (regions corresponding to the gaps in η of Table 6.2 are excluded). Pannels (c) and (d) present the efficiencies as a function of the variables x and y for the endcaps ($1.6 < |\eta| < 2.4$). Structures are also observed, in particular the separation between endcap Dees for $x = 0$.

Table 6.3 summarises e^+ and e^- losses, estimated with "single gun" samples with $p_t = 100$ and $500 \text{ GeV}/c$. The intermodule η cracks are defined as in Table 6.2. The losses in ϕ cracks are computed for the barrel region ($|\eta| < 1.44$), outside the η crack limits and within $\pm 1.5^\circ$ of the supermodule limits. Within statistical precision,

⁴Outside the gap and crack regions, the longitudinal extension of electromagnetic showers beyond the ECAL only affects very high energy showers (typically above 500 GeV), at the % level [47]. In the gap region, only a small fraction of the electron energy is split into two superclusters, reconstructed separately in EB and EE (see section 6.4.1).

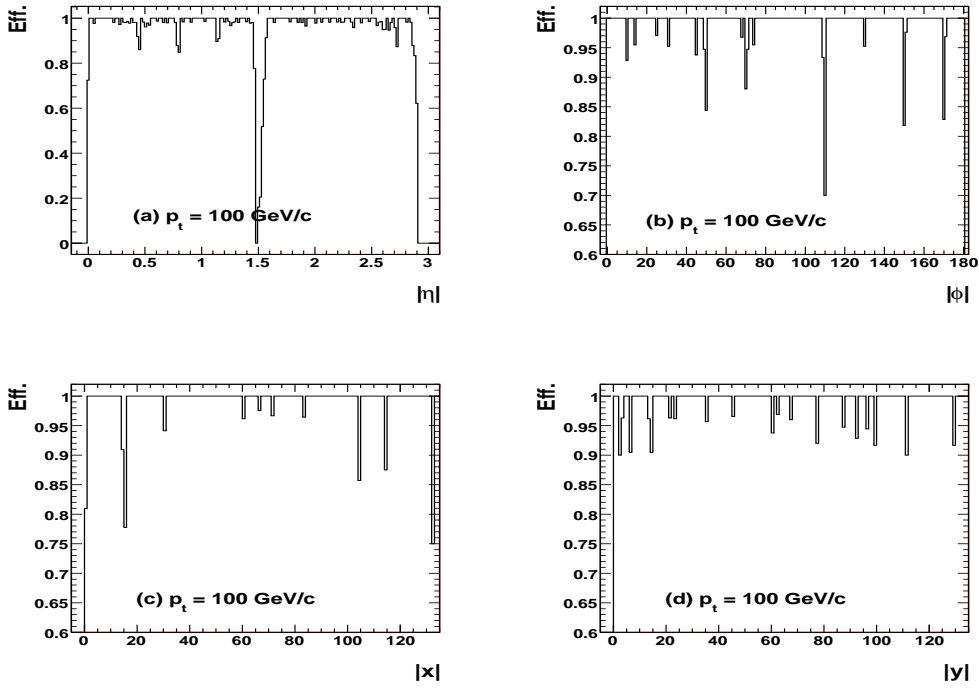


Figure 6.4: Efficiency for reconstructing electrons with ECAL $p_t > 80$ GeV/ c and $H/E < 0.10$, for “single gun” samples with $p_t = 100$ GeV/ c , as a function of (a) the pseudorapidity $|\eta|$; (b) the azimuthal angle $|\phi|$ (the η cracks and gap regions quoted in Table 6.2 are excluded), for the barrel region with $|\eta| < 1.44$; (c) and (d) the x and y coordinates, for the endcap region ($1.6 < |\eta| < 2.4$) [52].

Losses	$p_t = 100$ GeV/ c		$p_t = 500$ GeV/ c	
	e^+	e^-	e^+	e^-
in η cracks	$0.35 \pm 0.07\%$	$0.51 \pm 0.08\%$	$0.28 \pm 0.06\%$	$0.30 \pm 0.07\%$
in EB-EE gaps	$1.91 \pm 0.16\%$	$1.98 \pm 0.17\%$	$1.76 \pm 0.16\%$	$1.68 \pm 0.15\%$
in ϕ cracks (EB)	$0.49 \pm 0.08\%$	$0.37 \pm 0.07\%$	$0.67 \pm 0.10\%$	$0.54 \pm 0.09\%$
total losses ($ \eta < 2.4$)	$3.22 \pm 0.18\%$	$3.49 \pm 0.19\%$	$3.29 \pm 0.17\%$	$3.09 \pm 0.17\%$

Table 6.3: Fractions of e^+ and e^- “single gun” electrons (uniformly distributed in η with $|\eta| < 2.4$), lost because of intermodule cracks and of EB-EE gaps (defined as in Table 6.2), for $p_t = 100$ and 500 GeV/ c . The losses in ϕ cracks are computed in the barrel ($|\eta| < 1.44$), outside the η crack limits and within $\pm 1.5^\circ$ of the supermodule limits.

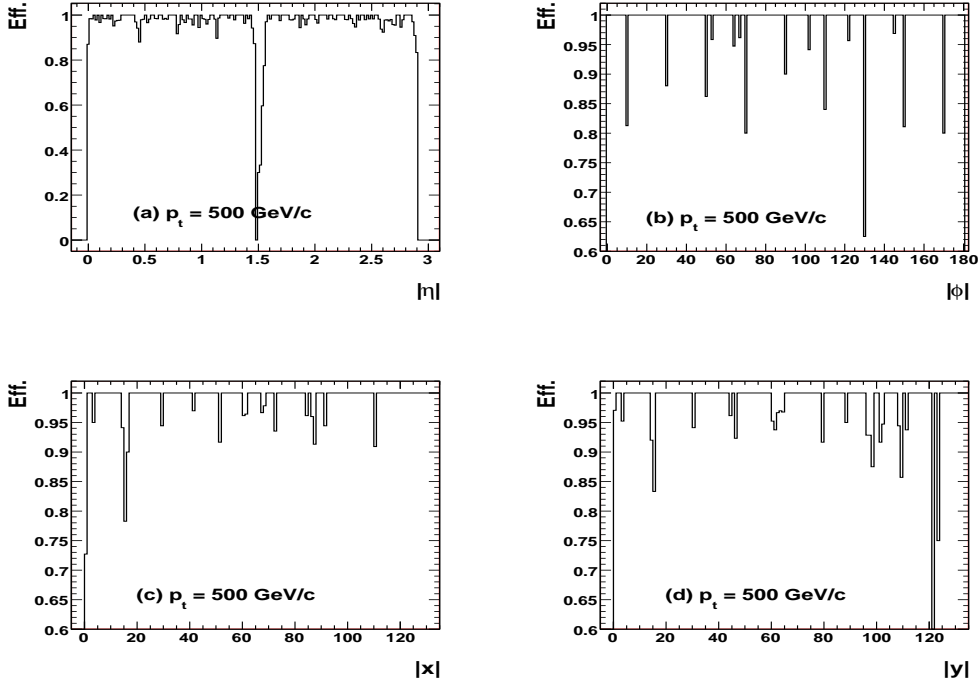


Figure 6.5: Same as figure 6.4, for $p_t = 500 \text{ GeV}/c$ [52].

losses are quite similar for electrons and positrons, and are slightly lower for $500 \text{ GeV}/c$ than for $100 \text{ GeV}/c$ particles (this is because the cut at $80 \text{ GeV}/c$ is less sensitive at higher p_t).

6.3.2 Drell-Yan event losses

The number of events for which both reconstructed electrons pass the minimum identification conditions (6.2) represents $91.1 \pm 0.7\%$ of the total number of Drell-Yan events with $M_{\gamma/Z} > 200 \text{ GeV}/c^2$ for which both (real) final state electrons are emitted with $|\eta| < 2.4$ and $p_t > 80 \text{ GeV}/c$. The sample used for this study corresponds to a luminosity of $\approx 1.9 \text{ fb}^{-1}$. Generated momenta are quoted here for final state (“real”) electrons, after possible hard electromagnetic radiations which carry away part of the momentum of the (virtual) electron emitted at the γ/Z decay vertex. Radiated final state photons can however be detected in the ECAL in the same supercluster as the final state (real) electron. This makes a direct comparison of generated and reconstructed numbers of electrons passing momentum cuts convention dependent, but Monte Carlo simulations allow reliable calculations of this effect.

Table 6.4 gives the repartition of the “lost” events, i.e. the events for which both (real) electrons were generated with $|\eta| < 2.4$ and $p_t > 80 \text{ GeV}/c$ but for which one of the reconstructed electrons does not pass the minimum identification conditions (6.2).

The losses due to the EB-EE gaps amount to 4% of the total number of events. Among these, 20% have no reconstructed ECAL supercluster.

total loss of events	$8.9 \pm 0.7\%$
events lost because of η cracks and EB-EE gaps	$4.5 \pm 0.5\%$
events lost because of ϕ cracks (EB)	$1.5 \pm 0.3\%$
other losses	$2.9 \pm 0.4\%$
events lost because of EB-EE gaps only	$3.7 \pm 0.5\%$
of which: events with no ECAL supercluster	$0.7 \pm 0.2\%$

Table 6.4: Repartition of the “lost” Drell-Yan events, i.e. events generated with $M_{\gamma/Z} > 200 \text{ GeV}/c^2$ and both (real) electrons generated with $|\eta| < 2.4$ and $p_t > 80 \text{ GeV}/c$, and for which one of the electrons does not pass the minimum identification conditions (6.2). The cracks are defined as in Table 6.2. The errors are the statistical errors for a luminosity of 1.9 fb^{-1} .

6.4 Electron recovery in the EB-EE gap regions

This section is devoted to the study of a procedure to recover electrons lost in the EB-EE gaps, which forms the largest source of losses. For that purpose, several samples of “single gun” electrons uniformly distributed over the gap region ($1.453 < |\eta| < 1.563$), with no additional particle pile-up, were generated with fixed p_t values ($p_t = 100$ and $500 \text{ GeV}/c$) to study the responses of the ECAL and HCAL calorimeters in the gap region. The recovery of events lost because of the gaps does not only contribute to collecting a few additional events in small statistics samples, which is useful, but also provides a tool for controlling the detector response in that specific region.

Geometrically, the EB-EE gap corresponds to tower 18 of the HCAL, which is longitudinally segmented, like other HCAL endcap towers (see section 3.5). The first segmentation, closer to the interaction vertex and hereafter called H1, corresponds to $26.6 X_0$; the second segmentation (H2) corresponds to $87.8 X_0$. The width of tower 18 is of 0.087 units in η ($1.479 < |\eta| < 1.566$); in ϕ , it is divided in 72 sectors of 5° width. Each cell of HCAL tower 18 thus corresponds roughly to a 5×5 ECAL crystal matrix. In spite of a reduced transverse granularity, the HCAL calorimeter provides an efficient tool to identify electrons in the gap region and reconstruct their energy.

In section 6.4.1, electron energy reconstruction, including energy deposits in the HCAL, is studied for the gap region. In section 6.5.1, electron identification criteria in this region, permitting electron recovery, are defined from the comparison of the HCAL response to Drell-Yan electrons and QCD jets.

6.4.1 Electron energy reconstruction

The events under study are those which do not pass the minimum identification conditions (6.2), i.e. $p_t > 80 \text{ GeV}/c$ and $H/E < 10\%$.

(i) In case an ECAL supercluster has been reconstructed in the gap region $1.453 < |\eta| < 1.563$ (i.e. for gap limits as given in Table 6.2), either in EB or in EE, the associated HCAL energy is computed in the following way⁵.

⁵When the electron energy is split into a barrel and an endcap supercluster, the higher energy supercluster is used.

In tower 18, the energies of recorded rechits in the first longitudinal segmentation (H1) and located within a range of $|\Delta\phi| < 0.25$ from the ECAL supercluster position are summed (with the condition that individual rechit contents must be above the threshold of 1.4 GeV). Energy deposits in the ϕ -adjacent HCAL cells of tower 17 “ E_{17} ” (which is not segmented) and in the first segmentation of tower 19 “ E_{19} ” are also collected. These contributions are, for all lost events, significantly smaller than those of tower 18 “ E_{18} ”, and represent, on average, some 16% of the total as seen from Figure 6.6.

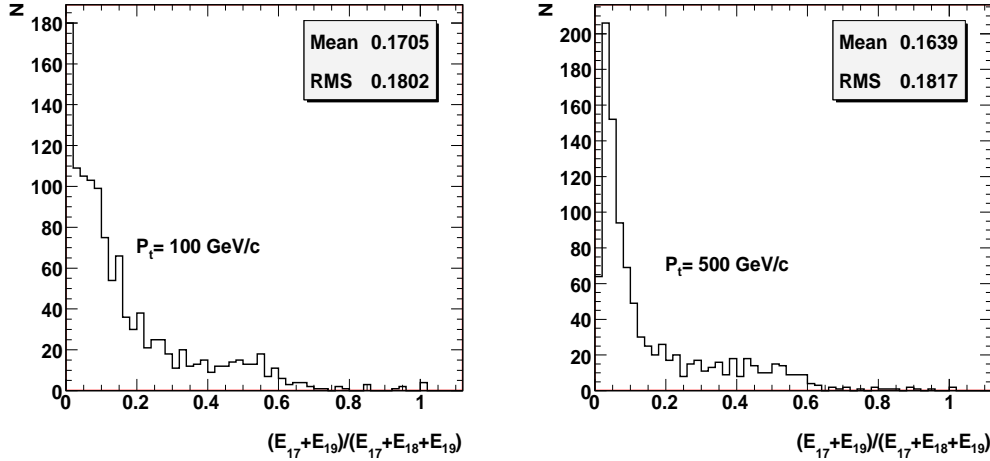


Figure 6.6: Ratio $(E_{17} + E_{19})/(E_{17} + E_{18} + E_{19})$ of the energy deposits in the ϕ -adjacent HCAL cells of tower 17 and in the first segmentation of tower 19 over the energy deposits in towers 17, 18 and 19 (including HCAL recalibration), for “single gun” electrons emitted toward the EB-EE gap region and which do not pass the minimum identification conditions (6.2); (left) $p_t = 100$ GeV/ c ; (right) $p_t = 500$ GeV/ c .

The energy dependent factor, in equ. 6.1, for electromagnetic showers in the HCAL (see section 6.2) is then applied to the sum of these energies, giving the recalibrated HCAL energy E_{H1} .

For 15% of the lost “single gun” electrons, the energy deposit in the ECAL is split in two superclusters, reconstructed in EB and EE, respectively; the superclusters are associated if their directions match, with $|\Delta\eta| < 0.10$ and $|\Delta\phi| < 0.25$. In such cases, the lower energy supercluster contributes on the average $\approx 25\%$ of the higher energy one, and the HCAL energy deposit contributes $\approx 80\%$ of the total ECAL energy.

The final electron candidate energy E_{reco} is then computed as the sum of the (possibly split) ECAL supercluster energy and of the (recalibrated) HCAL energy E_{H1} .

(ii) If no ECAL supercluster is reconstructed in the gap region, the highest energy rechit in the first segmentation of tower 18 is used as a seed, and the energy deposits in the two ϕ adjacent cells are added. “Single gun” simulations indicate that, when no ECAL supercluster is reconstructed, no energy is deposited in the adjacent towers 17 and 19. The electron candidate energy E_{reco} is defined as the energy collected in tower 18 after appropriate HCAL recalibration.

Figure 6.7 presents the distribution of the ratio $R_{\text{reco}} = E_{\text{reco}}/E_{\text{true}}$, the reconstructed energy E_{reco} before

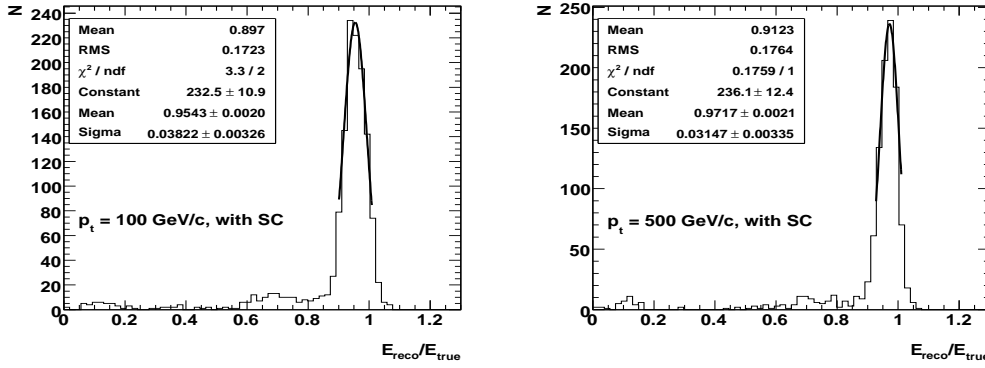


Figure 6.7: Ratio $R_{\text{reco}} = E_{\text{reco}}/E_{\text{true}}$ of the reconstructed (including HCAL recalibration) over generated energies, for “single gun” electrons emitted toward the EB-EE gap region and which do not pass the minimum identification conditions (6.2); the reconstructed energy E_{reco} is computed before adding the energy of a possible second associated supercluster: (left) $p_t = 100 \text{ GeV}/c$; (right) $p_t = 500 \text{ GeV}/c$.

adding the energy of a possible second associated supercluster over generated (“true”) energies, for electrons with $p_t = 100$ and $500 \text{ GeV}/c$, emitted toward the EB-EE gap region and which do not pass the minimum identification conditions (6.2). Figure 6.8 is the same as figure 6.7 except that the energy of the second associated supercluster has been added, which improves the tail of the distributions and does not affect the position of the peak. Events with and without a reconstructed ECAL supercluster are shown separately.

Table 6.5 presents the corresponding peak values and resolutions, from Gaussian fits over $\pm 1.5 \sigma$.

p_t		with ECAL supercluster	no ECAL supercluster
100 GeV/c	peak	0.95	0.96
	resolution	0.04	0.06
500 GeV/c	peak	0.97	0.95
	resolution	0.03	0.03

Table 6.5: Peak values and resolutions of the distributions in Figure 6.8.

The reconstructed energies, which take into account the HCAL energy recalibration (6.1), peak at some 4% below the generated values, with resolutions of the order of 3.5% and relatively long tails.

The few events accumulated with values of $R_{\text{reco}} < 0.2$ are all due to electrons for which a supercluster was reconstructed in the ECAL endcaps with $1.53 < \eta < 1.57$ and with ϕ values comprised between -10 and $+10^\circ$ (see figure 6.9) and between 170 and 190° , with no corresponding energy deposit in the HCAL.

6.4.2 Electron efficiency after energy reconstruction

When the procedure, presented in section 6.4.1, is used to estimate the fraction $R_{\text{ECAL}} = E_{\text{reco}} / E_{\text{true}}$ in the gap region ($1.453 < |\eta| < 1.563$), the plots 6.10 and 6.11 are obtained.

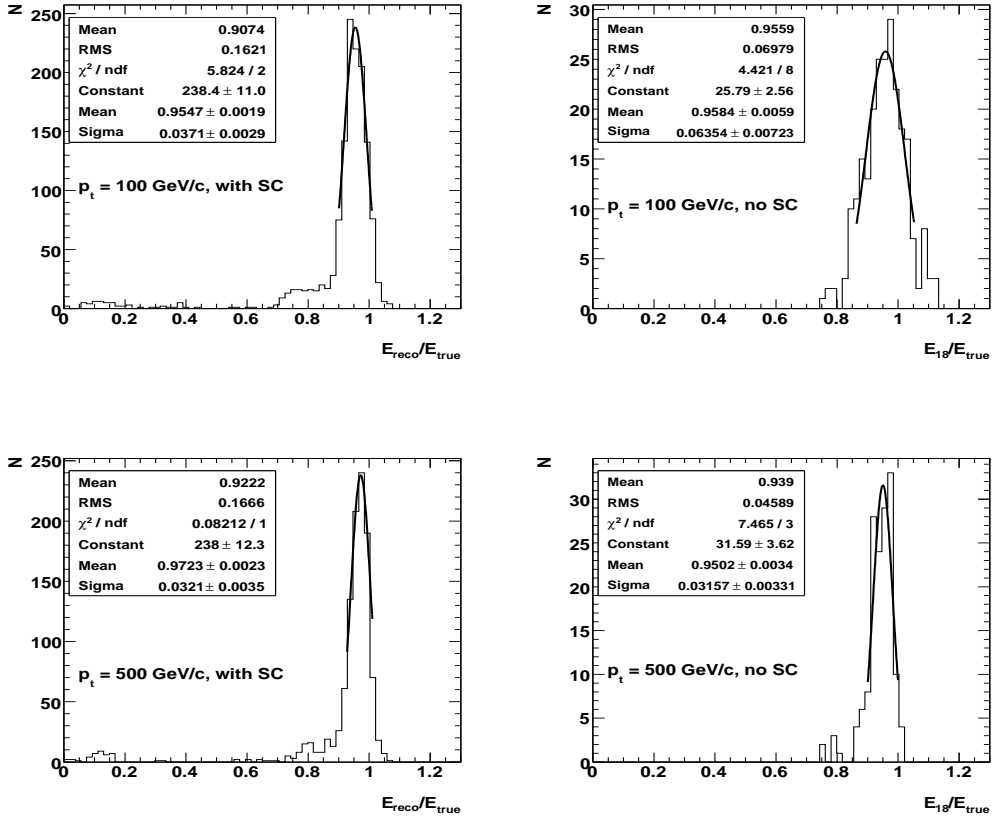


Figure 6.8: Ratio $R_{\text{reco}} = E_{\text{reco}}/E_{\text{true}}$ of the reconstructed (including HCAL recalibration) over generated energies, for "single gun" electrons emitted toward the EB-EE gap region and which do not pass the minimum identification conditions (6.2); the reconstructed energy E_{reco} is computed after adding the energy of a possible second associated supercluster: (top) $p_t = 100 \text{ GeV/c}$, bottom $p_t = 500 \text{ GeV/c}$; (left) events with a reconstructed ECAL supercluster; (right) events with no supercluster [52].

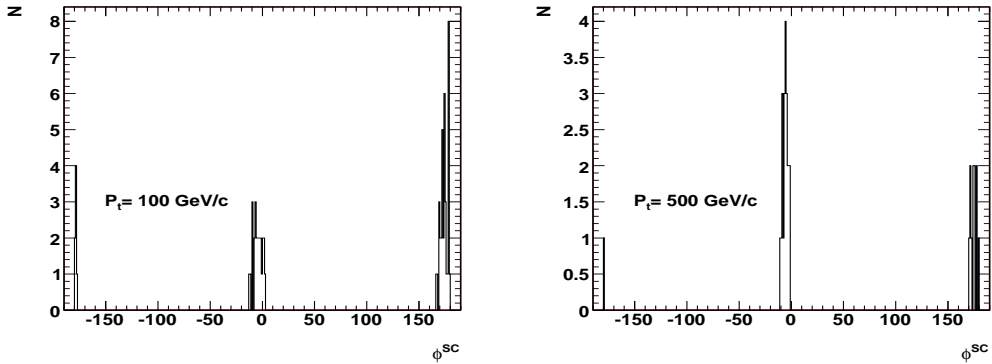


Figure 6.9: Distribution of the azimuthal angle ϕ corresponds to no energy deposit in the HCAL.

Figure 6.10 presents the fraction R_{ECAL} of the generated energy measured in the ECAL supercluster, far from the EB-EE gap regions ($1.453 < |\eta| < 1.563$), while in the gap regions it is the ratio of energy reconstructed “ E_{reco} ”, which has been introduced in section 6.4.1, plotted as a function of the supercluster pseudorapidity $|\eta|$, for “single gun” electrons with $p_t = 100 \text{ GeV}/c$ (left plots) and $p_t = 500 \text{ GeV}/c$ (right plots); the error bars on the bottom plots represent the rms of the distributions.

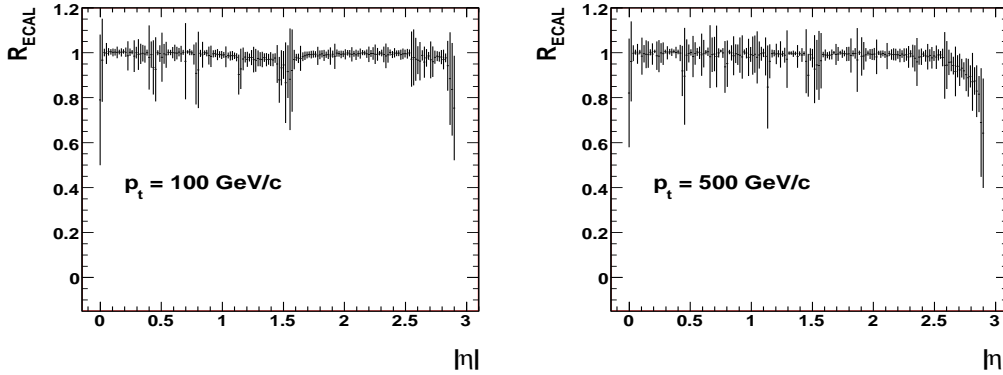


Figure 6.10: Fraction R_{ECAL} of the generated energy measured in the ECAL supercluster, after energy correction “ E_{reco} ” in the gap region ($1.453 < |\eta| < 1.563$), plotted as a function of the supercluster pseudorapidity $|\eta|$, for “single gun” electrons with $p_t = 100 \text{ GeV}/c$ (left plots) and $p_t = 500 \text{ GeV}/c$ (right plots); the error bars on the bottom plots represent the rms of the distributions.

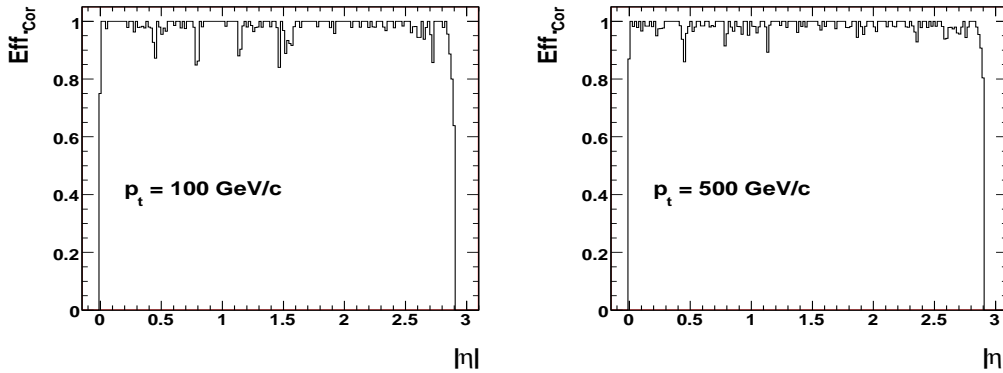


Figure 6.11: After energy reconstruction (E_{reco}) in the gap region ($1.453 < |\eta| < 1.563$), plots for efficiency are introduced as a function of the supercluster pseudorapidity $|\eta|$, for “single gun” electrons with $p_t = 100 \text{ GeV}/c$ (left plots) and $p_t = 500 \text{ GeV}/c$ (right plots), for reconstructing electrons with $p_t > 80 \text{ GeV}/c$ and $H/E < 0.10$.

In Figure 6.11, after energy reconstruction (E_{reco}) in the gap region ($1.453 < |\eta| < 1.563$), plots for efficiency are introduced as a function of the supercluster pseudorapidity $|\eta|$, for “single gun” electrons with $p_t = 100 \text{ GeV}/c$ (left plots) and $p_t = 500 \text{ GeV}/c$ (right plots), for reconstructing electrons with $p_t > 80 \text{ GeV}/c$

and $H/E < 0.10$.

6.5 Recovery of lost Drell Yan events in the EB-EE gap regions

6.5.1 Electron identification criteria

Identification criteria for recovery of electrons in the gap region which do not pass the minimum identification conditions (6.2) are studied in this section, using the Drell-Yan event sample with $M_{\gamma/Z} > 200 \text{ GeV}/c^2$ and the QCD and W+jet samples defined in section 6.1.2. The various \hat{p}_t background samples are normalised to the same luminosity, and in the figures, the Drell-Yan and background distributions are normalised to unity.

Electron candidates are reconstructed using the ECAL and HCAL energy deposits (see section 6.4.1) and required to pass the cut $p_t > 80 \text{ GeV}/c$, as computed from the reconstructed energy E_{reco} , for particles which fall in the EE-EB gap regions as explained previously in section 6.4.1. When this condition is satisfied, isolation variables are computed and the following recovery criteria are defined. The distributions of the discriminating variables presented in this section are for events where at least one electron passes the HEEP conditions (given in Table 5.9) outside the gap regions.

Longitudinal isolation; R_{H2} variable The quantity E_{H2} is computed as the sum of (recalibrated) energy deposits larger than 1.4 GeV, recorded in rechits belonging to the second longitudinal segmentation (H2) of tower 18 in the same ϕ domain (i.e. within $|\Delta\phi| < 0.25$). Figure 6.12 (left) presents the ratio $R_{\text{H2}} = E_{\text{H2}}/E_{\text{reco}}$ for electron candidates in the gap region which do not pass the minimum identification conditions (6.2), for the Drell-Yan event sample, the QCD jet and and W+jet samples. Given the effective depth of the first segmentation H1 of tower 18 ($26.6 X_0$), electromagnetic showers from Drell-Yan events are essentially fully contained in H1 and the ratio R_{H2} is 0 for most electrons (the same observation is made for the sample of Z' bosons with mass 1 TeV/ c^2). In contrast, significant energy deposits in H2 are observed for the jet samples. The cut $R_{\text{H2}} < 0.01$ thus has 100% efficiency for electrons, and efficiently rejects hadron background.

HCAL lateral isolation; ΣE_t The lateral isolation of the electron candidates is quantified using the total transverse energy deposit in the HCAL between two cones with axes along the electron candidate direction; this direction is defined by the ECAL supercluster direction or, when no ECAL supercluster is reconstructed, by the direction of the highest energy rechit in tower 18. Figure 6.12 (centre) presents, for electron candidates in the gap region with $80 < p_t(E_{\text{reco}}) < 200 \text{ GeV}/c$ (as computed from E_{reco}), the total transverse energy deposit ΣE_t between two cones with $0.25 < \Delta R < 0.50$. For higher p_t electron candidates ($p_t(E_{\text{reco}}) > 200 \text{ GeV}/c$), figure 6.12 (right) presents the ratio of ΣE_t by $E_{t,\text{reco}}$. The isolation cut $\Sigma E_t < 4 \text{ GeV}$ for $E_t < 200 \text{ GeV}$ and $\Sigma E_t/E_t < 0.02$ for $E_t > 200 \text{ GeV}$ have high efficiencies for electrons and helps rejecting a large fraction of the hadronic background.

Tracker isolation; N_{tr} and R_{pt} When (and only when) a supercluster is reconstructed, the isolation of the electron candidate is also quantified using the two following variables:

- N_{tr} is the number of tracks with $p_t > 1.5 \text{ GeV}/c$ emitted between two cones ($0.1 < \Delta R < 0.2$) around the supercluster direction;
- R_{pt} is the vectorial sum of the transverse momenta of these tracks, divided by the transverse momentum $p_t(E_{\text{reco}})$ of the electron candidate. Figures 6.13 (left) and (right) present these two variables, respectively, indicating that the cuts $N_{\text{tr}} < 2$ and $R_{\text{pt}} < 0.05$ are efficient to suppress the hadronic background and affect only slightly electron selection.

Track matching; $N_{\text{tr}}^{\text{match}}$ Finally, at least one track with $p_t > 20 \text{ GeV}/c$ is required within $|\Delta\eta| < 0.15$, $|\Delta\phi| < 0.15$ of the electron candidate direction. This cut, which helps rejecting e.g. low multiplicity jets with a leading π^0 , efficiently reduces the background surviving the above cuts, as shown in figure 6.13 (right). Figure 6.14 illustrates the distribution for the number of track matching for electron candidates emitted toward the EB-EE gap, (left plot) for electron candidates with $p_t(E_{\text{reco}}) > 80 \text{ GeV}/c$; while only electron candidates passing the isolation criteria are selected in (right plot). Figure 6.14 shows that the current order of applying the isolation criteria is important to have better efficiency, as will be summarized in the next section, and to reduce the background contribution.

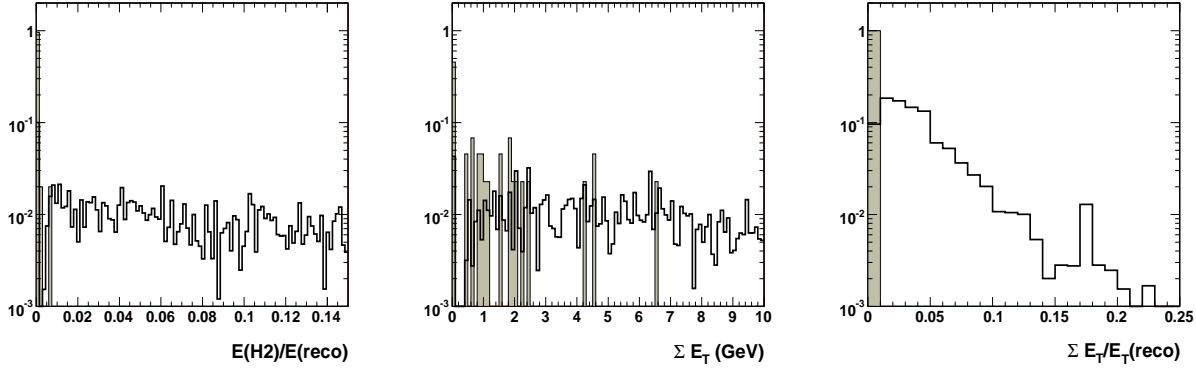


Figure 6.12: Discriminating variables for electron identification, for particles emitted toward the EB-EE gap, which do not pass the minimum electron identification conditions (6.2) and for which the transverse momentum computed from E_{reco} is larger than $80 \text{ GeV}/c$: (left) ratio $E_{\text{H2}}/E_{\text{reco}}$ of the energies deposited in the second segmentation of tower 18, E_{H2} , and the energies deposited in the first segmentation and (when applicable) the ECAL supercluster(s), E_{reco} ; (centre) total transverse energy, ΣE_t , deposited in the HCAL between two cones with axes along the electron candidate direction with $0.25 < \Delta R < 0.50$, for $80 < p_t(E_{\text{reco}}) < 200 \text{ GeV}/c$; (right) $\Sigma E_t/E_{t,\text{reco}}$, for $p_t(E_{\text{reco}}) > 200 \text{ GeV}/c$. At least one electron in the event has to pass the HEEP conditions (given in Table 5.9). The distributions for electrons candidates from the Drell-Yan signal are shown as shaded histograms, those from the QCD and W+jet backgrounds as white histograms. The signal and background distributions are normalised to unity [52].

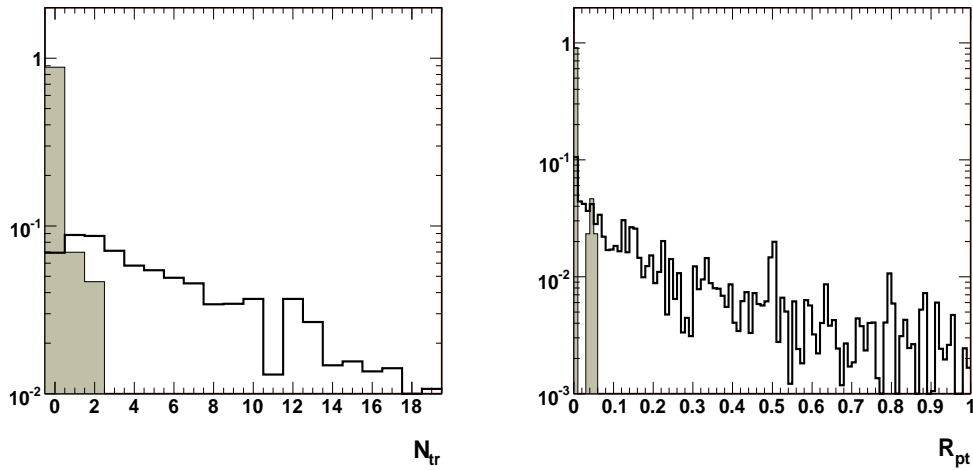


Figure 6.13: Same as in figure 6.12, for (left) tracker isolation: number of tracks with $p_t > 1.5$ GeV/ c emitted between two cones ($0.1 < \Delta R < 0.2$) around the electron candidate direction; (right) tracker isolation: vectorial sum of the transverse momenta of these tracks, divided by $p_t(E_{reco})$ [52].

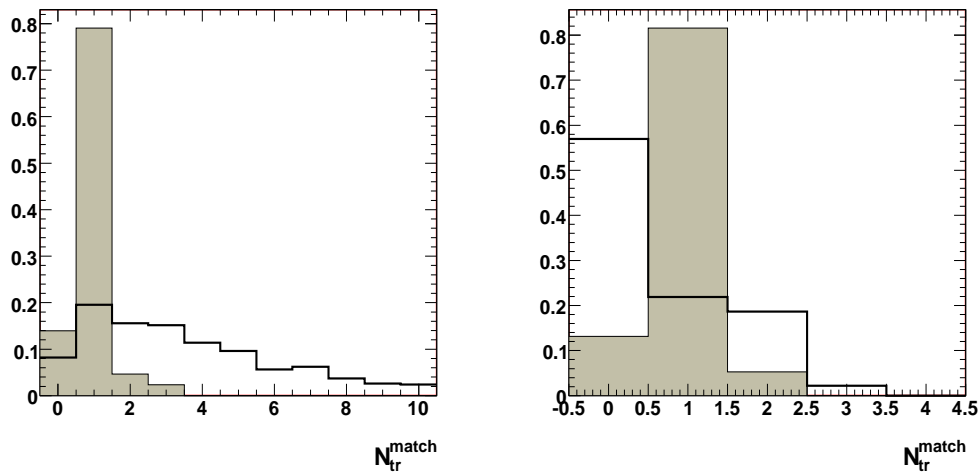


Figure 6.14: Track matching for electron candidates emitted toward the EB-EE gap: number of tracks with $p_t > 20$ GeV/ c emitted from the vertex and directed within a cone of radius $\Delta R < 0.15$ around the electron candidate direction; (left) electron candidates with $p_t(E_{reco}) > 80$ GeV/ c ; (right) only electron candidates passing the isolation criteria are selected [52].

6.5.2 Recovery conditions

In summary, the following identification criteria are applied to electron candidates emitted toward the EB-EE gap, which do not pass the minimum identification conditions (6.2):

$$\begin{aligned}
& 1.453 < |\eta| < 1.563, \\
& p_t(E_{\text{reco}}) > 80 \text{ GeV}/c, \\
& R_{H2} = E_{H2}/E_{\text{reco}} < 0.01, \\
& \Sigma E_t < 4 \text{ GeV (within } 0.25 < \Delta R < 0.50) \text{ for } E_{t,\text{reco}} < 200 \text{ GeV}, \\
& \Sigma E_t/E_t < 0.02 \text{ (within } 0.25 < \Delta R < 0.50) \text{ for } E_{t,\text{reco}} > 200 \text{ GeV}, \\
& N_{\text{tr}} < 2 \text{ (} p_t > 1.5 \text{ GeV}/c, 0.1 < \Delta R < 0.2), \\
& R_{\text{pt}} < 0.05 \text{ (} p_t > 1.5 \text{ GeV}/c, 0.1 < \Delta R < 0.2), \\
& N_{\text{tr}}^{\text{match}} > 0 \text{ (} p_t > 20 \text{ GeV}/c, |\Delta\eta| < 0.15, |\Delta\phi| < 0.15).
\end{aligned} \tag{6.3}$$

These criteria are similar (but tighter for tracker isolation) to those for the HEEP selections which are given in Table 5.9.

6.5.3 Efficiency of Drell-Yan and heavy resonance production recovery

The efficiency of the electron recovery criteria (6.3) is studied for the two e^+e^- signal samples: Drell-Yan production with mass $M_{\gamma/Z} > 200 \text{ GeV}/c^2$ and Z' boson production with mass $1 \text{ TeV}/c^2$, with both real electrons being generated with transverse momentum $p_t > 80 \text{ GeV}/c$ and $|\eta| < 2.4$. For these subsamples, 4% of the events were lost because one of the electrons is emitted in the EB-EE gap direction and does not pass the minimum electron identification conditions (6.2) (see Table 6.4).

Criterion for electron recovery	fraction of events passing the recovery cuts (6.3)	
	Drell-Yan, $M_{\gamma/Z} > 200 \text{ GeV}/c^2$	Z' , $M = 1 \text{ TeV}/c^2$
$p_t(E_{\text{reco}}) > 80 \text{ GeV}/c$	90.7% \pm 4.1%	100%
AND $R_{H2} < 1\%$	90.7% \pm 4.1%	100%
AND $\Sigma E_t < 4 \text{ GeV}$		
OR $\Sigma E_t/E_t < 0.02$	87.1% \pm 4.8%	95.3% \pm 1.7%
AND $N_{\text{tr}} < 2$	83.3% \pm 5.5%	93.5% \pm 1.9%
AND $R_{\text{pt}} < 0.05$	83.3% \pm 5.5%	90.6% \pm 2.4%
AND $N_{\text{tr}}^{\text{match}} > 0$	72.7% \pm 7.0%	90.6% \pm 2.4%

Table 6.6: Effect of the recovery conditions (6.3) for Drell-Yan events with mass $> 200 \text{ GeV}/c^2$ and for Z' bosons with mass $= 1 \text{ TeV}/c^2$, with two (real) electrons generated with $p_t > 80 \text{ GeV}/c$ and $|\eta| < 2.4$, when one of the electrons is emitted in the EB-EE gap direction and does not pass the minimum electron identification conditions (6.2). The errors are the statistical errors for a luminosity of 1.9 fb^{-1} for Drell-Yan events and 19.2 fb^{-1} for Z' production.

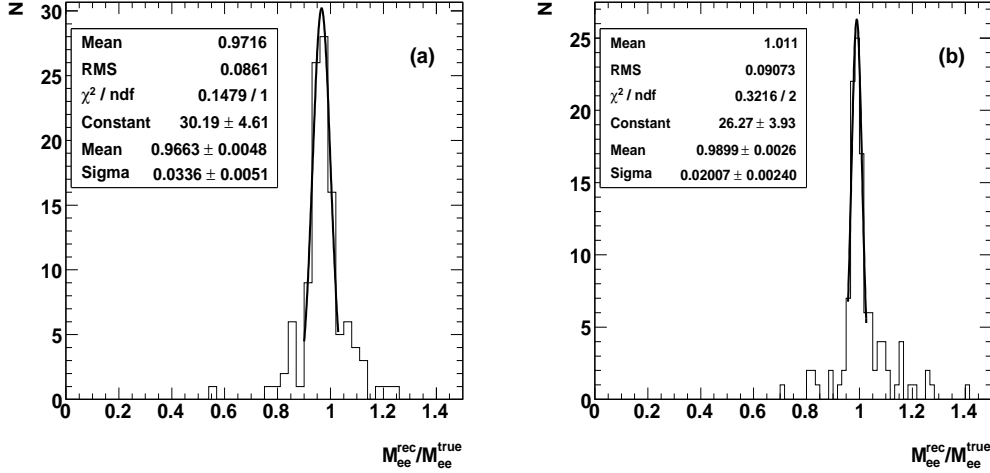


Figure 6.15: Distribution of the ratio of the reconstructed M_{ee} over generated $M_{\gamma/Z}$ mass for e^+e^- events with both electrons emitted in the angular domain $|\eta| < 2.4$, when one of the electrons is emitted in the EB-EE gap direction and does not pass the minimum electron identification conditions (6.2), and which are recovered following the criteria (6.3): (a) Drell-Yan events with generated mass larger than $200 \text{ GeV}/c^2$; (b) Z' bosons with mass of $1 \text{ TeV}/c^2$ [52].

Figure 6.15 presents the resolution of the reconstructed $M_{e^+e^-}$ mass for Drell-Yan events and for $1 \text{ TeV}/c^2$ resonances, after the recovery procedure (6.3). The distributions peak slightly below the generated values (cf. figure 6.8), with rms of 9% for Drell-Yan while for Z' bosons the resolution in the peak region of 2%.

6.6 Backgrounds

6.6.1 QCD jet background

The background to genuine electron pair events due to the recovery procedure discussed above has been studied using the QCD jet samples listed in Table 6.7, which correspond to different \hat{p}_t jet scales. The Table gives, for each sample, the integrated luminosity used for this analysis, the corresponding number of generated events, and the number of events containing at least one electron candidate passing the HEEP identification criteria, which are given in Table 5.9. In the generated samples containing 8540 kevents, 1708 events are thus selected, which are heavily dominated by the two lowest \hat{p}_t bins. None of these events contains a second electron candidate emitted toward the gap region and which passes the recovery cuts (6.3).

6.6.2 W+jet background

The W+jet background is presented in Table 6.8. The cross sections corresponding to the quoted luminosities and numbers of events are for W bosons decaying into an electron and a neutrino. They are much smaller than for QCD multijet events, but very large fractions of the generated events contain an electron passing the HEEP criteria (5.9).

\hat{p}_t (GeV/c)	int. lumi (pb ⁻¹)	nb. gen. (kevents)	nb. with 1 HEEP el. cand. passing (5.9)	nb. with a 2d el. cand. passing (6.3)	for 1 fb ⁻¹
80-120	0.362	1113	33	0	0
120-170	1.98	977	121	0	0
170-230	8.03	802	91	0	0
230-300	25.3	620	124	0	0
300-380	201	1256	263	0	0
380-470	613	1090	306	0	0
470-600	1.93×10^3	1318	434	0	0
600-800	3.03×10^3	611	154	0	0
800-1000	21.4×10^3	743	182	0	0

Table 6.7: QCD jet background to the gap recovery procedure: \hat{p}_t scale range, integrated luminosity, number of generated events, number of events containing an electron candidate passing the HEEP identification criteria (5.9), number of events containing in addition an electron candidate passing the recovery cuts (6.3), corresponding number of di-electron events for 1 fb⁻¹.

\hat{p}_t (GeV/c)	int. lumi (pb ⁻¹)	nb. gen. (kevents)	nb. with 1 HEEP el. cand. passing (5.9)	nb. with a 2d el. cand. passing (6.3)	for 1 fb ⁻¹
80-120	85.2	20.3	3189	0	0
120-170	365	25.8	7322	1	2.70
170-230	1.32×10^3	26.9	10000	1	0.75
230-300	4.66×10^3	29.0	13109	2	0.43
300-380	13.7×10^3	28.3	14317	0	0
380-470	40.5×10^3	28.8	15524	3	0.07
470-600	95.5×10^3	28.0	16379	0	0

Table 6.8: Same as Table 6.7, but for W+jet jet background (the quoted luminosities and numbers of events are for W bosons decaying into an electron and a neutrino).

From a total of 187k generated events, about 80k events are thus selected. The background of events with a second electron passing the recovery cuts (6.3) is of 7 in total, which amounts to $4.0 \text{ events for } 1 \text{ fb}^{-1}$. When in addition the charges of the two electron candidates are required to be opposite, 3 events survive, corresponding to $1.2 \text{ events for } 1 \text{ fb}^{-1}$.

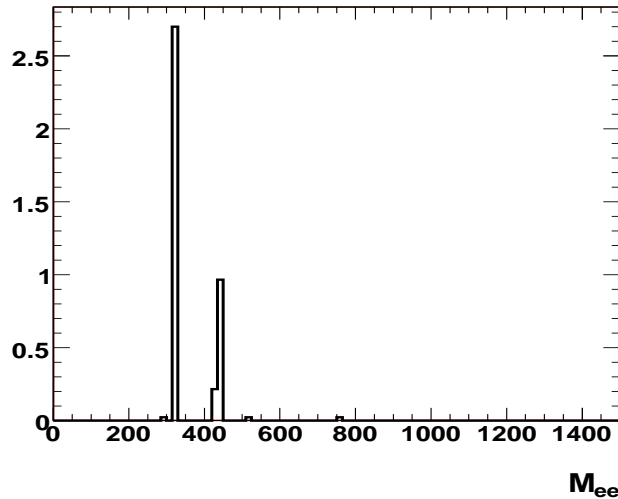


Figure 6.16: Mass distribution of QCD and W+jet background for an integrated luminosity of 1 fb^{-1} , when one of the fake electrons is emitted toward the gap region, and which are passing the criteria (6.3).

6.7 Electron recovery in case of a missing ECAL endcap at start-up

In addition to the work done in this chapter, similar analysis has been done to use the hadronic calorimeter (HCAL) to recover electrons emitted in the direction of a missing ECAL endcap. Since one year ago, there was a possibility that, at start-up, one of the ECAL endcaps will not be installed, for this reason the analysis done in Appendix B was urgently needed. On 19 September 2008 during powering tests of the main dipole circuit, an electrical fault in the bus between magnets caused a rupture and a leak of six tonnes of liquid helium. The operation was then delayed for several months allowing the installation of the missed ECAL endcap.

Chapter 7

Calibration of CMS ECAL crystals for high p_t electrons

The CMS electromagnetic calorimeter ECAL (defined in section 3.3) has been designed such that electromagnetic showers initiated by high energy electrons or photons, including most of Bremsstrahlung emission effects, are essentially contained in matrices of 5×5 PbWO_4 crystals (see section 4.1), both in the ECAL barrel (EB) and endcaps (EE). Due to this containment, the energy deposit E_1 in the central crystal of a 5×5 matrix can be measured with good precision from the energy deposit distribution in the surrounding crystals. This can be used to check the energy calibration, to validate electron measurements.

As shown in section 7.1, the energy deposit E_1 depends on the total energy deposit in the 5×5 matrix, E_{25} , and on the location of the electron impact point on the inner face of the central crystal. Two variables, X and Y , related to the impact position are introduced, taking into account the ECAL geometry.

The discussion in section 7.2 shows that it is possible to parameterise with good precision the energy ratio E_1/E_{25} in the form of functions $F(X, Y; E, \eta)$, which have only a small dependence in the incident electron energy and η . The energy E_1 can thus be reconstructed using the deposits in the surrounding 24 crystals, with the help of these normalised energy functions.

Section 7.3 shows how this feature can be exploited to validate the extrapolation to high energy of the ECAL calibration performed in test beams [41,42]. The expected precision achieved using electrons from high mass Drell-Yan events for integrated luminosities of 100 pb^{-1} at 10 TeV is presented.

Conversely, the difference between the measured and the reconstructed energies in the central crystal of a high energy electromagnetic shower provides a new shower shape related variable, useful to validate samples of high energy electrons in potentially interesting events, e.g. for new physics search. The relevant informations are presented in section 7.4.

7.1 Distribution of the E_1/E_{25} energy ratio

7.1.1 Simulation of energy deposits

The methods discussed in this section rely on the parameterisation of the energy deposit distributions in the ECAL by high energy electromagnetic showers. They are obtained from Monte Carlo simulations of “single gun” electrons or positrons with fixed energy (500, 1000, 1500, 2000, 2500, 3500 and 4500 GeV) and no additional particle pile-up. Electrons are generated uniformly in η (outside the EB-EE crack region with $1.44 < |\eta| < 1.56$) and in ϕ , the position of the emission point being distributed along the beam direction according to a Gaussian law centred at the nominal interaction point (IP) with the expected width of 53 mm. The full detector is simulated, including the η dependent amount of material in front of the ECAL. The simulations were performed using the CMSSW software [34], version 1.6.11.

The energy collected in a 5×5 matrix, E_{25} , can differ from the true, generated electron energy, E_{true} , for a variety of reasons, in particular Bremsstrahlung emission, energy deposit in the material in front of the ECAL, energy leakage to the HCAL at high energy [47] and losses in η and ϕ cracks between ECAL modules and supermodules, which have been presented in chapter 6. These effects are globally small. They are not corrected for in the following, since the goal of the present work is the study of the reconstruction of the energy deposit in the hottest crystal, E_1 , from the energy deposits in the surrounding 24 crystals, leaving to other studies the question of the reconstruction of E_{true} from electromagnetic cluster measurements.

7.1.2 X and Y variables

The E_1/E_{25} energy fraction has only a small dependence on the incident electron energy, but it depends strongly on the location of the electron impact point on the inner face of the central crystal: the ratio is largest for central impacts, and it decreases as the impact point comes closer to the crystal border. This effect is quantified with the help of two variables, X and Y , defined separately for EB and EE. Each of these variables is obtained from the ratio of the total energy deposit in the 10 crystals situated on one side of the hottest crystal, to the energy deposit in the 10 crystals situated on the other side, as illustrated in figure 7.1 for the EB case.

The ECAL crystals, both in EB and EE, are disposed such that they are nearly pointing to the nominal IP, which ensures shower containment in square matrices. They are not exactly pointing, however, in order to avoid particle loss in cracks. As a consequence, asymmetries appear in the lateral energy distributions, even for central impacts. This is illustrated in figure 3.7 (see section 3.3.2), figuring EB crystal off-pointing in η . As will be seen, off-pointing creates asymmetries in the X and Y distributions.

7.1.3 Barrel

In EB, the crystals are placed such that their lateral faces have constant values of η and ϕ , respectively, and the 5×5 matrices thus contain five rows of 5 crystals with fixed η values and five rows of 5 crystals with fixed ϕ

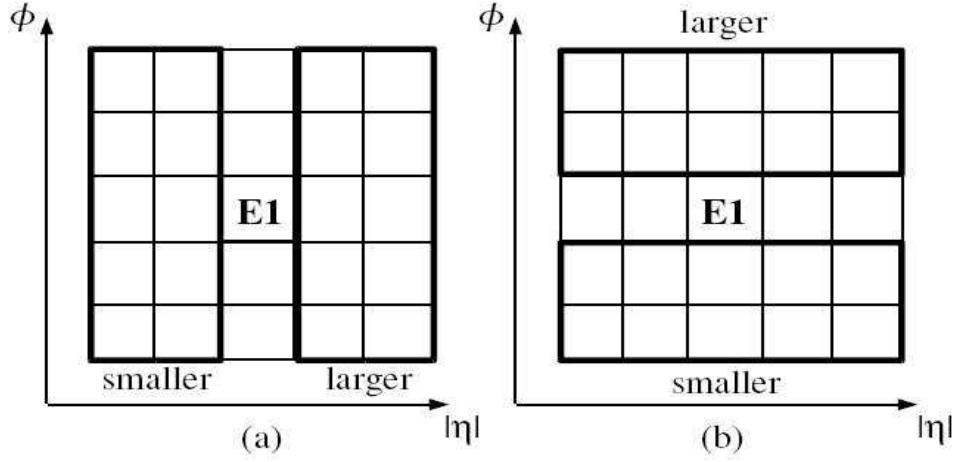


Figure 7.1: Contributions of crystals from a 5×5 (η, ϕ) matrix to the quantities (a) $\Sigma E_{\text{smaller } |\eta|}$ and $\Sigma E_{\text{larger } |\eta|}$, for the X variable; (b) $\Sigma E_{\text{smaller } \phi}$ and $\Sigma E_{\text{larger } \phi}$, for the Y variable.

values. The X and Y variables in EB are defined with respect to η and ϕ :

$$X = \ln \left(\frac{\Sigma E_{\text{larger } |\eta|}}{\Sigma E_{\text{smaller } |\eta|}} \right), \quad (7.1)$$

where the sums run over the energy deposits in the 10 crystals of the 5×5 matrix with larger (resp. smaller) absolute values of the pseudorapidity η than the central crystal;

$$Y = (\eta/|\eta|) \ln \left(\frac{\Sigma E_{\text{larger } \phi}}{\Sigma E_{\text{smaller } \phi}} \right) \quad (7.2)$$

where the sums run over the energy deposits in the 10 crystals with larger (resp. smaller) ϕ values than the central crystal; the ± 1 factor in front of the log ensures that the Y distributions are the same for the two half-barrels, given the symmetry in the construction.

In EB, crystals are off-pointing by 3° , both in θ and ϕ (see Figure 3.7, which is explained in section 3.3.2). The ensuing difference between the axes of the crystals and of the electromagnetic shower induces a skewing of the X and Y distributions. The definitions of eqs. (7.1) and (7.2) are chosen such that they are skewed to positive values.

In EB, on the average $\approx 63\%$ of the energy deposit in a 5×5 matrix is contained in the hottest crystal; the E_1/E_{25} energy ratio increases to $\approx 81\%$ for central impacts with $|X|$ and $|Y| \simeq 0$. The correlation between the energy deposits and the variables X and Y is illustrated in figure 7.2, which presents the ratio E_1/E_{25} as a function of X (resp. Y) for two slices in the variable Y (resp. X). The E_1/E_{25} fraction remains high for energy deposit asymmetries up to factors of $\approx 3 - 5$ ($|X|$ or $|Y| \lesssim 1 - 1.5$), and then decreases rapidly with increasing $|X|$ or $|Y|$. The lowest values of the energy ratio are fixed, by construction, from the fact that it is the hottest crystal of a matrix which defines E_1 .

The energy ratio E_1/E_{25} for 1500 GeV electrons is presented in figure 7.3 as a function of X (resp. Y),

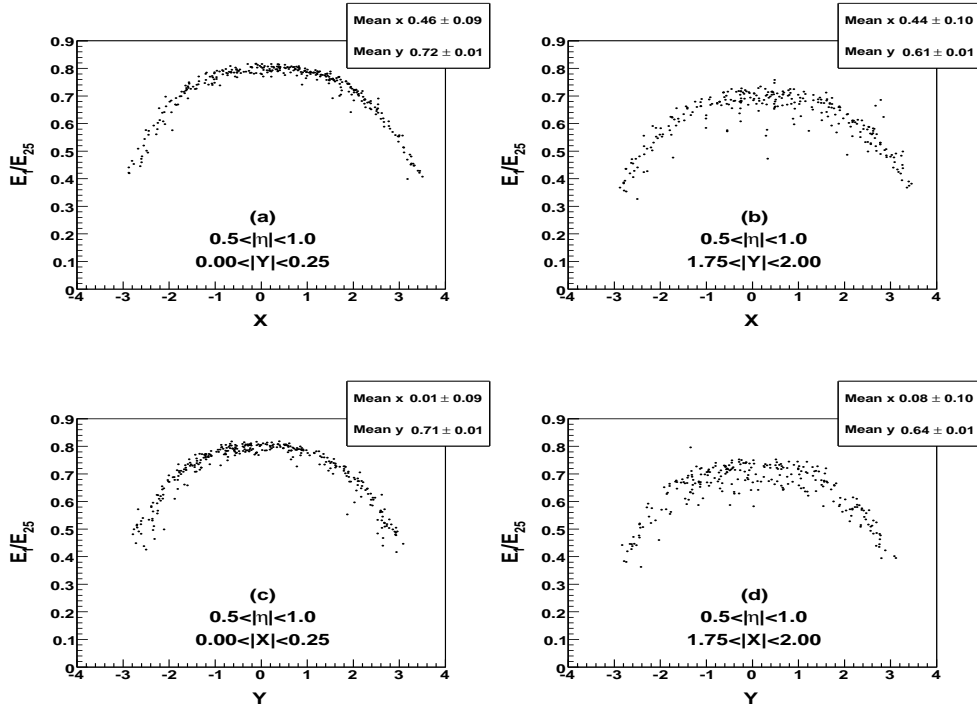


Figure 7.2: Energy ratio E_1/E_{25} for 1500 GeV incident electrons with $0.5 < |\eta| < 1.0$ (EB), plotted as a function of the variable X for (a) $0 < |Y| < 0.25$ and (b) $1.75 < |Y| < 2.00$, and as a function of the variable Y for (c) $0 < |X| < 0.25$ and (d) $1.75 < |X| < 2.00$ [48].

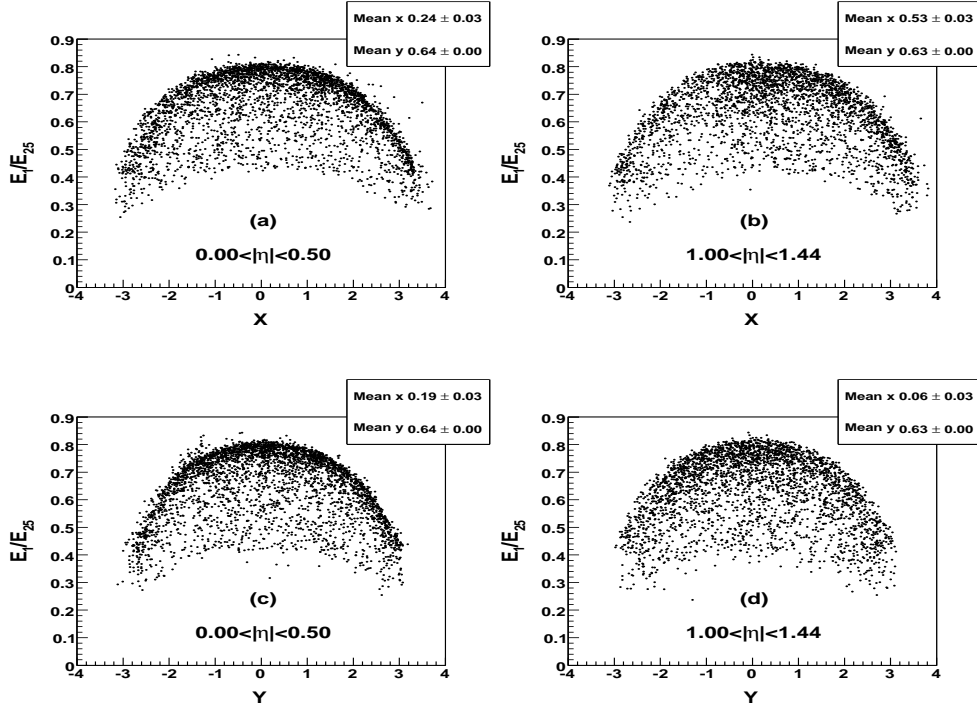


Figure 7.3: Energy ratio E_1/E_{25} for 1500 GeV incident electrons in EB, plotted as a function of the variables X and Y for (a, c) $|\eta| < 0.5$ and (b, d) $1.00 < |\eta| < 1.44$ [48].

integrated over all values of Y (resp. X), for two η ranges in EB: $|\eta| < 0.5$ and $1.00 < |\eta| < 1.44$. A strong skewing of the X distributions is observed, which increases with $|\eta|$, with $\langle X \rangle$ passing from ≈ 0.24 for $|\eta| < 0.5$ to ≈ 0.53 for $1.00 < |\eta| < 1.44$ (see figure 7.3a-b). The distribution of the emission vertex along the beam direction tends to slightly decrease this skewing (a decrease of ≈ 0.05 of $\langle X \rangle$), whereas the magnetic field tends to increase the skewing. The skewing of the Y distributions is smaller, and decreases with increasing $|\eta|$. For energies of 500 GeV and above, the difference in the skewing of the X and Y distributions for electrons and positrons is small. No significant energy dependence of the skewing is observed.

7.1.4 Endcaps

In the endcaps, the crystals are placed along a square grid, with horizontal (x direction) and vertical (y direction) axes (see figure 3.9 in section 3.3.3). They are pointing to a point situated 1.3 m beyond the nominal IP.

The following definitions are used for X and Y :

$$X = \ln \left(\frac{\sum E_{\text{smaller } |x|}}{\sum E_{\text{larger } |x|}} \right), \quad (7.3)$$

$$Y = \ln \left(\frac{\sum E_{\text{smaller } |y|}}{\sum E_{\text{larger } |y|}} \right), \quad (7.4)$$

where the sums run over the energy deposits in the 10 crystals of the 5×5 matrix with smaller or larger absolute values of the x (resp. y) coordinate than the central crystal. With these definitions the X and Y variables are skewed to positive values by the off-pointing effects.

Distributions of the energy ratio E_1/E_{25} are presented in figures 7.4 and 7.5 as a function of X and Y for 2500 GeV electrons. The general features are similar to EB. The average value of $E_1/E_{25} \approx 67\%$ and the maximum value $\approx 84\%$, which is larger than for EB because of the larger crystal size in EE. The skewing is similar for the X and Y variables, in view of the symmetric role of the x and y coordinates. It decreases with increasing $|\eta|$ (i.e. from outer to inner EE), because of the η dependence of the off-pointing angle.

7.2 Parameterisation of the E_1/E_{25} distributions and E_1 reconstruction

7.2.1 $F(X, Y; E, \eta)$ functions

A parameterisation of the distribution of the energy fraction E_1/E_{25} , as a function of the variables X and Y , has been proposed in [47]:

$$F(X, Y; E, \eta) = \langle E_1/E_{25}(X, Y; E, \eta) \rangle = a \cdot (1 + bX + cX^2) \cdot e^{dX + eX^2} \cdot (1 + fY + gY^2) \cdot e^{hY + iY^2}. \quad (7.5)$$

The decrease of the fractional energy deposit with increasing $|X|$ or $|Y|$ is described through the quadratic terms in the polynomial and the exponential factors, and the off-pointing effects through the linear terms. This could be seen in the plots shown in Figure 7.6 for different choices of the one dimensional function as an example; where plot (a) shows the effect of the quadratic term in the polynomial, which explains the decrease

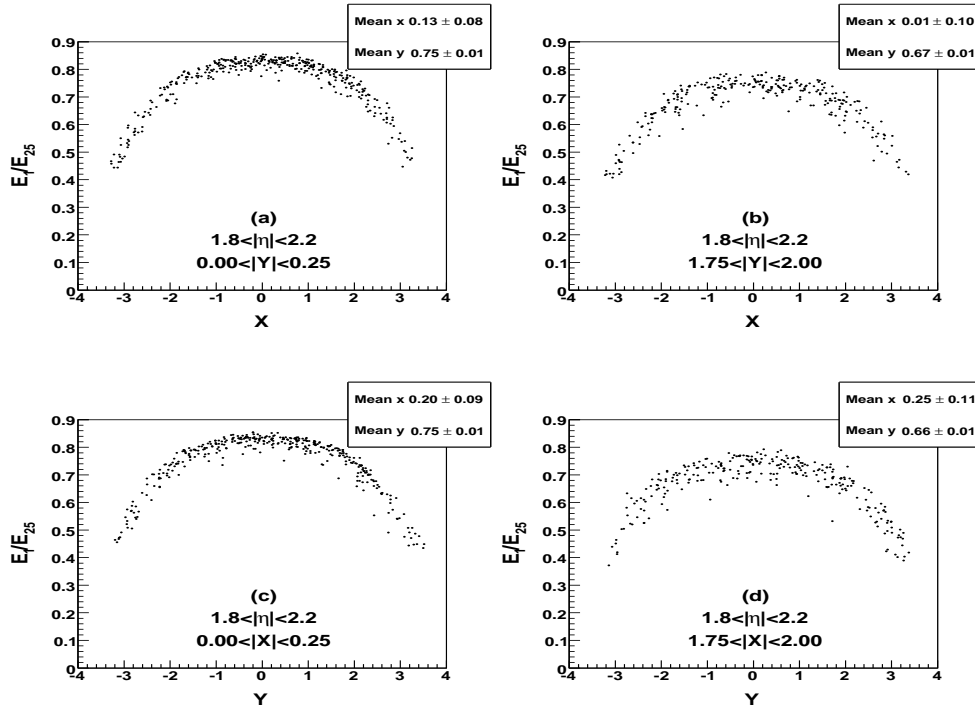


Figure 7.4: Energy ratio E_1/E_{25} for 2500 GeV incident electrons with $1.8 < |\eta| < 2.2$ (EE), plotted as a function of the variable X for (a) $0 < |Y| < 0.25$ and (b) $1.75 < |Y| < 2.00$, and as a function of the variable Y for (c) $0 < |X| < 0.25$ and (d) $1.75 < |X| < 2.00$ [48].

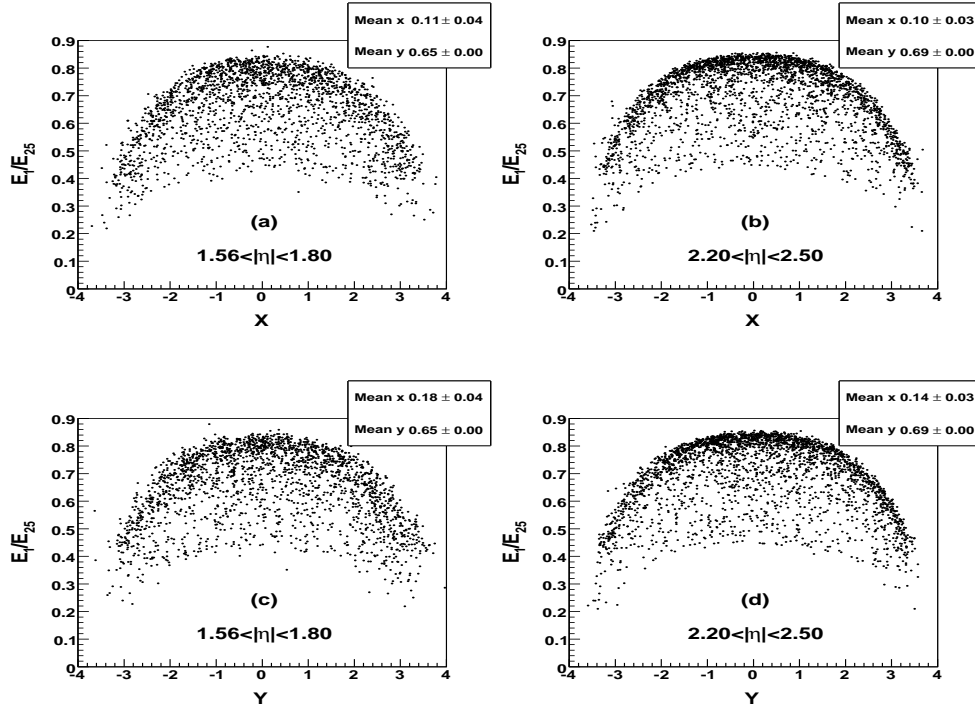


Figure 7.5: Energy ratio E_1/E_{25} for 2500 GeV incident electrons in EE, plotted as a function of the variables X and Y for (a, c) $1.56 < |\eta| < 1.8$ and (b, d) $2.2 < |\eta| < 2.5$ [48].

of the fractional energy deposit with increasing $|X|$ or $|Y|$, while by adding the linear term in the polynomial and the exponential factors one can describe well the off-pointing effect as seen in plot (b and c); finally it was needed to add also a quadratic terms in the exponential factors to explain the flatness seen in Figure 7.2 (a). The parameter values may a priori depend on the incident energy and on the pseudorapidity η . To determine

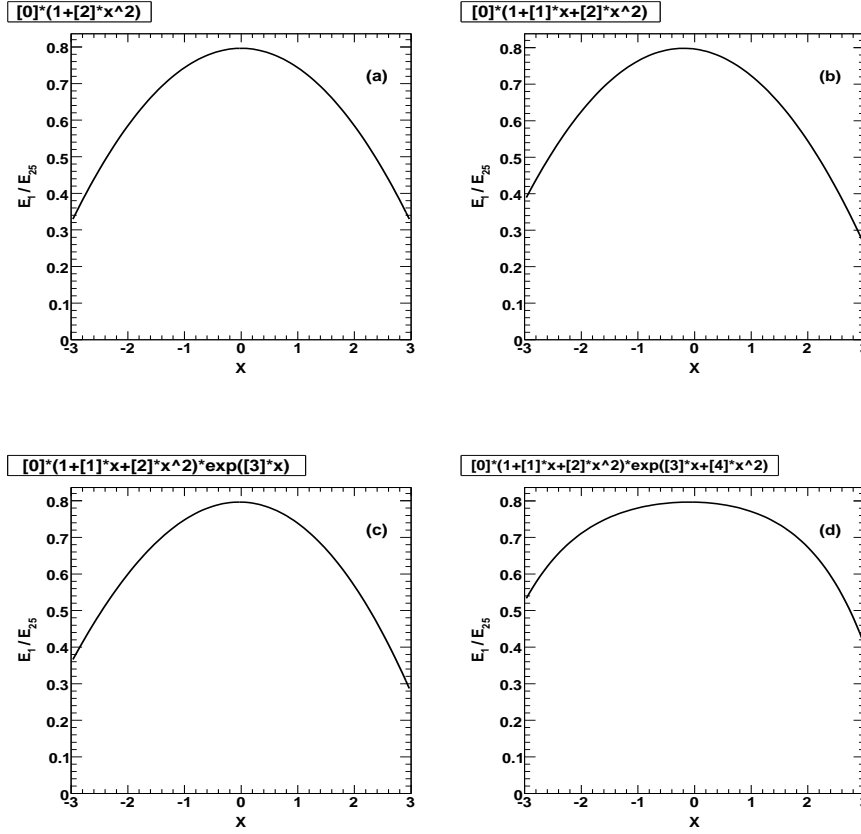


Figure 7.6: Different choices of the one dimensional fit function; (a) $a \cdot (1 + cX^2)$, (b) $a \cdot (1 + bX + cX^2)$, (c) $a \cdot (1 + bX + cX^2) \cdot e^{dX}$ and (d) $a \cdot (1 + bX + cX^2) \cdot e^{dX+eX^2}$.

the function F , the average value $\langle E_1/E_{25} \rangle$ in each $|X|$ and $|Y|$ bin is used.

Examples of parameter values, fitted over the range $|X|, |Y| < 3$, are presented in Table 7.1 for 1500 GeV electrons and two $|\eta|$ ranges in EB and EE, respectively. The parameter a characterises the highest energy ratio E_1/E_{25} , for $X = Y = 0$. Pairs of parameters ($b - d, c - e, f - h, g - i$) are strongly anti-correlated.

The corresponding functions are shown in figure 7.7a,c. The residuals, defined as the relative difference between the original distribution and the fit function, $1 - [F(X, Y; E, \eta) / \langle E_1/E_{25} \rangle]$, are shown in figure 7.7b,d. They are small, $\lesssim 2\%$ over most of the X, Y range, with larger fluctuations at the edges. The good behaviour of the residuals demonstrates that the parameterisation of eq. (7.5) gives a good functional description of energy ratio. The relevance of this functional form was verified for different electron energies, from 500 to 4500 GeV, for three bins in $|\eta|$ in EB and three bins in EE.

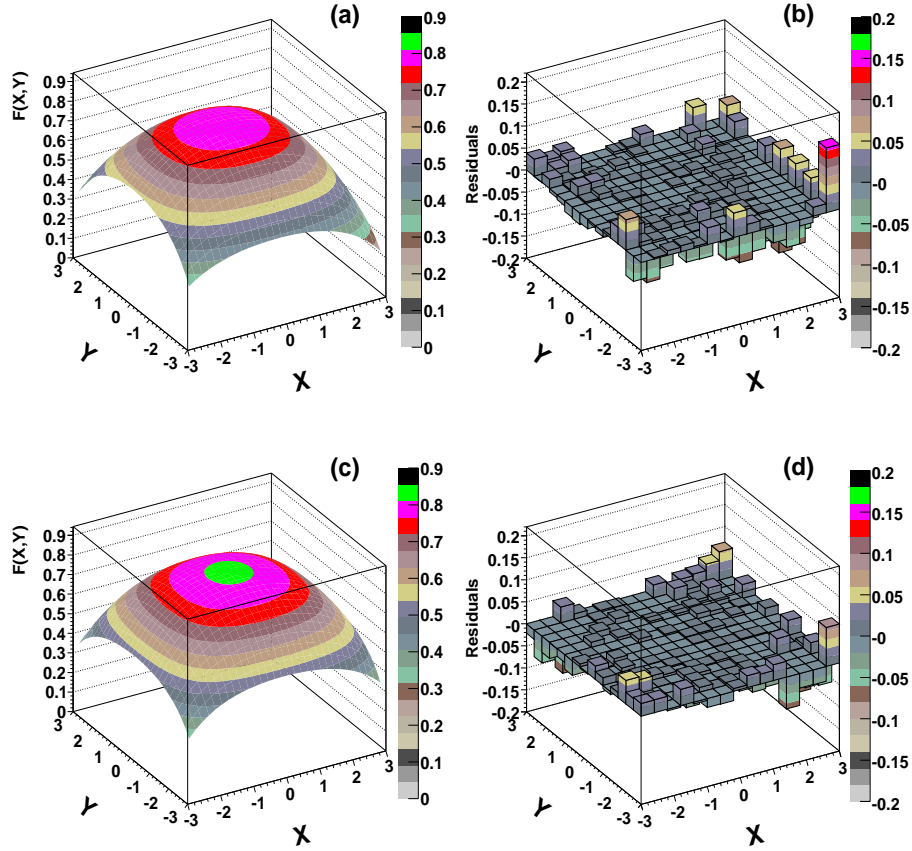


Figure 7.7: (left) Fitted functions $F(X, Y; E, \eta)$ for 1500 GeV electrons and corresponding distributions of the residuals $1 - [F(X, Y; E, \eta) / \langle E_1/E_{25} \rangle]$ for EB with $0.5 < |\eta| < 1.0$ (a-b) and for EE with $1.8 < |\eta| < 2.2$ (c-d) [48].

E	η range	a	b	c	d	e	f	g	h	i
1500	0.5 – 1.0	0.8069	-0.0231	-0.0649	0.0183	0.0423	0.0097	-0.0733	-0.0066	0.0447
1500	1.8 – 2.2	0.8419	-0.0109	-0.0584	0.0135	0.0343	0.0099	-0.0575	-0.0108	0.0331

Table 7.1: Fit parameters of the $F(X, Y; E, \eta)$ functions given by eq. (7.5), for 1500 GeV fixed energy “single gun” electrons in the $|\eta|$ ranges $0.5 < |\eta| < 1.0$ (EB) and $1.8 < |\eta| < 2.2$ (EE).

7.2.2 Energy and η dependences of the $F(X, Y; E, \eta)$ functions

Sets of parameters for the functions $F(X, Y; E, \eta)$ are computed from the energy deposit distributions in the 5×5 matrices, using E_1 , E_{25} and the X and Y variables. This is done separately for $|\eta|$ values in the ranges $0 - 0.5 - 1.0 - 1.44$ (EB) and $1.56 - 1.8 - 2.2 - 2.5$ (EE) and for various “single gun” electron samples with energy from 500 to 4500 GeV.

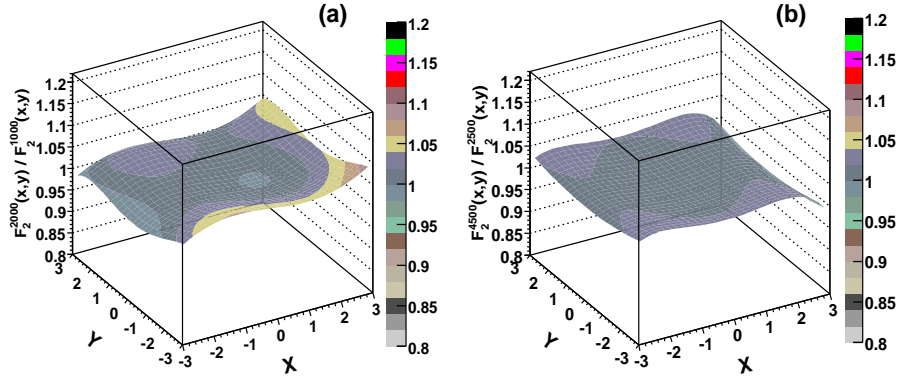


Figure 7.8: Ratio of fitted functions $F(X, Y; E, \eta)$ (a) for 2000 GeV electrons to 1000 GeV electrons, in the η range $0.5 < |\eta| < 1.0$ (EB); (b) for 4500 GeV electrons to 2500 GeV electrons, in the η range $1.8 < |\eta| < 1.2$ (EE) [48].

The $F(X, Y; E, \eta)$ functions show only a small dependence on the electron energy, $< 2\%$ over most of the X, Y range. This is illustrated in figure 7.8, which presents ratios of the functions $F(X, Y; E, \eta)$ fitted in the same $|\eta|$ ranges for two different initial electron energies. This approximate scaling allows extracting with good precision a first estimate of E_1 . An even better estimate can be obtained in a second iteration, using the function $F(X, Y; E, \eta)$ corresponding to the first estimate.

The η dependence of the $F(X, Y; E, \eta)$ functions is illustrated in figure 7.9, which presents ratios of the functions fitted for two different $|\eta|$ ranges, for fixed 1500 GeV electrons in EB and for 3500 GeV electrons in EE. Only small differences, below 3 – 5% over most of the X, Y range are observed. In EB, they reflect the η dependence of the skewing of the X distribution, whereas no significant η dependence is observed in Y . In EE, the decrease of the off-pointing angle with increasing η explains the behaviour of the ratio, which slightly exceeds 1.1 for large negative values of X and Y .

Figure 7.10 shows that the $F(X, Y; E, \eta)$ functions for 1500 GeV electrons and positrons are within 2% over most of the X, Y domain.

7.2.3 Reconstruction of E_1 using the $F(X, Y; E, \eta)$ functions

E_1^{rec} is the reconstructed energy in the central crystal of a 5×5 matrix, obtained from the energy deposits in the 24 surrounding crystals using the $F(X, Y; E, \eta)$ functions. E_1^{rec} is defined in equ. C.2 (see Appendix C).

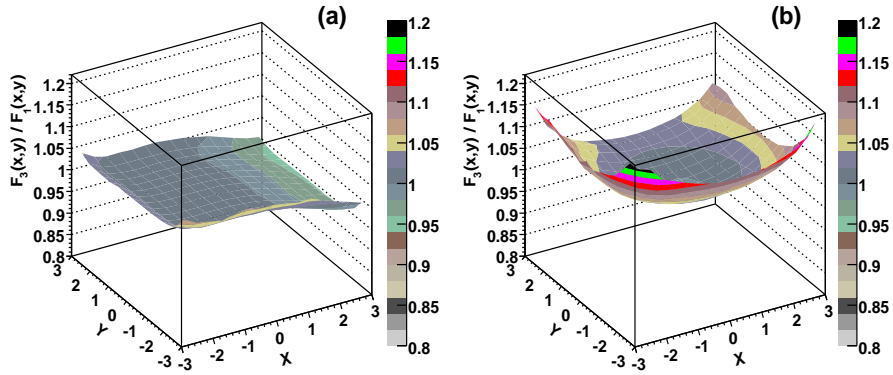


Figure 7.9: Ratio of fitted functions $F(X, Y; E, \eta)$ (a) in EB, for the η range $1.0 < |\eta| < 1.4$ to the η range $|\eta| < 0.5$, for 1500 GeV electrons; (b) in EE, for the η range $2.2 < |\eta| < 2.5$ to the η range $1.56 < |\eta| < 1.8$, for 3500 GeV electrons [48].

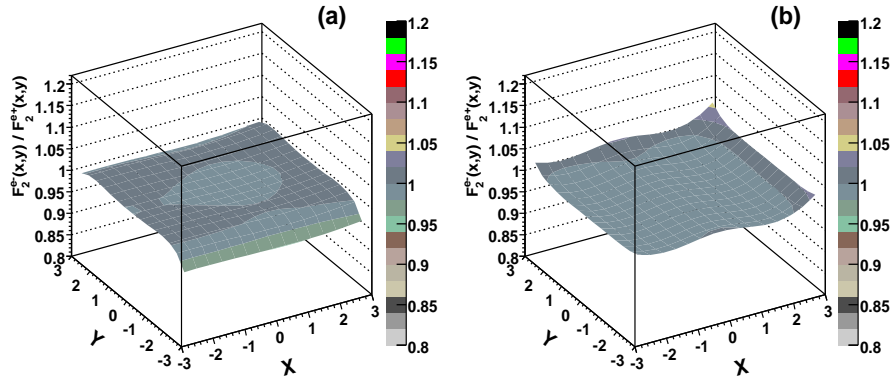


Figure 7.10: Ratio of the fitted functions $F(X, Y; E, \eta)$ for 1500 GeV electrons to 1500 GeV positrons, (a) for $0.5 < |\eta| < 1.0$ (EB); (b) for $1.8 < |\eta| < 1.2$ (EE) [48].

The quality of the reconstruction for a given energy and η range is quantified through the distribution of the normalised difference $(E_1^{\text{meas}} - E_1^{\text{rec}})/\langle E_1^{\text{meas}} \rangle$, E_1^{meas} being the measured energy deposit.

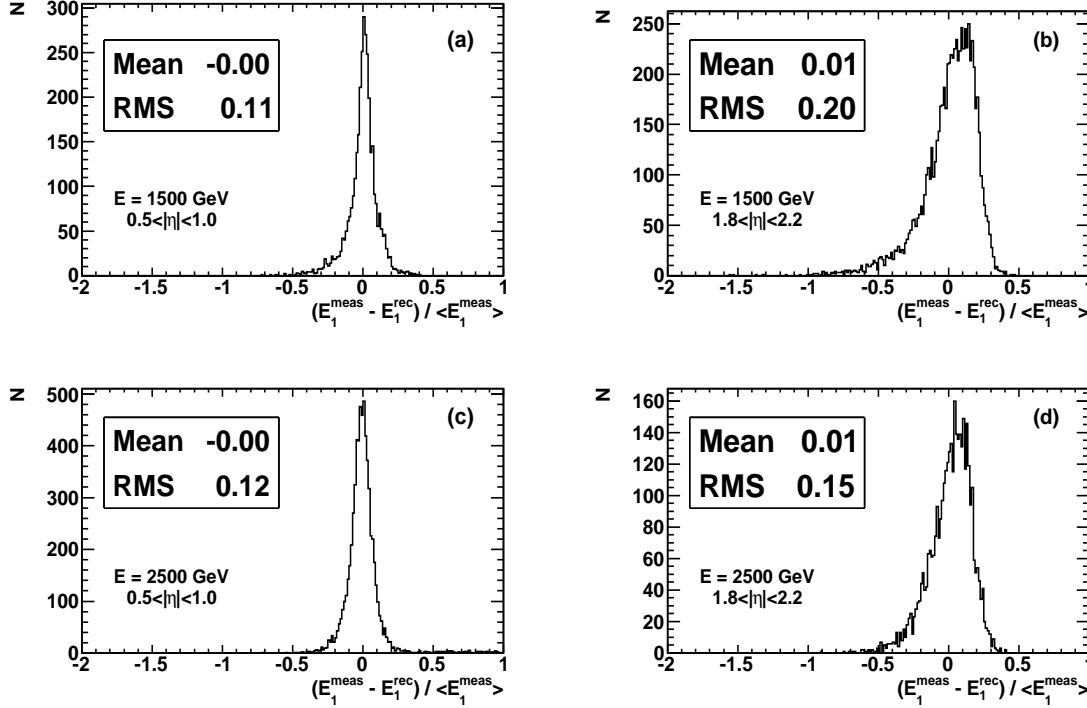


Figure 7.11: Distributions of the normalised difference $(E_1^{\text{meas}} - E_1^{\text{rec}})/\langle E_1^{\text{meas}} \rangle$, for 1500 GeV electrons with $0.5 < |\eta| < 1.0$ (EB) and $1.8 < |\eta| < 2.2$ (EE) (a-b), and for 2500 GeV electrons (c-d) [48]. The errors on the average difference are less than 0.002.

Figure 7.11 presents, for two electron energies and two $|\eta|$ ranges, the distribution of the normalised difference. The average values of the distributions are close to 0, indicating that, as expected, $\langle E_1^{\text{rec}} \rangle \simeq \langle E_1^{\text{meas}} \rangle$. However, small off-sets of the averages from 0 are observed. They are due to the spread, for a given value of the parameters X and Y , of the E_1/E_{25} ratios, due to shower to shower fluctuations (see Appendix C). The offset is larger for small p_t electrons, where Bremsstrahlung emission increases the spread of values of E_1/E_{25} . The asymmetry observed in the distributions, which is energy and η dependent, is also due to effects of Bremsstrahlung emission, as will be discussed in the next section.

In Figure 7.12, the distributions of the normalised difference $(E_1^{\text{meas}} - E_1^{\text{rec}})/\langle E_1^{\text{meas}} \rangle$ are presented for (a-b-c-d-e-f-g) 500, 1000, 1500, 2000, 2500, 3500 and 4500 GeV electrons respectively, with $|\eta| < 1.44$ (EB), and similarly in Figure 7.13, for $1.56 < |\eta| < 2.50$ (EE). The mean values and RMS of these distributions are quoted in Table 7.2.

Table 7.2 presents the mean values and the RMS of the distributions, separately for EB and EE, using the $F(X, Y; E, \eta)$ functions for the relevant η values.

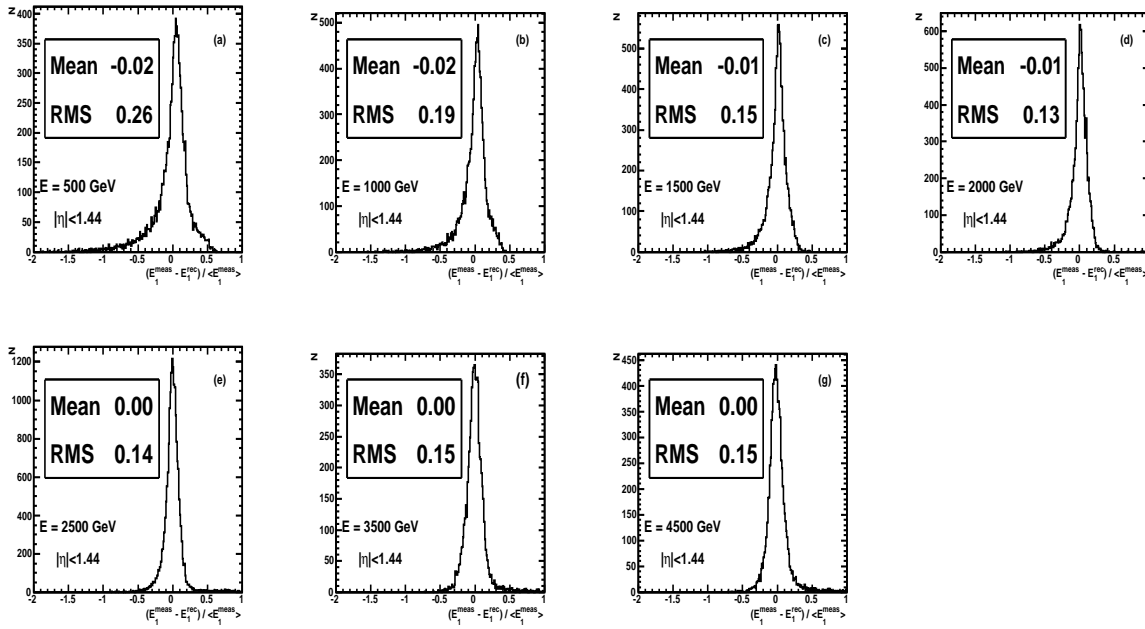


Figure 7.12: Distributions of the normalised difference $(E_1^{\text{meas}} - E_1^{\text{rec}}) / \langle E_1^{\text{meas}} \rangle$ for (a-b-c-d-e-f-g) 500, 1000, 1500, 2000, 2500, 3500 and 4500 GeV electrons with $|\eta| < 1.44$ (EB). The errors on the average difference are less than 0.003.

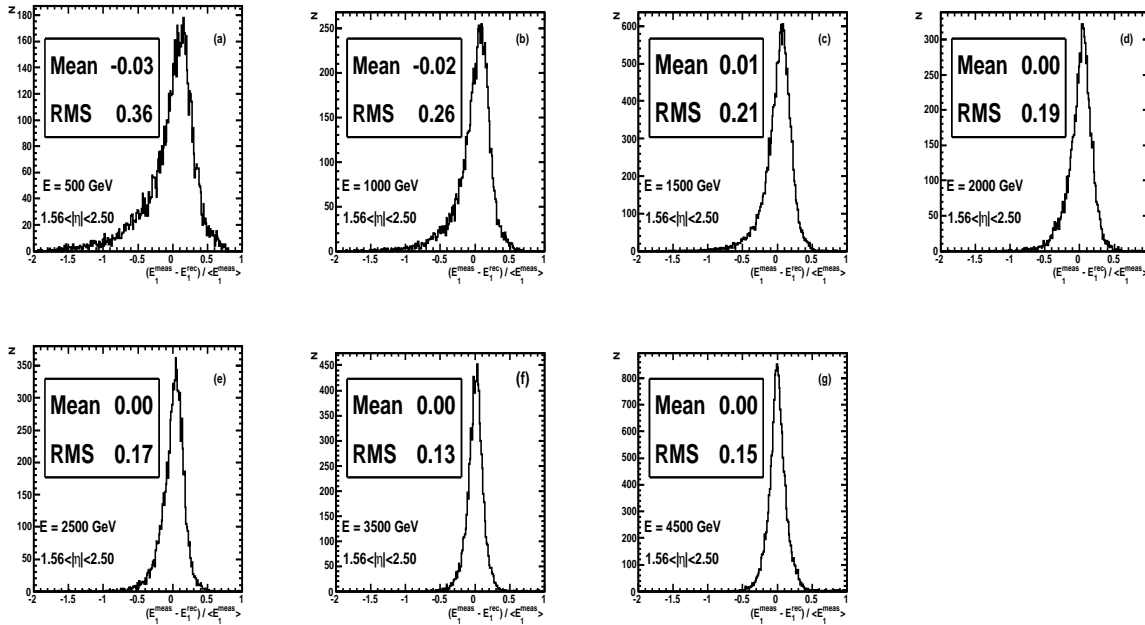


Figure 7.13: Distributions of the normalised difference $(E_1^{\text{meas}} - E_1^{\text{rec}}) / \langle E_1^{\text{meas}} \rangle$ for (a-b-c-d-e-f-g) 500, 1000, 1500, 2000, 2500, 3500 and 4500 GeV electrons with $1.56 < |\eta| < 2.50$ (EE). The errors on the average difference are less than 0.004.

E (GeV)	Barrel		Endcaps	
	mean	RMS	mean	RMS
500	-0.02	0.26	-0.03	0.36
1000	-0.02	0.19	-0.02	0.26
1500	-0.01	0.15	0.01	0.21
2000	-0.01	0.13	0.00	0.19
2500	0.00	0.14	0.00	0.17
3500	0.00	0.15	0.00	0.13
4500	0.00	0.15	0.00	0.15

Table 7.2: Mean values and RMS of the distribution of the normalised difference $(E_1^{\text{meas}} - E_1^{\text{rec}})/\langle E_1^{\text{meas}} \rangle$, for several electron energies and for EB and EE, respectively.

7.2.4 Effects of Bremsstrahlung emission

Figure 7.14 shows, for electrons with fixed energy of 500 GeV, the distribution of the normalised difference $(E_1^{\text{meas}} - E_1^{\text{rec}})/\langle E_1^{\text{meas}} \rangle$, for three EB and three EE $|\eta|$ bins. Both the width and the asymmetry of the distributions increase significantly with $|\eta|$ in EB, and they decrease in EE. This dependence reflects the amount of material in front of the ECAL, which is described by figure 4.9 (see section 4.4.3).

Bremsstrahlung emission at moderate energy distorts the distributions in the following way. In the present p_t range, the emitted photon and the electron usually hit the same crystal: as an extreme example, the distance on the crystal front face between the impact point of a straight line from the vertex and the impact of a 500 GeV electron with the same emission angles is 3 mm for $\eta = 1$ (EB, $p_t = 324$ GeV/c) and 7 mm for $\eta = 2$ (EE, $p_t = 132$ GeV/c), which is much less than a crystal width. The E_1/E_{25} ratio is thus not significantly modified by Bremsstrahlung emission, but the distribution of energy deposits among the 24 surrounding crystals in the 5×5 matrix is modified, since it results from the superposition of two laterally displaced showers. As a consequence, the variables X and Y are different from the case with no significant Bremsstrahlung emission. Random fluctuations from event to event due to Bremsstrahlung emission thus affect the correlation between the E_1/E_{25} energy ratio and the X and Y variables, and this effect is larger at lower electron p_t . This deterioration can be judged by comparing the distributions in pairs of $|\eta|$ bins at 500 GeV, shown in figure 7.15 for EB and EE, with the corresponding distributions in the intermediate $|\eta|$ bins at 1500 GeV, shown in figures 7.2c-d and 7.4c-d, respectively. The deterioration is largest in the region where the amount of tracker material in front of the ECAL is largest (figure 4.9 (right)).

The fitted $F(X, Y; E, \eta)$ functions thus describe correctly the average distributions of E_1/E_{25} , but the fluctuations imply a degradation of the resolution of the reconstructed energy, measured through the $(E_1^{\text{meas}} - E_1^{\text{rec}})/\langle E_1^{\text{meas}} \rangle$ variable. In addition, for fixed X and Y values, the distribution of the E_1/E_{25} energy ratio is asymmetric, with longer tails toward smaller values than for larger values. Since the $F(X, Y; E, \eta)$ functions are fitted to the average of E_1/E_{25} value, this implies more significant overestimates than underestimates in the reconstructed E_1 value. This results in the asymmetries towards negative values of the normalised difference

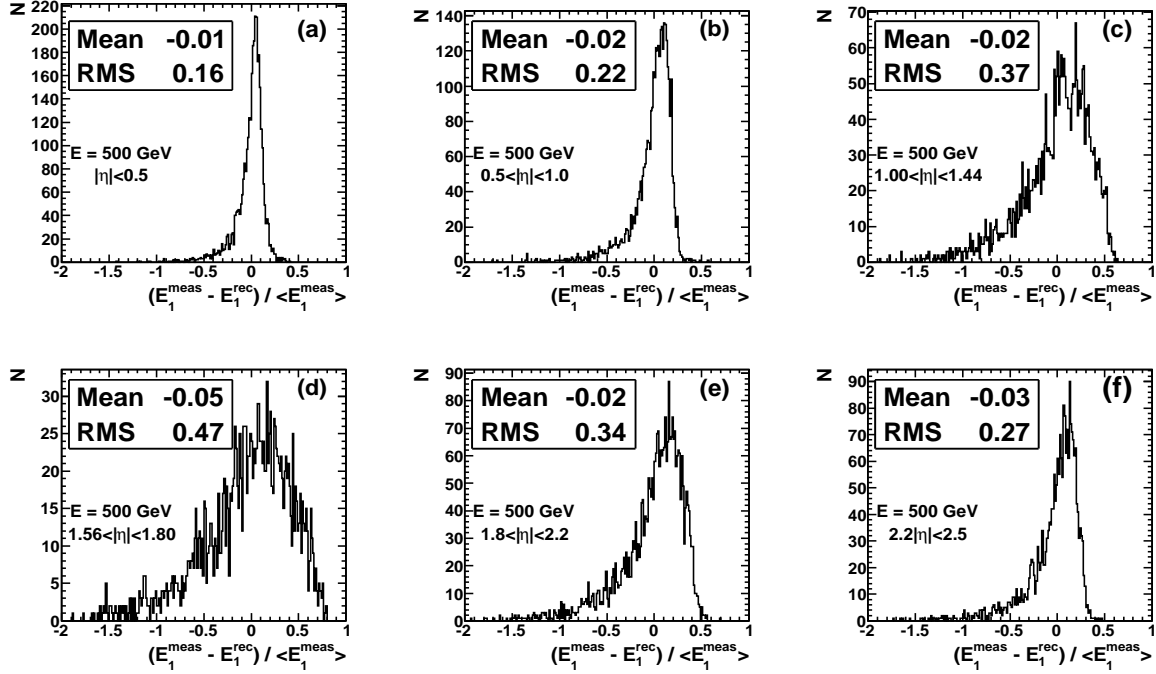


Figure 7.14: Distributions of the normalised difference $(E_1^{\text{meas}} - E_1^{\text{rec}})/\langle E_1^{\text{meas}} \rangle$ for 500 GeV electrons with (a) $|\eta| < 0.5$, (b) $0.5 < |\eta| < 1.0$, (c) $1.0 < |\eta| < 1.44$ (EB) and (d) $1.56 < |\eta| < 1.80$, (e) $1.8 < |\eta| < 2.2$, (f) $2.2 < |\eta| < 2.5$ (EE) [48]. The errors on the average difference are less than 0.01.

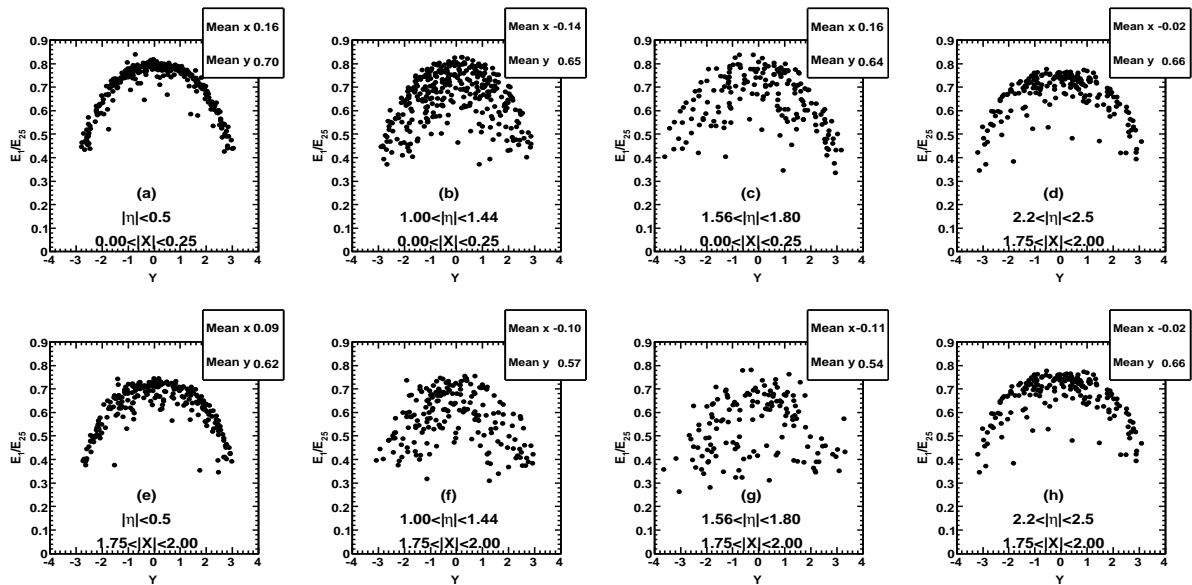


Figure 7.15: Energy ratio E_1/E_{25} for 500 GeV incident electrons, plotted as a function of the variable Y , for $0 < |X| < 0.25$ and (a) $|\eta| < 0.5$ (EB, $\langle p_t \rangle \simeq 470$ GeV/c); (b) $1.0 < |\eta| < 1.44$ (EB, $\langle p_t \rangle \simeq 260$ GeV/c); (c) $1.56 < |\eta| < 1.80$ (EB, $\langle p_t \rangle \simeq 170$ GeV/c); (d) $2.2 < |\eta| < 2.5$ (EB, $\langle p_t \rangle \simeq 90$ GeV/c); (e-h) idem, for $1.75 < |X| < 2.00$ [48].

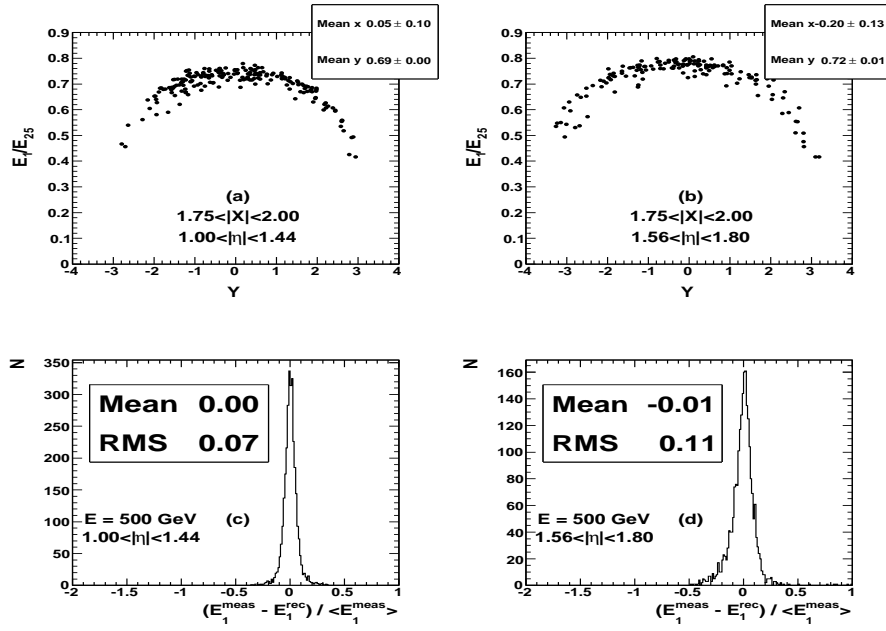


Figure 7.16: For 500 GeV incident electrons and no magnetic field: (a-b) energy ratio E_1/E_{25} plotted as a function of the variable Y for $1.75 < |X| < 2.00$, for $1.0 < |\eta| < 1.44$ and $1.56 < |\eta| < 1.8$, respectively; (c-d) distribution of the normalised difference $(E_1^{\text{meas}} - E_1^{\text{rec}})/\langle E_1^{\text{meas}} \rangle$ for electrons with $p_t > 80 \text{ GeV}/c$ and all values of X and Y , in the same $|\eta|$ bins [48]. The errors on the average difference are less than 0.002.

$(E_1^{\text{meas}} - E_1^{\text{rec}})/\langle E_1^{\text{meas}} \rangle$ observed e.g. in figure 7.14.

That this interpretation of the effect is correct was checked with “single gun” electron simulations with no magnetic field. This is illustrated in figure 7.16, which shows the strong correlation between the X , Y values and the E_1/E_{25} energy ratio in the absence of magnetic field (compare with figure 7.15f-g) and the resulting good and symmetric resolution (compare with figure 7.14c-d).

7.3 Validation of high energy crystal calibration

One of the important features of the CMS ECAL is the expected linearity of the crystal response to high energy electromagnetic showers. This is particularly important for the search of new high mass resonances. The linearity of the response has been checked with good precision in test beams up to electron energies of 300 GeV [41, 42]. Although this behaviour can be extrapolated with good confidence to higher energies, it is important to check it.

This can be achieved using the data themselves, following a method proposed in [7]. The principle is to compare the measurement of the energy deposit in the hottest crystal of a high energy shower, E_1^{meas} , with the value E_1^{rec} reconstructed from the surrounding 24 crystals in the 5×5 matrices, using the function $F(X, Y; E, \eta)$ corresponding to the measured energy and the relevant value of η . Quantitatively, the measured average of the normalised energy difference, $(E_1^{\text{meas}} - E_1^{\text{rec}})/\langle E_1^{\text{meas}} \rangle$ for a sample of selected electrons can be compared to the expected average. The error on the measured average is given by the RMS of the distribution

of the normalised difference, divided by the square root of the number of electrons in the sample, which is defined in this section as $\delta(\text{av.})$.

In practice, for energies above 300 GeV, electrons pairs from Drell-Yan sample can be used. Such electrons are selected with very small background using the HEEP criteria (given in Table 5.3), for pairs with invariant mass $M_{ee} > 120 \text{ GeV}/c^2$ and electron $p_t > 50 \text{ GeV}/c$. The reconstructed energy deposit E_1^{rec} in the central crystal is computed using the $F(X, Y; E, \eta)$ function, it has been checked that, within the present simulation precision, these functions describe the X and Y dependences of the energy deposit distribution in Drell-Yan events reasonably well. The distributions of the normalized difference $(E_1^{\text{meas}} - E_1^{\text{rec}})/\langle E_1^{\text{meas}} \rangle$ are shown in Figure 7.17; plots (a-c-e) represent electrons chosen in 3 energy bins, $300 \text{ GeV} < E_{5 \times 5} < 400 \text{ GeV}$, $400 \text{ GeV} < E_{5 \times 5} < 650 \text{ GeV}$ and $650 \text{ GeV} < E_{5 \times 5}$, with $0.00 < |\eta| < 1.44$ (EB); similarly are plots (b-d-f), with $1.56 < |\eta| < 2.50$ (EE).

		$300 < E < 400 \text{ GeV}$	$400 < E < 650 \text{ GeV}$	$E > 650 \text{ GeV}$
Barrel	av. norm. diff.	-0.01	-0.00	-0.00
	RMS	0.30	0.22	0.24
	$100 \text{ pb}^{-1}, 10 \text{ TeV}$			
	nb. el.	4.8	2.2	0.3
	$\delta(\text{av.})$	0.14	0.15	-
Endcaps	av. norm. diff.	-0.01	-0.00	-0.00
	RMS	0.41	0.22	0.26
	$100 \text{ pb}^{-1}, 10 \text{ TeV}$			
	nb. el.	49.1	28.1	6.0
	$\delta(\text{av.})$	0.06	0.04	0.11

Table 7.3: For three electron energy ranges, average value and RMS of the normalized difference $(E_1^{\text{meas}} - E_1^{\text{rec}})/\langle E_1^{\text{meas}} \rangle$, for EB and EE separately; expected number of electrons with $p_t > 50 \text{ GeV}/c$ from Drell-Yan events with mass $M_{e^+e^-} > 120 \text{ GeV}/c^2$, selected using the HEEP criteria for electron identification (see Table 5.3), and error on the mean of the normalized difference, for an integrated luminosity of 100 pb^{-1} at 10 TeV. The Drell-Yan sample is fitted using fit parameters obtained from the Drell-Yan sample itself for different energy bins. The errors on the average difference are less than 0.002.

Table 7.3 presents the expected precision achieved for the 3 electron energy ranges ($300 < E < 400$, $400 < E < 650$ and $E > 650 \text{ GeV}$), for an integrated luminosity of 100 pb^{-1} for a center of mass energy of 10 TeV. The expected average of the normalised difference distribution and its RMS are given, together with the numbers of selected electrons in both ECAL barrel and ECAL endcaps, and the expected errors $\delta(\text{av.})$ on the measured average of the normalised differences, for both beam energies. For a given electron energy range, the distance of the measured average to the expected average, computed in terms of $\delta(\text{av.})$, provides a measurement of the level of confidence with which the ECAL calibration can be validated. The precision reached is of 4 to 11% with 100 pb^{-1} at 10 TeV in the ECAL endcaps. It should be noted that the number of electrons in each energy bin, and thus the precision of the validation, could be improved by using electrons from Drell-Yan events in the Z peak, with the condition of a sufficient electron p_t for the reconstruction method

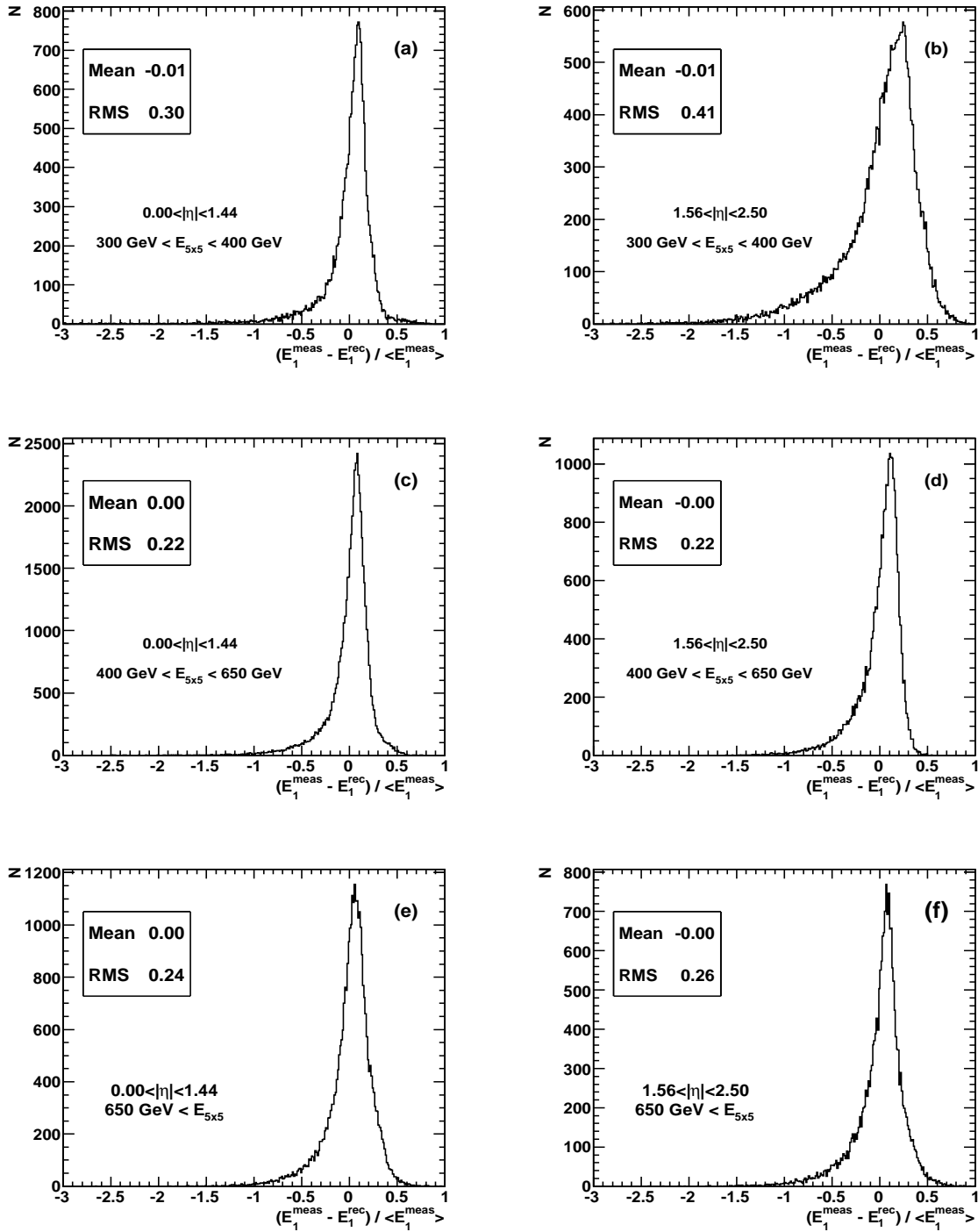


Figure 7.17: Distributions of the normalized difference $(E_1^{\text{meas}} - E_1^{\text{rec}}) / \langle E_1^{\text{meas}} \rangle$, for electrons (and positrons) from Drell-Yan sample generated with invariant mass $M_{ee} > 120 \text{ GeV}/c^2$, electrons are chosen with $p_t > 50 \text{ GeV}/c$, electrons and positrons are selected with very small background using the HEEP criteria (given in Table 5.3); plots (a-c-e) represent electrons chosen in 3 energy bins, $300 \text{ GeV} < E_{5 \times 5} < 400 \text{ GeV}$, $400 \text{ GeV} < E_{5 \times 5} < 650 \text{ GeV}$ and $650 \text{ GeV} < E_{5 \times 5}$, with $0.00 < |\eta| < 1.44$ (EB) and similarly plots (b-d-f) for $1.56 < |\eta| < 2.50$ (EE). The errors on the average difference are less than 0.002.

to apply, e.g. $p_t > 50$ GeV/ c .

For a cross check, we have repeated the same study, but the reconstructed energy deposit E_1^{rec} in the central crystal was computed using the $F(X, Y; E, \eta)$ function obtained from 300 GeV “single gun” electrons for the energy ranges between 300 and 400 GeV, and 500 GeV “single gun” electrons for the two energy ranges between 400 and 650 GeV, finally from 1000 GeV “single gun” electrons for the energy range above 650 GeV.

The result of this study is quoted in Table 7.4, which is the same as in Table 7.3, except that the Drell-Yan sample is fitted using fit parameters obtained from single gun electron samples as explained in the text.

		$300 < E < 400$ GeV	$400 < E < 650$ GeV	$E > 650$ GeV
Barrel	av. norm. diff.	-0.03	-0.02	-0.01
	RMS	0.36	0.19	0.18
	$100 \text{ pb}^{-1}, 10 \text{ TeV}$			
	nb. el.	4.8	2.2	0.3
	$\delta(\text{av.})$	0.16	0.13	-
Endcaps	av. norm. diff.	-0.04	-0.02	-0.03
	RMS	0.42	0.21	0.23
	$100 \text{ pb}^{-1}, 10 \text{ TeV}$			
	nb. el.	49.1	28.1	6.0
	$\delta(\text{av.})$	0.06	0.04	0.09

Table 7.4: Same as Table 7.4, except that the Drell-Yan sample is fitted using fit parameters obtained from single gun electron samples as explained in the text.

The achieved precisions ($\delta(\text{av.})$), which have been obtained from fitting the Drell-Yan sample using fit parameters obtained from single gun electron samples, are almost the same (within 2% difference in some energy bins) as if the Drell-Yan sample is fitted using fit parameters obtained from the Drell-Yan sample itself for different energy bins. This result shows that the effect of final state electromagnetic radiation (FSR) in the Drell-Yan sample is almost negligible, as seen from Figure 7.18, which shows the ratio of the energy of final state radiation E_{gen}^γ (energy of final state electron before the FSR minus that after FSR) to that of the generated final state electrons after FSR E_{gen}^e , for the Drell-Yan sample generated with invariant mass $M_{ee} > 120$ GeV/ c^2 , and electrons with $p_t > 50$ GeV/ c and $E_{5 \times 5} > 300$ GeV.

7.4 Shower shape variable for the validation of high energy electron candidates

Conversely to the validation of crystal calibration discussed in section 7.3, the studies presented here provide a new shower shape variable, $(E_1^{\text{meas}} - E_1^{\text{rec}})/\langle E_1^{\text{meas}} \rangle$, which can be used to validate high energy electron candidates in a sample of events of interest, e.g. in the tail of the Drell-Yan spectrum or candidates for new physics signal. Table 7.5 gives the expected average value and the RMS of the distribution.

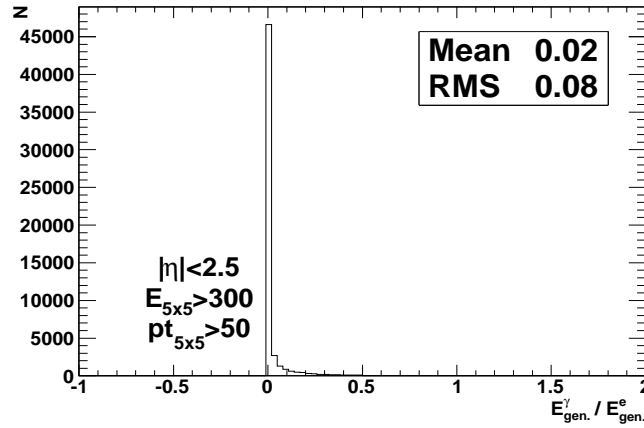


Figure 7.18: Ratio of the energy of final state radiation and that of the generated final state electrons after FSR, for the Drell-Yan sample generated with invariant mass $M_{ee} > 120 \text{ GeV}/c^2$ and electrons with $p_t > 50 \text{ GeV}/c$ and $E_{5 \times 5} > 300 \text{ GeV}$.

	$0 < \eta < 0.5$		$0.5 < \eta < 1.0$		$1.0 < \eta < 1.44$	
E (GeV)	av.	RMS	av.	RMS	av.	RMS
500	-0.01	0.16	-0.02	0.22	-0.02	0.37
1000	-0.01	0.13	-0.01	0.14	-0.02	0.27
1500	0.00	0.11	-0.01	0.12	-0.01	0.21
2000	-0.01	0.11	-0.01	0.10	-0.01	0.18
	$1.56 < \eta < 1.8$		$1.8 < \eta < 2.2$		$2.2 < \eta < 2.5$	
E (GeV)	av.	RMS	av.	RMS	av.	RMS
500	-0.05	0.47	-0.02	0.34	-0.03	0.27
1000	-0.04	0.36	-0.01	0.24	-0.01	0.17
1500	0.01	0.29	0.01	0.20	0.01	0.14
2000	-0.01	0.26	0.01	0.17	0.00	0.13
2500	-0.01	0.25	0.01	0.15	0.00	0.12
3500	-0.01	0.17	-0.01	0.12	-0.01	0.08

Table 7.5: Average and RMS values of the distributions of the normalised difference $(E_1^{\text{meas}} - E_1^{\text{rec}})/\langle E_1^{\text{meas}} \rangle$ for electrons with non-saturating electronics, with energies from 500 to 3500 GeV: average and RMS values of the distributions, for three $|\eta|$ bins in EB and three $|\eta|$ bins in EE.

Chapter 8

Saturation effect for high energy electrons in CMS ECAL crystals and correction

8.1 Energy reconstruction in the case of electronics saturation

The ECAL Very Front End (VFE) electronics will saturate for energy deposits $\gtrsim 1650$ GeV in a single crystal of electromagnetic calorimeter ECAL in the barrel part (EB) and $\gtrsim 2820$ GeV for the endcap part (EE) [53,54], detail description is presented in Appendix A.1. The fractions of electron showers with electronics saturation in EB and in EE are given in Table 8.1 for different energies.

E (GeV)	EB	EE
2500	58%	-
3000	79%	-
3500	91%	15%
4000	97%	70%

Table 8.1: Fractions of electron showers of various energies with electronics saturation in EB ($|\eta| < 1.44$) and in EE ($1.56 < |\eta| < 2.5$).

It was proposed in [47] to use the parameterisation of electromagnetic showers given by eq. (7.5) to reconstruct the energy deposit E_1^{rec} in the saturated crystal (even at very high energy, only the central crystal in a 5×5 matrix is affected by electronics saturation). These studies were performed (see ref. [47]) for EB using Monte Carlo simulation versions 365 of OSCAR and 873 of ORCA (old version). They are repeated here for EB and EE with the new CMSSW software [34], version 1.6.11, following the studies presented in section 7.2.3.

In the context of saturation, the approximate scaling with energy of the functions $F(X, Y; E, \eta)$, observed in section 7.2.2, is a very useful feature. It allows the extraction with good precision of a first estimate of E_1 from the energy deposit in the surrounding crystals, using e.g. the $F(X, Y; E, \eta)$ function determined for 3500 GeV electrons. A better approximation can then be reached, using the more appropriate energy function.

It must be noted that saturation effects are simulated in the present CMS software, and that only the “saturated” energy is kept throughout the simulation chain. As the truly “measured” value of the E_1 energy is not kept through the simulation chain, the quantity E_1^{meas} is recomputed for the present studies in the case of saturation as the difference, $E_1^{\text{meas},*} = E_{\text{true}} - E_{24}$, between the generated, true, electron energy, E_{true} , and the

energy deposit in the surrounding 24 crystals, E_{24} . This implies that, by construction, the quantity E_{25} is equal to E_{true} and that small effects affecting E_1 are neglected, in particular the energy leakage to the HCAL [47]. The $E_1^{\text{meas},*}$ quantities are used for fitting the $F(X, Y; E, \eta)$ functions. In spite of a small systematic shift, the results are however hardly affected, since the average difference between E_{true} and E_{25} is smaller than the resolution of the reconstructed energy. A more precise determination of the functions $F(X, Y; E, \eta)$ above the saturation limit could be used if the truly “measured” values of E_1^{meas} is kept throughout the simulation procedure. This implies significant coding work at the digitisation and reconstruction levels of CMSSW.

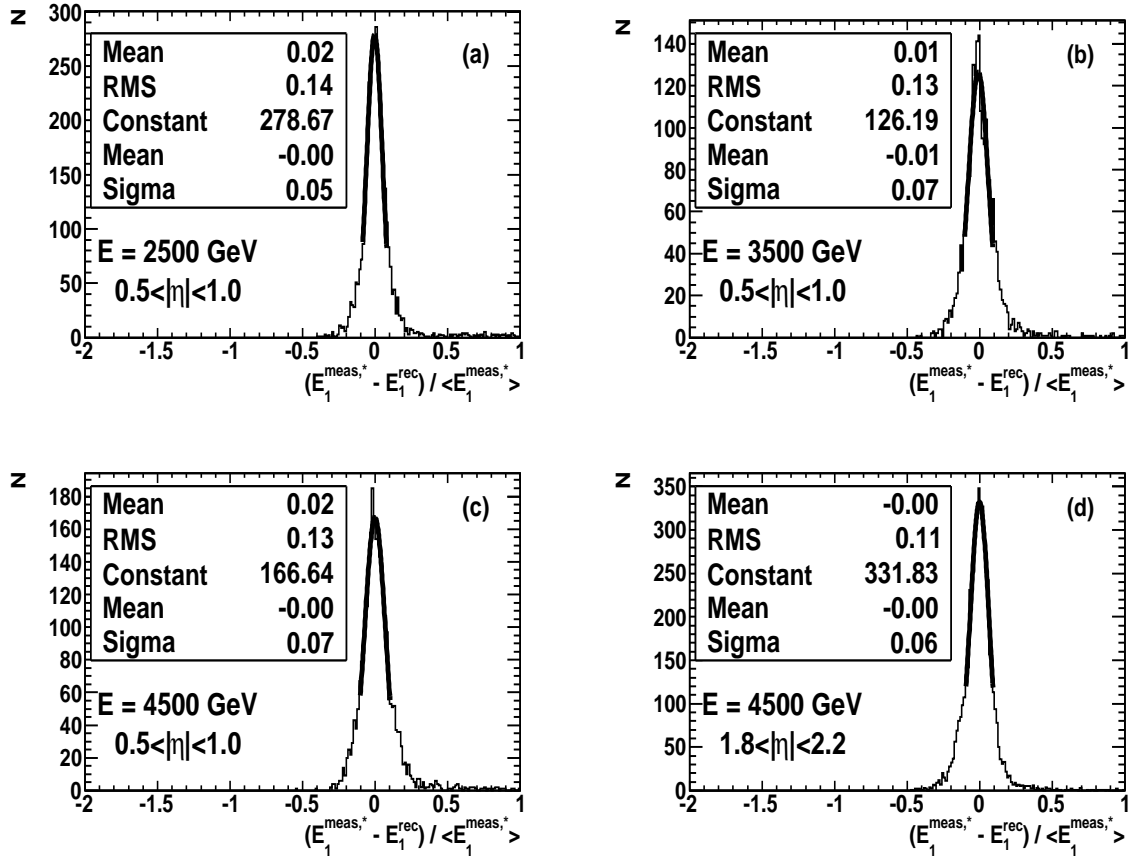


Figure 8.1: Distributions of the normalised difference $(E_1^{\text{meas},*} - E_1^{\text{rec}}) / \langle E_1^{\text{meas},*} \rangle$ for (a-b-c) 2500, 3500 and 4500 GeV electrons with $0.5 < |\eta| < 1.0$ (EB) and (d) for 4500 GeV electrons with $1.8 < |\eta| < 2.2$ (EE). Only “single gun” events with electronics saturation are included. The superimposed curves show the results of Gaussian fits distributions of the peak region over $\pm 1.5\sigma$ [48].

Figure 8.1 presents the distributions of the normalised difference $(E_1^{\text{meas},*} - E_1^{\text{rec}}) / \langle E_1^{\text{meas},*} \rangle$ for 2500, 3500 and 4500 GeV electrons, obtained for events with electronics saturation using the $F(X, Y; E, \eta)$ functions for the relevant η values, separately for EB and EE. Results of Gaussian fits to the central part of the distributions ($\pm 1.5\sigma$) are superimposed.

In Figure 8.2, the distributions of the normalised difference $(E_1^{\text{meas},*} - E_1^{\text{rec}}) / \langle E_1^{\text{meas},*} \rangle$ are presented for (a-

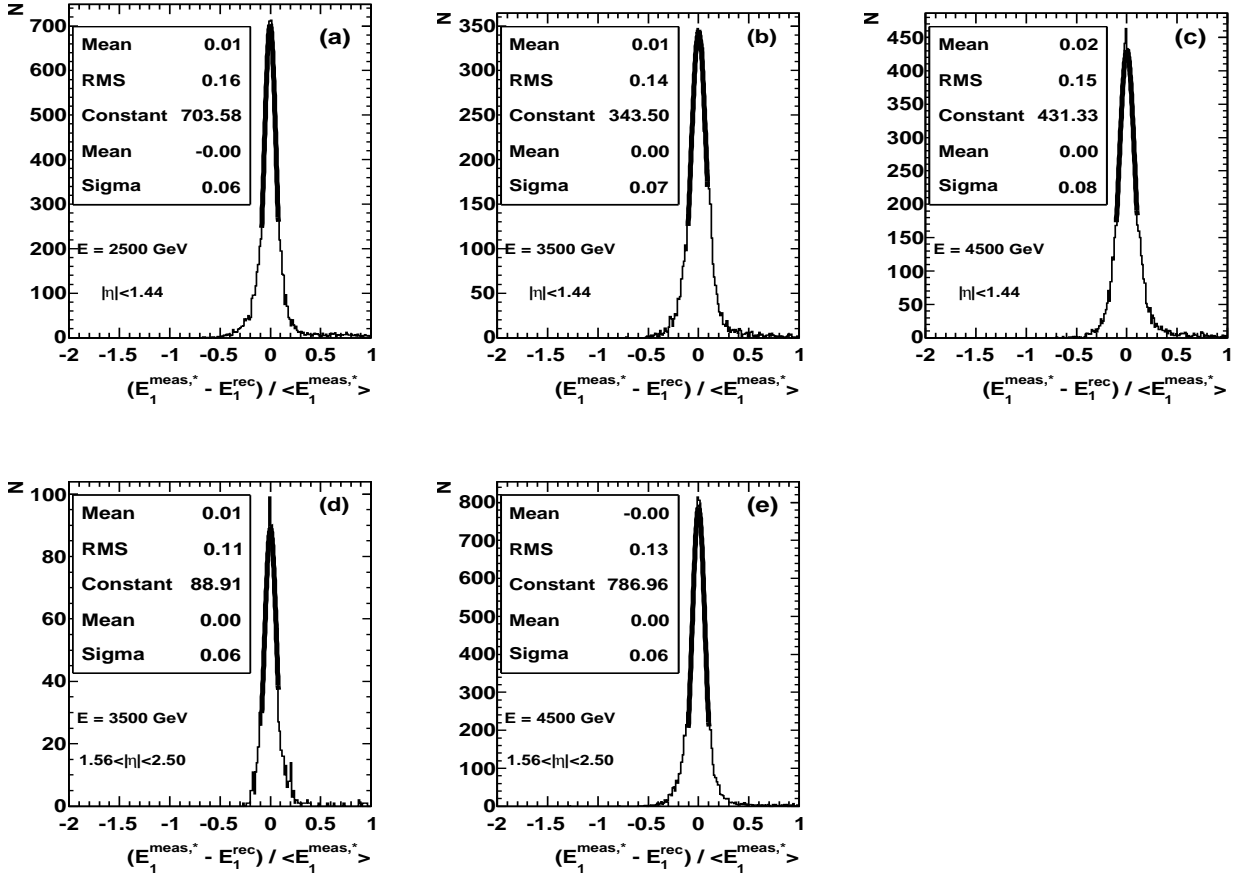


Figure 8.2: Distributions of the normalised difference $(E_1^{\text{meas},*} - E_1^{\text{rec}})/\langle E_1^{\text{meas},*} \rangle$ for (a-b-c) 2500, 3500 and 4500 GeV electrons with $|\eta| < 1.44$ (EB) and (d-e) for 3500 and 4500 GeV electrons with $1.56 < |\eta| < 2.50$ (EE). Only “single gun” events with electronics saturation are included. The superimposed curves show the results of Gaussian fits distributions of the peak region over $\pm 1.5\sigma$.

energy	EB				EE			
	average	RMS	μ	σ	average	RMS	μ	σ
2500 GeV	0.01	0.16	0.00	0.06	-	-	-	-
3500 GeV	0.01	0.14	0.00	0.07	0.01	0.11	0.00	0.06
4500 GeV	0.02	0.15	0.00	0.08	0.00	0.13	0.00	0.06

Table 8.2: Normalised differences $((E_1^{\text{meas},*} - E_1^{\text{rec}})/\langle E_1^{\text{meas},*} \rangle)$ for electrons with saturated electronics, with energies 2500, 3500 and 4500 GeV: average and RMS values of the distributions (see Figure 8.2), and mean μ and width σ of Gaussian fits in the peak, for EB and EE.

b-c) 2500, 3500 and 4500 GeV electrons with $|\eta| < 1.44$ (EB) and (d-e) for 3500 and 4500 GeV electrons with $1.56 < |\eta| < 2.50$ (EE). Only "single gun" events with electronics saturation are included. The superimposed curves show the results of Gaussian fits distributions of the peak region over $\pm 1.5\sigma$.

Table 8.2 presents, separately for EB and EE, the average values (≈ 0.01) and the RMS (0.11 – 0.16) of the distributions for several electron energies, as seen from Figure 8.2. For Gaussian fits (within $\pm 1.5\sigma$), the peak values are 0 and the peak width ≈ 0.06 .

Chapter 9

Summary and conclusions

The Compact Muon Solenoid (CMS), is a detector operating at the Large Hadron Collider (LHC) at CERN. The LHC will provide proton proton collisions at a designed centre-of-mass energy of 14 TeV. It has been designed to search for and study Higgs bosons and new physics beyond the Standard Model (BSM). In particular new heavy resonances are predicted by various BSM models, GUT models and extra spatial dimension models. Promising decay channels for Z' gauge bosons or gravitons G are the leptonic ones; $Z' \rightarrow l^+l^-$ or $G \rightarrow l^+l^-$, where l is an electron or a muon, and also $G \rightarrow \gamma\gamma$.

The HEEP (High Energy Electron Pair) group at CERN has done a full analysis, based on Monte Carlo (MC) simulations, to prepare for a possible discovery of heavy resonances at the CMS experiment in dielectron decay channel. The HEEP group has published two analyses at centre-of-mass energy of 14 TeV and 10 TeV (energy expected for the first year of data taking), for 100 pb^{-1} of integrated luminosity. The analysis strategy of the HEEP group uses the Drell-Yan sample, including two control regions at Z pole ($60 < M_{ee} < 120 \text{ GeV}/c^2$) and at the higher mass region $120 < M_{ee} < 600 \text{ GeV}/c^2$, to check the detector response to high energy electrons and all triggering and reconstruction efficiencies. The first control region, at the Z pole, is characterised by large statistics of electrons with low p_T and small contribution from the background, where a comparison between MC and data is performed to check that the MC describes well the data. The second control region of the Drell-Yan spectrum, will be used to study electron identification, the estimate of backgrounds to the heavy resonances from new physics and calibration of the electromagnetic calorimeter crystals. The HEEP studies (for 10 TeV centre-of-mass energy and integrated luminosity of 100 pb^{-1}) show that the expected 95% confidence level lower limits on masses of SSMZ' and Z'_ψ are $1590 \text{ GeV}/c^2$ and $1260 \text{ GeV}/c^2$ respectively. While for RS Gravitons masses, they are $1490 \text{ GeV}/c^2$ and $1210 \text{ GeV}/c^2$ for coupling c equal to 0.1 and 0.05 respectively.

The analyses done in this thesis are contributions to the CMS HEEP group effort to prepare for the data taking. Our personal work has focused on developing tools to identify and reconstruct electrons with high transverse momenta using the various sub-detectors (tracker, electromagnetic calorimeter (ECAL) and hadronic calorimeter (HCAL)) of CMS. Our main contribution is divided into three main parts.

Firstly, due to the emission of one of the 2 electrons, from high mass pair production ($M_{ee} > 200 \text{ GeV}/c^2$), in the EB-EE gap direction and does not pass the minimum electron identification conditions (6.2) 4% of the events were lost. A procedure has been designed to recover these lost electrons in the EB-EE gap. The HCAL

calorimeter is used for energy reconstruction, and electron identification criteria are defined, which use the longitudinal segmentation and the transverse granularity of the HCAL and the tracker. The designed procedure permit the recovery of 3% of the total number of Drell-Yan production with $M_{ee} > 200 \text{ GeV}/c^2$. The efficiencies are about 73% and of 91% for Drell-Yan production and SSMZ' boson production with $M = 1 \text{ TeV}/c^2$, respectively. The rms of the mass reconstruction distributions are of 9% for both Drell-Yan production and SSMZ', with for Z' bosons a resolution in the peak region of 2%.

In the ECAL barrel – endcap transition regions, a total of 4.0 background events containing a misidentified electron pair is expected from the QCD multijet and W+jet channels, for an integrated luminosity of 1 fb^{-1} . This should be compared to a total of 22 Drell-Yan events with mass larger than $200 \text{ GeV}/c^2$. In the mass region $M_{ee} > 600 \text{ GeV}/c^2$, 0.02 background events are found, whereas 10 SSMZ' events with $M_{ee} = 1 \text{ TeV}/c^2$ might be recovered. The backgrounds among the recovered events, due to misidentified jets from QCD multijet and W+jet events, are of the order of 18% for the Drell-Yan events; they are situated below the $1 \text{ TeV}/c^2$ region.

In addition, $t\bar{t}$ production is a significant background to direct lepton pair production, when the two W bosons from the top quarks decay into an electron and a neutrino. At variance with the QCD multijet and W+jet background, the top background is not reducible through electron identification, since the electrons are genuine. It will thus contaminate the sample of gap recovered electron pair events in the same proportion as for the total samples of Drell-Yan and heavy resonance events.

Secondly, a method has been proposed to validate the extrapolation to high energy ($> 300 \text{ GeV}$) of the response of CMS ECAL crystals to electromagnetic showers. It is shown that the energy deposit in the central crystal, E_1 , of a 5×5 matrix of the CMS ECAL can be parameterised, for high energy electromagnetic showers, from the energy deposits in the surrounding 24 crystals. The parameterisation functions, $F(X, Y; E, \eta)$, depend on two variables, X and Y , which are defined for two orthogonal directions in the ECAL geometry (these directions are different for the ECAL barrel and endcaps). These variables are obtained from the ratio of the energy deposits on the two sides of the central crystal, i.e. the asymmetry in the 5×5 matrix. They are directly related to the position of the incident electron impact point with respect to the crystal centre. The functions $F(X, Y; E, \eta)$ are skewed, due to crystal off-pointing. They depend slightly on the electron energy E and on the pseudorapidity η of the impact point, computed with respect to the nominal interaction point in CMS.

The energy in the central crystal, E_1^{rec} , is reconstructed using the energy deposits in the surrounding 24 crystals and the relevant function $F(X, Y; E, \eta)$. The quality of the reconstruction is quantified for a sample of electrons from the distribution of the normalised difference $(E_1^{\text{meas}} - E_1^{\text{rec}})/\langle E_1^{\text{meas}} \rangle$, where E_1^{meas} is the measured energy deposit in the central crystal. The average of the distribution is close to 0 by construction of the functions $F(X, Y; E, \eta)$. The RMS decreases with energy, from 0.26 (0.36) for 500 GeV electrons to 0.14 (0.17) for 2500 GeV electrons in the barrel (endcaps), and they depend significantly on η , with a maximum around the ECAL barrel – endcap transition region. The distributions are asymmetric, the larger wing being for values of $E_1^{\text{rec}} > E_1^{\text{meas}}$, which is due to the spread of E_1^{meas} energy deposits for a given value of X and

Y . It was checked with a simulation without magnetic field that this spread is due to Bremsstrahlung emission, which explains the observed correlation between the RMS of the distribution and the amount of dead material in front of the ECAL.

The possibility to reconstruct the E_1 energy using the surrounding crystals and the $F(X, Y; E, \eta)$ parameterisations provides a procedure for cross-checking the extrapolation to a higher energy range of the ECAL crystal calibration, performed in test beams up to 300 GeV. For a sample of high energy electrons, the expected mean and RMS of the distribution of the normalised difference $(E_1^{\text{meas}} - E_1^{\text{rec}})/\langle E_1^{\text{meas}} \rangle$ is known from Monte Carlo simulations. The observed average for a sample of selected electrons can thus be compared to the expected value. Given the number of electrons, the precision reached with an integrated luminosity of 100 pb^{-1} at 10 TeV is of 4 to 11%, using electrons with $p_t > 50 \text{ GeV}/c$ from Drell-Yan events with mass $M_{ee} > 200 \text{ GeV}/c^2$, selected using the HEEP criteria.

Conversely, the quantity $(E_1^{\text{meas}} - E_1^{\text{rec}})/E_1^{\text{meas}}$ provides a shower shape variable, with known resolution, which can be used for validating high energy electron candidates.

Finally, the method described above is used at very high energy. Indeed the E_1 energy can be reconstructed for very high electromagnetic showers, when the electronics of the highest energy crystal is saturated ($\gtrsim 1650 \text{ GeV}$ in a single crystal of the ECAL barrel and $\gtrsim 2820 \text{ GeV}$ in the endcaps). The RMS of the energy resolution distribution is ≈ 0.13 and the width of a Gaussian fit in the peak region is ≈ 0.06 .

On December 2009, the LHC will have the first collisions at 450 GeV per proton beam. Starting from January 2010, it will run for 4 months with centre-of-mass energy of about 7 TeV, corresponding to integrated luminosity $\sim 30 - 50 \text{ pb}^{-1}$. After a break of one month, it is planned that the LHC will run at centre-of-mass energy of 10 TeV for another 5 months, the achieved integrated luminosity will be $\sim 270 \text{ pb}^{-1}$. The collected data by the CMS detector will be enough to check the proposed techniques, for gap recovery and the calibration of ECAL crystals.

Appendix A

ECAL readout electronics

The CMS-ECAL electronics can be divided into 2 subsystems. The on-detector electronics, which composed of radiation resistant circuits located just behind the crystals, and the off-detector electronics housed in the underground counting rooms close to the experimental area. Both systems are communicating through 90 m long high speed optical links, operated at 800 MB/s.

A.1 Front-end read-out electronics

The function of the front end electronics of the ECAL is to amplify and shape the signal from the sensors, digitize the signal at 40 MHz, buffer the data until receipt of a Level-1 trigger, and then transmit the data to the off-detector electronics for insertion of the CMS data stream. In addition the front end electronics uses the digitized data to calculate the trigger requirements which are transmitted at 40 MHz to be used in Level-1 trigger decision.

The building block of the front end electronics is a group of 25 crystals (grouped in a 5×5 geometry), i.e. a trigger tower in EB or supercrystals in EE. The trigger towers are composed of 4 different electronics boards. Each trigger tower contains of a motherboard (MB), a Low Voltage Regular Board (LVRB), 5 Very Front End (VFE) boards, and a Front End (FE) card.

The motherboards are located under the cooling system for the electronics and are used to route the signals from the photodetectors, APDs in the EB or VPTs in the EE, to the VFE cards, to distribute high voltage to the photodetectors, and to distribute Low Voltage to VFE cards. Each supermodule contains 68 motherboard which each connect to the photodetectors of the 25 crystals via kapton flexible-print cables. In addition signals for temperature monitoring thermistors are routed from the sensor capsule to the VFE cards. The LVRBs are connected directly to the external Low Voltage power supplies which sit in the CMS racks attached to the outside of the CMS iron yoke, approximately 20 meters from the supermodule. Each LVRB contains radiation-hard voltage regulators which provide the 2.5 V needed by the front end electronics. This regulated 2.5 V is distributed to the FE card. by small connector on the LVRBs, and to the 5 VFE cards in a trigger tower via the motherboard.

Each VFE card contains amplification and digitization for the signals from 5 crystals. In order to achieve the low noise dynamic range requirements for the ECAL, 2 new radiation-hard ASICs were developed. The

Multi Gain Pre-Amplifier (MGPA) contains 3 parallel gain stages which process sensor signals. The signals from these 3 stages are routed to the AD41240, a custom designed Analogue to Digital Converter (ADC) which contains 4 channels each with 12 bits of information and an effective number of bits equal to 11. Three of the 4 ADCs on the AD41240 are used for each crystal. The ASIC digitizes these 3 inputs in parallel, determines whether each channel has saturated, and then outputs the data from the channel which has the highest gain and was not saturated. The 3 MGPA gains are arranged so that the highest gain range has amplification of a factor of 12 and least significant bit of ~ 35 MeV. This range has a noise around 40 MeV for the barrel and saturates at approximately 160 GeV. The other 2 gains are a factor of 6 and unity. The unity gain determines the upper end of the dynamic range and saturates at approximately $\gtrsim 1650$ GeV for the ECAL barrel and $\gtrsim 2820$ GeV in the ECAL endcap. The ADC is also designed so that once a range saturates, the ADC returns the next 5 samples without changing the gain, which in turn prevents a second (return) gain change within the waveform of the digitized sample. The same chip is used for both the APDs and the VPTs with a small change of external components on the VFE cards. The signals from the 5 VFEs are collected on the FE card, where they are buffered in a custom ASIC designed for the ECAL front end - the FENIX ASIC. Each FENIX contains 7 FENIX ASICs.

The data are transmitted to the Level-1 trigger and the DAQ (Data Analysis Quality) system using 2 opto-hybrids on each FE card. These hybrids contain radiation-tolerant laser diodes for electrical to optical conversion, and the CERN developed radiation-hard GOL ASIC, which provides parallel to serial conversion. The FE card also contains the clock distribution, and the control unit for allowing local configuration of all ASICs. Clock signals and configuration are distributed to the FE cards using 8 independent electrical token rings. These rings communicate optically to the off-detector electronics using a digital opto-hybrid (DOH) developed originally from the CMS tracker project. The DOHs are mounted on token ring link boards which then connect to the token ring. There are 2 rings which run in parallel and are designed to allow the recovery of the ring, in the event that one of the FE card fails.

A.2 Off-detector electronics

The ECAL off-detector read-out and trigger architecture is illustrated in figure A.1. The system is composed of different electronic boards sitting in 18 VME-9U crates (the **CCS**, **TCC** and **DCC** modules) and in 1 VME-6U crate (the selective readout processor, **SRP**, systems). They service both the DAQ and the trigger paths. In the DAQ path, the DCC performs data readout and data reduction based on the selective readout flags computed by the SRP system.

The clock and control system (**CCS**) board distributes the system clock, trigger and broadcast commands, configures the FE electronics and provides an interface to the trigger accelerating system. The TTC signals are translated and encoded by the suppression of clock edges and sent to the mFEC mezzanine cards. The mFEC interfaces optically with a FE token ring. The 8 mFECs of the CCS board control a supermodule. The TCC and DCC cards in the off-detector crate receive the encoded TTC signals from the CCS card through a

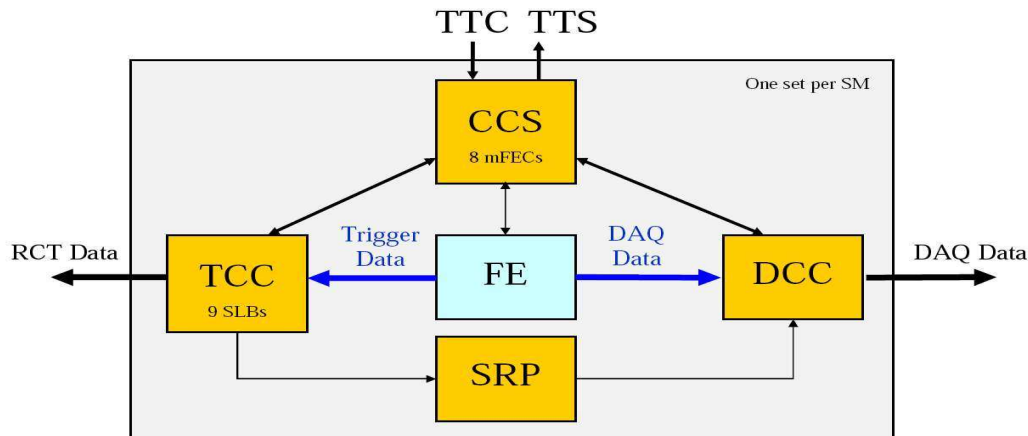


Figure A.1: Schematic view of the ECAL off-detector electronics [31].

dedicated backplane. The main function of the trigger concentration card (TCC) is to include the completion of the trigger primitive generation and their transmission to the synchronization and link board (SLB) mezzanines at each bunch crossing, the classification of each trigger tower and its transmission to the Selective Readout Processor at each Level-1 trigger accept signal, and the storage of the trigger primitive during the Level-1 latency for subsequent reading by the DCC.

Each TCC collects trigger data from 68 FE boards in the barrel, corresponding to one supermodule, and from 48 FE boards in the endcap corresponding to the inner or outer part of a 20° sector. In the endcap, trigger primitive computation is completed in the TCCs, which must perform a mapping between the collected pseudo-strip trigger data from the different supermodules and the associated towers. The encoded trigger primitive (8 bit for nonlinear representation of the trigger tower E_T plus 1 bit for the fine grain veto) are time aligned and sent to the regional trigger processors by the SLB. The trigger primitives are stored in the TCC during the Level-1 latency for subsequent reading by the DCC (see below). In the barrel region a single TCC is interfaced with 1 DCC. In the endcap region, one DCC serves 4 TCCs covering a 40° sector.

The data concentration card (DCC) is responsible for collecting crystal data from up to 68 FE boards. Two extra FE links are dedicated to the read-out of laser monitoring data (pin diodes). The DCC also collects trigger data transmitted from the TCC modules and the selective read-out flags transmitted from the SRP system. A data suppression factor near 20 is attained using a programmable selective read-out algorithms. When operating in the selective read-out module the SRP flags indicate the level of suppression that must be applied to the crystal data of a given FE read-out. For the application of zero suppression, time samples pass through a finite impulse response filter with 6 consecutive positions and the result is compared to a threshold. If any time sample of the 6 has been digitized at a gain other than the maximum, then zero suppression is not applied to the channel.

Input and output memory occupancy is monitored to prevent buffer overflows. If a first occupancy level is reached, the Trigger Throttling System (TTS) signal “Warning Overflow” is issued, requesting a reduction of the trigger rate. In a second level, a TTS signal “Busy” inhibits new trigger and empty events (events with

just the header words and trailer) are stored. DCC events are transmitted to the central CMS DAQ using the S-LINK64 at maximum data rate of 528 MB/s, while an average transmission data flow of 200 MB/s is expected after ECAL data reduction. Laser trigger (for crystal transparency monitoring) will occur with a programmable frequency and synchronously with the LHC gaps. No data reduction is applied for these events, which are read-out following a TTC test enable command. A VME memory is used for local DAQ, allowing VME access to physics events and laser events in spy mode.

The selective read-out processor (**SRP**) is responsible for the implementation of the selective read-out algorithm. The system is composed by a single VME-6U crate with 12 identical algorithms boards (**AB**). The AB computes the selective read-out flags in different calorimeter partitions. The flags are composed by 3 bits, indicating the suppression level that must be applied to the associated read-out units.

Appendix B

Electron recovery in case of a missing ECAL endcap at start-up

One year ago, there was a possibility that, at start-up, one of the ECAL endcaps will not be installed, for this reason the analysis in this chapter was urgently needed.

Table B.1 presents how this may lead to losses of Drell-Yan electron pairs with $M_{\gamma/Z} > 200 \text{ GeV}/c^2$ and of SSM Z' bosons with mass of $1 \text{ TeV}/c^2$, for which both (real) electrons were generated with $|\eta| < 2.4$ and $p_t > 80 \text{ GeV}/c$. The fractions of events for which one or both electrons are emitted toward the missing endcap are indicated, separately for cases where the second electron is emitted toward the barrel or toward the installed endcap.

	Drell-Yan, $M_{\gamma/Z} > 200 \text{ GeV}/c^2$	Z' bosons, $M = 1 \text{ TeV}/c^2$
1 electron in missing endcap and - second electron in barrel	$16.0 \pm 0.9\%$	$16.0 \pm 1.5\%$
- second electron in the installed endcap	$0.11 \pm 0.08\%$	$1.4 \pm 0.5\%$
2 electrons in missing endcap	$4.9 \pm 0.5\%$	$1.4 \pm 0.5\%$

Table B.1: Percentages of the total number of Drell-Yan electron pairs with $M_{\gamma/Z} > 200 \text{ GeV}/c^2$ and of Z' bosons with mass of $1 \text{ TeV}/c^2$ with both (real) electrons generated with $|\eta| < 2.4$ and $p_t > 80 \text{ GeV}/c$, for which one or both electrons are emitted in the direction of the missing endcap.

The loss of events due to the missing endcap amounts to 21% for Drell-Yan pairs with $M_{\gamma/Z} > 200 \text{ GeV}/c^2$ and 19% for Z' bosons with $M = 1 \text{ TeV}/c^2$. The differences between the two sets are due to the production kinematics (the Drell-Yan events are slightly more centrally produced than Z' bosons) and to the decay kinematics (the average larger p_t of electrons from Z' decays make them less likely to be both emitted in the missing endcap). It should be noted that, except for cases with both electrons emitted toward the missing endcap, the event is expected to be triggered (with very high efficiency) by the second electron.

B.1 HCAL energy deposits and recovery criteria

The recovery procedure discussed in this section applies to the case when one (and only one) of the electrons has been emitted toward the missing ECAL endcap (with $1.56 < |\eta| < 2.4$), the other electron being identified with the HEEP criteria (given in Table 5.9) in the barrel or in the installed endcap.

If the ECAL is absent, the electromagnetic shower is essentially contained in the first longitudinal segmentation, H1, of the HCAL. The isolation of the shower with respect to the surrounding H1 cells and the upper limit on the energy fraction deposited in the second segmentation, H2, can be used for electron identification, in a spirit similar to that of section 6.4 (energy deposits are considered only if they exceed 1.4 GeV). Recovery conditions will be defined in section B.4 such as to ensure both high efficiency for electron identification and high background rejection.

For the studies in this section, samples of events generated with full CMS detector simulation were re-processed with the ECAL being taken as absent. Initial informations, in particular those concerning electron identification in EB and in the installed ECAL endcap, are kept through the reprocessing. In what follows, the HCAL measured energy is recalibrated for electrons following parameterisation (6.1) of section 6.2.

B.2 Electron energy reconstruction; energy deposit $E_{2 \times 2}$

Electron candidates in the region of the missing ECAL endcap are selected in the domain $1.56 < |\eta| < 2.4$, which is covered by the tracker. In this region, HCAL cells vary in size from 0.087 to 0.178 in $|\eta|$ and from 5 to 10° in $|\phi|$ [31], thus typically with dimensions of the order of $10 \times 10 \text{ cm}^2$ or larger. As the Moliere radius of brass is about 1.9 cm, electromagnetic showers are fully contained in an HCAL cell when the impact point is close to the cell centre. However, to take into account of the fact that electrons may be directed toward cell edges, matrices of 2×2 HCAL cells (explained in section 6.2.1) will be used as the basic units for collecting (recalibrated) electron energy, noted as $E_{2 \times 2}$ ¹. The barycentre of the 2×2 unit is used for determining the electron candidate direction.

For electron recovery, the HCAL cell situated in the region of the missing endcap and containing the highest energy in H1 is first selected. The electron energy is then computed from the largest energy 2×2 matrix which contains the largest energy cell. Figure B.1 shows the fraction $R_{2 \times 2} = E_{2 \times 2}/E_{\text{true}}$ of the generated electron energy E_{true} which is reconstructed (after HCAL energy recalibration) in the highest energy 2×2 H1 unit containing the highest energy cell, for “single gun” electrons uniformly distributed in the missing endcap region ($1.56 < |\eta| < 2.4$), with $p_t = 100$ and 500 GeV/ c . The average values are of about 0.98, with peak values of 0.99. The resolution, computed from a Gaussian fit in the peak region, is of 2 to 4% (with larger values for smaller energy), the rms values of the distributions being of the order of 4 to 6%.

¹In view of the varying cell size in the HCAL, this definition is more convenient than a definition based on cones around the electron direction. In addition, the latter is poorly defined, because of the coarse granularity of the HCAL compared to electromagnetic shower extension.

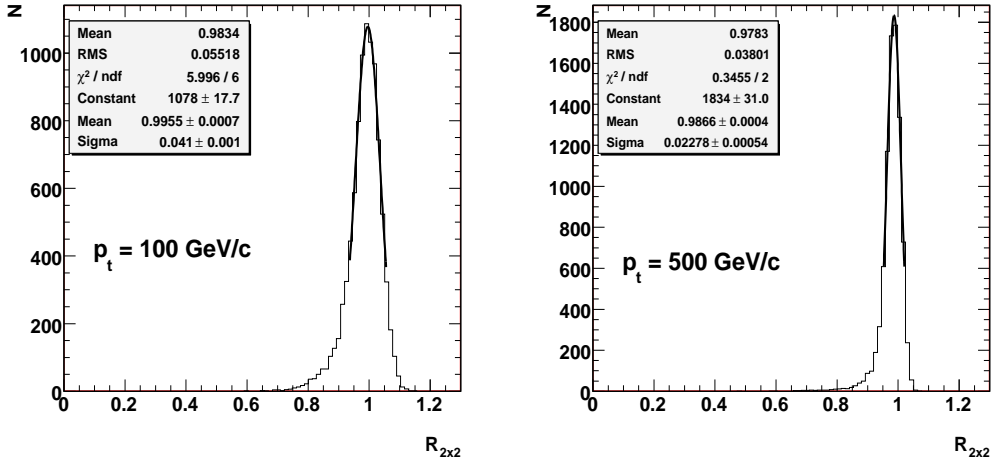


Figure B.1: Fraction $R_{2 \times 2} = E_{2 \times 2} / E_{\text{true}}$ of the generated electron energy E_{true} which is reconstructed (after HCAL energy recalibration) in the highest energy 2×2 H1 unit containing the highest energy cell, for “single gun” electrons uniformly distributed with $1.56 < |\eta| < 2.4$ and with $p_t = 100$ (left) and $500 \text{ GeV}/c$ (right) [52].

B.3 Electron identification criteria

Similar to the case of gap recovery (section 6.5.1), electrons emitted toward the missing endcaps, with $p_t(E_{2 \times 2}) > 80 \text{ GeV}/c$, are identified using isolation criteria. In addition, a track with $p_t > 20 \text{ GeV}/c$ is requested in the tracker, with direction matching that of the highest energy HCAL cell.

As in section 6.5.1, the identification criteria are defined using the Drell-Yan and background samples, with events for which a second electron has passed the HEEP selection cuts (given in Table 5.9). The QCD multijet and W+jet samples are normalised to the same luminosity, and the signal and background samples subsequently normalised to unity.

Longitudinal shower extension; R_{H2} variable The longitudinal extension of electron showers in the HCAL, in the absence of an ECAL endcap, is quantified from the comparison of the energy deposits in the second and first HCAL segmentations. The quantity $R_{H2/H1}$ is defined using the transverse energy deposits in the highest energy 2×2 unit in H1 which contains the highest energy cell, and the transverse energy deposits in the corresponding cells of H2. The distribution of $R_{H2/H1}$ is shown in Figure B.2 (left), for $1.56 < |\eta| < 2.4$ and $p_t(E_{2 \times 2}) > 80 \text{ GeV}/c$, for Drell-Yan events with $M_{\gamma/Z} > 200 \text{ GeV}/c^2$ and for background samples. The condition $R_{H2/H1} < 0.05$ leads to small electron losses, while it efficiently suppresses QCD backgrounds.

HCAL lateral isolation; R_{12} The lateral extension of electromagnetic showers in the HCAL and the electron isolation are studied with the transverse energy deposit $E_{t,12}$ in the set of 12 cells of H1 which immediately surround the highest energy 2×2 unit containing the highest energy cell, i.e. the set of cells in H1 which

complete the 4×4 square around the 2×2 unit. Figure B.2 (right) presents the transverse energy ratio $R_{12} = E_{t,12}/E_{t,2 \times 2}$ for candidate electrons emitted toward the missing ECAL endcap.

Tracker isolation; N_{tr} and R_{pt} Tracker measurements contribute ensuring a good separation between electrons and jets in the case of a missing ECAL endcap. For this, two cones with radii 0.1 and 0.2 for $|\eta| < 1.74$ and radii 0.15 and 0.25 for $|\eta| > 1.74$ are defined around the electron candidate direction; the large value chosen for the inner cone reflects the poor precision of the electron candidate direction determination on basis of the HCAL deposits. Figure B.3 (left) presents, for the Drell-Yan and jet samples, the numbers N_{tr} of tracks with $p_t > 1.5$ GeV/c comprised between the two cones, for candidates emitted toward the missing ECAL endcap with $1.56 < |\eta| < 2.4$ and $p_t(E_{2 \times 2}) > 80$ GeV/c. Figure B.3 (centre) similarly presents the transverse momentum ratio $R_{\text{pt}} = |\Sigma \vec{p}_t| / p_t(E_{2 \times 2})$, computed from the total transverse momentum of tracks contained between the two cones, divided by the electron candidate p_t obtained from the deposits in the highest energy 2×2 unit. Clear differences are observed between signal and background distributions.

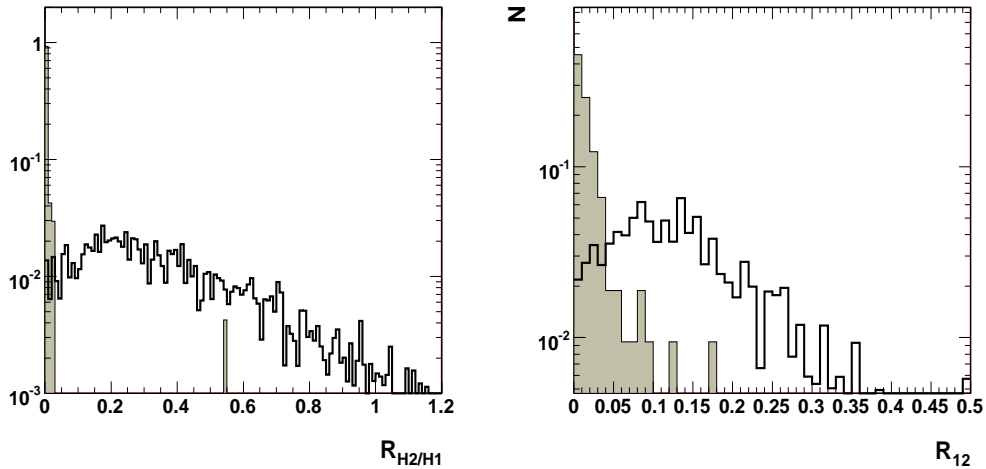


Figure B.2: Isolation criteria for electron candidates emitted toward the missing ECAL endcap with $1.56 < |\eta| < 2.4$ and $p_t(E_{2 \times 2}) > 80$ GeV/c: (left): ratio $R_{\text{H2/H1}}$ of the energy deposit $E_{2 \times 2}$ in the 2×2 unit of H2 corresponding to the highest energy 2×2 unit in H1 containing the highest energy cell, divided by the corresponding unit in H2; (right): ratio $R_{12} = E_{t,12}/E_{t,2 \times 2}$, where $E_{t,12}$ is the transverse energy collected in the set of 12 HCAL cells surrounding the highest energy 2×2 unit of H1 containing the highest energy cell. The distributions for electron candidates from the Drell-Yan signal are shown as shaded histograms, those from the QCD and W+jet backgrounds as white histograms. The signal and background distributions are normalised to unity [52].

Track matching Finally, it is requested that a track with $p_t > 20$ GeV/c be emitted from the vertex and directed within the $|\eta|$ and ϕ limits of the highest energy cell of the highest energy 2×2 HCAL unit. Figure B.4 (right) presents the distribution of the number $N_{\text{tr}}^{\text{match}}$ of such tracks, for the Drell-Yan and the back-

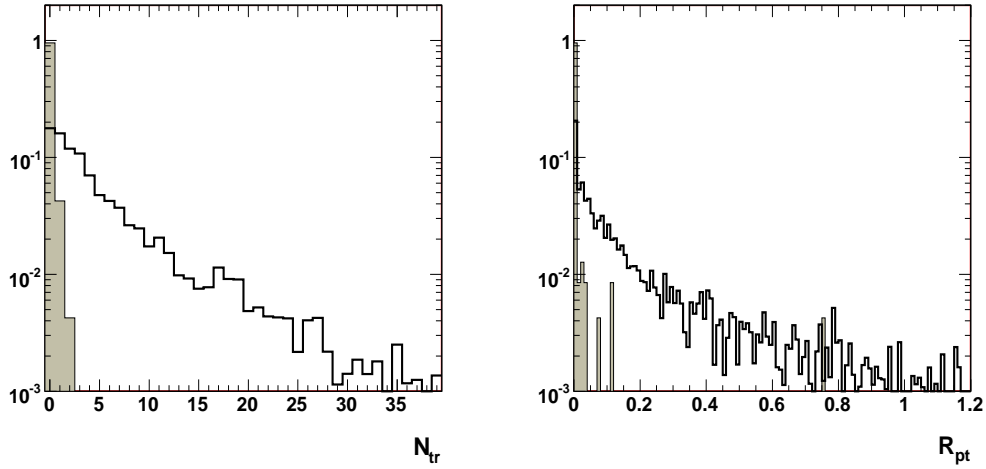


Figure B.3: Same as in figure 6.12, for (left) tracker isolation: number of tracks with $p_t > 1.5 \text{ GeV}/c$ emitted between two cones ($0.1 < \Delta R < 0.2$) around the electron candidate direction; (right) tracker isolation: vectorial sum of the transverse momenta of these tracks, divided by $p_t(E_{2 \times 2})$ [52].

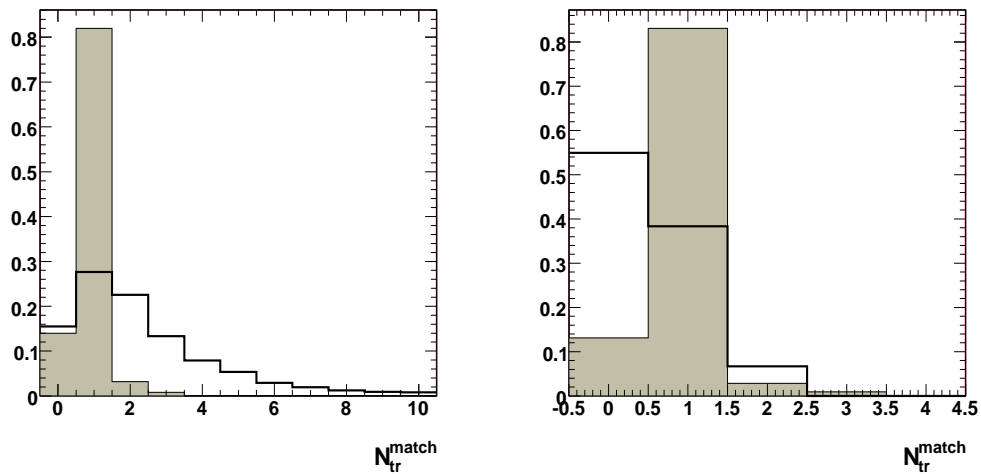


Figure B.4: For electron candidates emitted toward the missing ECAL endcap with $1.56 < |\eta| < 2.4$ the track matching: number of tracks with $p_t > 20 \text{ GeV}/c$ emitted from the vertex and directed within the $|\eta|$ and ϕ limits of the highest energy cell of the highest energy 2×2 HCAL unit, (left) electron candidates with $p_t(E_{2 \times 2}) > 80 \text{ GeV}/c$; (right) only electron candidates passing the isolation criteria are selected [52].

ground samples after applying the previous isolation criteria, while the figure B.4 (left) shows only electron candidates with $p_t(E_{2 \times 2}) > 80 \text{ GeV}/c$.

Clearly the current order of the isolation criteria is very important to have better efficiency as it will be explained in the next section.

B.4 Recovery conditions

As a consequence of the studies presented above, a procedure is defined to recover events lost because of a missing ECAL endcap. It is applied to events containing one and only one electron candidate, emitted toward the EB or the installed ECAL endcap and passing the HEEP identification criteria (given in Table 5.9)². This search is thus not concerned by cases where a second electron has been identified in the gap region after application of the criteria (6.3)³.

After event reconstruction in the absence of the missing endcap, the cell with the largest energy is identified in the first HCAL segmentation H1 corresponding to the missing endcap, i.e. towers 19 to 26, $1.56 < |\eta| < 2.4$. The highest energy 2×2 unit in H1 containing the highest energy cell is then identified, and the barycentre position is computed.

The following cuts are applied to the energy ratios $R_{H2/H1}$ and R_{12} , the number N_{tr} of tracks with $p_t > 1.5 \text{ GeV}$ comprised between cones with radii 0.1 and 0.2 (or 0.15 and 0.25, depending on $|\eta|$) around the electron candidate direction, the transverse momentum ratio $R_{\text{pt}} = \Sigma p_t / p_t(E_{2 \times 2})$ and the number of track matching the electron candidate direction:

$$\begin{aligned}
 &1.56 < |\eta| < 2.4, \\
 &p_t(E_{2 \times 2}) > 80 \text{ GeV}/c, \\
 &R_{H2/H1} < 0.04, \\
 &R_{12} < 0.05, \\
 &N_{\text{tr}} < 2 \quad (p_t > 1.5 \text{ GeV}/c, 0.1(0.15) < \Delta R < 0.2(0.25) \text{ for } |\eta| < (>)1.74, \\
 &R_{\text{pt}} < 0.03 \text{ (same definitions),} \\
 &N_{\text{tr}}^{\text{match}} > 0 \quad (p_t > 20 \text{ GeV}/c). \tag{B.1}
 \end{aligned}$$

B.5 Efficiency of Drell-Yan and heavy resonance production recovery

The efficiency of the recovery procedure designed in section B.4 in case of a missing ECAL endcap at start-up is studied for both signal productions: Drell-Yan electron pairs with mass $M_{\gamma/Z} > 200 \text{ GeV}/c^2$ and Z' bosons with mass of $1 \text{ TeV}/c^2$ (cf. similar discussion in section 6.5.3).

²This implies that, if two electron candidates are found in the installed ECAL parts, no search is performed of an electron in the missing endcap region. The probability of a third particle being wrongly identified as an electron in Drell-Yan events is neglected.

³This procedure is intended to be first applied to all events, with no specific account of a possibly missing ECAL endcap.

	Drell-Yan, $M_{\gamma/Z} > 200 \text{ GeV}/c^2$	Z' , $M = 1 \text{ TeV}/c^2$
Criterion for electron recovery	fraction of events passing the recovery cuts (B.1)	
$p_t(E_{2 \times 2}) > 80 \text{ GeV}/c$	$95.9\% \pm 1.3\%$	100%
AND $R_{H2/H1} < 0.04$	$95.5\% \pm 1.4\%$	$95.9\% \pm 2.0\%$
AND $R_{12} < 0.05$	$88.6\% \pm 2.1\%$	$95.9\% \pm 2.0\%$
AND $N_{tr} < 2$	$88.6\% \pm 2.1\%$	$92.9\% \pm 2.7\%$
AND $R_{pt} < 0.03$	$86.6\% \pm 2.3\%$	$91.8\% \pm 2.9\%$
AND $N_{tr}^{match} > 0$	$74.4\% \pm 3.2\%$	$84.7\% \pm 4.0\%$

Table B.2: Effect of the recovery conditions (B.1), for Drell-Yan events with $M_{\gamma/Z} > 200 \text{ GeV}/c^2$ and for Z' production events with mass = $1 \text{ TeV}/c^2$, with two (real) electrons generated with $p_t > 80 \text{ GeV}/c$ and $|\eta| < 2.4$, when one of the electrons is emitted toward the missing ECAL endcap with $1.56 < |\eta| < 2.4$.

Table B.2 presents the effects of the successive cuts (B.1) for recovering events generated with two electrons generated with $p_t > 80 \text{ GeV}/c$ and $|\eta| < 2.4$, when one of the electrons is emitted toward the missing endcap. The overall efficiencies are of 74% for the Drell-Yan and 85% for the Z' data samples.

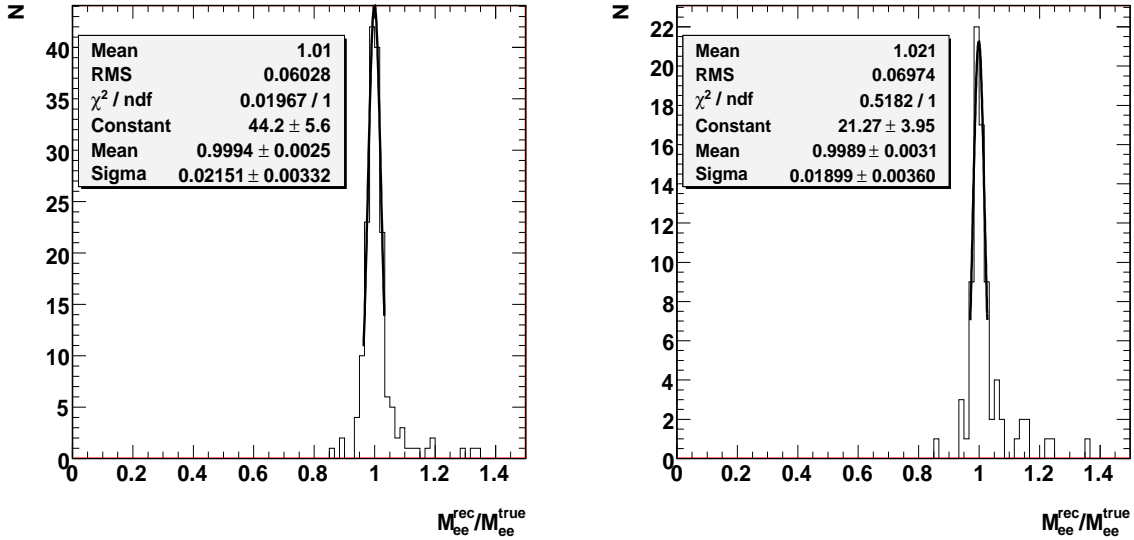


Figure B.5: Distribution of the ratio of the reconstructed over generated M_{ee} mass for e^+e^- events with both electrons emitted in the angular domain $|\eta| < 2.4$, when one of the electrons is emitted toward the missing ECAL endcap, and which are recovered following the criteria (B.1): (left) Drell-Yan events with $M_{\gamma/Z} > 200 \text{ GeV}/c^2$; (right) Z' production events with $M = 1 \text{ TeV}/c^2$ [52].

Figure B.5 presents the resolution of the reconstructed $M_{e^+e^-}$ mass for Drell-Yan events with $M_{\gamma/Z} > 200 \text{ GeV}/c^2$ and for $1 \text{ TeV}/c^2$ resonances, when an electron is emitted toward the missing ECAL endcap, and which are recovered following the procedure based on the criteria (B.1). The mass distributions peak at the generated values, as a consequence of the recalibration procedure, with rms of the distributions of 7%, and for Z' bosons a resolution in the peak region of 2%.

B.6 Backgrounds

The backgrounds to genuine electron pair events due to the recovery procedure in case of a missing endcap are studied in a way similar to the case of the recovery procedure of electrons lost in the EB-EE gaps (section 6.6)

Tables B.3 and B.4 give, for the QCD mulijet and the W+jet backgrounds, respectively, the integrated luminosities used for the analyses and the corresponding numbers of generated events. Columns 4 give the numbers of events containing one electron identified by the HEEP identification criteria (given in Table 5.9) in the ECAL barrel or installed endcap, and in addition a candidate (jet or electron) emitted toward the missing endcap, with transverse energy larger than 60 GeV collected within a cone of radius 0.2. Among these, the total numbers of events passing the recovery cuts (B.1) after reconstruction with a missing endcap are 2.5 for the QCD jet samples and 7.2 for the W+jet sample, for 1 fb^{-1} see (figure).

\hat{p}_t (GeV/c)	int. lumi (pb^{-1})	nb. gen. (kevents)	nb. with 1 HEEP el. (5.9) in EB and 1 possible cand. in missing EE	nb. with a 2d el. cand. passing (B.1)	for 1 fb^{-1}
80-120	0.362	1113	0	0	0
120-170	1.98	977	6	0	0
170-230	8.03	802	5	0	0
230-300	25.3	620	13	0	0
300-380	201	1256	54	1	2.5
380-470	613	1090	49	0	0
470-600	1.93×10^3	1318	63	0	0
600-800	3.03×10^3	611	37	0	0
800-1000	21.4×10^3	743	30	0	0

Table B.3: QCD jet background to the gap recovery procedure: \hat{p}_t scale range, integrated luminosity, number of generated events, number of events containing one electron candidate passing the HEEP identification criteria (given in Table 5.9) in the ECAL barrel or installed endcap and a candidate emitted toward the missing endcap with $E_T > 60 \text{ GeV}$ collected within a cone of radius 0.2, number of events containing in addition an electron candidate passing the recovery cuts (B.1), corresponding number of di-electron events for 1 fb^{-1} .

\hat{p}_t (GeV/c)	int. lumi (pb^{-1})	nb. gen. (kevents)	nb. with 1 HEEP el. (5.9) in EB and 1 possible cand. in missing EE	nb. with a 2d el. cand. passing (B.1)	for 1 fb^{-1}
80-120	85.2	20.3	81	0	0
120-170	365	25.8	390	2	5.48
170-230	1.32×10^3	26.9	699	2	1.51
230-300	4.66×10^3	29.0	1019	0	0
300-380	13.7×10^3	28.3	858	2	0.15
380-470	40.5×10^3	28.8	1185	1	0.02
470-600	95.5×10^3	28.0	1106	3	0.03

Table B.4: Same as Table B.3, but for W+jet jet background (the quoted luminosities and numbers of events are for W bosons decaying into an electron and a neutrino).

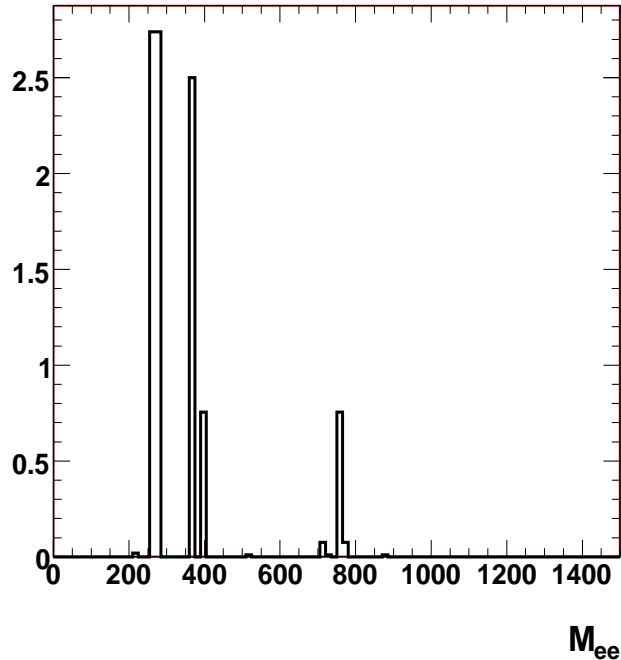


Figure B.6: Mass distribution of QCD and W+jet background for an integrated luminosity of 1 fb^{-1} , when one of the fake electrons is emitted toward the missing ECAL endcap, and which are passing following the criteria (B.1).

The total background from the recovery procedure (B.1) in case of a missing endcap at start-up thus amounts to 9.7 events for an integrated luminosity of 1 fb^{-1} , to be compared to 91.5 recovered Drell-Yan events and 41.5 Z' events. The background events have masses such that they do not contaminate a possible Z' boson signal (0.92 events have masses between 600 and 800 GeV/c) see (figure B.6).

It should be noted that the quality of the recovery procedure can be checked with the data. Indeed, for symmetry reasons, the number of recovered events in the missing endcap region has to be consistent with the corresponding number of events in installed endcap region.

B.7 Conclusions

Procedures have been designed to recover electrons from high mass pair production (Drell-Yan production with $M_{ee} > 200 \text{ GeV}/c^2$ and SSM Z' boson production with $M = 1 \text{ TeV}/c^2$), lost in case of electron emission toward the ECAL barrel – endcap gaps, and in case of a missing ECAL endcap at start-up. The HCAL calorimeter is used for energy reconstruction, and electron identification criteria are defined, which use the longitudinal segmentation and the transverse granularity of the HCAL and the tracker. The designed procedures permit the recovery of 3% of the total number of produced events for the gap procedure; for the missing endcap procedure, 12% of the Drell-Yan events are recovered production, and 14% of the Z' events.

The efficiencies are slightly below 75% and of 85-90%, respectively. The rms of the mass reconstruction distributions are of 7% to 9%, with for Z' bosons a resolution in the peak region of 2%. The backgrounds among the recovered events, due to misidentified jets from QCD multijet and W +jet events, are of the order of 10% for the Drell-Yan events; they are situated below the $1 \text{ TeV}/c^2$ region.

Appendix C

Reconstruction of E_1 using the $F(X, Y; E, \eta)$ functions

For a 5×5 matrix collecting the energy E_{25} , with energy deposits E_1 in the central crystal and E_{24} in the 24 surrounding crystals, one has:

$$E_1 = E_{24} \cdot \frac{E_1/E_{25}}{1 - E_1/E_{25}}. \quad (\text{C.1})$$

The reconstructed E_1 energy, E_1^{rec} , is obtained as

$$E_1^{\text{rec}} = E_{24} \cdot \frac{F}{1 - F}, \quad (\text{C.2})$$

where the $F(X, Y; E, \eta)$ function is obtained from the X, Y, η dependence of the average ratio $\langle E_1/E_{25} \rangle$ (in a first iteration, the energy dependence is neglected).

The average reconstructed value of E_1 is thus:

$$\langle E_1^{\text{rec}} \rangle = \langle E_{24} \cdot \frac{F}{1 - F} \rangle = \langle E_{24} \cdot \frac{\langle E_1/E_{25} \rangle}{1 - \langle E_1/E_{25} \rangle} \rangle = \langle E_{24} \rangle \cdot \frac{\langle E_1/E_{25} \rangle}{1 - \langle E_1/E_{25} \rangle}, \quad (\text{C.3})$$

where the last equality follows from the fact that the ratio $\frac{\langle E_1/E_{25} \rangle}{1 - \langle E_1/E_{25} \rangle}$ is a constant for fixed values of X, Y and η .

This quantity may differ of the average measured value

$$\langle E_1^{\text{meas}} \rangle = \langle E_{24} \cdot \frac{E_1/E_{25}}{1 - E_1/E_{25}} \rangle. \quad (\text{C.4})$$

References

- [1] A. Leike, “*The Phenomenology of extra neutral gauge bosons*”, *Phy. Rep.* **317**, 143 (1999) [arXiv:hep-ph/9805494].
- [2] L. Randall and R. Sundrum, “*A large mass hierarchy from a small extra dimension*”, *Phys. Rev. Lett.* **83** (1999) 3370 [arXiv:hep-ph/9905221].
- [3] “*The Tevatron Collider*”, <http://www-bdnew.fnal.gov/tevatron/>.
- [4] “*The CDF experiment*”, <http://www-cdf.fnal.gov/physics/physics.html>.
- [5] “*The D0 experiment*”, <http://www-d0.fnal.gov/>.
- [6] “*The HEEP Group*”, <https://twiki.cern.ch/twiki/bin/view/CMS/SUSYBSMHeep>.
- [7] D. Evans et al., “*Search for high mass resonance production decaying into an electron pair in the CMS experiment*”, **CMS AN 2008-048** (2008).
- [8] CMS Collaboration, “*Search for high mass resonance production decaying into an electron pair in the CMS experiment*”, **CMS PAS EXO 2008-001** (2008).
- [9] O. Charaf et al., “*Search for high mass resonance production decaying into an electron pair in the CMS experiment at 10 TeV with 100 pb⁻¹*”, **CMS AN 2009-097** (2009).
- [10] CMS Collaboration, “*Search for high mass resonance production decaying into an electron pair in the CMS experiment at 10 TeV with 100 pb⁻¹*”, **CMS PAS EXO 2009-006** (2009).
- [11] M. Cvetič, P. Langacker and B. Kayser, “*Determination of g-R / g-L in left-right symmetric models at hadron colliders*”, *Phys. Rev. Lett.* **68** (1992) 2871.
- [12] S. Dimopoulos and H. Georgi, “*Softly Broken Supersymmetry And SU(5)*”, *Nucl. Phys. B* **193** (1981) 150.
- [13] M. B. Gavela et al., “*Calculation Of Proton Decay In The Nonrelativistic Quark Model*”, *Phys. Rev. D* **23** (1981) 1580.
- [14] M. B. Wise, R. Blankenbecler and L. F. Abbott, “*Three-Body Decays Of The Proton*”, *Phys. Rev. D* **23** (1981) 1591.

- [15] D. A. Sparrow, “*Pion Attenuation Following Nuclear Proton Decay*”, Phys. Rev. Lett. **44** (1980) 625.
- [16] M. Cvetič and S. Godfrey, “*Discovery and identification of extra gauge bosons*”, arXiv:hep-ph/9504216.
- [17] K. S. Babu, C. F. Kolda and J. March-Russell, “*Leptophobic $U(1)$ s and the $R(b) - R(c)$ crisis*”, Phys. Rev. D **54** (1996) 4635 [arXiv:hep-ph/9603212].
- [18] J. Kang and P. Langacker, “ *Z' Discovery limits for supersymmetric $E(6)$ models*”, Phys. Rev. D **71** (2005) 035014 [arXiv:hep-ph/0412190].
- [19] K. Hagiwara et al., [Particle Data Group Collaboration], Phys. Rev. D. **66** (2002) 010001.
- [20] H. Davoudiasl, J. L. Hewett and T. G. Rizzo, “*Phenomenology of the Randall-Sundrum Gauge Hierarchy Model*”, Phys. Rev. Lett. **84** (2000) 2080 [arXiv:hep-ph/9909255].
- [21] CDF Collaboration, “*Search for High-Mass $e^+ e^-$ Resonances in $p\bar{p}$ Collisions at $\sqrt{s} = 1.96\text{-TeV}$* ”, Phys. Rev. Lett. **102** (2009) 031801 [arXiv:0810.2059 [hep-ex]].
- [22] T. Sjöstrand, S. Mrenna, and P. Skands, “*A Brief Introduction to PYTHIA 8.1*”, Comput. Phys. Commun. **178** (2008) 852-867.
- [23] D0 Collaboration, “*Search for high-mass narrow resonances in the di-electron channel at D0*”, **D0 Note 5923-CONF** (2009).
- [24] F. Halzen and A. D. Martin, “*Quarks and Leptons: An Introduction Course in Modern Particle Physics*”, (1984) John Wiley and Sons.
- [25] R. K. Ellis, W. J. Stirling and B. R. Webber, “*QCD and Collider Physics*”, 1996, Cambridge University Press.
- [26] A. Heister et al., “*Measurement of Jets With The CMS Detector at the LHC*”, **CMS NOTE 2006-036** (2006).
- [27] R. Harris et al., “*QCD studies in CMS with high transverse momentum jets at $\sqrt{s} = 10\text{ TeV}$* ”, **CMS AN 2008-080**.
- [28] H. Pi et al., “*Measurement of Missing Transverse Energy With The CMS Detector at the LHC*”, **CMS NOTE 2006-035**, EPJC in press.
- [29] CDF Collaboration, “*Evidence for top quark production in $p\bar{p}$ collisions at $\sqrt{s} = 1.8\text{ TeV}$* ”, Phys. Rev. D **50** (1994) 2966.
- [30] CMS Collaboration, “*The CMS experiment at the CERN LHC*”, **JINST 3 S08004**, 2008.
- [31] CMS Collaboration, “*CMS Physics - Technical Design Report*”, Volume 1: Detector Performance and Software, **CERN-LHCC-2006-001**, 2006.

- [32] CMS Collaboration, “*The Electromagnetic Calorimeter Project, Technical Design Report*”, CERN/LHCC-1997-033, CMS TDR 4 (December 1997).
- [33] Edwige Tournefier, “*The Preshower Detector of CMS at LHC*”, CMS CR 2000-010.
- [34] “*The CMS Offline SoftWare Guide*”, <https://twiki.cern.ch/twiki/bin/view/CMS/SWGuide>
- [35] CMS Collaboration, “*CMS High Level Trigger*”, CERN-LHCC 2007-021, LHCC-G-134.
- [36] CMS Collaboration, “*The TriDAS Project Technical Design Report*”, Volume II: Data Acquisition and High-Level Trigger, CERN-LHCC 2002-026, CMS TDR 6.2 (December 2002).
- [37] CMS Collaboration, “*The Hadron Calorimeter Project, Technical Design Report*”, CERN/LHCC-1997-031, CMS TDR 2 (June 1997).
- [38] E. Meschi, T. Monteiro, C. Seez and P. Vikas, “*Electron Reconstruction in the CMS Electromagnetic Calorimeter*”, CMS NOTE 2001-034.
- [39] S. Baffioni et al., “*Electron Reconstruction in CMS*”, CMS NOTE 2006-040;
“*Electron Reconstruction: e classes, E scale Corrections and E-p Combination*”, CMS NOTE 2005-062.
- [40] C. Shepherd-Themistocleous, Sam Harper, Chris Seez, David Futyan, Dave Evans, “*Robust ECAL Clustering for Early Data*”, CMS NOTE, in preparation.
- [41] F. Ferri and P. Govoni “*The CMS Electromagnetic Calorimeter Pre-calibration with Cosmic Rays and Test Beam Electrons*”, CMS CR 2007-012.
- [42] F. Cavallari, A. Palma, R. Paramatti, “*Linearity of the CMS Electromagnetic Calorimeter from H2 test beam data*”, CMS DN 2007-019.
- [43] P. Adzic et al., “*Energy Resolution of The Barrel of The CMS Electromagnetic Calorimeter*”, CMS NOTE 2006-148.
- [44] G. Grindhammer and S. Peters, “*The parametrized Simulation of Electromagnetic Shower in Homogeneous and Sampling Calorimeters*”, hep-ex/0001020.
- [45] C. Bauer et al., “*Recent results from the RD42 Diamond Detector Collaboration*”, Second International Symposium on development and Application of Semiconductor Tracking Detectors, Hiroshima 1995, Nucl. Instrum. Meth. Phys. Res. A383 (1996) 64.
- [46] Claude Leroy and Pier-Giorgio Rancoita, “*Principles of Radiation Interaction in Matter and Detection*”, 2004, Co. Pte. Ltd.
- [47] B. Clerbaux, Sh. Elgammal, T. Mahmoud and P. Marage, “*Saturation and energy corrections for TeV electrons and photons*”, CMS NOTE 2006-149.

- [48] Sh. Elgammal, B. Clerbaux, G. De Lentdecker and P. Marage, “*Validation of ECAL calibration at high energy and correction for electronics saturation*”, **CMS AN-NOTE** 2009-049.
- [49] V.V. Abramov et al., “*Studies of the Response of the Prototype CMS HADRON Calorimeter, Including Magnetic Field Effects, to Pion, Electron and Muon Beams*”, **CMS NOTE** 2000-003;
G. Baiatian (CMS HCAL Collaboration), “*Energy Response and Longitudinal Shower Profiles Measured in CMS HCAL and Comparison With Geant4*”, **CMS NOTE** 2006-143.
- [50] C.W. Fabjan and T.Ludlam, “*Calorimetry in High-Energy Physics*”, *Ann. Rev. Nucl. Part. Sci.* 32 (1982), reprinted in *Formulae and Methods in Experimental Data Evaluation*, R.K. Bock ed., European Physical Society 1984.
- [51] D. Newbold et al., “*Electron ID at High Energies*”, **CMS AN** 2008-045 (2008).
- [52] Sh. Elgammal, B. Clerbaux, G. De Lentdecker and P. Marage, “*Recovery of high p_t electrons from large mass pairs, lost in CMS ECAL cracks and in case of a missing endcap*”, **CMS AN-NOTE** 2008-029.
- [53] M. Raymond, J. Crooks, M. French and G. Hall, *The MGPA Electronic Calorimeter Readout Chip for CMS*, Proceedings of the 2003 LECC Conference, CERN-2003-006.
- [54] Ph. Miné et al., *Effect of ECAL electronics saturation on L1 trigger and reconstruction*, **CMS IN-NOTE** 2007-056.